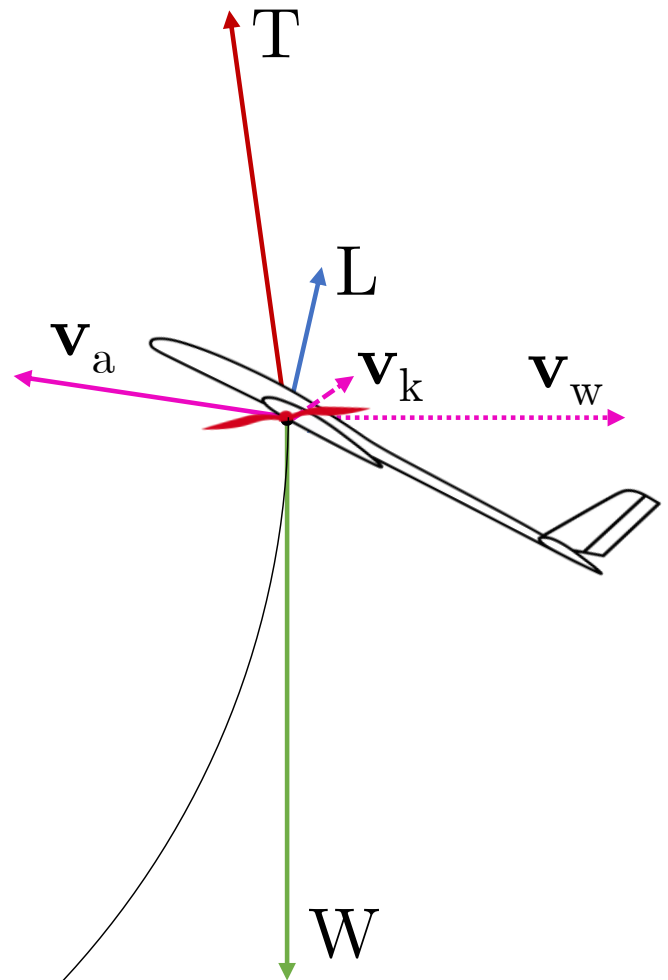


A methodology for design, analysis and optimization of a vertical take-off system for rigid-wing airborne wind energy systems

Niels Pynaert



A methodology for design, analysis and optimization of a vertical take-off system for rigid-wing airborne wind energy systems

by

Niels Pynaert

to obtain the degree of Master of Science
at the Delft University of Technology,
to be defended publicly on Friday January 17, 2020 at 13:00 AM.

Student number: 4277635
Project duration: March 11, 2019 – January 17, 2019
Thesis committee: S. Rapp M.Sc., TU Delft, PhD candidate, Daily supervisor
Dr. ing. R. Schmehl, TU Delft, Associate Professor, Chair & responsible supervisor
Dr. ir. G. la Rocca, TU Delft, Assistant Professor, Examiner
Dr. ir. E. van Kampen, TU Delft, Assistant Professor, Examiner

An electronic version of this thesis is available at <http://repository.tudelft.nl/>.

Abstract

Airborne wind energy (AWE) is a new technology aiming at converting wind energy by flying crosswind patterns with a tethered aircraft. One of the main challenges of this technology is the launching and retrieving of the aircraft. A promising solution is the use of a vertical take-off and landing (VTOL) system in the form of multiple electrically driven rotors. Contrary to other approaches, such as a rotational and catapult assisted take-off, no detailed studies on a VTOL system for AWE have been conducted so far. The goal of this research is to investigate the opportunities and limitations of a VTOL system as a take-off system for a rigid-wing AWE system (AWES), by designing and simulating a VTOL system for the AP2, an AWES prototype of Ampyx Power B.V.

The main research question to be answered by this research is how such a VTOL system can be designed. After having conducted a thorough state-of-the-art analysis (aka. literature study) the main research questions remain and are refined as: 1. What VTOL concept is most suitable for AWE applications? and 2. How do the aerodynamic forces of the AWES effect the VTOL system design? These are addressed and thoroughly analyzed in this report.

The proposed and applied design methodology is based on the mass estimation of the VTOL system and its components: motors, battery and rotors. The sizing of the motors and battery is done by calculating the power and energy demand during take-off. Rotor mass is estimated using a statistical model. To calculate the required power, a blade element momentum model (BEM) combined with generalized momentum theory (MT) is used considering both inflow velocity and angle. A flight mechanics model is derived to calculate the required thrust and aircraft attitude. This model considers propulsion, gravity, and aerodynamic forces.

A multi-disciplinary optimization (MDO) framework is developed to ensure consistency between the above-mentioned models and to calculate the minimum VTOL system mass for certain wind and operating conditions. A Simulink model of the VTOL system is developed using a multicopter flight path controller and a 2D dynamic model. This simulation model serves as a dynamic feasibility check on the VTOL system design and is used to iterate on assumptions taken in the design model.

One of the main findings of this research is that by tilting the rotor depending on wind and flight conditions the minimum VTOL system mass is obtained. The VTOL system mass is estimated at 4.3 kg at wind speeds below 4 m/s and decreases to a mass of 2.1 kg at 10 m/s wind speed. However, for a fixed rotor tilt of -30 degrees (knee-sitter concept, newly introduced in this report), the VTOL system mass is only 100 grams higher for speeds between 5 and 10 m/s. Because a fixed rotor does not require any tilting mechanism, it can be concluded that this concept is most optimal in terms of mass for a direct take-off approach. For the tail-sitter and quad-plane concepts, the VTOL system mass increases with wind speed.

A dynamic simulation has proved the feasibility of the sizing results for the tail-sitter, quad-plane and the new knee-sitter concept for a wind speed of 5 m/s and 10 m/s and a target elevation angle of 41.8 degrees. These simulations have shown that, under the assumptions of the simulation, the maximum motor power (from sizing model) is sufficient to successfully fulfill the take-off phase. It is found that the maximum motor power is only used to accelerate the rotor initially. It is not required in the transient flight phases. Furthermore, it is found that the additional power and energy, required for acceleration and transient phases is sufficiently low compared to the safety factor of 1.5 which has been taken into account in the preliminary sizing model.

Acknowledgements

I would first like to thank my thesis supervisors S. Rapp M.Sc., TU Delft, PhD candidate, and Dr. ing. R. Schmehl, TU Delft, Associate Professor. Both were always available whenever I had a question about my research or writing. They consistently on a weekly basis provided feedback on my project and progress, and allowed this thesis to be my own work, but steered me in the right the direction. Special thanks to my daily supervisor S. Rapp from which I got a swift reply on my e-mails almost before I asked the question.

I would also like to thank the sources who were used in this research project. Without their passionate papers and input, the thesis could not have been successfully conducted.

Finally, I must express my very profound gratitude to my parents for providing me with unfailing support and continuous encouragement throughout my years of study and through the process of researching and writing this thesis. This accomplishment would not have been possible without them.

Thank you.

*Niels Pynaert
Delft, December 2019*

Contents

1	Introduction	1
1.1	Fundamental working principles of airborne wind energy	1
1.2	Classification of airborne wind energy systems	2
1.3	Launching and retrieving mechanism.	3
1.4	Research aim and questions	5
1.5	Research framework	6
2	State-of-the-art review	7
2.1	Research on vertical take-off for airborne wind energy systems	7
2.2	Design methods.	9
2.2.1	Design methods for VTOL systems in airborne wind energy	9
2.2.2	Hybrid drone and multicopter design methods	10
2.3	VTOL system requirements	18
2.3.1	Functional requirements.	18
2.3.2	Performance requirements.	19
2.4	VTOL concepts	20
2.4.1	VTOL system concepts used for airborne wind energy systems	20
2.4.2	General VTOL system concepts	20
2.5	Thrust calculations	25
2.5.1	Flight mechanics.	25
2.5.2	Dynamics transition	26
2.6	Component sizing	27
2.6.1	Rotors	27
2.6.2	Electric motor	35
2.6.3	Battery	38
2.7	System interactions	42
2.8	Synthesis and refinement of research questions.	44
3	Design methodology applied	47
3.1	Requirements and mission profile	48
3.1.1	Take-off requirements	48
3.1.2	Performance criteria	51
3.1.3	Take-off approaches	51
3.1.4	Transition approaches	51
3.2	VTOL concepts	53
3.2.1	Rotor orientation	53
3.2.2	Number of rotors	54
3.2.3	Rotor configuration	54
3.3	System sizing model	55
3.4	Flight mechanics model.	56
3.4.1	Assumptions.	56
3.4.2	Reference frames.	56
3.4.3	Transformation matrices.	56
3.4.4	Forces and moments.	58
3.4.5	Steady flight model	58
3.4.6	Aerodynamic model	59

3.5	Component models	61
3.5.1	Rotor model	61
3.5.2	Motor model	68
3.5.3	Battery model	70
3.5.4	Other subsystems	71
3.6	Design parameters	72
3.7	Multi-disciplinary design optimization (MDO) framework	73
3.7.1	Sizing model	73
3.7.2	Optimization architecture	73
3.7.3	Variables, objective and constraints	75
3.7.4	Optimizer and settings	76
3.7.5	Feasibility and optimality check	76
3.8	Dynamic feasibility	79
3.8.1	Controller	79
3.8.2	Dynamics	84
4	Concept design and analysis	87
4.1	Preliminary results	87
4.2	Direct take-off approach	88
4.2.1	Tilt-rotor concept	89
4.2.2	Tail-sitter concept	97
4.2.3	Quad-plane concept	105
4.2.4	Knee-sitter (-30°) concept	113
4.2.5	Knee-sitter variants	121
4.2.6	Concept comparison.	122
4.3	Synthesis of concept analysis	123
4.3.1	Concept choice	123
4.3.2	Target elevation angle choice	124
4.3.3	Wind speed range choice	124
4.3.4	Operational considerations	124
4.3.5	Landing considerations	124
5	Sensitivity analysis	125
5.1	Effect of requirements	125
5.1.1	Clearance height and non-tilting.	125
5.1.2	Minimum height and tether length	126
5.2	Effect of assumed design parameters	129
5.2.1	Average, optimal and conservative design parameters	129
5.2.2	Battery specific power	131
5.2.3	Rotor diameter.	132
5.2.4	Number of rotors	133
5.3	Dynamic feasibility results	135
5.3.1	Tail-sitter concept	135
5.3.2	Quad-plane concept	141
5.3.3	Knee-sitter (-30°) concept	148
5.4	Synthesis dynamic feasibility	154
6	Conclusions, recommendations and future work	155
6.1	Conclusions.	155
6.2	Recommendations and future work.	157
	Bibliography	161

Introduction

In the context of climate change, environmental sustainability and emission reduction, a transition from fossil based towards renewable energy plants is taking place. Among these plants wind turbines play a major role with increasing installed renewable power around the globe [11]. Wind energy is, in theory, sufficient to provide global energy needs [13]. Most of the wind energy is, however, to be found in higher layers above the ground unreachable with current ground-based wind turbines. At these high altitudes, wind is both stronger and more consistent [13]. In light of this problem, a new technology might offer a solution namely airborne wind energy (AWE). A flying machine aiming at extracting wind energy from these higher altitudes. A variety of airborne wind energy concepts have been proposed. Of them, most resemble an aircraft attached to a tether connecting the aircraft to a ground station. Reaching stronger and more consistent winds is not the only advantage AWE is offering. Compared to ground based wind turbines, AWE needs much less material while producing the same power. This renders the technology more cost effective [13]. Furthermore, AWE has, in theory, the capability of generating power at a megawatt scale for a single plant. With basic calculations it can be shown that a power in the order of 30 MW could be reached with a tethered Airbus A380 [13].

1.1. Fundamental working principles of airborne wind energy

The basis principle on which most AWE systems are flying is cross-wind flight (see Figure 1.1). In this flight the tethered aircraft is flying almost perpendicular through the wind with a velocity higher than the wind velocity. In this condition, the aerodynamic forces extracted with the tether to produce electrical energy, are much higher. Therefore, cross-wind power can provide power with one or two orders of magnitude higher than non-crosswind [11]. In non-crosswind flight, velocity entering the power generating system is of similar magnitude as the wind speed. The concept of cross-wind flight was first introduced by Loyd [29]. He was the first to calculate the maximum power that can be extracted from the wind by an AWES flying cross-wind. Under a series of idealized assumptions (e.g. force balance and constant kite velocity, gravity force negligible with respect to the aerodynamic force, only horizontal wind, no induced effects, no conversion losses), the following power can be extracted [11];

$$P_{AWE} = \frac{1}{2} \rho A (V_w \cos \theta)^3 \frac{4}{27} C_L \left(\frac{L}{D} \right)^2 \quad (1.1)$$

Note that the above equation defines a theoretical limit of the power that can be generated. Some important observations can be made on this first assessment. It can be observed that the lift over drag ratio, as it appears quadratically, is an important property. It should be mentioned however that the tether drag plays an important role in the total drag of the system [13].

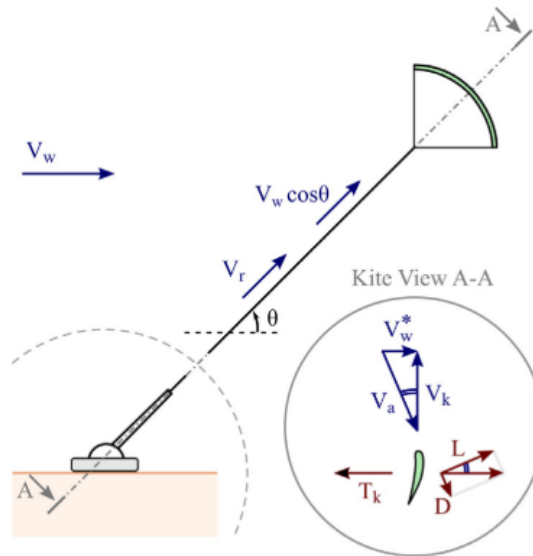


Figure 1.1: Cross-wind model [11]

1.2. Classification of airborne wind energy systems

A first distinction that can be made between Airborne Wind Energy System concepts (AWES) are "ground-gen" (or "lift power") and "fly-gen" (or "drag power") as depicted in Figure 1.2 [11]. Fly-gen systems produce the electrical energy on board by means of turbines. The electricity is then conducted to ground via an integrated electrical cable in the tether. With ground-gen systems, mechanical energy is converted into electrical energy on the ground by means of a force pulling on a tether.

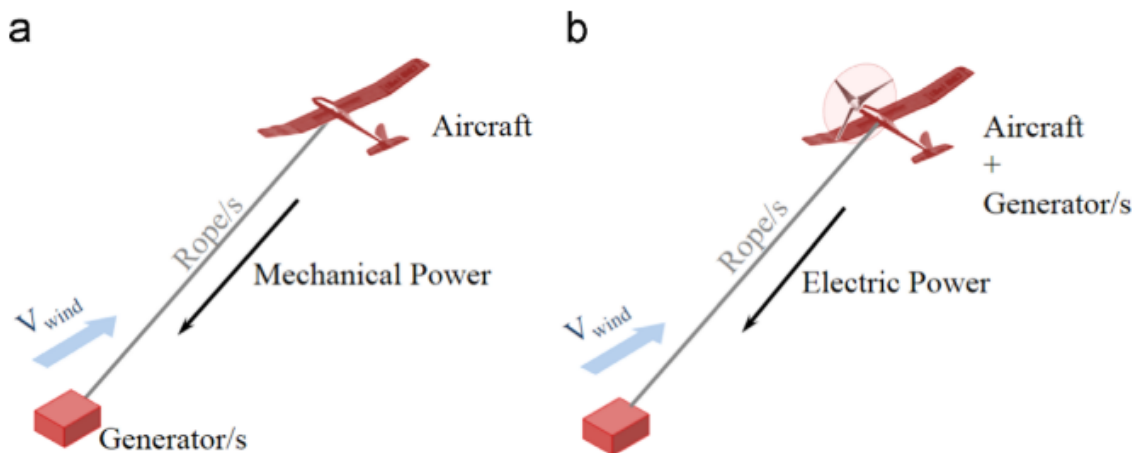


Figure 1.2: Ground-gen (a) and fly-gen (b) AWESs [11]

Another classification is given in Figure 1.3 [43]. Here, ground-gen systems are further categorized whether the ground station (GS) is stationary or moving. For fly-gen (on flying device) crosswind and rotational flight operations are possible. For the fixed ground station crosswind, tether-aligned and rotational flight operations are possible. For the moving ground station, only a crosswind flight operation is pursued. In a tether-aligned flight operation, there is no significant cross-wind component [43].

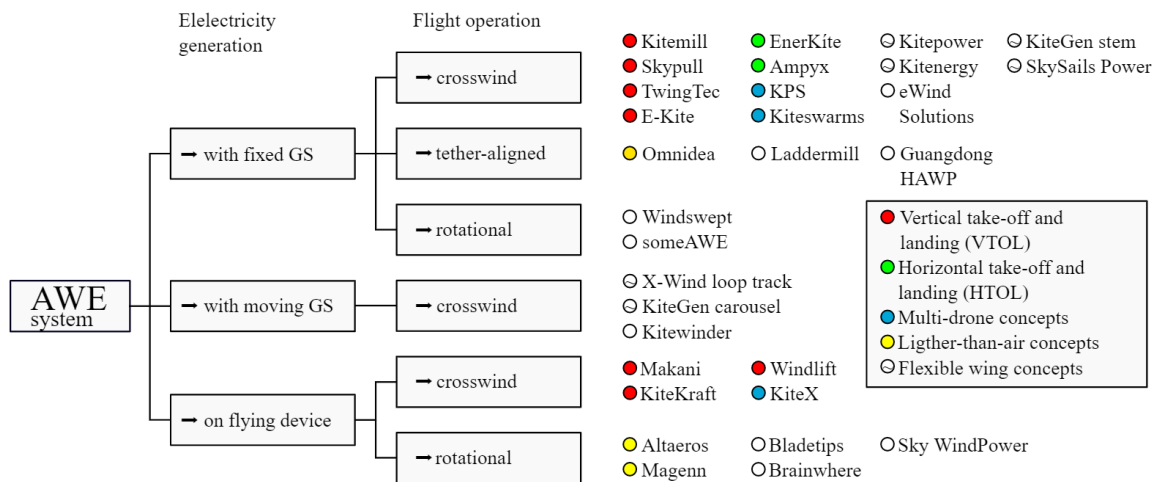


Figure 1.3: AWE technology classification [43]

From latter mentioned concepts, ground-gen with fixed ground station and crosswind flight operation is currently most used in academic research and companies [11]. An exception to this is Makani, using a cross wind fly-gen system, currently leader in AWE technology¹.

Apart from above classification, AWE systems can also be classified based on: aircraft type (e.g. flexible kite, rigid wing, magnus cylinder); steering mechanism (e.g. control ropes, control pod, on-board actuators) or launch and retrieve mechanism (VTOL, HTOL, rotating arm, catapult and winch).

Regarding aircraft type, flexible kite and rigid wing are most common. The main advantages of a flexible or "soft"-kite is that they are safer to test and have a lower weight. Rigid wings are heavier but have a higher aerodynamic efficiency and can therefore reach higher velocities leading to more power to wing area. They're also more durable than soft kites. The trend is that companies are switching from soft to rigid-kites/wings [11]. For this reason, the research presented here is focused to rigid-kites.

1.3. Launching and retrieving mechanism

The advantages of airborne wind energy are clear. But the technology, as all new technologies, comes with some major challenges. One of those challenges is launching and retrieving of the airborne system in a reliable, scalable and cost-efficient manner [8]. Moreover, launch and retrieve should be fully autonomous to render AWE viable [4],[11]. According to Fagiano [14], the takeoff and landing challenge is most pronounced for ground-gen, fixed wing concepts. For the fly-gen concept, the Makani concept, takeoff and landing can be done by using the generators as motors and fly like a multicopter. This concept has proven by Makani to be robust and autonomous. Furthermore, it is independent of wind condition near ground [4]. In this section, different launch and retrieve mechanism for ground-gen rigid AWES are summarized.

Winch launch - For a ground-gen fixed wing concept, without generators, the most conventional is a winch launch similar to gliders. Landing can take place by disconnecting the rigid-kite and land like a conventional sailplane. Soft-kite landing can be done by steering the kite into a "soft crash landing" [4]. This approach requires a large area of land, which would undo the advantage of AWE being installed in a large variety of locations and mobility [14]. Furthermore, it is difficult to automate.

Rotating arm - Another launch and retrieve approach which has been studied is by means of a rotating arm. A rotating arm brings the kite to take-off speed and the tether is extended gradually while rotating. It is according to [14], the only approach which has been studied with numerical simulations in addition to static equations and done by [51]. The approach is been used by company Enerkite. It works in low wind speed at the ground and launch direction can be adjusted. This approach requires no additional power and mass on-

¹Makani Power Inc., <http://www.makanipower.com>

board [14]. The main disadvantage is that the cost of such a complex system can be very high. Furthermore, it requires a very large ground-area occupation compared to the other approaches [14].



(a) Winch Launch (glider¹)



(b) Rotating arm (Enerkite)

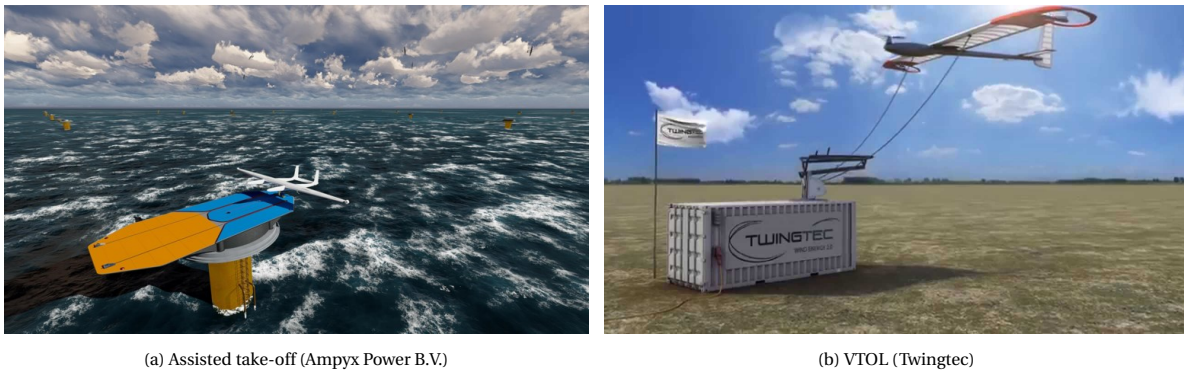
Figure 1.4

1

HTOL with accelerator device - Another more conventional approach is to have a horizontal, assisted take-off and landing (HTOL) using an accelerator device such as a catapult or slide. Small on-board propellers help to climb to operational height. This approach is mostly accompanied by using a break system such as a ground winch or hook to slow down the aircraft and allow short landing [4]. This approach is pursued by the company Ampyx Power. It is independent of the ground wind speed but requires additional infrastructure. On ground peak power for linear take-off is larger than the rotational take-off. The required ground area however is smaller and can be traded against power [14]. Another advantage is that on-board propellers can be used to charge batteries of the control systems and other electronics. The complexity is relatively small and it requires minor modifications to the AWE system [14]. The feasibility and robustness of this approach is, however, quite challenging according to Bauer [4].

VTOL - Last approach considered in literature for ground-gen fixed wing concept is vertical take-off by equipping the aircraft with vertical rotors. This is similar to the concept of on-board power take-off (Makani Power), only now the on-board rotors are used specifically as launch and retrieve system. This approach is pursued by companies TwingTec and Kitemill. It has the advantage that precise landing manoeuvres are possible because the rotors can stabilize the aircraft while it is pulled in with the tether. Furthermore, take-off can take place in an arbitrary direction and in all wind conditions using a small ground area [37]. The main disadvantage is the additional mass and power on-board. The design of the VTOL system can be complex as large accelerations during cross wind flight are expected. Furthermore, a redesign of the wing might be required. The additional mass will lead to a larger cut-in speed as a larger wind speed is required to maintain airborne. The additional rotors increase drag and might decrease lift due to their interference with the wing reducing the generated power of the AWES. Lastly, it is doubted whether control authority is sufficient to stabilize the system in strong winds and gusts [14].

¹East Sussex Gliding Club



(a) Assisted take-off (Ampyx Power B.V.)

(b) VTOL (Twingtec)

Figure 1.5

1.4. Research aim and questions

All launch and retrieve mechanisms have their advantages and disadvantages. There is no clear trend in the literature which is most likely to be successful. This is also clear from the different approaches taken by companies as they vary from company to company (e.g. Ampyx Power, Enerkite, Kitemill).

In contrary to rotating arm and assisted take-off, which has been studied in [18] and [15], such detailed studies are not found for vertical take-off. Nevertheless, as stated before, this approach has been pursued by several companies. It is the aim of this research, to fill this gap by providing a detailed study on the VTOL approach. The research aim is formally stated as follows;

"Investigate the opportunities and limitations of a VTOL system as launching and retrieving mechanism for a lift powered, rigid-kite system by designing and simulating a VTOL system for the AP2 prototype of Ampyx Power B.V."

From this research aim, two (2) main research questions arise: 1. What are the opportunities and limitations of the VTOL system as a launch and retrieve mechanism? 2. How to design a VTOL system for a ground-gen, rigid-kite system? A literature survey has been carried out to answer the latter question. This research develops the design methodology of a VTOL system and is applied on the AP2, prototype of Ampyx Power B.V (without VTOL capability), see Figure 1.6. This aircraft has a mass of 36.8kg, a wing span of 5.5m and a peak power production of 10kW [19]. By performing a design study of the AP2 VTOL system, the first research question is answered.



Figure 1.6: AP2, second prototype of Ampyx Power B.V

1.5. Research framework

The following research framework, depicted in Figure 1.7, is developed as part of and used for this thesis. The research framework has four (4) main processes. This research is initiated with a detailed state-of-the-art review and analysis (Chapter 2). Here the problem statement is further refined and state-of-the-art design methods are reviewed. One of the problems that came across from this analysis is that it is not clear what VTOL concept should be pursued. To tackle this problem, this research is constructed as a concept-driven approach. The design methodology and analysis are implemented accordingly.

The second process is the development of the design methodology. This process consist of four (4) sub-processes: requirements development, doing a system decomposition, defining the appropriate sizing models and finally developing an optimization framework. The optimization framework has the purpose to both solve the sizing model and to calculate the minimum VTOL system mass. The design methodology is explained in detail in Chapter 3.

Third process is the design and analysis of different concepts (Chapter 4). A detailed analysis on the behaviour of the optimization and system variables is done per concept (sub-process A). Furthermore, the general characteristics of each VTOL concept (in particular the VTOL system mass) is analysed (sub-process B) and then a comparative analyse between the different concepts is done (sub-process C).

Last step of the framework is the sensitivity analysis. The effect of design parameter assumptions and requirements is analysed and the dynamic feasibility is checked per concept in Chapter 5.

Note that iterations are required between the processes. In this research the main iterations took place between the design methodology and the concept analysis. The design methodology has been adapted throughout the research based on the results. In this report the final iteration is presented. The requirements and design methodology can be further iterated based on the results of the sensitivity analysis. These iterations are left for further research.

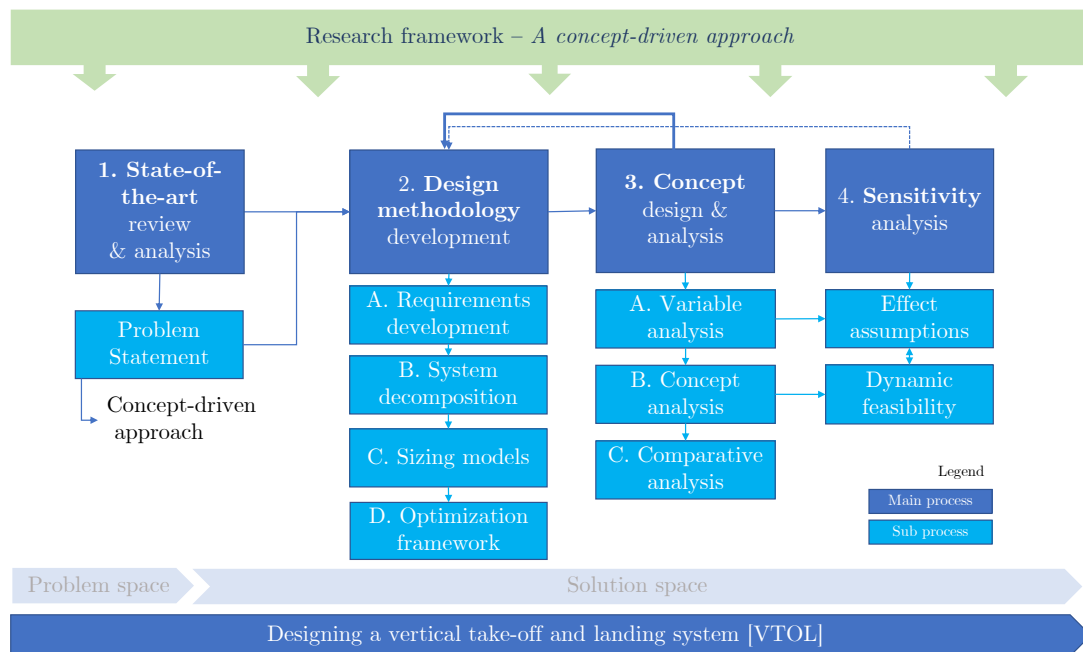


Figure 1.7: Research Framework

2

State-of-the-art review

In this chapter existing literature and research on design and sizing methods for AWE systems with VTOL capability, hybrid drones and multicopter is reviewed. The goal of this review is to propose a design methodology suitable for an AWE VTOL system. First, in Section 2.1 existing research on vertical take-off for airborne wind energy systems is summarized. In Section 2.2, design methods that have been found in the literature are presented. In Section 2.3, the requirements put on the system are discussed. In Section 2.4, different VTOL concepts for both AWE and hybrid drones are presented. In Section 2.5, methods to calculate required thrust are discussed. In Section 2.6, component models and sizing methods are presented. In Section 2.7, interactions between VTOL and aircraft are discussed. Finally, a synthesis of this chapter is given and a refinement of the research questions in Section 2.8.

As this state-of-the-art analysis and literature review were a first deliverable of this thesis the scope as originally delivered has been kept, and not updated reflecting the actual usage during the design process. In the design sections backward references are made.

2.1. Research on vertical take-off for airborne wind energy systems

Research that has been done so far on VTOL AWES is shortly presented here. In the effort of Fagiano [14] to compare several take-off approaches some initial sizing of a VTOL system has been performed. The VTOL take-off power has been calculated as well as the additional on-board mass consisting of battery and electric motor mass. A similar approach to vertical take-off is proposed by Bauer [4] and Rapp [37] for soft kites. A multicopter attached to the kite brings the kite to operational altitude and detaches once the kite is in place. Several soft kite multicopter launch concepts have been proposed. An important distinction is made between energy storage and electrical cable based concept. When using electrical cables, on board energy is not required, but this will not be considered here in this research due to its complexity. To a limited extent, rigid kite VTOL concepts are touched upon in [4]. Aerodynamic forces are neglected in the static analysis, but it is suggested that the wings can be placed in a way they support the rotors during hovering. A static analysis and initial sizing of the multicopter is performed similar to Fagiano [14]. Initial sizing included estimation of power, mass of propulsion unit and battery. The work of Bauer [4] has been extended by Rapp [37]. A similar multicopter sizing can be found in [37] as well. A dynamic simulation of the multicopter is performed by both Bauer [4] and Rapp [37].

The model proposed by Fagiano [14] is used for first analyses. In this model actuator disk or momentum theory as described by Horlock [24] is used. Assuming 1D axial inflow, the power required to deliver a certain thrust is given by Equation 2.1, where η represents a conversion efficiency, v_c the climb speed and A the rotor disk area. The required thrust is assumed to be equal the total weight of the aircraft given by Equation 2.2. The VTOL mass consists of battery and motor mass given by Equation 2.3, other subsystem masses are neglected. To size motor and battery, a specific energy (E_{bat}) and specific power (μ_{mot}) value for the battery and motor are assumed.

$$P = \frac{T}{\eta} \left(\sqrt{\frac{T}{2\rho A} + v_c^2/4} + 1/2 v_c \right) \quad (2.1)$$

$$T = (m_{kite} + m_{VTOL})g \quad (2.2)$$

$$m_{VTOL} = m_{bat} + m_{mot} = P \left(\frac{h_{target}}{v_c E_{bat}} + \frac{1}{\mu_{mot}} \right) \quad (2.3)$$

Equations 2.1-2.3 can be solved iteratively to obtain VTOL mass, thrust and power. For the design parameters given in 2.1 the required VTOL mass, thrust and power are 7.4 kg, 441 N and 13.7 kW respectively .

Table 2.1: Fagiano[14] Parameters

m_{kite} [kg]	37.5	g [m/s ²]	9.81
η_{prop}	0.7	v_c [m/s]	1
D_{prop} [m]	0.5	h_{target} [m]	100
n_{prop}	2	E_{bat} [kJ/kg]	720
ρ [kg/m ³]	1.225	μ_{mot} [kW/kg]	2.5

Few published research can be found on VTOL system design for AWES. Despite, another technology is emerging which resembles much of the VTOL AWES, namely the hybrid UAV. This new type of UAV takes off using VTOL system or multicopter mode and can fly like a fixed wing aircraft. Much more effort has been done so far in this UAV community in both design, simulation and prototyping. Because of the similarity of this technology, the methods used to design the hybrid UAV can be applied in this research. Finally, also literature on multicopter technology is reviewed in this report

2.2. Design methods

In this section various methods used in literature to design VTOL systems will be described. A distinction will be made between the state-of-the-art of VTOL AWE systems and hybrid drones/multicopter. The focus of the hybrid UAV literature is the integration of a VTOL system onto a fixed wing. Whereas, for multicopter the design of the components such as rotors, motors and batteries is performed in more detail.

2.2.1. Design methods for VTOL systems in airborne wind energy

In the design approach of Fagiano [14] the VTOL system mass, which consists of battery and motor mass, is estimated. Both masses are sized according to required power. Assuming an axial climb, momentum theory is used to calculate the power based on the required thrust. A more detailed description of the sizing of battery and motor is given in Section 2.6.

Similarly, sizing of the VTOL system in the papers of Bauer [4] and Rapp [37] consist of estimation the mass of battery and propulsion unit (rotor and drives). Also momentum theory, is used to estimate power. Different assumptions to calculate required power have been by Bauer used as compared to Fagiano. Bauer assumes a hover situation to calculate power, where Fagiano assumes an axial climb. Furthermore, a different strategy to provide a safety factor for taking into account counteracting aerodynamic forces (aircraft) and steering actuation's can be found in the papers. Bauers applies this safety factor on the resulting power, whereas Rapp considers a thrust to weight ratio of 1.5 to take into account aerodynamic forces and steering actuations.

Lastly, it should be noticed that in order to size battery and motor, iterations are required such that there is consistency in the weight of the total system before and after the power estimation. Results obtained by [4], [37] and [14] are given in Table 2.2.

Table 2.2: Initial sizing results VTOL AWE literature

Parameter	Bauer (S ¹)	Bauer (R ²)	Rapp (S)	Fagiano (R1)	Fagiano (R2)	Fagiano (R3)
Wing area [m ²]	20	15		2.5	10	40
Aircraft mass [kg]	5	37.5	15.91	37.5	150	600
Power VTOL [kW]	2.5	36	11	14	56	223
Prop. unit mass [kg]	0.5	7.2	2.7			
Battery mass [kg]	1.6	23.1	4.3			
Mass VTOL system [kg]	2.1	30.3	7	8	30	120
VTOL/aircraft m [kg/kg]	0.42	0.81	0.44	0.21	0.2	0.2
VTOL P/aircraft mass [kW/kg]	0.5	0.96	0.69	0.37	0.37	0.39

The results obtained by the design process taken by [14], [4] and [37], give an initial inside in the potential of VTOL for AWE systems. It can be concluded, while taking a similar approach, discrepancies arise by the different assumptions on certain parameters (see Table 4.2). First, a difference can already be observed in the system requirements expressed by climb velocity, target altitude and take-off time. It can be concluded that no clear requirements exist for VTOL for AWE. Secondly, differences can be observed in design parameters such as thrust-to-weight ratio, rotor efficiency, rotor area, energy density and power density of battery and motor. A more accurate estimation of these parameters can be obtained, by modelling of the components as done in hybrid UAV and multicopter literature.

¹S: Soft wing

²R: Rigid wing

Table 2.3: Parameter assumptions VTOL AWE literature

	Fagiano	Bauer	Rapp
Take-off velocity [m/s]	1	/	1
Target altitude [m]	100	/	180
Take-off time [min]	1.67	5	3
Thrust to weight ratio [-]	1	1	1.5
Safety factor on steering actuations [-]	/	1.5	/
Rotor efficiency [-]	0.7	0.5	0.8
Rotor area [m ²]	0.4 (R1),1.6 (R2),6.3 (R3)	1	0.28
Energy density battery [Wh/kg]	200	130	130
Specific mass motor [kg/kW]	0.4	0.2	0.2

Furthermore some major assumptions were taken by all VTOLAWES literature studies. First, the aerodynamic effect of the aircraft is not taken into account. This is a major assumption as the aerodynamic forces can be of the same order to those of the VTOL system. Furthermore the wing and VTOL configuration can be such that the wing supports the VTOL system during take-off [4]. Other aerodynamic forces are the drag of the wing while climbing. These forces can be high due to exposed area of the wing. Lastly, the transition strategy from take-off to power generation phase is not considered in the sizing method.

To resolve issues stated above, a more extensive design method can be used including the aerodynamic effects and sizing of the rotor diameter/efficiency. In literature on hybrid drone these aspects have been taken into account. In the following section, these methods will be presented.

2.2.2. Hybrid drone and multicopter design methods

Due to the increasing popularity of drones or unmanned aerial vehicles (UAVs) for variety of applications and enhanced miniature aircraft technology, effort has been done in proposing design methodology for both multicopter ([35], [50], [2], [17], [6]) and fixed wing UAV. Furthermore, a new type of aircraft, called the hybrid drone/UAV, has gained popularity during the recent years. This aircraft combines the advantages of fixed wing flight and rotary wing. Although a new technology, efforts have also been made in the literature proposing design methodologies for these type of aircraft ([36], [42], [49],[46], [41], [45], [12], [1]). Design methodologies for both multicopter and hybrid UAV have been found to be similar and are treated in parallel in this section. The design of the hybrid UAV also includes the sizing of the wing. In the proposed methods for hybrid UAV the VTOL system is designed in parallel with the fixed wing aircraft. Note that sizing of the fixed wing is not necessary for the problem at hand.

A distinction between two (2) design approaches is found in the literature. First, an approach that will be described as the classical approach. This approach has been derived from the well-known sizing methodology of fixed wing aircraft proposed by Raymer [38]. Here, an initial weight estimation method is introduced based on mission profile and empirical equations. The method is however limited to fuel-based aircraft. This has been addressed by [21], which includes sizing of electric fixed wing UAV by introducing a method to calculate the battery mass fraction. With fundamentals lying in this method, sizing methods for VTOL hybrid UAV have been proposed by [36], [42], [49] and for multicopter by [35] and [17]. The second approach found in literature is an optimization based approach. Here, the design process is formulated as an optimization problem where a certain objective (e.g. weight) is minimized. This approach will be explained later in this section.

A. General design process with classical approach

The general design process taken in the literature is visualized in Figure 2.1. For step 5, the sizing process, the classical approach will be presented here.

1. Requirements

Before starting the design process, it should first be understood what the system has to do. Only then, a proper design can be proposed [6]. 2 types of requirements are considered: Functional and performance requirements. The requirements for VTOL systems are further described in Section 2.3.

2. Market analysis

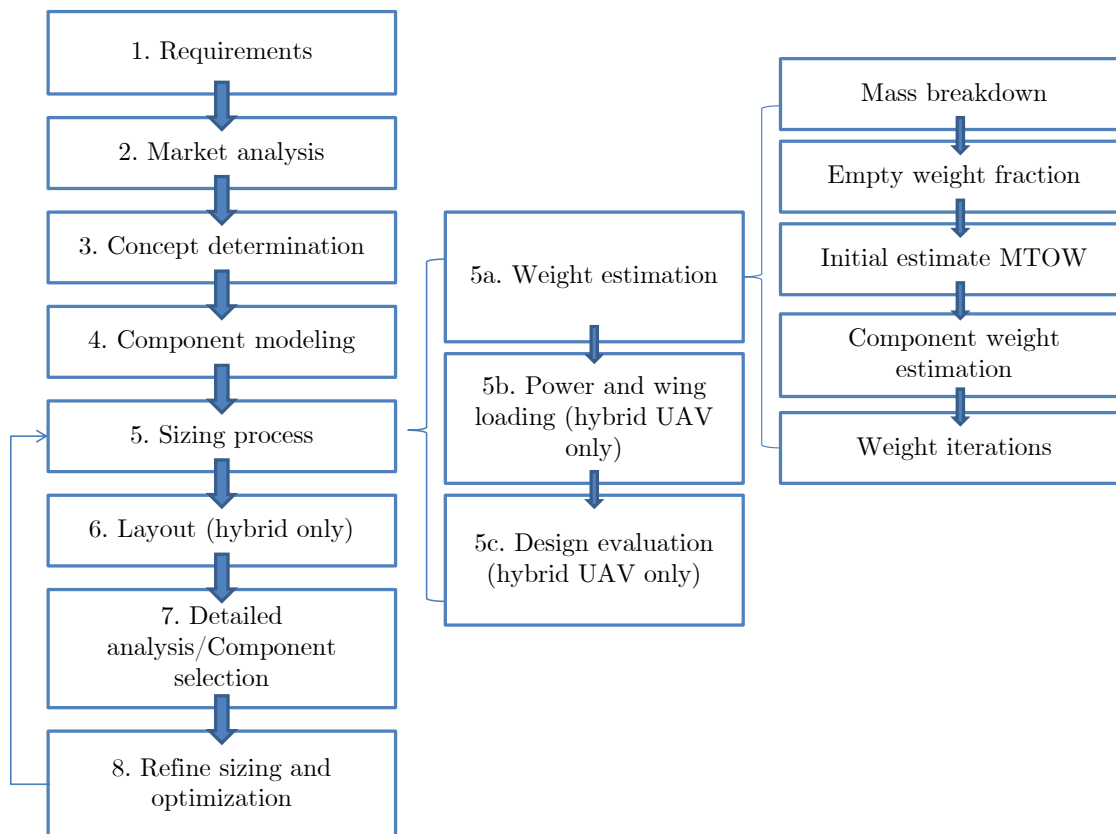


Figure 2.1: General design process with classical approach (own work)

A market analyze should be performed by investigating similar systems. In this step, statistical data is gathered to derive empirical relations for the empty weight relation and component models (see Section 2.6).

3. Concept determination

Based on the requirements and market analysis, a trade-off between concepts should determine which concept will be designed further. Aksugur [1] uses a concept trade-off table to decide which concept is most fit considering the system requirements. Different VTOL system concepts will be presented in Section 2.4.

4. Component modeling

Once the concept is decide upon, appropriate component models should be chosen. Models considered in the literature are rotor, battery and motor models. A summary of all the models can be found in Section 2.6.

5. Sizing process: classical approach

The goal of this process is to match aircraft parameters with requirements. Once the requirements are set and the concept is determined, the initial sizing of the system can take place. This is done by a weight estimation, power and wing loading diagrams and design evaluation. Note that the last two steps are required to size the aircraft (of the hybrid UAV) and are not necessary for the problem at hand.

5a. Weight estimation

The classical weight estimation method consist of several subprocesses being mass breakdown, empty weight estimation, initial estimate maximum take-off weight (MTOW), component weight estimation and weight iterations.

Mass breakdown - The first step in weight estimation is the mass breakdown. A clear definition of what the total system weight and empty weight consists of should be obtained. Ong [35] defines the total weight W_o to be the sum of structure weight W_{str} , motor weight W_m , systems/avionics weight W_{sys} , payload weight W_{pl} , battery weight W_b , non-removable payload W_{fix} . The empty weight is defined as the sum of the structure,

motor and systems weight. The exact definitions can however differ from paper to paper. In the case of a VTOL system for AWE, the payload can be considered to be the aircraft.

$$W_o = W_{str} + W_m + W_{sys} + W_{pl} + W_b + W_{fix} \quad (2.4)$$

$$W_e = W_{str} + W_m + W_{sys} \quad (2.5)$$

Empty weight fraction - Based on statistical data obtained from the market analysis or based on historical data, a relation between empty weight and maximum take-off weight can be obtained. An example of such a relation is given in [42], where empty weight (without multirotor motor, ESC and rotor) is given by Equation 2.6. Gatti [17] uses data from multirotor manufacturers such as Microdrones and Dragonflyer. Based on this data equation 2.7 has been found linking empty weight to total take-off weight. In [35], equations 2.8 and 2.9 are found.

$$W_e = 10^{0.155+0.91 \log W_o} \quad (2.6)$$

$$\frac{W_e}{W_o} = -0.0049W_o + 0.6303 \quad (2.7)$$

$$\frac{W_e}{W_o} = 0.4666W_o^{-0.02} \quad (2.8)$$

$$W_e = 0.37W_o \quad (2.9)$$

Initial estimate MTOW - An initial guess for the MTOW can now be calculated based on the payload requirement and empty weight fraction. This can be done by assuming either no battery weight, obtaining a statistical relation for battery weight fraction (Equation 2.10) or selecting a certain battery (Equation 2.11).

$$W_o = \frac{W_{pl}}{1 - \frac{W_e}{W_o} - \frac{W_b}{W_o}} \quad (2.10)$$

$$W_o = \frac{W_{pl} + W_b}{1 - \frac{W_e}{W_o}} \quad (2.11)$$

Component weight estimation - Based on the initial estimation of the MTOW, weight of the components can be obtained. This can be done by the fraction method or by component models. Tyan [49] uses the fraction method for structure and subsystems. This method assumes the component weight to be a certain fraction of the MTOW based on reference aircraft. These fractions are based on [21], who proposes a fraction of 25-30 % for MF_{struct} . To take into account additional structure for VTOL, Tyan [49] proposes an MF_{struct} of 30-40 %. Furthermore, Gundlach [21] proposes 5% for $MF_{avionics}$ and 5-7 % for $MF_{subsystems}$. For other components, various component models have been proposed (see Section 2.6). For example, Tyan [49] uses empirical equation for the motors mass estimation based on power and voltage. For the battery, weight estimation is based on mission profile, required capacity (calculation of power and energy) and specific mass.

Weight iterations - Now the weight of all the components is determined, a new total weight W_o can be calculated. Iterations are necessary to provide a consistent sizing of the components.

5b. Power and wing loading diagrams (hybrid UAV only)

To size the wing and power plant of the UAV, functional relationships between requirements of wing and power loading are to be obtained and plotted (See Figure 2.2). Note that as this concerns the design of the fixed wing mode, this will only be added here for completeness of the design process. A complete description of this design step of hybrid UAV is not necessary for the problem at hand.

Some effort has been done to introduce a similar concept of power and wing loading for the VTOL system. Here, the thrust-to-weight T/W ratio for hover is determined based on requirements. Following equation is given by Tyan [48], relating T/W to the rate of climb (ROC) requirement.

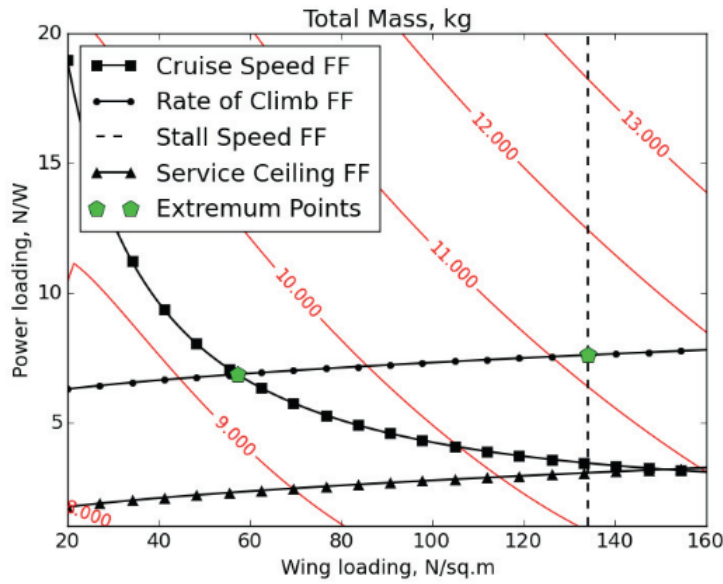


Figure 2.2: Sizing matrix plot of AC total mass[49]

$$TW_{VTOL} = 1 + \frac{1}{W/S} \rho ROC^2 \left(\frac{S_{tot}}{S_w} \right) \tag{2.12}$$

5c. Design evaluation (hybrid UAV only)

With the power and wing loading diagrams obtained from previous step, the best possible configuration of wing and power loading has to be determined. According to [49], this can be done either with sizing matrix plots (See Figure 2.2) or an optimization procedure. Note again that as this concerns the design of the fixed wing mode, this will only be added here for completeness of the design process. A complete description of this design step of hybrid UAV is outside the research.

As an example, the complete initial sizing procedure from Tyan [49] is given in Figure 2.3.

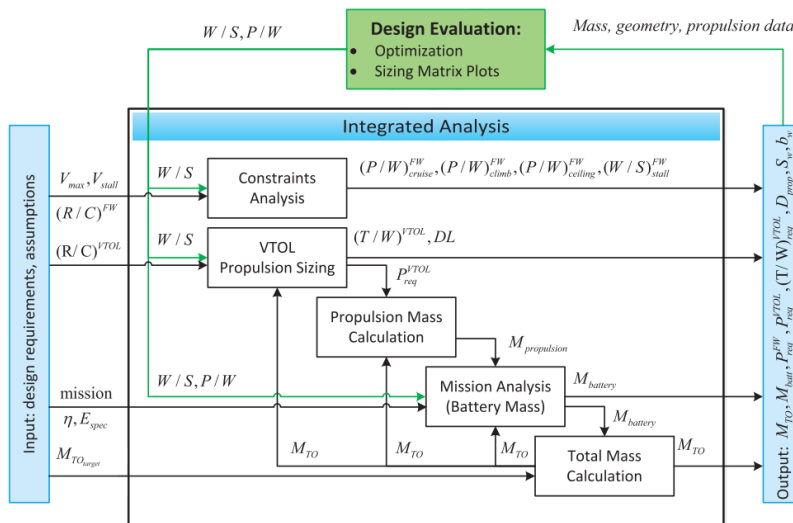


Figure 2.3: Initial sizing [49]

6. Layout (Hybrid UAV only)

In this step the geometry based of wing and power plant is determined based on wing and power loading [49]. This includes wing and tail parameter sizing.

7. Detailed analysis/ Component selection

From this point two different approaches can be taken according to the literature. Some literature obtain a more detailed design of the components. For that more detailed models are used to optimize propulsion, aerodynamics, structure and weight. Higher fidelity models are used here (FEM, CFD, design flight control computer, etc [36]). Another approach is to select existing, off-the-shelf components [49], e.g. battery and motor selection.

8. Refine sizing and optimization

In this step of the design process, the initial sizing design is re-evaluated with the updated design from step 7. The total mass of the aircraft is updated and together with updated aircraft parameters and geometry such as motor mass, rotor diameter, battery capacity the design requirements are checked. Iteration or selection of new components is necessary if this is not the case. This step is visualized in Figure 2.4.

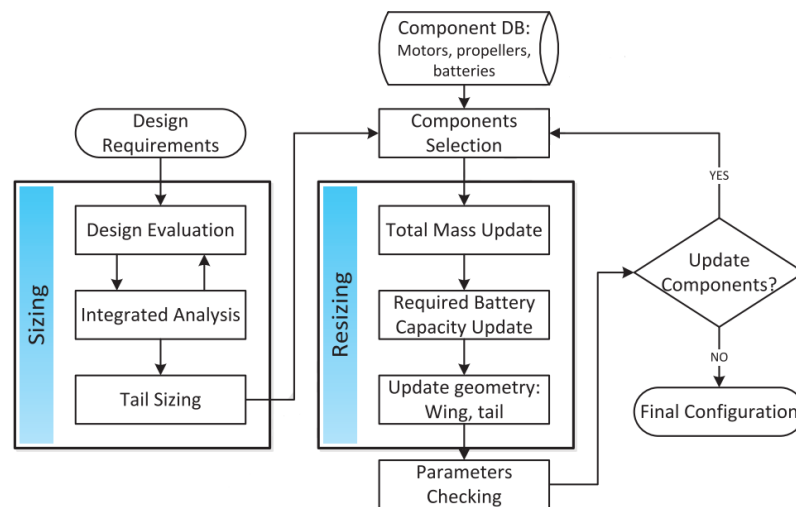


Figure 2.4: FW-VTOL Electric UAV Preliminary Sizing/Resizing Process [49]

B. Optimization based approach

Another design approach found in the literature is the optimization based approach. This approach is used to cope with conflicting directives that design requirements pose on the design [45]. Designing a system can be seen as an optimization problem. A search is to be performed for a design configuration, which minimizes a specific objective, under certain constraints [22]. This objective is mostly a requirement or performance characteristic. The optimization based approach has similar steps as the general design process such as requirements, market analysis, concept phase and component modelling and parameterization activities. However, sizing is approached differently. 4 activities can be identified to be characteristic for this approach, based on the work in [46], [1], [45], [6], [2] and [22]. These are system parameterization and modelling, the definition of the optimization algorithm, off-design performance assessment and sensitivity analysis.

1. System parameterization and modelling

The first activity in the optimization process is the parameterization of the system. Key parameters have to be identified for a preliminary design. Furthermore, the complete system has to be modelled. This is done by modelling the components of which the system consists and combining them in a consistent manner. Note that this step is also required in the classical approach, but it has been observed that component models are often more elaborated and contain more parameters than in the classical approach. As an example, Gur [22] uses a physical model (blade element method) for the rotor, and statistical models for motor and battery based on existing components. In [45] statistical models have been used for engine to power ratio. Physical models have been used for the rotor (blade element method) and aerodynamics (panel method). Furthermore, a structural analysis model, control model and drag model are considered.

2. Optimization algorithm

In this step the optimization algorithm is defined. First the design variables (design vector) and parameters are defined with proper bounds for the variables. Secondly, optimization constraints will have to be defined. Then, the component models will have to be combined to form a system model or function. This expresses itself as a sequence of calculations to calculate the objective. Finally, the optimization procedure will have to be defined. This procedure changes the variables based on the calculated objective and search for the variables that minimizes the objective. A flow diagram of the optimization algorithm is given in Figure 2.5.

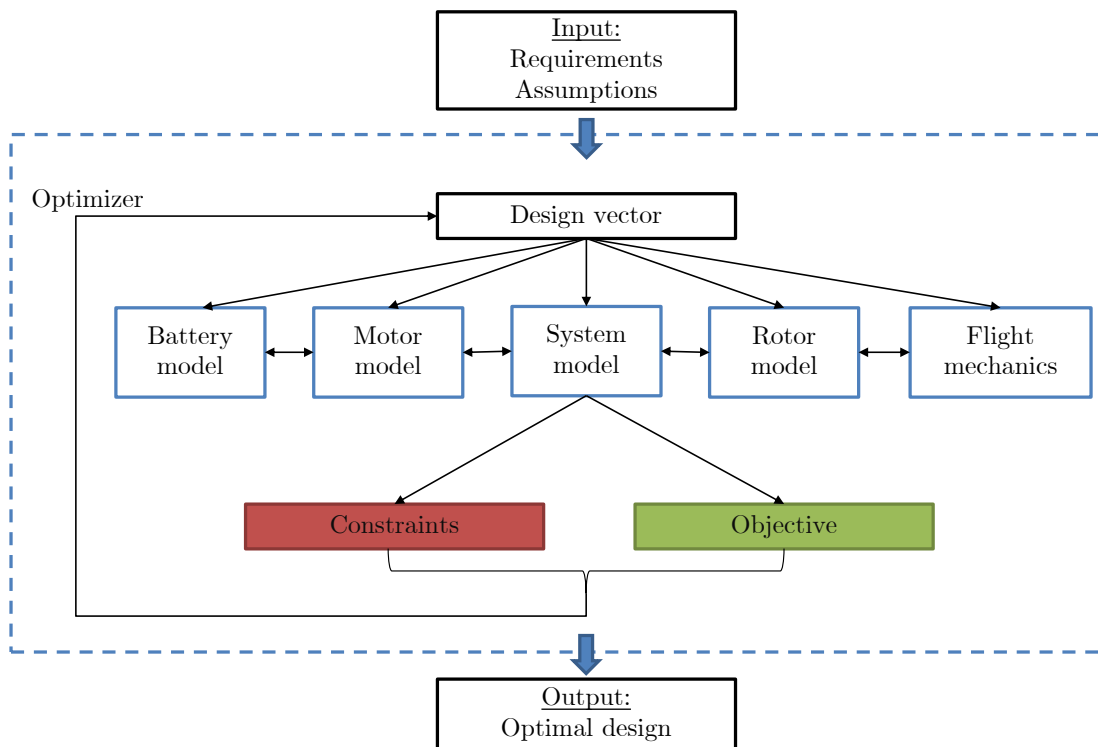


Figure 2.5: General optimizer algorithm (own work)

The goal of the optimization algorithm is to calculate the system variables (output) which minimizes a certain objective for certain user defined requirements (input). Examples of the input (requirements) are payload mass, flight duration, number of rotors [2]. Examples of objectives are weight, size and energy efficiency [6], [2].

2a. Design variables and parameters

By selecting the component models, the system is defined by a number of parameters such as the rotor diameter, battery mass, battery energy density etc. In an optimization algorithm a distinction is made between the system parameters that stay fixed (e.g. battery energy density) and parameters that can change, called design variables (e.g. rotor diameter). The designer is free to choose which variables are varied. For example in [1] some component weights (e.g. motor) are fixed and based on off the shelf components and wing loading and MTOW are design variables, whereas in [46] all these are design variables. In [45], system parameters variables include geometry (e.g. wingspan) parameters and flight conditions. While the fixed parameters include geometrical constraints, performance requirements (e.g. max speed) and assumptions (e.g. power to weight ratio motors). Example design variables and parameters for a VTOL system are given in Table 2.4 and 2.5.

Table 2.4: Example design variables

System	Total mass
Rotor	Mass, Diameter, Number, Number of blades, RPM
Motor	Mass, Dimensions, Number
Battery	Mass, Number of cells, Dimensions

Table 2.5: Example design parameters

System	Take-off speed, Mass payload, Flight time
Rotor	Rotor efficiency
Motor	Power to weight ratio
Battery	Energy density, depth of discharge

Bounds will need to be defined to the design variables such that the design does not end up with an unrealistic or unfeasible design. It should be noted that design variables and parameters are in close relation with the chosen system and component models. For example a low fidelity model will not contain low level parameter/variables such as rotor airfoil. Lastly, whether a system "parameter" is a fixed parameter or variable depends on the user or designer of the optimization algorithm.

2b. Constraints

Constraints can have multiple purposes. First of all constraints can be used to make sure the design is physically consistent [6]. For example to make sure that the MTOW used to calculate performance is the sum of all weight contributions. In this way constraints serves as a similar purpose as the weight iteration of the classical method. Furthermore, it can be used to make sure the system meets certain system requirements. In [45] constraints are used to ensure payload, range, endurance and speed requirements are met. In [22] system requirements are met with constraints such as max allowable stress, maximum motor mass, maximum rotor radius, etc.

2c. Calculations

A calculation procedure is necessary to calculate the objective and constraints based on the system variables and parameters. Following vehicle calculation function is proposed by Stone [45]:

$$[f, g] = \text{vehicle}(X, P) \quad (2.13)$$

Where f is the function value (objective), g contains the values of the constraints, X are the variables (design vector) and P the parameters. This vehicle calculation consist of the combination of components models or system model.

2d. Optimizer

The current optimization problem is multi-disciplinary and constraint based. Furthermore, depending on the objective(s) chosen by the designer, the problem can be multi-objective [1]. In [46] weights are applied to a set of objectives to determine the optimum design. Common used objectives are: weight (minimize) ([45]), payload and cruise (maximize) [1]. The optimizer should make sure that the design vector is searched for that minimizes the objective while meeting all the constraints. This is done mostly in literature by using existing methods and software. Most commonly an optimization algorithm provided by MATLAB is used such as SQP gradient based optimization algorithm in MATLAB [45], [2]. Aksugur [1] uses the MDO software "Esteco ModeFRONTIER 3.2". Bershadsky [6] uses an own developed optimization algorithm.

3. Off-design performance

The design has been optimized for a certain objective or certain conditions. In [46] performance is analyzed at other conditions, for which the design is not necessarily designed for. Performance parameters such as power, range and endurance have been plotted for various speeds. It is important to final check the design for performance at all possible flight conditions.

4. Sensitivity analysis

Throughout the optimization, some parameters were fixed. These include certain assumptions and performance requirements. To see the effect or sensitivity of these parameters, a sensitivity analysis is performed. In this activity the influence of a fixed parameter is examined. This is done by changing 1 fixed parameter and observing the effect on the optimized results. This type of analysis assumes that the parameters are uncorrelated, which is not always the case and can lead to misleading conclusions. This is done in [46] by changing a certain parameter with 10% and observe the change of speed and range on the design. This variation has to take place between different optimization runs. In [6] the effect of payload and number of rotors have

been examined. In [22] the effect of power to weight ratio of motor and battery energy density is examined. Furthermore also the rate of influence has been examined.

2.3. VTOL system requirements

A formulation of the requirements has been identified to be the first step in the design process (Figure 2.1). In the literature on UAV design, functional and performance requirements are considered. Functional requirements are telling "what" activities the system has to perform. In the case of an aircraft design, this is presented as a mission profile: specifications on take-off, cruise and landing. Furthermore, it should be clear "how-well" the system should perform certain activities. They indicate the performance of the system and are expressed in terms of performance requirements. For example, the VTOL system mass and drag are identified as performance parameters. A maximum amount of weight of the VTOL system can be set as a performance requirement.

2.3.1. Functional requirements

Generally speaking the launch and retrieve mechanism (for the problem at hand the VTOL system) should bring the AWE system in a state from which the power generation phase can start and bring it back to ground station if required. The mission profile of the aircraft is visualized in 2.6. However, on time of writing, no detailed descriptions on how the transition between take-off and power generation mode should be executed has been analyzed. Also no simulation studies on the complete mission profile for rigid-kites have been presented in the current literature.

Following observations have been made based on video's from Makani ¹ and TwingTec ² and visualized in Figures 2.6a and 2.6b. The approach of Makani is to hover downwind to a certain altitude and to transition, from that altitude, by acceleration upward into the power generation flight path. Landing takes place by decelerating and hovering back to ground base. Similarly, the TwingTec approach is to hover downwind to a certain altitude. However, instead of accelerating, the AWE aircraft dives to gain speed and transitions into the power generation flight path. It is not clear in both approaches whether the tether is assisting the transition or not. Functional requirements such as the take-off/landing height from which transition occurs, take-off/landing speed are not provided. However, following requirements (see Table 2.6) could be found in [14], [4] and [37] for the initial sizing of the VTOL system .

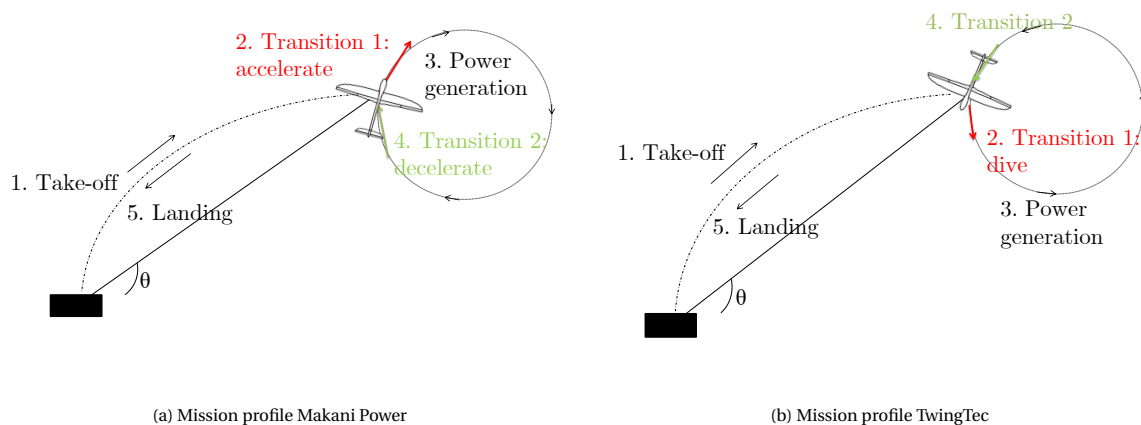


Figure 2.6

Table 2.6: Functional requirements VTOL AWE

	Fagiano	Bauer	Rapp
Take-off velocity [m/s]	1	/	1
Target altitude [m]	100	/	180
Take-off time [min]	1.67	5	3

¹Testing Makani's M600 energy kite in Spring 2017 (<https://www.youtube.com/watch?v=CKFIMDUHtLg>)

²Wind Energy 2.0 Demonstrated (TwingTec 2018) (<https://www.youtube.com/watch?v=d66udNrnMnU>)

Regarding the target altitude and position after take-off, it is argued in [7] that the take-off phase of the VTOL system is accomplished, once following conditions are met:

- An altitude is reached at which the wind velocity is large enough to lift the aircraft without aid of the VTOL system.
- Operational altitude is reached at which power generation patterns are flown.
- Unwound cable length is sufficiently long and the aircraft is in a position at which a transition manoeuvre to the power generation phase is possible.

Furthermore in [7], a further distinction is made between aircraft related and operational requirements. Aircraft related requirements are given by the aircraft dimensions, minimum and maximum velocity, maximum accelerations and additional weight.

2.3.2. Performance requirements

In Fagiano [14], performance criteria are introduced to trade-off the different take-off approaches. These criteria together are an indication of the levelized cost of electricity (LCOE). For the problem at hand, they could be used to trade-off different VTOL concepts and transition strategies as well as to optimize the VTOL system.

First performance criteria is the additional power installed onboard, relative to the maximum power the AWE system can produce. Bauer [4] argues that the additional power should be much lower than the AWE system power, if not applying fly-gen concept would make more sense. Second criteria is the additional on-board mass relative to the mass of the AWE system. Note that for a first power estimation (Equation ?? [11]), mass does not seem to play a role. However, Fagiano [14] argues that it is an important parameter in controllability and maneuverability of the aircraft and for the cut-in speed. He argues that the additional mass leads to larger cut-in speed. This has the consequence that a larger wind speed is required to guarantee power generation. Cherubini [11] argues however that increasing the on-board mass decreases tension on the cables. This means a decrease in power production for ground-gen systems and should not be neglected. In contrary, the additional mass would not decrease power production in fly-gen systems as it does not rely on the cable tension. A different observation is however made in [4], Bauer states the additional mass of rotors and battery might not necessarily lead to critical efficiency losses as the reel-in phase efficiency was increased by the additional mass. Also Diehl [13] argues that the gravity force is minor importance in cross-wind flight.

Finally, as can be observed from the theoretical power generated in crosswind flight (Equation 1.1 [11]), Lift over drag ratio plays an important role in the power production of the AWES. It can therefore be argued that additional drag and decrease in lift due aerodynamic interference with the VTOL system causes a decrease in the AWESs output power [14].

2.4. VTOL concepts

The third step in the general design process (see Figure 2.1), is the determination of a concept. Note that the second step, Market Analysis is not further considered in the literature review as at moment of writing, no specification can be found of existing VTOL systems for AWE. Concepts for both VTOL AWES and VTOL UAV or hybrid drones will be presented here.

2.4.1. VTOL system concepts used for airborne wind energy systems

On time of writing, no literature exist presenting an overview of VTOL AWE systems. However, different concepts are currently being developed by AWE companies/start-ups. Table 2.7 represents an overview of those concepts. Furthermore, concepts presented by student projects are found in Table 2.8. It can be observed that the companies pursue different concepts, there is no clear trend towards a certain concept.

Table 2.7: AWE companies VTOL concepts


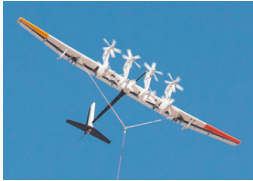




Company	Kitemill [1]	Makani [2]	Twingtec [3]	Skypull [4]
Concept	Fixed quadcopter	8 rotor tail-sitter	Fixed/tilting tri-copter	4 rotor tail-sitter
Image				

Table 2.8: AWE university student projects VTOL concepts

Team	FTERO (ETH Zurich) [5]	TU DELFT DSE [6]
Concept	2 rotor tail-sitter	Fixed tricopter
Image		

2.4.2. General VTOL system concepts

A systematic categorization of hybrid UAV's, integrated fixed wing and VTOL UAV, is given in [41]. A first distinction is made between a converti-plane and a tail-sitter as can be seen from Figure 2.7 given by [41]. The fundamental distinction can be made whether the hybrid UAV converts its propulsion system, in some way, to transition from vertical flight or hover to horizontal flight. Converti-planes are characterized by a different configuration for hover and horizontal flight and maintaining orientation of the airframe. For tail-sitters, the configuration doesn't change. Therefore, the airframe is positioned in a vertical direction for hover and has to take-off and land on the tail. Hence the name, tail-sitter. Both subtypes can be categorized further as can be seen from Figure 2.7.

A. Converti-planes

Tilt-rotor - As the name suggest, the rotors used to provide lift during hover are tilted forward gradually during transition. This will cause the UAV to accelerate forward due to the propulsive force of the rotors. Gaining speed the wings are taking over the lift of the rotors. Further distinction can be made between the amount of rotors (bi-rotor, tri-rotor, quad-rotor). Examples of tilt-rotor UAV can be found in Figure 4.2. The advantage of this mechanism is that the control of thrust direction offers more control authority [41]. Furthermore the transition mechanism is relatively simple compared to other hybrid UAV types. A disadvantages is the need for actuators to tilt the rotors, which adds weight and complexity to the system. Lastly, rotors tend to

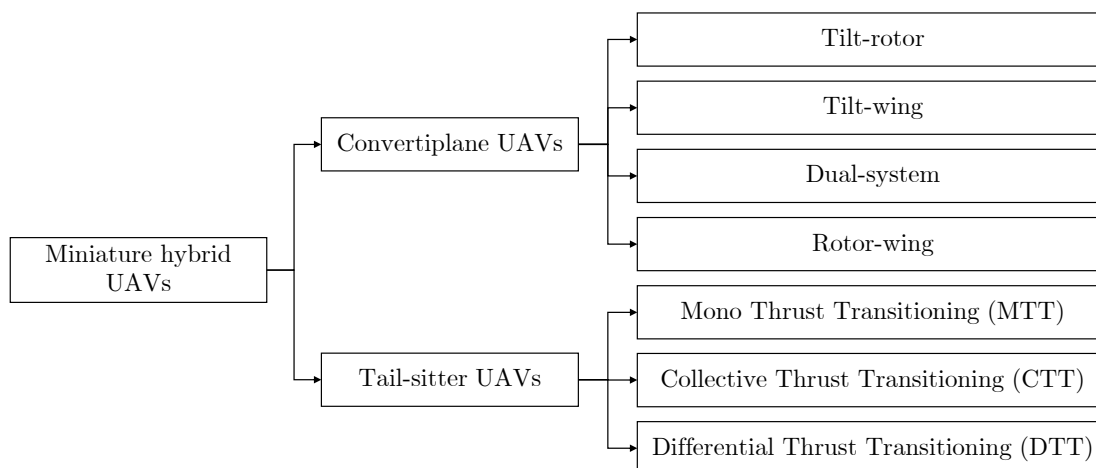


Figure 2.7: Categorization of miniature hybrid UAVs [41]

be most efficient at a certain speed. Therefore when designed for high speed flight, rotors tend to have low performance for hover and vice versa [1].

(a) Bi-rotor (Bell Eagle Eye) ¹(b) Tri-rotor (IAI Panther) ²(c) Quad-rotor (Quantum Tron) ³

Figure 2.8: Tilt-rotor UAV

Tilt-wing - In contrast with the tilt-rotor, the complete wing rotates to transition from vertical to horizontal flight. Further distinction can be made between a single-wing configuration and a tandem wing configuration. Tilt-wing UAV can be found in Figure 2.9. The advantage of this concept is that the propulsion unit can be better integrated into the wing, leaving an aerodynamic benefit. An advantage compared to tilt-rotor is that it allows more design freedom for the wing planform. Whereas tilt-rotor are usually mounted at the tip, forcing a shorter wing span [34]. Another advantage compared to the tilt-rotor is that the slipstream of the rotor hits a smaller part of the wing, so there are less losses in the slipstream [12]. Disadvantages are that it is more sensitive to cross wind and that it requires more powerfull and heavier actuators [41].

¹The eagle eye uav, URL http://www.odec.ca/projects/2004/flor4a0/public_html/v44.htm

²M. Streetly, IHS Jane's all the world aircraft: Unmanned 2013-2014, IHS, 2013

³Quantum tron URL <http://www.quantum-systems.com/products/quantum-tron/>

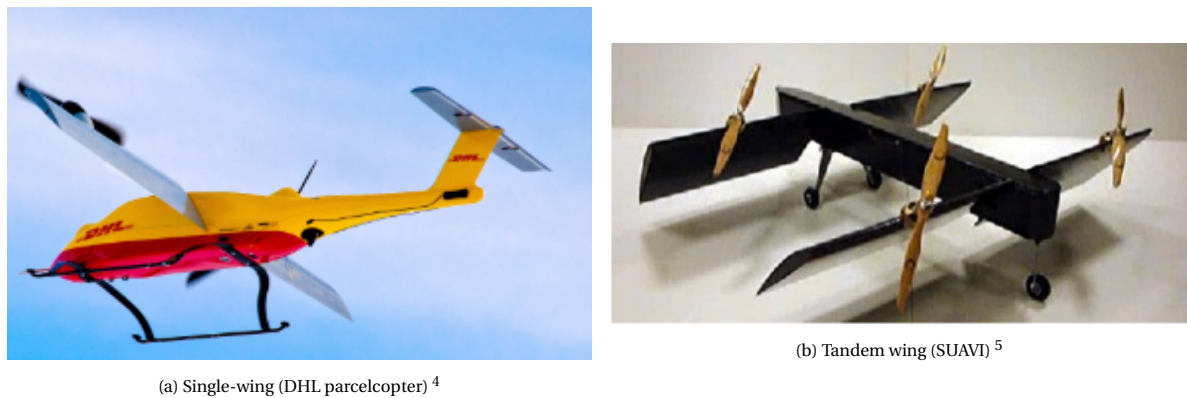


Figure 2.9: Tilt-wing UAV

Dual-System - This concept uses a separate propulsion system for horizontal and vertical flight. Transition occurs by speeding up the horizontal propulsion system and while gaining speed the lift of the wing takes over from the vertical propulsion system. A further classification can be made based on the amount of rotors: compound helicopter, bi-rotors and quadrotor. The quadrotor dual-system is the most popular among dual-system concepts for UAV, whereas the feasibility of bi-rotor is questionable [41]. Dual-system UAV can be found in Figure 2.10. The biggest advantage of a dual-system concept is that no complex tilting mechanism is needed, which enhances the reliability of the UAV. Furthermore, both systems can be optimized for either hover or vertical flight, rendering an efficient propulsion system. Lastly, also the transition mechanism is relatively simple. A disadvantage is the additional drag and weight of having 2 separate systems.

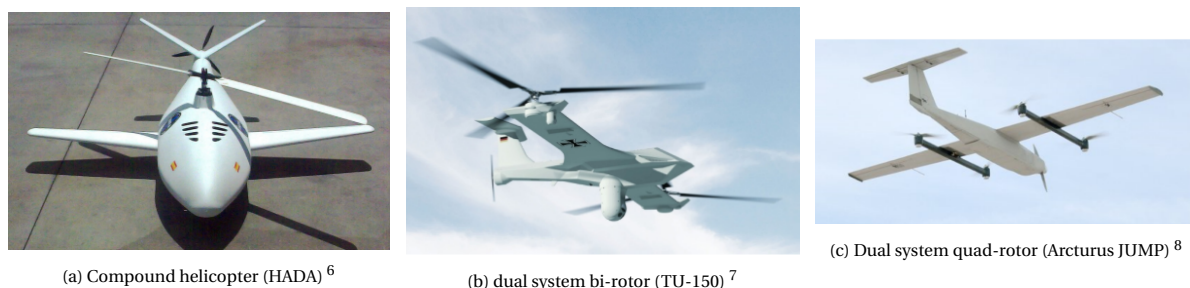


Figure 2.10: Dual-system UAV

Rotor-Wing - In this concept the rotor stops spinning during horizontal flight to provide lift as a normal wing. Not many prototypes of this concept have been found to complete the transition however. It has the advantage of being lightweight but is very complex in terms of both aerodynamics, mechanics and transition.

Hybrid concepts - Previously discussed concepts have their advantages and disadvantages. Creative concepts have been presented in the literature combining these advantages and disadvantages. The TURAC UAV concept [36] is such an example given in Figure 2.11. This concept features two tilt-rotors and two coaxial non-tilt-rotors. The tilt-rotors are active during all flight phases and the coaxial rotor only during VTOL (creating 70-80 % of total lift force). This has the advantage that there is stability in VTOL mode due to the multiple rotors. And it has the advantage that the main rotor can be optimized for hover (high thrust) while the tilt-rotors can be optimized for forward flight (low thrust). A similar concept is proposed by [3], with ducted rotors.

⁴Dhl parcelcopter 3.0,(2016). URL http://www.dpdhl.com/en/media_relations/specials/parcelcopter.html

⁵K. T. Oner et al, Mathematical modeling and vertical flight control of a tilt-wing uav, Turkish Journal of Electrical Engineering Computer Sciences 20 (1) (2012) 149–157.

⁶Hada-helicopter adaptive aircraft, URL <https://www.embention.com/en/projects/hada-helicopter-adaptive-aircraft>

⁷Rheinmetall airborne systems tactical hybrid uas, URL <http://www.uasvision.com/2012/09/03/rheinmetall-airborne-system>

⁸Arcturus uav - complete unmanned aircraft systems, URL <http://arcturus-uav.com/>

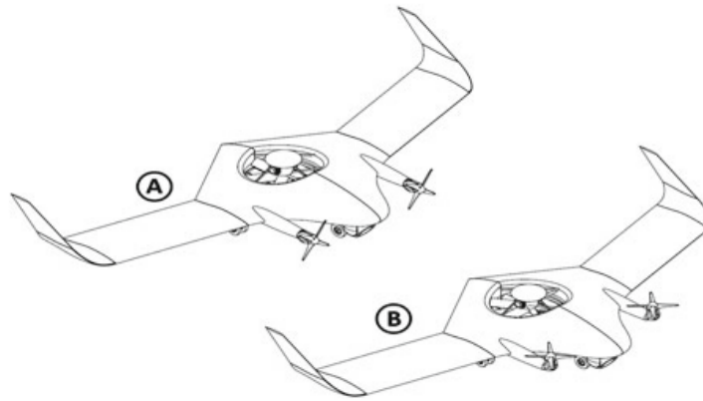


Figure 2.11: TURAC concept [[36]]

B. tail-sitters

Tail-sitter concepts can be found in Figure 2.12. The general advantage of tail-sitters is that no extra tilting mechanism or propulsion system is required, which is beneficial to the performance having less drag and weight. Lastly, there is more design freedom for the wing. The disadvantage is however that propulsion system has to be designed for both horizontal and vertical thrust, which is, as explained earlier, not efficient from a rotor design perspective. Furthermore facing the wing into the crosswind challenges control in high wind conditions.

Mono Thrust Transitioning - The mono thrust transitioning tail-sitter consists usually of a single rotor. Transition has to occur by vectoring the thrust. This can be done by means of ducted fan vanes, tilting propulsion system, cyclic or variable blade pitch propellers. This concept is still at an immature stage. It has the advantage of not having any extra actuators but that makes it very complex in terms of stabilization (unstable vertical flight). Furthermore, an often used transition mechanism is stall-tumble. In this manoeuvre potential energy is converted in kinetic energy by making a controlled stall [45]. However in such a manoeuvre control loss can easily occur.

Collective thrust transitioning - This concept has single or multiple fixed pitch non-cyclic blade rotors. Transition occurs by deflecting control surfaces accompanied by a collective increase or decrease in thrust. Also this concept is still in an immature stage. The advantage of this concept is that the stall-tumble manoeuvre can be avoided. Disadvantages are unstable vertical flight and the ones specific to tail-sitters.

Differential thrust transitioning - In this concept transition occurs by the pitching torque of multiple rotors. It has the advantage that control surfaces can be eliminated, also in horizontal flight which renders an aerodynamic benefit. The advantage is that it is much more stable and controllable in vertical flight than other tail-sitter concepts. This makes it much easier to take-off and land this concept. The disadvantage is the reduced efficiency in horizontal flight due to the multiple rotors.

(a) MTT (SkyTote)⁹(b) CTT (T-wing)¹⁰(c) DTT (ATMOS)¹¹

Figure 2.12: tail-sitters

Dual-system tail-sitter - This concept has not been included in the classification by [41], but proposed by [1]. This concept has the advantage over other tail-sitters that a high diameter and lower weight loading propeller can be used for efficient hovering, while a smaller diameter propeller is used for efficient high speed cruise.

⁹Skytote - the vtol uav that transitions into horizontal flight, URL <http://newatlas.com/skytote-the-vtol-uav-that-transitions-into-horizontal-flight/5>

¹⁰R. Stone, G. Clarke, The t-wing: a vtol uav for defense and civilian applications, University of Sydney

¹¹D. D. Sander Hulsman, Jurjen de Groot, Atmos uav, Leonardo Times.

2.5. Thrust calculations

In order to size the VTOL propulsion system it should be known what force should be generated by the system and for how long. This has been done in the literature on both VTOL AWE, hybrid drones and multicopter using simple flight mechanics. In contrary to dynamic simulations, static force balance is assumed to come up with an initial estimate of the required thrust. The required thrust together with the mission profile (e.g. time of hovering or climb) are used for the initial sizing of the VTOL system.

2.5.1. Flight mechanics

First, the flight mechanics considered in literature on VTOL AWE is discussed. Bauer [4] evaluates thrust by evaluating the weight divided by the amount of motors ($T = mg/n$). A safety factor is included to account for steering and aerodynamic forces of the aircraft. An exact value of the safety factor is not given. But a values of 3 is assumed for the combination of safety factor and propulsion efficiency. Note that this factor is applied on required power and not thrust. Rapp [37] assumes a thrust to weight ratio of 1.5 to calculate the required thrust. Similarly, the thrust in [14] is calculated by assuming force balance ($T=mg$). No safety factor is included accounting for steering.

The flight mechanics included in VTOL AWE neglect aerodynamic forces. According to Dewi [12] drag produced by wing during VTOL cannot be neglected in sizing of the hybrid UAV. More elaborate flight mechanics can be found in literature on hybrid drones where aerodynamic forces are included in some extend. Saengphet [42] considers different thrust requirements for climb, hover and landing. For hovering the required thrust is equal to the total weight [42], [6]. During take-off, thrust requirements is determined by:

$$T_{TO} = \frac{W_o + 0.5\rho V_{TO}^2 SC_{D0,axial}}{n} \quad (2.14)$$

With n the amount of rotors and $C_{D0,axial}$ the drag coefficient in axial direction (perpendicular to the wing). Latter equation assumes no wind and only vertical, steady climb motion. The wing is assumed to be a flat plate and $C_{D0,axial}$ is estimated accordingly to this assumption. Other aerodynamic forces are neglected. A similar equation is used by [49]. Furthermore in [49], to account for tail and fuselage area, the parameter S_{proj}/S is introduced, where S is the wing surface area and S_{proj} the total projected surface area. Based on different aircraft models this parameter is assumed to be between 1.3-1.4. Furthermore 20% thrust is added for trim and withstanding wind gusts. Also flat plate drag assumption is assumed with a drag coefficient $C_{D0,axial}$ of 2. The total thrust-to-weight ratio is than given by:

$$(T/W)_{climb} = 1.2 \left(1 + \frac{1}{W/S} \rho V_{TO}^2 (S_{proj}/S) \right) \quad (2.15)$$

Assuming now vertical, steady descent motion, following equation is used by Saengphet [42] to estimate thrust required for landing:

$$T_{LD} = \frac{W_o - 0.5\rho V_{LD}^2 SC_{D0,axial}}{n} \quad (2.16)$$

Aksugur [1] calculates hover thrust by adding a drag force created by the propeller's induced velocity to the weight of the aircraft (Equation 2.17, with q_i dynamic pressure). To be conservative not only the part of the aircraft wetted by the propeller's induced velocity is used, but the drag coefficient for the whole aircraft. It should be noted that not in every VTOL configuration the aircraft is "wetted" by the induced velocity of the propellers. In [1] this was the case due to the concept of a tailsitter with mounted propeller on the nose of the fuselage.

$$T = W_o + q_i SC_{D0} \quad (2.17)$$

Bershadsky [6] includes lift and drag forces of both lifting and non-lifting bodies, based on the angle of attack, for non-hover situations such as climbing or cruising. The angle of attack at which there is force balance is determined by iterating. No explicit equations are given in the paper however. Similarly, Theys [46] includes the drag of the body and lift and drag of the wing (Equations 2.18 - 2.19). Note that also multicopter thrust is used to provide lift during cruise in the hybrid drone design of Theys [46]. Drag coefficient C_D (based on frontal area) of the body is assumed to be 1. For the drag of the wing, a parabolic lift polar is assumed. D_{D0} represents the drag coefficient at zero lift, AR the aspect ratio and e the span efficiency factor. The lift coefficient is assumed to vary linearly with the angle of attack.

$$D_{\text{body}} = 1/2 V_{\text{cr}}^2 \rho A_{\text{eq}} \quad (2.18)$$

$$L_{\text{wing}} = 1/2 \rho V_{\text{cr}}^2 A_w C_{L_w} \quad (2.19)$$

$$D_{\text{wing}} = 1/2 C_{D_w} V_{\text{cr}}^2 \rho A_w \quad (2.20)$$

$$C_{D_{\text{wing}}} = D_{D0} + \frac{C_L^2}{\pi A R e} \quad (2.21)$$

Rotor forces are given by Equations (2.22- 2.24). The cruise speed can now be calculated by assuming force balance according to Figure 2.13. There is no wind assumed in this model and only previously discusses aerodynamic forces and rotor forces are considered. Furthermore, it is assumed that there is only horizontal (cruise) speed and no vertical (climb) speed. Using system of equations 2.25 and 2.26, the cruise speed can be calculated. The system of equations can also be used to calculated other properties such as F_{plr} or α_{plr} . Note subscripts plr stands for a single propeller and prp for the complete propulsion.

$$F_{\text{prp}} = F_{\text{plr}} n_{\text{plr}} \quad (2.22)$$

$$L_{\text{prp}} = F_{\text{prp}} \sin(\alpha_{\text{plr}}) \quad (2.23)$$

$$T_{\text{prp}} = F_{\text{prp}} \cos(\alpha_{\text{plr}}) \quad (2.24)$$

$$T_{\text{prp}} = D = \frac{1}{2} \rho V_{\text{cr}}^2 (A_{\text{eq}} + A_w C_{D_w}) \quad (2.25)$$

$$L_{\text{prp}} + L_{\text{wing}} = m_{\text{tot}} g \quad (2.26)$$

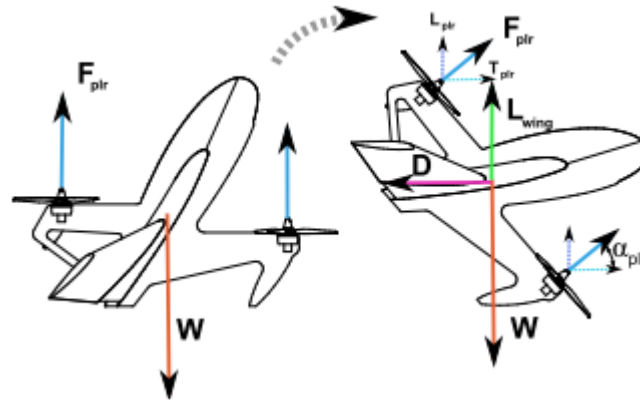


Figure 2.13: Forces acting in hover and cruise [46]

2.5.2. Dynamics transition

The flight mechanics discussed in previous section are purely static. VTOL thrust requirements can be calculated for hover, climb, landing and forward flight. The transition from hover/climb to power generation phase or to vertical flight for hybrid drones is expected to be highly dynamic. A dynamic simulation is therefore required to estimate the required thrust during transition.

2.6. Component sizing

A VTOL system consists of a set of components. The main components are rotor, motor and battery. Sizing of these components has been extensively described in UAV design literature and has the largest influence on the system's performance [22]. Other components include electronic speed controller (ESC), structure, electrical wiring and avionics. In order to design the VTOL system, these components need to be modelled. According to [46] 3 types of methods exist for component modelling: statistical methods, analytical or quasi-analytical methods and design based methods [46]. In a statistical model component characteristics are determined from a large data-set of existing components. A high density is necessary to provide high accuracy. Extrapolating is to be avoided as it can lead to errors, therefore a large variety in the database is required [46]. Analytical or quasi-analytical methods are based on the underlying physics. It therefore does not require a large data-set of existing components. Lastly, a design-based method determines component characteristics based on component-specific parameters

Based on the literature, it is observed that requirements flow from component to component. Using simple flight mechanics the thrust to be produced by the rotors can be calculated. Using a suitable rotor model, the power needed for the rotor to produce this thrust can be determined. The motors will be required to be able to deliver the required power and torque to speed up the rotor. The battery will be required to provide enough energy such that power can be delivered for a certain period of time. All components determine the mass of the VTOL system, which again determines the amount of thrust to be delivered.

In the following subsections models for rotor, motor and battery found in the literature are presented.

2.6.1. Rotors

In this section models used to size the rotors will be used. Note that also the term "propeller" is widely used for this component. Typically, the name propeller is used for a set of rotary blades providing thrust for an aircraft. For a set of rotary blades keeping a helicopter or multicopter airborne, the term "rotor" is used [44]. In hybrid UAV this distinction is not always clear. However, while dealing with a VTOL system, the term "rotor" will be used.

Most important rotor characteristics are rotor diameter, composition, amount of blades, power loading (W/P), disk loading (W/S) and pitch. These characteristics largely determine the multicopter hover, climb, speed, range and autorotate capabilities [28], they should be chosen appropriately based on rotor requirements. According to Aksugur [1], a rotor designed for hovering and low speed is most efficient with a high diameter. This is because for larger rotor diameters, for the same thrust, the induced velocities are smaller, increasing propulsive efficiency [6]. On the other hand, to reach high speeds, a smaller diameter rotor with high induced velocity is more appropriate. The rotor diameter is correlated to the disk loading, defined as weight over rotor disk area [28]. Low weight loading is therefore preferably used for hovering applications. Regarding the pitch of the propeller, rotors/propellers designed for hovering and low speed have a low pitch angles. For high speed, rotor tend to have a high pitch. These rotors are however inefficient at low speeds as they tend to stall in these conditions [1]. Generated thrust can be increased by increasing pitch and amount of blades, but it comes at the cost of decreased efficiency and higher power demand [6]. Bershadsky [6] mentions the effect of the rotor material on the efficiency at different RPMs. Especially for softer and more flexible materials, the blades may change effective angle of attack due to deformations at higher aerodynamic loads.

In [28], following design phases are distinguished in the design of a helicopter rotor:

- 1. General sizing: rotor diameter, disk loading, rotor tip speed
- 2. Blade platform: chord, solidity, number of blades, blade twist
- 3. Airfoil sections

Different methods are used in literature to design the rotor or estimate the rotor performance. Although implemented slightly different, most methods are either based on momentum theory and/or the blade element method (BEM).

A. Momentum theory

The most simple model used in literature to model the rotor is the actuator disk model, also called "momentum theory". It is described in [28] to be the first order prediction of rotor thrust and power. In this model

the rotor is assumed to be infinitely small and has an infinite amount of blades. Over this disk a pressure difference exist causing the generation of thrust. Furthermore, a steady 1D incompressible uniform inflow is assumed. A visualization of this model is given in Figure 2.14 for an axial climb where the velocity is increased by the rotor in order to provide thrust. Following these assumptions and applying mass, momentum and energy conservation on this flow field, an expression for power and thrust can be derived. This is done for hover, axial climb, axial descent and forward flight.

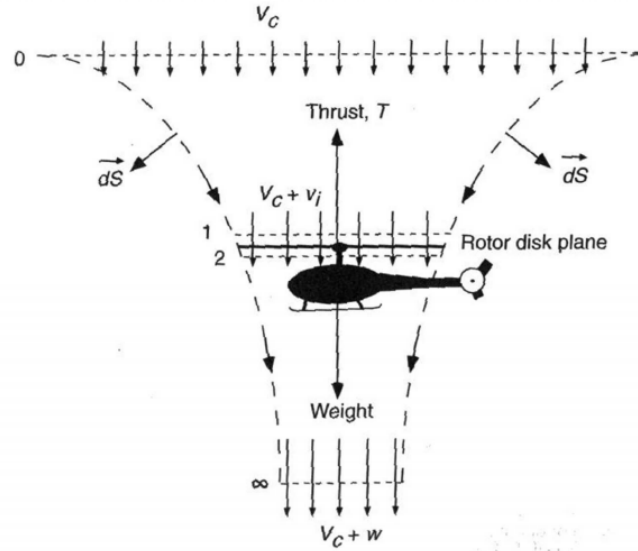


Figure 2.14: Momentum theory flow model (axial climb) [28]

Hover

The simplest form of momentum theory is given in hover mode. The model is given by setting climbing speed to 0 in Figure 2.14. Applying mass, momentum and energy conservation, thrust and power can be related to the induced velocity v_i at the rotor disk and to each other by Equations 2.27-2.29

$$T = 2\rho A v_i^2 \quad (2.27)$$

$$P = T v_i = 2\rho A v_i^3 \quad (2.28)$$

$$P = \sqrt{\frac{T^3}{2\rho A}} \quad (2.29)$$

Equation 2.29 is very powerful as it is a first prediction of the power required to generate a certain thrust. Note that this gives ideal power and assumes uniform inflow with no viscous losses. This formula has been used in the literature by [4], [37], [49],[3],[36],[42]. In literature on VTOL for AWE, equation 2.29 has been used by [4] and [37] to estimate the required power. However, a certain efficiency is accounted ($P_r = P_i/\eta$) for as real propellers require more power than the ideal power. Note that this efficiency represents a total efficiency from energy storage power to propulsion power and includes therefore more than just propeller losses.

Axial climb

Momentum theory can also be used to predict climb performance using the momentum theory model (Figure 2.14). Fagiano [14] uses the actuator disk theory from Horlock [24]. This model is similar to Figure 2.14, where v_{in} equals the climb speed v_c and v_{out} equals climb speed v_c plus velocity at far wake w . Applying mass, momentum and energy conservation, thrust and power can be related to the velocities and to each other by Equations 2.30-2.32.

$$T = \frac{1}{2} \rho A (v_{out}^2 - v_{in}^2) \quad (2.30)$$

$$P = \frac{1}{2} (v_{out} + v_{in}) T \quad (2.31)$$

$$P = T \left(\sqrt{\frac{T}{2\rho A} + v_c^2/4} + 1/2 v_c \right) \quad (2.32)$$

Note that also a conversion efficiency ($P_r = P_i/\eta$) has been accounted by Fagiano [14] for the losses between shaft power and fluid-dynamic power. The rotor efficiency is assumed to equal 0.7.

Estimation of non-ideal effects

Using the momentum theory, as described above, ignores airfoil drag losses, tip losses and losses due to wake rotations. (6% non uniform flow, 30% airfoil profile drag, 3% tip losses, 1 % slipstream)[38]. This has been corrected in the literature on VTOL AWE ([37], [4], [14]) by assuming a certain rotor efficiency. A parameter often defined in rotor design literature is "figure of merit" (FM) defined by Equation 2.33, with P_{ideal} given by momentum theory (Equation 2.29). It is a non dimensional measure of rotor efficiency in hover [28]. For helicopter rotors with good hovering performance, FM values range between 0.7-0.8. [28].

$$FM = \frac{P_{ideal}}{P_{meas}} \quad (2.33)$$

Multicopter rotors used by UAV are much simpler in design and are found to have lower efficiency as compared to manned helicopters. Tyan [49] suggest a statistical model to relate FM and rotor thrust. Using 85 motor-rotor combinations with a thrust range of 3 to 97N³, following regression model has been derived:

$$FM = 0.4742T^{0.0793} \quad (2.34)$$

Ong [35] calculated an average FM of 0.59 for heavy UAV by comparing ideal and measured thrust using Equation 2.35 for propeller sizes between 17-30 inches (0.44-0.76m).

$$FM = \frac{T_{act}^{3/2}}{\sqrt{2\rho A P_{in}}} \quad (2.35)$$

Leishman [28] proposes the following formula for FM using a non-ideal approximation of the power.

$$FM = \frac{\text{Ideal power}}{\text{Induced power} + \text{profile power}} = \frac{P_{ideal}}{\kappa P_{ideal} + P_0} = \frac{\frac{C_T^{3/2}}{\sqrt{2}}}{\frac{\kappa C_T^{3/2}}{\sqrt{2}} + \frac{\sigma C_{d0}}{8}} \quad (2.36)$$

$$C_T = \frac{T}{\rho A (\Omega R)^2} \quad (2.37)$$

$$C_P = \frac{P}{\rho A (\Omega R)^3} \quad (2.38)$$

$$\sigma = \frac{N_b c}{\pi R} \quad (2.39)$$

In Equation 2.36, C_T represents the thrust coefficient, defined by Equation 2.70, κ represents the induced power correction factor taking into account non-uniform inflow, tip losses, finite number of blades and wake swirl. A typical value of κ is 1.15 [28]. It should be noted that a value for κ can also be estimated from more advanced models such as BEM, which will be explained later.

The profile power (P_0) is defined to be the power required to overcome the drag of the blades. To derive the profile power contribution in 2.36, a constant blade section profile drag (C_{d0}) which is independent of Re and M and a rectangular blade is assumed. The effect of a non-constant profile drag, Reynolds and Mach effects can be taken into account in more advanced models such as BEM. σ represents the rotor solidity defined as the ratio of blade area to rotor disk area and given by Equation 2.39 for a rectangular blade.

According to Winslow [50], empirical factor (κ) used by Leishman [28] are not applicable to small scale quad rotors. Winslow [50] conducted windtunnel experiments on a "symba X" quadrotor with different shaft tilts in the upstream flow. Winslow [50] suggest, based on the performed windtunnel tests, to use an induced power factor (κ) of 1.5 for MAV scale rotor as opposed to 1.15 for full-scale helicopter as proposed by Leishman [28].

³"T-MOTOR." [Online]. Available: <http://www.rctigermotor.com/>

Axial descent

Saengphet [42] uses momentum theory to estimate hover and climb performance of the rotor. Furthermore, as opposed to literature on VTOL for AWE, also the axial descent performance is estimated. In the case of an axial descent, the flow velocity in momentum theory model (Figure 2.14) can be either positive or negative when the descent velocity is between 0 and 2 times the hover induced velocity (V_h). In such a flow conditions, no definitive control volume containing the rotor slipstream can be properly defined and therefore momentum theory cannot be used [28]. Because no analytic formula can be derived, such as the momentum theory for hover and climb, power estimations are based on experimental data. Saengphet [42] uses following estimation given by [28].

$$V_i = V_h(1.2 - 1.125x - 1.372x^2 - 1.718x^3 - 0.655x^4), \quad x = -\frac{V_{LD}}{V_h} \quad (2.40)$$

$$V_h = \sqrt{\frac{T}{2\rho A}} \quad (2.41)$$

$$P_{LD} = \left(\frac{T}{FM}\right)(V_i - V_{LD}) \quad (2.42)$$

Where, V_{LD} is the axial descent velocity, V_i the axial descent induced velocity and V_h the hover induced velocity. Note that when the descent velocity is greater than 2 times the hover induced velocity (V_h), the rotor is operating in a windmill break state and extracts power from the flow [28].

Forward flight

The rotor model used in [46] takes into account the effect of forward flight velocity or a rotor operating in a flow non-parallel to the rotor axis. Axial momentum theory has been generalized by Glauert [20] to take into account oblique flow and can be found in textbooks such as [28] and [16].

A rotor in a forward flight flow condition can be found in Figure 2.15, where V the resultant forward flight velocity and V_1 is the resultant velocity at the disk. Applying conservation of mass, momentum and energy, in a similar manner as for hover and climb, one can derive the following equations 2.43 - 2.45.

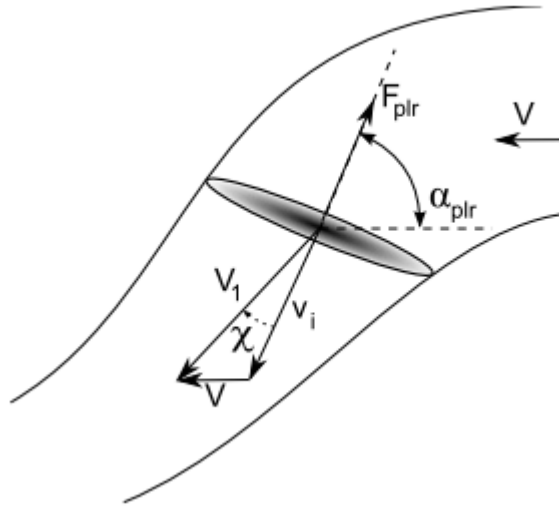


Figure 2.15: Rotor in oblique flow ([46])

$$V_1 = \sqrt{(V \sin(\alpha))^2 + (V \cos(\alpha) + v_i)^2} \quad (2.43)$$

$$F = 2\rho A v_i V_1 \quad (2.44)$$

$$P_i = F(v_i + V \cos(\alpha)) \quad (2.45)$$

Combining Equations 2.43 - 2.45, the required induced power (P_i) to produce thrust F can be calculated provided knowledge of V , α and A . The mechanical power can be calculated if the efficiency η is known. Theys [46] suggest, based on wind tunnel tests that the rotors efficiency is decreasing with skewing angle χ , according to [47]:

$$\eta = \frac{\eta_{\text{hover}}}{4.1e - 6\chi^3 - 0.00028\chi^2 + 0.006\chi + 1} \quad (2.46)$$

where,

$$\chi = \arctan \frac{V \sin \alpha}{(v_i + V \sin \alpha)} \quad (2.47)$$

Blade element method (BEM)

Momentum theory represents a powerful tool to estimate the required power for a rotor to generate a certain thrust. Using the FM power losses can be taken into account which are not included in momentum theory. Estimations of the FM are mostly based on empirical data of existing rotors. Momentum theory therefore does not take into account the effect of higher level rotor parameters such as blade profile, twist and chord distribution. Therefore, some multicopter design papers [2], [45], [50], [1] make use of BEM. This theory/-model is more sophisticated than momentum theory yet computationally inexpensive compared to even more advanced CFD methods. BEM is therefore an important tool in rotor design [28].

The basic idea of BEM is to represent the rotor by 2D airfoil profiles (blade elements) distributed over the rotor radius (see Figure 2.16 [40]). Forces are calculated for all the elements and integrated to compute total rotor forces and performance. By desecrating the rotor in blade elements, the effect of the blade profile, twist and chord distribution can be taken into account. Furthermore as 2D airfoil aerodynamics are considered, the effect of Reynolds number, Mach number and stall can be considered [28]. Iterations in the force calculations are necessary because, not only does the flow field determines the force (as in many aerodynamic application), but now also the force is influencing the flow field.

There are three major velocity components that determine the local velocity U , encountered by the blade element. First, there is the free stream velocity, denoted by V_∞ . Secondly, the speed induced by the rotating motion of the rotor, given by Ωr . Thirdly, there is the velocity V_i , induced by the rotor helical vortex system. This velocity consists of an axial and vertical component. Introducing velocity factors a and a' , for the axial and radial inflow correction factor respectively, the total axial and radial velocity is given by Equations 2.48 and 2.49 [40].

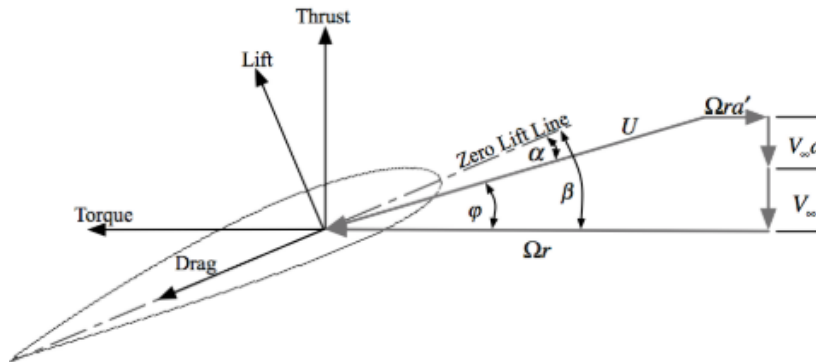


Figure 2.16: blade element Velocity diagram and forces [40]

$$V_a = V_\infty(1 + a) \quad (2.48)$$

$$V_r = \Omega r(1 - a') \quad (2.49)$$

$$U = \sqrt{V_a^2 + V_r^2} \quad (2.50)$$

$$\phi = \arctan \frac{V_a}{V_r} \quad (2.51)$$

The magnitude and direction of the total velocity U , determined by its axial and radial components V_a and V_r , determine the resulting aerodynamic forces on the blade element. From 2D aerodynamic tables, the lift coefficient (C_L) and drag coefficient (C_D) can be obtained as a function of α . The thrust and torque increments on the blade element are then given by:

$$dT = B \frac{1}{2} \rho U^2 (C_L \cos(\phi) - C_D \sin(\phi)) c dr \quad (2.52)$$

$$dQ = B \frac{1}{2} \rho U^2 (C_L \sin(\phi) + C_D \cos(\phi)) c r dr \quad (2.53)$$

dT and dQ are used to indicate that a blade element is considered and need to be integrated along the blade length. B indicates the amount of blades. In order to determine U , first the induced velocity factors must be calculated. The induced velocity correction factors can be calculated by equating the local aerodynamic forces with the bulk momentum transfer [33]. This momentum equation follows from momentum theory which states that the change in momentum along a stream-tube passing the rotor equals the thrust of the rotor [40]. Likewise the change in angular momentum of the stream must be equal to the torque on the rotor. Note that while using the momentum theory in BEM, the model is often referred to as blade element momentum theory (BEMT). Momentum theory applied along a control volume containing the blade element, incremental thrust and torque dT and dQ are given by [40]:

$$dT = 4\pi r \rho V_\infty^2 (1+a) a dr \quad (2.54)$$

$$dQ = 4\pi r^3 \rho V_\infty^2 \omega (1+a) a' dr \quad (2.55)$$

Equating both definitions of thrust and torque, the induced velocity factors can be determined implicitly by:

$$a = \left[\frac{4 \sin^2(\phi)}{\sigma (C_L \cos(\phi) - C_D \sin(\phi))} - 1 \right]^{-1} \quad (2.56)$$

$$a' = \left[\frac{4 \sin(\phi) \cos(\phi)}{\sigma (C_L \sin(\phi) + C_D \cos(\phi))} + 1 \right]^{-1} \quad (2.57)$$

where σ is the local solidity, defined by $cB/2\pi r$. These equations are implicit because ϕ is depending on the velocity correction factors. Iterating is necessary after making an initial guess to obtain the correct values of the velocity correction factors.

While uniform induced inflow velocity was assumed with the actuator disk model/momentum theory. Non-uniform inflow is accounted for in BET by a change of AoA (due to change in relative velocity direction) in each blade section. When a induced velocity distribution is assumed a priori, the forces can be calculated by BET. However as the induced velocity is unknown, BET and momentum theories are linked to form the Blade Element Momentum Theory (BEMT). The major assumption in BEMT remains that there is no mutual influence of neighbouring blade sections. Furthermore, aerodynamic forces are purely based on 2D profile characteristics [40]. However, some 3D effects have been studied by applying empirical factors. Prandtl's tip-loss function is a well known example of this.

Contribution multicopter literature

A diversity of implementations of the BEM have been studied in literature based on different assumptions. A complete description of all implementations is beyond the scope of this report. Instead, implementations used by multicopter design papers will be described here.

Performance parameter used by Ampatis [2] are thrust, power and torque. These quantities are determined by rpm, rotor pitch and diameter. Ampatis uses following definitions for thrust and power coefficient (Equations 2.58 and 2.59). Note the difference with the definitions from Leishman (Equations 2.37 and 2.38).

$$C_T = T / \rho (N/60)^2 D^4 \quad (2.58)$$

$$C_P = 2\pi C_M = P / \rho (N/60)^3 D^5 \quad (2.59)$$

Using blade element analysis, the following equations have been derived under the following assumptions for helicopter rotors [28] and have been used by Ampatis [2]. The out of plane velocity U_P is assumed to be

much smaller than the in-plane velocity U_T , so that $U = \sqrt{U_T^2 + U_p^2} \approx U_T$. The induced angle ϕ is assumed small, so that $\phi = U_p/U_T$. The drag is assumed at least one order of magnitude less than the lift. A rectangular blade is assumed.

$$dC_T = \frac{1}{2} \sigma C_L r^2 dr \quad (2.60)$$

$$dC_Q = \frac{1}{2} \sigma (\phi C_L + C_D) r^3 dr \quad (2.61)$$

These equations can only be solved numerically as C_L and C_D function of α , Reynolds and Mach number. An analytic formulation can be obtained by following assumptions. $C_{l\alpha}$ is assumed constant over the blade. The twist over the blade is assumed zero and $C_D = C_{d0} = \text{constant}$. Lastly, the rotor is assumed to hover and the inflow velocity is uniform. Under these assumptions and using thrust and power coefficient definitions by Ampatis, these coefficients can be calculated according to:

$$C_T = \frac{\pi^3}{4} \frac{1}{2} \sigma C_{l\alpha} \left(\frac{\theta_{0.75}}{3} - \frac{1}{2} \sqrt{\frac{4C_T}{\pi^3 2}} \right) \quad (2.62)$$

$$C_P = \frac{2}{\pi^2} \frac{C_T^{3/2}}{\sqrt{2}} + \frac{1}{8} \sigma C_{d0} \quad (2.63)$$

Note that Ampatis [2] uses the rotor pitch angle at 75% of the rotor radius $R \theta_{0.75}$. According to Ampatis [2] this model can be further simplified assuming constant solidity σ , $C_{l\alpha}$, C_{d0} (no significant change in Reynolds). Therefore thrust and power coefficients are determined by rotor pitch $\theta_{0.75}$. Following model is proposed:

$$C_T = k_1 (p/D_p) + k_2 \quad (2.64)$$

$$C_P = k_3 (p/D_p)^{3/2} + k_4 \quad (2.65)$$

$$\theta_{0.75} = \arctan(4/3\pi p_{0.75}/D_p) \quad (2.66)$$

The constants k are to be calculated using experimental data of geometrically scaled propellers. Data of SPORT type APC rotors are used from experiments conducted at University of Illinois, Urbana-Champaign (UIUC). Measurements were taken on rotor with diameter 17-36 cm.

$$C_T = 0.0266(p/D_p) + 0.0793, R^2 = 0.31 \quad (2.67)$$

$$C_P = 0.0723(p/D_p)^{3/2} + 0.0213, R^2 = 0.83 \quad (2.68)$$

The method used by Stone [45] is based on Goldstein's vortex Blade element theory [32]. A NACA0012 has been used for 2D airfoil data over an angle of attack range from 0 to 180 deg [9]. Mach effect and correct Reynolds number have been taken into account. Induced velocities are calculated and added to the flow field (both axial and tangential) of the wing during hover to simulate rotor-wing interaction. The rotor is characterized in [45] by following twist distribution:

$$\beta = \arctan \frac{p/D}{\pi x} - wx + \theta \quad (2.69)$$

Winslow [50] uses BEM wherein the airfoil forces are determined using in-House CFD software (TURNS2D), proven to have reliable results at low Reynolds. The rationale behind using CFD is to capture aerodynamic effects at low Reynolds number. The BEMT-CFD combination is used to relate hover efficiency (FM) vs C_T/σ , thrust vs rpm, power vs rpm, torque vs rpm, power vs thrust. Results are validated against experiments for a Syma X5 rotor.

Aksugur [1] determines rotor characteristics using JavaProp software (BEM) after selecting a certain rotor and a physical modeling of the rotor's variables. Rotor parameters used in [1] are pitch distribution, chord distribution, rotor airfoil data. Furthermore, a specific thrust (T/P) approach has been used. To do so the following model has been used. Thrust and power coefficients are modelled as a quadratic function of the

advance ratio J (Equation 2.70 and 2.71), where V is the axial flow velocity. Coefficients can be determined using JavaProp software (BEMT) or windtunnel data.

$$C_T = aJ^2 + bJ + c \quad (2.70)$$

$$C_P = aJ^2 + bJ + c \quad (2.71)$$

$$J = \frac{V}{nD} \quad (2.72)$$

C. Statistical models

Momentum theory and BEM are physical models which can be used to estimate rotor performance parameters such as thrust and power. However, they do not provide means to estimate the mass of the rotor. Therefore, statistical models have been introduced in the literature to do so. Furthermore, also statistical relations have been found for rotor diameter, chord and pitch.

Rotor mass

Tyan [49] and Theys [46] use Roskam's method [39] has been to determine rotor mass. In SI units given by:

$$m_{\text{prop}} = 6.514e - 3K_{\text{material}}K_{\text{prop}}n_{\text{props}}n_{\text{blades}}^{0.391} \left(\frac{D_{\text{prop}}P_{\text{max}}}{1000n_{\text{prop}}} \right)^{0.782} \quad (2.73)$$

Where a $K_{\text{prop}} = 15$ is suggested for power lower than 50 HP (37.2 kW). K_{mat} of 1.3, 1.0 and 0.6 are suggested for wood, plastic and composite rotor respectively. Calculating the mass per rotor thereby taking P_{max} for 1 motor for plastic and composite rotor is given by Equation 2.74 and 2.75 respectively. A comparison is made in Figure 2.17a.

$$m[\text{kg}] = 4.4e - 4n_{\text{blades}}^{0.782} (D[m]P_{\text{max}}[\text{W}])^{0.391} \quad (2.74)$$

$$m[\text{kg}] = 2.64e - 4n_{\text{blades}}^{0.782} (D[m]P_{\text{max}}[\text{W}])^{0.391} \quad (2.75)$$

To estimate rotor mass, Winslow [50] suggest a correlation between the rotor mass and design parameters such as radius and blade area. This relation is given by equation 2.76, where R : radius, σ : solidity, N_b : number of blades. It is based on data from rotors with a mass to 25g.

$$m_R = 0.0195R^{2.0859}\sigma^{-0.2038}N_b^{0.5344} \quad (2.76)$$

Ampatis [2] gives following relation (Equation 2.77 based on data of SPORT type APC rotors and experiments conducted at University of Illinois, Urbana-Champaign (UIUC). Bershady [6] provides Equation 2.78 for the estimation of rotor mass. Here, $p_1 = 0.08884, 0.05555, 0.2216, 0.1178, 0.1207$ and $p_2 = 0, 0.2216, -0.3887, -0.5122$ for wooden, plastic, nylon reinforced plastic, carbon fibre rotor respectively. Data of rotors up to 100g have been used. A comparison of these methods can be found in Figure 2.17b.

$$m_p = 0.97573D_p^{2.5741}, R^2 = 0.98 \quad (2.77)$$

$$m_p[\text{g}] = p_1(2R[\text{in}])^2 + p_22R[\text{in}] \quad (2.78)$$

Rotor diameter

Tyan [49] suggest following relation between disc loading and take-off mass to calculate rotor disk area. The relation is based on statistics using 11 multicopters with takeoff masses between 2 and 18 kg.

$$DL[\text{N/m}^2] = 3.2261M_{\text{TO}}[\text{kg}] + 74.991 \quad (2.79)$$

$$S_{\text{prop}} = \frac{W_{\text{TO}}}{DL \cdot n_{\text{prop}}} \quad (2.80)$$

Rotor chord and pitch

Bershady [6] gives [6] a parameterization for the pitch and chord distribution of the rotor based on slowly and direct drive rotors.

$$\beta = p_1r_R^3 + p_2r_R^2 + p_3r_R + p_4 \quad (2.81)$$

where $p_1 = 30.322, p_2 = -64.731, p_3 = 23.008, p_4 = 20.558$.

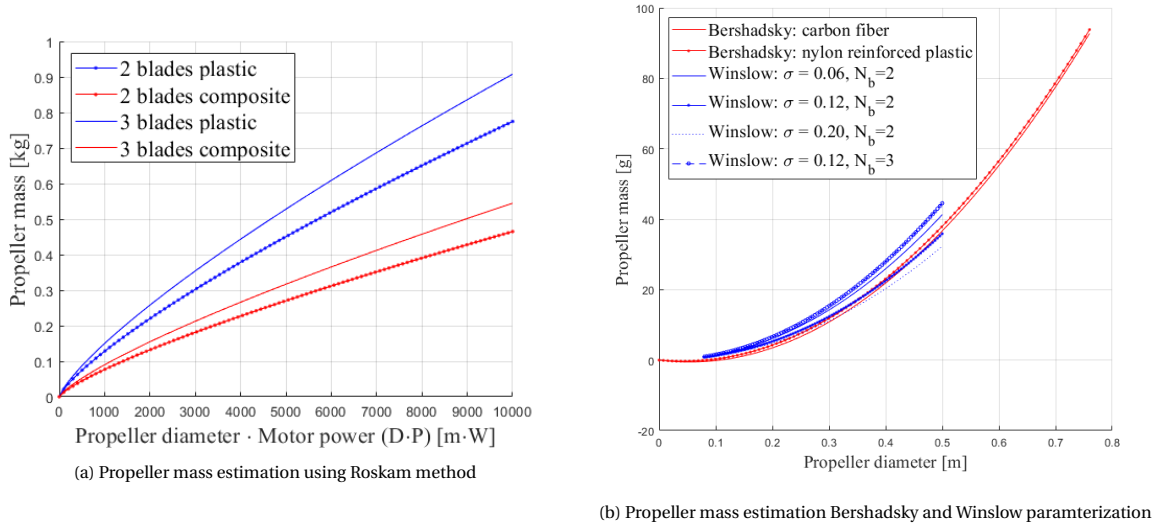


Figure 2.17: Propeller mass parameterization

$$c_R = p_1 r_R^3 + p_2 r_R^2 + p_3 r_R + p_4 \quad (2.82)$$

where $p_1 = -0.2872$, $p_2 = -0.1637$, $p_3 = 0.4551$, $p_4 = 0.05648$.

2.6.2. Electric motor

Several types of electric motor exist. A first distinction can be made between AC (Alternating current) and DC (Direct Current) motor. Because a battery is used as an energy source for multicopter and UAV, the DC motor is used in these types of aircraft. Furthermore, a distinction between brushless (BL) and brushed DC motors can be made. Due to the simple design of a brushed motor in which the static brushes are in contact with the rotating commutator, the brushed DC motors renders itself less efficient and more noisy than the brushless counterpart. For this reason Brushless direct motors are therefore the first choice in multicopter design [2]. For brushless DC motors another distinction can be made between inner and outer runner types. The difference is whether the permanent magnet is located on the inside (inrunner) or outside (outrunner). Mostly outrunner are preferred as they don't require a gearbox as compared to inrunner due to their height torque constant [2]. Furthermore, inrunner allow for a tighter installation, while outrunner produce more torque. Furthermore, inrunners are heavier for a certain K_v than outrunners [6]. Inrunner is only used for very small UAV [6].

Gur [22] characterized electric motors in three groups of manufacturers. Manufacturers of heavy duty/high voltage electric motors, high performance electric motors and aeromodel/ hobby electric motors. The main difference of these motors is the torque and speed. Where heavy duty motors are designed to have high torque and low speed, the opposite is true for aeromodel motors and high performance industrial motors fall somewhere in between.

The motor is required to deliver the required power to the rotor. Furthermore, a sufficient torque must be provided to speed up the rotor. An important parameter in DC motor design is the no-load speed constant K_v [RPM/V]. K_v should be just sufficient to achieve maximum required RPM and matched to the rotor and battery [6].

A. Electrical model

Ampatis [2], Gur [22] and Gatti [17] use a classic three-constant model to model a BLDC. this simple performance model assumes a power factor of 1 and neglects magnetic losses [22]. The model is given by equations 2.83 (Kirchoff's law) and 2.84. Here V_k is the voltage provided to the motor, e_a is the back-electromotive force, i_a the current that flow through the motor and R_a the internal resistance. The electromotive force can be related to the motor angular velocity according to 2.84. Here K_e is the motor back EMF constant [Vs/rad], K_T is the motor torque constant [Nm/A], N is the motor rpm, and K_v is motor speed constant [rpm/V] [2].

$$V_k = e_a + i_a R_a \quad (2.83)$$

$$e_a = K_e \omega = K_T \omega = N / K_v \quad (2.84)$$

The output torque and motor input power is given by Equations 2.85 and 2.86. Here, i_0 is the no-load current.

$$M_{\text{mot}} = K_T (i_a - i_0) \quad (2.85)$$

$$P_{\text{in}} = V_k i_a \quad (2.86)$$

The motor output and motor speed is given by Equations 2.87 and 2.88.

$$P_{\text{mot}} = (V_k - i_a R_a)(i_a - i_0) \quad (2.87)$$

$$N = (V_k - i_a R_a) K_v \quad (2.88)$$

In this model, the parameters K_v , R_a and i_0 determine the motors performance. The electric system efficiency η_s is given by:

$$\eta_s = \eta_D \left(1 - \frac{i_a R_a}{V_k}\right) \left(1 - \frac{I_0}{I_a}\right) \quad (2.89)$$

where, $\eta_D \approx 0.95$ is the driver efficiency considered by Gur [22]. 122

B. Motor sizing and parameterization

In the electric model presented in previous section, the parameters K_v , R_a and i_0 were identified to determine the motors performance. Relations have been found in the literature, based on existing motors, to link these parameters to other characteristics such as mass and power. This section will give an overview of these relations.

Bauer [4] and Rapp [37] consider the mass of the motor in the mass of the propulsion unit (rotor + drives). A specific mass μ_p (0.2 kg/kW) is used to estimate propulsion unit mass (Equation 2.90). In [14] the mass of the electric motor is determined based on the power density E (2.5 kW/kg) and required power (Equation 2.91). Design of motor components in VTOL AWE literature is limited to estimation of mass.

$$m_p = \mu_p P_e \quad (2.90)$$

$$m_m = \frac{P}{E_{\text{mot}}} \quad (2.91)$$

Tyan [49] uses the empirical equation proposed by Gundlach [21] to estimate motor mass:

$$\frac{W_{\text{mot}}}{P_{\text{max}}} = F_1 P_{\text{max}}^{E1} U_{\text{max}}^{E2} \quad (2.92)$$

Here F_1 , $E1$, and $E2$ are empirical factors based on the motor class (Brushless ferrite, Brushed rare earth, Brushless inrunner, Brushless outrunner). For brushless outrunner, these constants are 0.889, -0.288 and 0.1588 respectively.

The design of motors is more detailed in [50]. A relation is obtained between mass of the motor, motor speed constant, max rated power output, motor casing length and outer motor diameter based on regression of data from manufacturers such as Turnigy, ProTronik, NeuMotores, and Portescap. Note that these motors are aimed for MAV and have a mass up to 100g. For brushless motors this equation becomes:

$$m_{BL} = 0.0109 K_v^{0.5122} P^{-0.1902} (\log l_{BL})^{2.5582} (\log d_{BL})^{12.8502} \quad (2.93)$$

Furthermore following relations has been found between diameter and length of the motor and performance parameters being maximum power, maximum current and motor speed constant. Note that different formulas and relations have been found for Brushed DC motors. For brushed motor the max torque has been used to predict motor length and diameter.

$$l_{BL} = 4.8910 I^{0.1751} P^{0.2476} \quad (2.94)$$

$$d_{BL} = 41.45K_v^{-0.1919}P^{0.1935} \quad (2.95)$$

Outrunner BLDC motor from AXI have been parametrized by Ampatis [2]. This parameterization has been done based on the equivalent length (l_{mot}). This equivalent length is defined as the cubic root of the volume. Performance parameters (K_T , R_a and i_0) from the electrical model are related to this equivalent length through Equations 2.96-2.100.

$$K_T/R_a = 2.6533 \cdot 10^4 l_{mot}^{3.6032}, R^2 = 0.902 \quad (2.96)$$

$$K_T^2/R_a = 1.7548 \cdot 10^5 l_{mot}^{5.4833}, R^2 = 0.94 \quad (2.97)$$

$$M_0 = K_T i_0 = 5.7721 \cdot 10^2 l_{mot}^{3.1888}, R^2 = 0.908 \quad (2.98)$$

$$M_{max} = K_T(i_{max} - i_0) = 4.5004 \cdot 10^5 l_{mot}^{4.2222}, R^2 = 0.96 \quad (2.99)$$

$$N_{m,max} = (n_{c,max}3.7 - i_0 R_a)K_v = 25604e^{-17.687l_{mot}}, R^2 = 0.35 \quad (2.100)$$

Here, $n_{c,max}$ being the maximum number of battery cells in series. Finally, the motor mass can be calculated by the mean motor density $\rho_{mot} = 2942 \text{ kg/m}^3$ [2].

Based on a selection of Motocalc databases⁴ with motor masses between a few grams and 2.5kg, following trends have been determined by Gatti [17] (Equations 2.101, 2.102).

$$P_{out-max} = 4140.8m_M \quad (2.101)$$

$$K_v = 286.5m_M^{-0.586} \quad (2.102)$$

Bershadsky [6] made the following parameterization (Equation 2.103) based on motor of weight ranging between a few grams and 10 kg. Equation 2.104 is given by Gur [22]. The value of B_{PM} is very dependent on the type of motor as can be seen in Figure 2.18a (heavy duty; solid symbols, high performance; empty symbols, aeromodel + or x). Heavy duty motors exhibit low power to weight ratio, while aeromodel motors exhibit high power to weight ratio. For the reason of better reliability and endurance, Gur [22] suggest the use of high performance motors for UAV design. This motor group exhibits a B_{PM} between 110 and 800 W/kg. A typical value of 200 W/kg is taken in further analysis. However, as can be observed from Figure 2.18b, relations provided by other papers uses the higher power to weight ratio provided by aeromodel motors.

$$m_m = 10^{4.0499}K_v^{-0.5329}[\text{g}] \quad (2.103)$$

$$P_{out-max} = B_{PM}m_M \quad (2.104)$$

Relation 2.105 is used by [22] for the speed constant. Using data from previous mentioned manufacturers (data power) and data from MotoCalc it can be observed that B_{Kv} falls between 50 and 600 [RPM kg/V]. A typical value of 170 is used. Relation 2.106 is used by [22] for the motors resistance. Using data from previous mentioned manufacturers (data power) and data from MotoCalc it can be observed that B_{Ra} falls between 2,500 and 1,000,000 [$V^2\omega/RPM^2$]. A typical value of 60,000 is used. Relation 2.107 is used by [22] for no-load current. Using data from previous mentioned manufacturers (data power) and data from MotoCalc it can be observed that B_{I0} falls between 0.1 and 0.4 [$A\Omega^{0.6}$]. A typical value of 0.1 is used.

$$K_v = B_{Kv}/m_M \quad (2.105)$$

$$R_a = \frac{B_{Ra}}{K_v^2} \quad (2.106)$$

$$I_0 = \frac{B_{I0}}{R_a^{0.6}} \quad (2.107)$$

Based on a market survey performed by Ong [35] and limited to a K_v of 500, the following relations were found. Lastly, a motor is selected in [35] based on the power requirement. To make sure the motor is operating at optimal conditions, the motor is selected such that $0.4P_{max} \leq P_{req} \leq 0.7P_{max}$ based on [10].

⁴Data available online at <http://www.motocalc.com/>

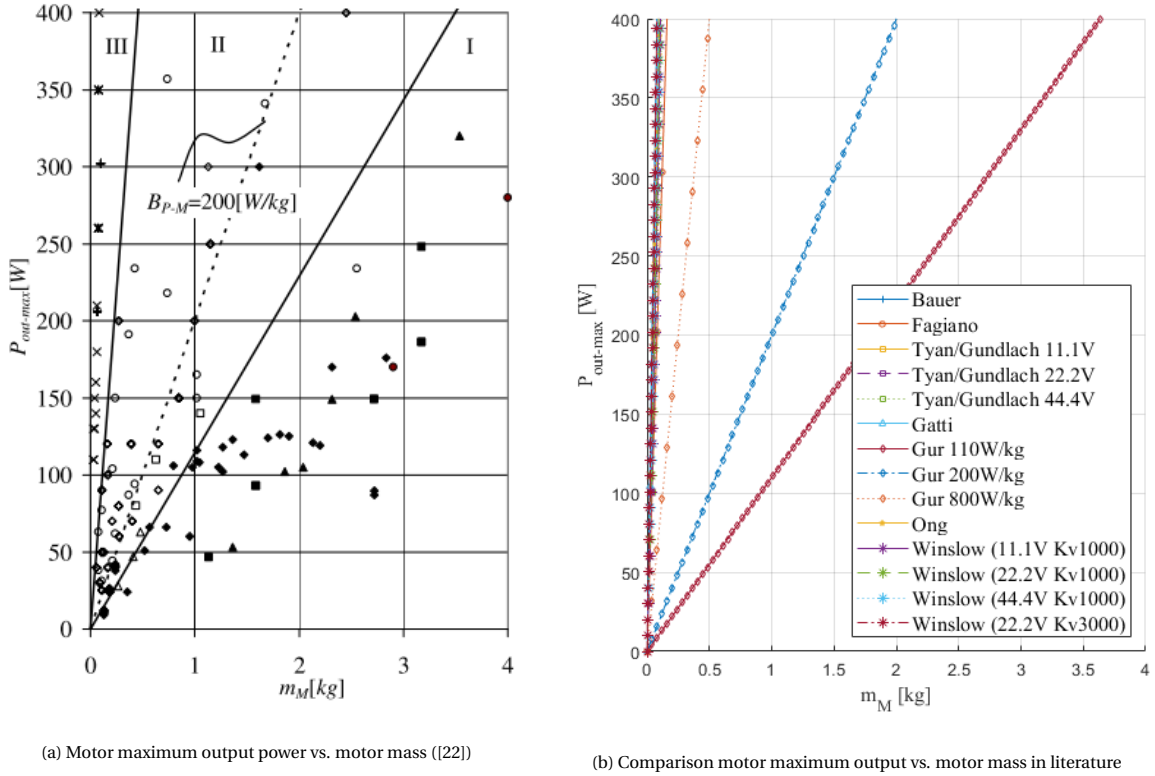


Figure 2.18

$$K_v = 3313.8W_m^{-0.4} \quad (2.108)$$

$$P_{\max} = 3.95W_m \quad (2.109)$$

A comparison of the relation between motor maximum output power and mass for different literature is given in 2.19. These relations are plotted in a mass range which was provided in the literature. It can be observed that these relations differ for different literature. First, the power to weight prediction given by Gur [22] is much lower due the choice for high performance motors. For literature on VTOL AWE Bauer [4] uses a higher power to weight ration than Fagiano [14]. On the smaller scale (Figure 2.20b), relations by Bauer [4], Gatti [17], Ong [35], Tyan [49] and Winslow [50], seem to agree more than on a larger scale, this could more extensive motor data on small scale. Tyan predicts to higher power to weight ratio for a lower voltage, while the opposite is true for Winslow's prediction. Lastly, Winslow predicts a higher power to weight for a higher K_v .

2.6.3. Battery

For multicoper and UAV, the battery is often the heaviest component [22]. Key characteristics of the battery are: specific energy [Wh/kg], energy density [Wh/L], depth of discharge [%], energy capacity [mAh], Voltage [V], cell count and C-rating [50], [17], [35]. The capacity determines the amount of current that the battery can provide for 1h when fully discharged. The depth of discharge determines the percentage of full discharge which is recommended for the required durability of the battery. The C-rating determines the discharge capability of the battery. The cell count is the amount of cells in series. Bauer [4] also considered power density, but concluded that the mass of the battery is driven by the energy density and not power density.

Because of their high specific energy and discharge rate, LiPo batteries are currently first choice for UAV and multirotor [50], [2]. LiPo batteries have a specific energy of up to around 250 Wh/kg [6], [35]. LiPo have taken the place of NiCd and NiMH batteries in hobby-grade vehicles [6]. Another lithium composition is Li-ion, which has a specific energy 50% higher then LiPo's. However, maximum discharge rates are found too low for multicoper purposes [6]. Another lithium type is the LiFe composition, these battery types are more stable, safer and can withstand more discharges than LiPo. However, it comes a price of lower specific energy

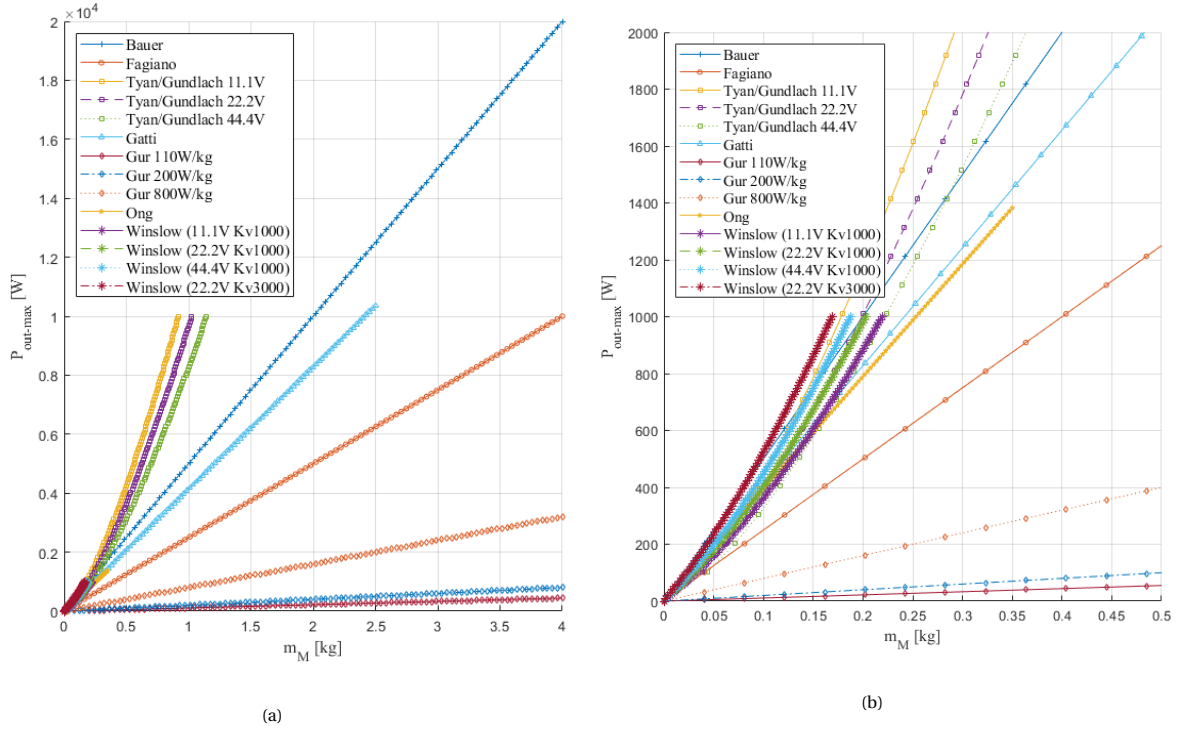


Figure 2.19: Comparison motor maximum output vs. motor mass in literature

of around 100 Wh/kg [6]. Considering emerging technologies, it is forecasted by Luongo [30] and Hepperle [23] that the lithium-sulfur and lithium-oxygen composition will obtain an energy density of 500-1250, and 800-1750 Wh/kg respectively by 2025 [49].

LiPo batteries have a nominal voltage of 3.7V. This voltage can be increased by connecting in series. Increasing voltage requires less drawn current for the same power requirements [50]. The total capacity can be raised by connecting battery cells in parallel, while voltage remains unchanged [2]. The configuration of the cell (amount of series and parallel) must be chosen appropriately to achieve endurance and discharge rate goals. Furthermore, the voltage must be considered together with the K_v of the motor and rpm of the rotor in order to meet thrust and power requirements [6].

A. Battery model

Following electrical model is proposed by Ampatis [2] for modeling the battery. 1 LiPo cell has a nominal voltage of 3.7 V, therefore the total nominal voltage of the battery is given by Equation 2.110, where n_c is the amount cells connected in series. The battery however has an internal total resistance R_{bat} . When connected to a load the output voltage is given by 2.111. Provided the cell internal resistance R_{sc} , The total internal resistance of the battery can be calculated using Kirchoff's law (Equation 2.124). Here n_p represents the amount of identical packs connected in parallel. Lastly, battery total power and energy are given by Equations 2.113 and 2.114.

$$V_b = n_c 3.7 \quad (2.110)$$

$$V_{b,out} = V_b - i R_{bat} \quad (2.111)$$

$$R_{bat} = \frac{n_c R_{sc}}{n_p} \quad (2.112)$$

$$P_{bat} = P_{sc} n_c n_p \quad (2.113)$$

$$E_{bat} = E_{sc} n_c n_p \quad (2.114)$$

Other important battery characteristic are battery capacity Q_b and C-rating. The battery capacity is defined by Equation 2.115, where V is the voltage of the battery. C-rating indicates the fastest rate at which batteries

can be discharge. The maximum current can be calculated according to Equation 2.116. The drawn current should not exceed this maximum required current (Equation 2.117). When selecting a battery, flight time can be calculated according to Equation 2.118 [35].

$$Q_b[Ah] = \frac{E[Wh]}{V} \quad (2.115)$$

$$A_{max} = Q_b \cdot C_{rate} \quad (2.116)$$

$$A_{draw} = \frac{P_{req}}{V_{nom}} \quad (2.117)$$

$$t_{avail} = \frac{Q_b}{A_{draw}} \quad (2.118)$$

In the literature battery weight is calculated based specific energy and required energy. Generally, Equation 2.119 ([49]) is used, where t_i and P_i are the time and power required for a certain flight phase (e.g. climb). A summation of the energy required for all the flight phases gives the total energy. E_{spec} is the specific energy of the battery, η_{bat} the battery or discharge efficiency and f_{usable} the usable fraction of the battery or depth of discharge. Gatti [17] uses a depth of discharge of 80 % and a discharge efficiency η_{bat} of 95%. Ozdemir [36] uses a depth of discharge of 85%. For the case of the climb, the time to climb is given by 2.120 [14].

$$M_{bat} = \frac{\sum t_i P_i}{E_{spec} \eta_{bat} f_{DOD}} \quad (2.119)$$

$$t_{climb} = \frac{h}{v_c} \quad (2.120)$$

B. Battery parameterization

In this subsection the efforts in literature to parameterize the performance characteristics introduced in the battery model will be summarized. Rapp [37] makes use of an specific energy γ_E of 130 Wh/kg to calculate battery mass based on required energy. In [4], Equation 2.121 is used to ensure that energy storage is large enough to provide both required energy and power. $\gamma_{e,E}$ and $\gamma_{e,E}$ are 130 Wh/kg and 5 kW/kg respectively based on LiPo batteries⁵. Bauer concluded however that the specific energy was determined. Fagiano [14] uses an energy density of $E_{batt} = 720$ kJ/kg. Tyan [48] uses a LiPo battery specific energy E_{spec} of 50-220 Wh/kg.

$$m_b = \max\left(\frac{E_e}{\gamma_{e,E}}, \frac{P_e}{\gamma_{e,E}}\right) \quad (2.121)$$

Parameterization used by Ampatis [2] relates the battery total equivalent length l_{bat} to the electric model parameters: $P_{bat,tot}$, $P_{bat,tot}$, $E_{bat,tot}$. The equivalent length is defined as the cubic root of the volume. Batteries from Kokam have been used. Battery specifications are given for 3.7V battery cells. Cells connected in parallel result in a larger single cell with volume B_{vol} (Equation 2.122), Power P_{bat} and energy E_{bat} . A relation for the single cell and equivalent cell internal resistance based on reference batteries is given by Equation 2.123 and 2.124.

$$B_{vol} = n_p B_{vol,sc} = l_{bat}^3 / n_c \quad (2.122)$$

$$R_{sc} = 2.84668 \cdot 10^{-7} B_{vol,sc}^{-0.951154} \quad (2.123)$$

$$R_{bat} = 2.84668 \cdot 10^{-7} B_{vol}^{-0.951154} \quad (2.124)$$

Combining previous equations and approximating $n_p^{0.05} \approx 1$, battery total resistance is given by Equation 2.125. Cell energy and power are observed to be proportional to its volume. Total battery energy and power can be calculated using Equations 2.126 and 2.127. Lastly, the mean battery cell density have been found by Ampatis to be $\rho_{bat} = 1907.8 \text{ kg/m}^3$.

$$R_{bat,tot} = n_c R_{bat} \quad (2.125)$$

⁵Conrad Electronic SE: Modellbau-Akkupack (LiPo) 22.2 V 5000 mAh 40 C. <https://www.conrad.de/de/modellbau-akkupack-lipo-222-v-5000-mah-40-c-conrad-energy-offene-kabelenden-239016.html>. Accessed 20 Jan 2016

$$P_{bat,tot} = n_c 7.0899 \cdot 10^6 B_{vol} \quad (2.126)$$

$$E_{bat,tot} = n_c 9.0833 \cdot 10^8 B_{vol} \quad (2.127)$$

Ong [35] provides a relation between the battery capacity Q_b and battery mass W_b (Equation 2.128) and C-rating and battery capacity (Equation 2.129) based on LiPo batteries surveyed from online markets with mass lower than 3kg⁶.

$$Q_b = 0.008 W_b \quad (2.128)$$

$$C_{rate} = 66.77 Q_b^{-0.538} \quad (2.129)$$

A comparison of the relations between battery energy and mass for different papers are given in Figure 2.20. The relations can be found in Table 2.9. Multiple relations have been found in the literature correlating battery energy and mass. As can be observed from Figure 2.20, the trend is linear. The specific energy, which is defined as the slope of this relation, lies between 132 and 220 Wh/kg.

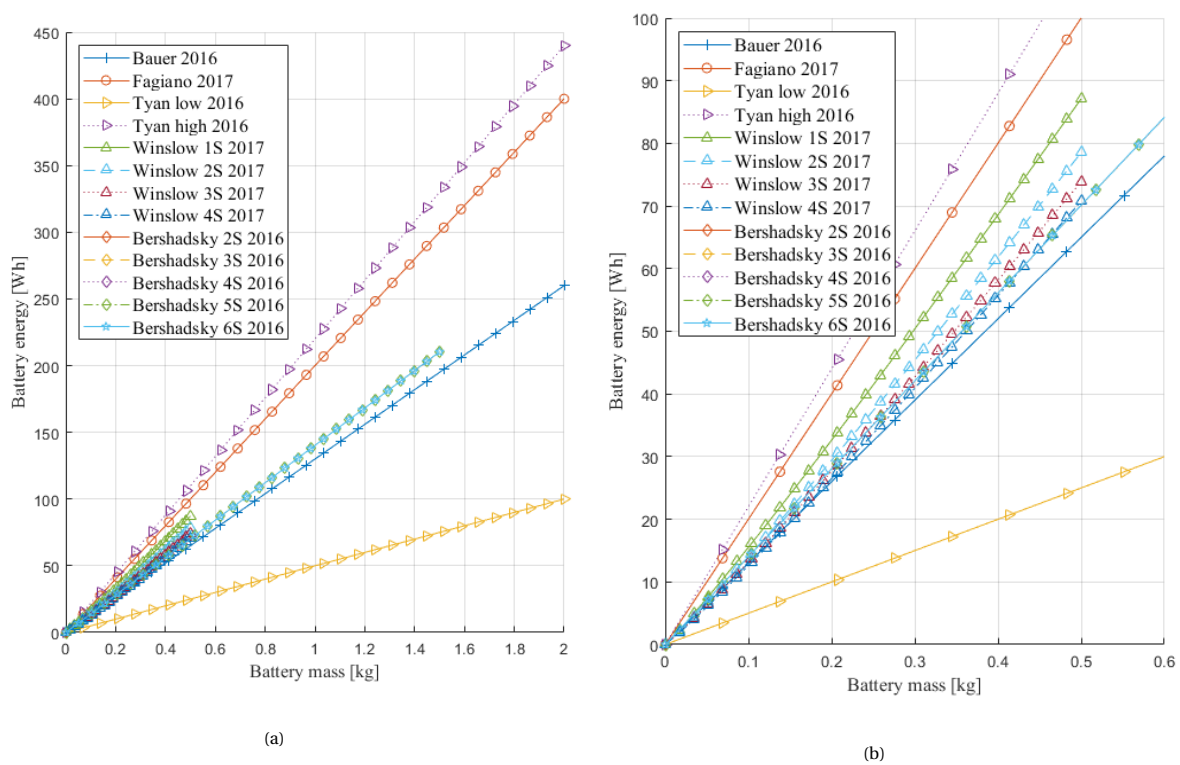


Figure 2.20: Battery energy vs mass

⁶Sources for batteries: www.foxtechfpv.com, www.4fpv.com, www.hobbyking.com, and shop.rotor.com.sg (28 Jan 2018)

Table 2.9: Relation between battery energy and battery mass for different papers

Paper	Relation	E_{spec} [Wh/kg]	Notes
Bauer/Rapp		130	
Fagiano		200	
Tyan		50-220	
Theys		120-360	
Winslow	$m_B[g] = 0.0418C[mAh]^{0.9327} S^{1.0725}$	1S: 183 2S: 165 3S: 155.5 4S: 149	LiPo 0-500g
Ampatis	$E_{bat}[J] = 9.0833 \cdot 10^8 l_{bat}[m]^3, \rho_{bat} = 1907.8 kg/m^3$	132	
Gatti	$E_b[Wh] = 138.17m_b[kg] - 0.0422$	138.17	160 LiPo 0-1kg
Gatti	$E_b[Wh] = 145.95m_b[kg] - 3.5682$	145.95	Data Flightpower
Gur	$E_b[Wh] = 4.04m_b[kg]^2 + 139m_b[kg] + 0.0155$	180	240 LiPo 0-10kg
Ong	$Q_b[Ah] = 0.008W_b[g]$	6S: 177.6	LiPo <3kg
Bershadsky	$m_b[g] = (0.026373S + 2.0499e - 05)C[mAh]$	140	30 LiPo <1.5kg

2.7. System interactions

It is discussed in Section 2.3 that the use of a VTOL system influences the performance of the aircraft by adding weight and drag. However, the VTOL system also influences the stability, control, aerodynamics and the structural integrity of the aircraft. On the other hand, the aircraft system also influences the VTOL system design. These interactions should be taken into account of the design of the VTOL system. Following interactions have been discussed in the literature and are summarized in the form of an N2 diagram 2.22.

As the aircraft and VTOL system are to be integrated, some geometrical constraints are imposed on both systems from each other. These constraints are mainly affecting the stability and control of both types of flying modes. According to [49], multicopter control is very sensitive to changes in moments of inertia. This is especially true for yawing and the length of the aircraft contributes significantly to inertia in the yawing axis. Secondly, the center of gravity (CG) of both aircraft and VTOL system should be aligned. Misalignment increases power required to trim the aircraft and makes it harder to control in both flight modes. Lastly, enough clearance is required between rotors and airframe. This clearance is required for safety and to prevent blockage of the rotor wake [49]. Assuming an aircraft layout as depicted in Figure 2.21, the locations of the front and rear VTOL rotors are constraint by the wing planform, rotor clearances and diameters [49].

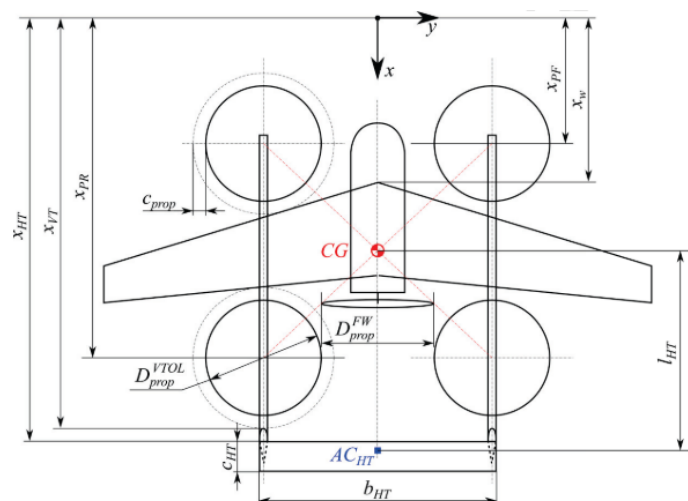


Figure 2.21: FW-VTOL Aircraft Layout [49]

Performing an aerodynamic analysis using Computational Fluid Dynamics (CFD), Dewi [12] concluded that

the drag increases and the lift of the aircraft decreases, by adding the VTOL rotors. Furthermore the drag of the rotors creates a nose up pitching moment during flight. The considered aircraft has a layout similar to 2.21. A suggestion is made to reduce the drag by using folding rotors. Lastly, it was concluded that the drag of the wing in VTOL mode cannot be neglected in the selection of the VTOL thrust-to-weight. In [45], wing and rotor interaction is studied in more detailed. Note, that as in [45] a tail sitter concept is analyzed in which the rotors are mounted up front the wing, wing interaction will be more severe than other hybrid concepts. The wing-rotor interaction has been taken into account by adding rotor slipstream into flow field of the wing in the wing model. BEM has been used to estimate the rotor slipstream and an aerodynamic panel has been used to model the wing and estimate it characteristics.

Aerodynamics AWE aircraft		<ul style="list-style-type: none"> ○ Wing-propeller interaction ○ Drag wing 	
	Stability and Control AWE aircraft		<ul style="list-style-type: none"> ○ Center of Gravity ○ Inertia
<ul style="list-style-type: none"> ○ Wing propeller interaction ○ Decrease in lift ○ Increase in drag 	Pitching moment	Aerodynamics VTOL system	
	<ul style="list-style-type: none"> ○ Center of gravity ○ Inertia 		Stability and Control VTOL system

Figure 2.22: N2 Chart (own work)

It is to be expected that system interaction also exist in terms of structural integrity, load calculations, aeroelastic consideration. However, these matters have not been addressed in the current literature.

2.8. Synthesis and refinement of research questions

The goal of the state-of-the-art review is to answer the first research question: How to design a VTOL launch and retrieve system for a rigid-wing airborne wind energy system? An initial sizing for an AWE VTOL system has been done by Fagiano [14], Bauer [4] and Rapp [37]. Different assumptions have been made through this sizing process such as battery energy density, rotor diameter and efficiency. Aerodynamic forces of the wing are neglected in all papers. A suggestion has been made by Bauer [4] to place the wings in such a way to support the rotors while hovering. To have a more accurate estimation of these component parameters and to include the aerodynamic effects of the wing, design literature for multicopter and hybrid UAV have been consulted and studied. A clear overview of the design methodology of hybrid drones and multicopter has been established in this work. Due to the similarity of the system components and functions, this design methodology can be applied to design a VTOL system for AWE.

First step in the design process is to develop and solicit requirements. No clear mission profile for an AWE VTOL system is provided in the literature. Estimations of target height, climb speed and hover time have been given in the papers of Fagiano, Bauer and Rapp. However, there is no strong agreement on the figures. Therefore, from this research it can be concluded that the establishment of functional requirements for VTOL AWESs are not fully understood yet. Regarding performance, the effect of the additional mass on the AWES on the output power of the AWES is not completely clear from the literature. Fagiano claimed that the additional mass will affect the cut-in speed, but an estimation on how much is not provided by the literature.

Second step in the design process is a market analysis. This is done to obtain statistical data on a system and sub-system level. No data is available on the VTOL systems developed by AWE companies.

The third step is concept determination. Different VTOL concepts are pursued by the AWE companies and even more concepts are to be found in hybrid UAV literature. Main considerations are amount of rotors, configuration of rotors w.r.t. the wing and whether the rotors can be tilted or not. There is no clear preference for one concept in the literature. Furthermore, no methods have been found on making a proper trade-off between the concepts. In this research, the tilt-rotor, tail-sitter and quad-plane concept are all analyzed with the developed sizing tool. A trade-off can be made based on these results.

Fourth step is thrust calculations and component modelling. Aerodynamic forces of the wing have been taken into account in the calculation of thrust for the hybrid drone. Mainly the drag of the wing for an axial climb and descent have been considered. Theys [46] also provides a model to take into account lift and drag during forward flight. Transition strategy and models are not addressed in the literature (both AWE and hybrid UAV). In this research a 2D flight mechanics model is derived from a 6 degree of freedom (DOF) aircraft dynamical model.

Physical and statistical models to size the components found in the literature have been summarized. For modelling the rotor, momentum theory and blade element method (BEM) have been used in the literature. Momentum theory is used as a first order estimation of the power required to produce certain thrust. Models have been found for hover, climb, descend, forward flight and forward climb. Due to the assumptions made in the model, an appropriate rotor efficiency is required in order for the power estimate to be accurate. Momentum theory is applicable for the initial sizing of the VTOL system for AWESs. Using a blade element method (BEM), thrust and power can be calculated for a certain RPM. It represents an important tool to size rotor parameters such as pitch, profile and chord distribution. Statistical models are found to estimate rotor mass and are also used in the proposed design model.

Brushless outrunner DC motors are the first choice for UAV and multicopter motors. An electrical model has been found in the literature and no-load speed constant K_v , internal resistance R_a and no-load current i_0 have been identified to define the motors performance [2]. A parameterization has been performed in the literature linking these parameters to the motors mass. Furthermore, estimations are given for the dimensions and maximum output power. LiPo batteries are the first choice for UAV and multicopter motors. However, emerging battery technologies such as lithium-sulfur and lithium oxygen are predicted to have higher energy densities. An electrical battery model and battery weight estimation method have been provided by the literature. Parameterizations of specific energy and battery resistance are also provided.

The fifth step in the design process is sizing. Two different approaches have been found in the literature to do so. First, the "classical approach" based on the conceptual design method of Raymer [38]. This method

is based on empty weight relations based on historical aircraft and/or market analysis. However, as no data is available on AWE VTOL systems, this empty weight relation is difficult to obtain. This problem can however be addressed by providing an appropriate model to estimate the empty weight. Weight iterations are performed to ensure consistency of the weight. Second approach is the "optimization approach", this offers freedom to the designer to choose design variables, parameters and the objective(s). This approach can cope with a larger design space and more complex models. The classical method can be used to get a first estimate for the VTOL design for AWE and can be validated by comparing results with Bauer [4] and Fagiano [14]. The optimization approach can extend this design tool by using more complex models and larger design space to see the effect of certain assumptions and parameters. Once the sizing is performed it is important to check off-design performance and to do a sensitivity analysis. In this way the effect of certain assumptions and requirements can become clear. In this research a sensitivity analysis on design parameter assumptions and requirements is done as well as a dynamic feasibility check.

Last steps in the design process are the layout, detailed analysis of component selection and the resizing process. In these steps a more detailed design is considered. The system interactions should be analyzed in this design phase. The following interactions are identified in the literature: aerodynamic interference of the VTOL system and the aircraft, wing-rotor interaction and stability interaction due to changes in center of gravity, inertia and pitching moment. Aerodynamic interactions have been analyzed in literature by use of CFD. No low fidelity models to estimate aerodynamic interactions are provided. These steps are left for future work.

In light of these conclusions following research questions follow from the literature study. These questions are addressed and answered in this research and next chapters and as such contribute to the work found and done in the literature.

- What functional requirements impose the AWES on the VTOL system design?
- What are the effects of the requirements on the VTOL system design?
- What are the effect of the VTOL system design parameters on VTOL system mass?
- Which VTOL concept is most suitable for AWE applications?
- How do the aerodynamic forces of the AWES effect the VTOL system design?
- What strategy should be taken to transition from take-off to power generation phase?

3

Design methodology applied

Based on the state-of-the-art review and the research that is done, the following design methodology is developed, depicted in Figure 3.1. Requirements, mission profile and assumptions are identified as input of the design process. The VTOL system requirements are explained in Section 3.1. The mission profile is discussed in Section 3.1.3 and Section 3.1.4 by proposing take-off and transition approaches. Assumptions are found to be an input at every design phase. The assumptions are mostly related to system and component modelling used in the particular design phase. They are given throughout the following sections.

Three (3) design phases are identified being conceptual design, preliminary sizing and detailed design. In Section 3.2, conceptual considerations for the VTOL system are explained consisting of rotor orientation, number of rotors and rotor configuration. For the preliminary sizing phase, system sizing consists of sizing of the main components being rotors, motors and battery. In this phase the mass of the system and its components is determined. This also requires an accurate estimation of required thrust and power. In Section 3.3 the system model is described, followed by a flight mechanics model in Section 3.4, to predict the required thrust. The component models are described in Section 3.5. Finally, the design parameters are given in Section 3.6, where also the main assumptions for the preliminary sizing are summarized.

The last phase in the design methodology is the detailed design. This includes activities such as a detailed rotor design, electrical design consisting of the detailed motor, battery and electronic speed controller (ESC) design (or alternatively component selection), and lay-out design consisting of an aerodynamic analysis of the VTOL-aircraft system interaction. These design activities are to be further elaborated in future work. An outlook of these activities is given in Chapter 6, based on the findings from this research.

At the end of the design phases, the VTOL system must be simulated in order to check the feasibility of the design. Once feasibility is proven, prototyping of the VTOL system can start. If the simulation proves infeasibility of the design, refinements are required on the assumption in design phases. For example, the safety factor on required power to cope with gusts. Such refinements can also be required based on the detailed design of a certain component. For example, the assumed specific energy of the battery. Last note on the design methodology is that requirements flow from one design phase to the other, including refinement feedback loops between the different phases. In the conceptual phase, the rotor orientation is determined which influences the required thrust and power in the preliminary sizing. In the preliminary sizing the mass and power of the motor is determined, this will have to be met in the detail design of the motor.

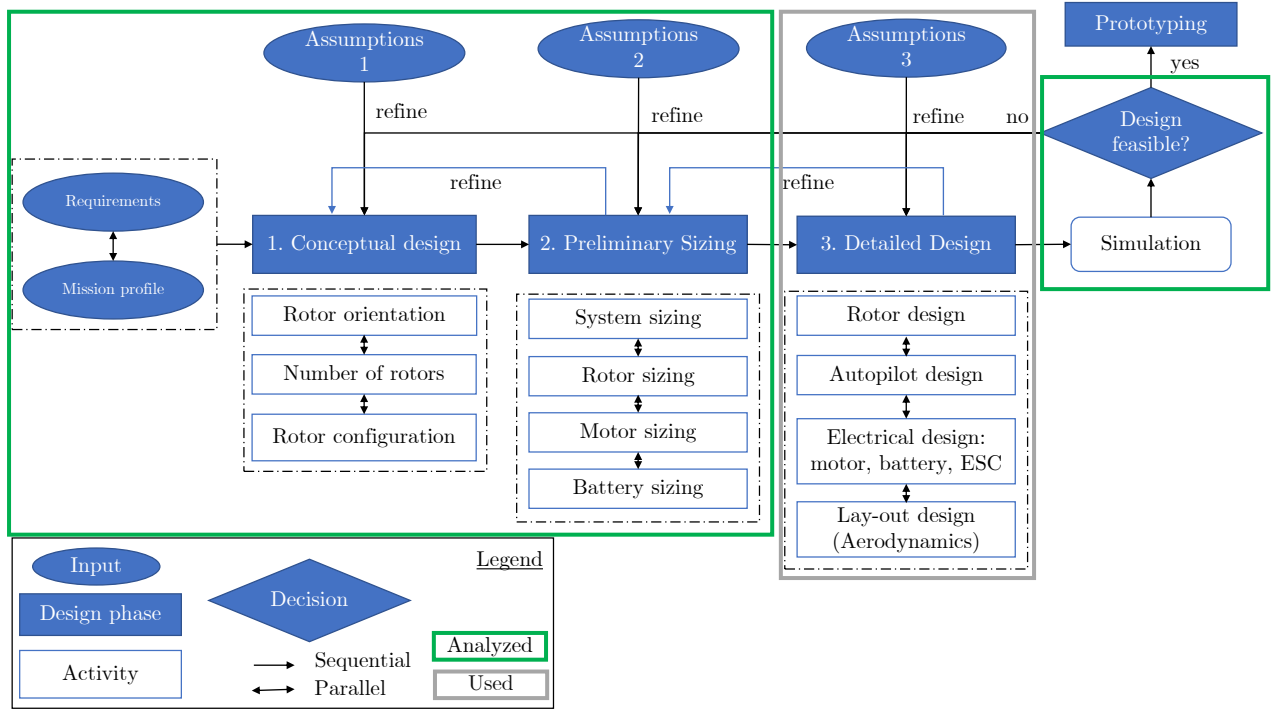


Figure 3.1: VTOL system design methodology

3.1. Requirements and mission profile

The requirements for VTOL AWES mentioned in the literature are documented in the state-of-the-art review. It could be concluded that no clear requirements could be extracted from the literature. This can be explained by the fact that at time of writing, it is not exactly clear how the take-off and transition for a VTOL AWES system should look like. In this section the take-off requirements and performance criteria that are used in this research are given. Furthermore, the mission profile is defined by proposing take-off and transition approaches.

3.1.1. Take-off requirements

The considered requirements are: aircraft related requirements, target position, take-off velocity and wind condition.

Aircraft related requirements

The aircraft parameters that are used in this research are given in Table 3.1, based on the AP2. Maximum allowable velocity and acceleration of the aircraft system, designed for the power generation phase, is assumed not to be exceeded during the take-off phase. The minimum velocity is not required during take-off phase due to the use of a VTOL system. The additional weight of the VTOL system to the aircraft is not set as a requirement, but is minimized as explained later.

Table 3.1: Aircraft (AP2) parameters

Requirement	value
Mass aircraft ($m_{A/C}$) [kg]	36.8
Wing area (S) [m ²]	3

Target position

In the state-of-the-art review a mission profile is developed based on videos from the companies Twingtec and Makani. Furthermore, a minimum height and tether length are identified as critical take-off requirements. For this research, the values of these requirements are given in Table 3.2 based on the state-of-the-art

review. The target position is then defined by the elevation angle θ as visualized in Figure 3.2. The elevation angle is varied in order to see the effect on the VTOL system design. Next to the minimum height, a clearance height is required in this work. This height is defined by perfect vertical take-off, so no inclined flight path is allowed until the clearance height is reached. Last requirement concerning the mission profile is that the aircraft starts from ground station. Values for the requirements are summarized in Table 3.2. Final note regarding the target position is that the take-off is treated in a 2D scenario with the target position in a plane parallel to the wind direction and ground station-aircraft direction.

$$h_{\text{target}} = l_{\text{min}} \sin \theta_t \quad (3.1)$$

$$x_{\text{target}} = l_{\text{min}} \cos \theta_t \quad (3.2)$$

$$\theta_{t,\text{min}} = \arcsin \frac{h_{\text{min}}}{l_{\text{min}}} \quad (3.3)$$

Table 3.2: Functional requirements

Requirement	value
Minimum height (h_{min}) [m]	100
Minimum tether length (l_{min}) [m]	150(-200)
Maximum tether length (l_{max}) [m]	700
Clearance height (h_{clear}) [m]	10
Minimum target elevation angle ($\theta_{t,\text{min}}$) [deg]	41.81

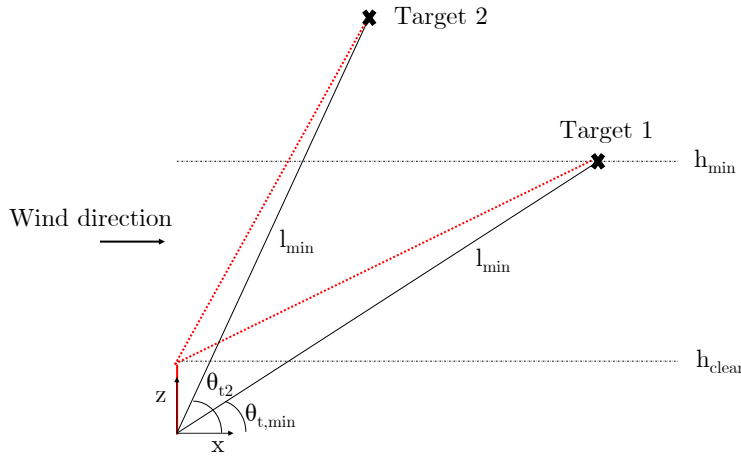


Figure 3.2: Take-off requirements

Take-off velocity

In the state-of-the-art review, take-off velocity and time have been set as requirements in the sizing procedure of [14], [4] and [37]. It is however assumed that take-off time is negligible compared to operating time of the AWES. Furthermore, it is assumed that take-off velocities are small compared to operating velocities and therefore not limiting the design loads. Therefore, take-off velocity and time are left as design variables instead of requirements.

Wind condition

Regarding operational conditions, the wind speed plays a major role. In Figure 3.3, the power production for the AP2 is plotted against wind speed for a certain case study conducted in [19]. To fully obtain this power production the take-off system must operate between 4-25 m/s. It can be argued that the AWE aircraft is not required to take-off when the wind speed is below 4m/s (cut-in speed). However, the AWE aircraft is only on the ground for several occasion such as in the case of no wind, when an emergency landing has been

performed, when a cut-off wind speed has been predicted or for maintenance [7]. Therefore, it makes more sense to look at the probability of the wind speed at such an event. In Figure 3.4, the probability of a wind class-1A (high wind) is plotted. When the take-off system is able to operate in a wind speed range of 0-10 m/s, there is around 55 % chance that take-off is possible. It is not clear what the effect of this take-off limitation on the total power production is at the moment of writing, as there is no clear prediction on the amount of time the AWE system is on the ground. Because the wind speed is an unpredictable parameter, a requirement on the wind speed is not set during the analysis, instead the effect of the wind speed on the VTOL system design is analyzed in detail.

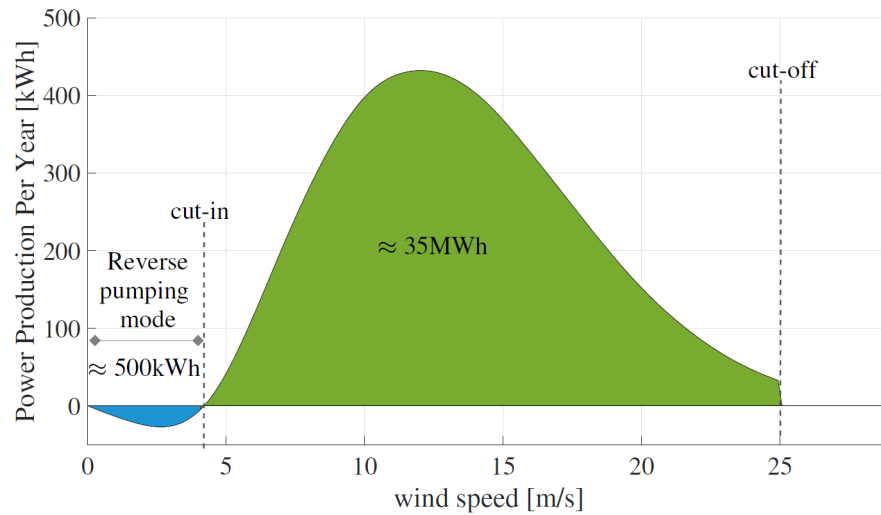


Figure 3.3: Power production per year for AP2 (case study conducted in [19])

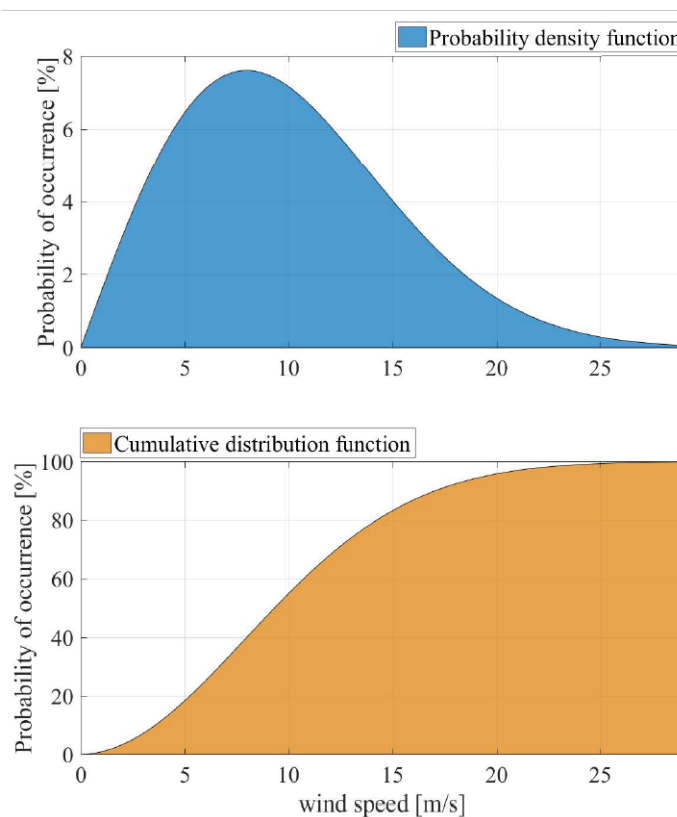


Figure 3.4: Wind class-1A density function with corresponding cumulative distribution function [19]

3.1.2. Performance criteria

In the state-of-the-art review, VTOL power, mass, additional drag and decrease in lift are identified to be effecting the AWE aircraft's performance. During the preliminary sizing procedure, VTOL system mass and power is estimated. The VTOL system's drag however is highly dependent on the way the VTOL system is integrated on the aircraft and can only be predicted by high fidelity models, e.g. CFD. Same holds for the decrease in lift and other aerodynamic interference effects. Therefore, the VTOL system mass is considered the parameter of interest here and is minimized in an optimization procedure.

3.1.3. Take-off approaches

In Section 3.1.1 it was explained that a certain target position should be reached. There are however multiple ways to reach this position. A complete flight path optimization could calculate the optimal flight path to reach this position. Two (2) different take-off approaches are given here. A classification is made between a direct and indirect take-off.

Direct take-off approach

In Figure 3.5, the flight path of a direct take-off approach is visualized. In this approach the shortest path is taken towards the target position after a vertical take-off to clearance height. Such an approach is taken by Makani and TwingTec. Therefore, this approach will be the focus in this research.

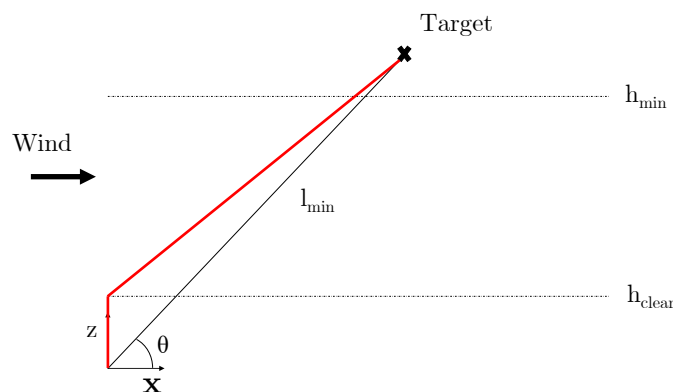


Figure 3.5: Direct take-off approach

Indirect take-off approach

Taking the shortest path is not necessarily the most optimal one. In Figure 3.6, an example is given of an indirect take-off approach. Here, the climb is performed by an inclined path into the wind. In this way, aerodynamic lift can be exploited to full extend to facilitate the work of the rotors. The aircraft is then turned at a certain point and aimed for the target position. This turn can be a normal flight turn and acceleration can be aided by use of the winch. Nevertheless, it is to be expected that the power of the rotors is large enough as the requirement of vertical take-off is already imposed. It is suggested to implement this approach by dividing the flight path in 3 segments (see Figure 3.6) on which a force equilibrium is imposed. This approach can further investigate the potential of flight path optimization in the take-off phase.

3.1.4. Transition approaches

When the target position is reached, the AWE aircraft should transition towards a power generation state (position, attitude, velocity). In Figure 3.7 a typical state and flight path are given for the AP2 power generation phase. It can be observed that the state of the aircraft highly depends on the location in the power generation flight path. However, in essence, the wings should take over the lift from the rotors and the rotor thrust should decrease towards 0. This condition can be met once the apparent speed is greater than the stall speed. In the approach to do so, a distinction is made between a tether-assisted and non-assisted approach.

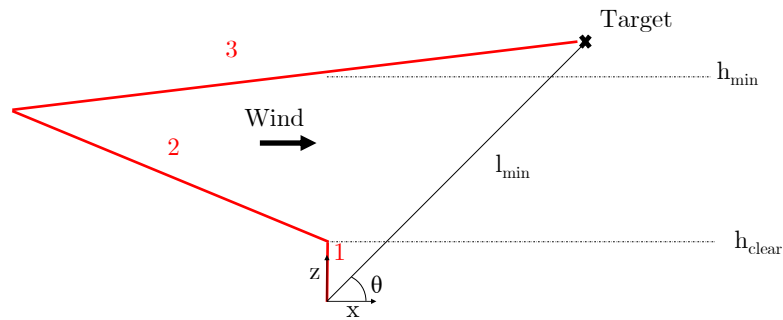


Figure 3.6: Indirect take-off approach

In this work it is assumed that the take-off phase is the main driver of the VTOL system. Required energy to perform a transition manoeuvre to the required attitude and velocity is assumed negligible with respect to energy required to perform the take-off phase up to target position, especially if transition is assisted with the winch. The winch is the mechanical part of the ground station that reels the tether in and out. Furthermore the available power of battery and motors in order to take-off vertically is assumed sufficient to safely perform a transition manoeuvre. Of course this is an important assumption and must be verified in a simulation study.

Non-assisted transition approach

For the non-assisted approach, transition has to occur without assistance of the tether. In the state-of-the-art review, two (2) such approaches are documented. First one, pursued by Makani, is to accelerate using the rotors. This is possible for the concept Makani is pursuing, the tail-sitter concept, as speed is increased in the direction of the wing. For the concept Twingtec is pursuing, a quad-plane concept, such a manoeuvre is not possible. Instead transition is obtained by making a dive manoeuvre. For the tilt-rotor concept, both manoeuvres are possible as the rotors can be tilted in any desirable direction. For the newly introduced knee-sitter concept, the acceleration could also be established by accelerating on the rotors as the aircraft can be tilted forward, while the wing is still operating at a positive angle of attack.

Winch assisted transition approach

Another approach that can be taken is to accelerate by pulling in the tether. This will create a force component in the direction of the ground station which accelerates the aircraft. Also a force component is acting down. This force component can be balanced initially by the rotors and eventually by the wing once the aircraft is accelerated. This force component can be reduced by pulling in at a low elevation angle. This approach can help to reduce requirements put on the VTOL system.

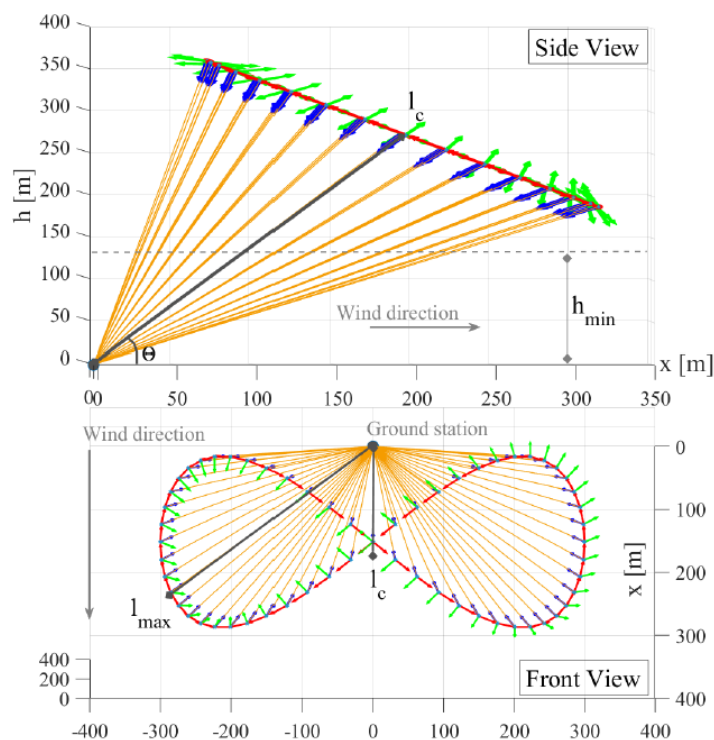


Figure 3.7: Power generation flight path [19]

3.2. VTOL concepts

From the design methodology depicted in Figure 3.1, the conceptual design phase is the first design phase. From the state-of-the-art review it was clear that different VTOL concepts are pursued by the AWE companies. At moment of writing, a proper trade-off between these concepts is difficult as little is known yet about the effect of certain conceptual parameters. Therefore, the approach taken in this research is to analyze the different concepts and comparing them. In the literature on hybrid drones, a classification is made between converti-planes and tail-sitter UAV's [41] (see Figure 2.7), based on how transition between vertical and horizontal flight is obtained. For the problem at hand, the aircraft design is already fixed. Therefore the research will be focused on the tilt-rotor, dual-system and tail-sitter concepts. The dual-system concept is referred to here as the quad-plane concept as forward propulsion is not required for the AWE aircraft. For the purpose of designing a VTOL system for an AWE system, a distinction between the following conceptual design parameters is considered: rotor orientation with respect to the wing, amount of rotors and rotor configuration.

3.2.1. Rotor orientation

This design parameter is defined by the angle the rotor axis makes with the length axis of the body (see Figure 3.8). It is this parameter that mainly determines the classification made in hybrid drones. First of all, the rotor orientation mainly determines how the transition takes place. Therefore the transition manoeuvre needs to be considered with the chosen concept in mind. This is also the case for AWE aircraft systems as discussed in Section 3.1.4. Furthermore, by own analysis, this parameter has been deemed most influential on the aerodynamic forces resulting from the wind. Therefore, this parameter has an important effect on the sizing of the VTOL system. For this research, following concepts are considered:

- **Tilt-rotor:** rotor orientation can be varied.
- **Tail-sitter:** rotor orientation fixed 90 degrees (body x-axis).
- **Quad-plane:** rotor orientation fixed 0 degrees (body z-axis).
- **Knee-sitter:** rotor orientation fixed at arbitrary angle between 0 and 90 degrees.

Multiple rotors can have different orientation and can have both fixed and tilt-rotors. However, the upcoming analysis is focused to the same orientation for each rotor in order to analyze the main effect of the parameter.

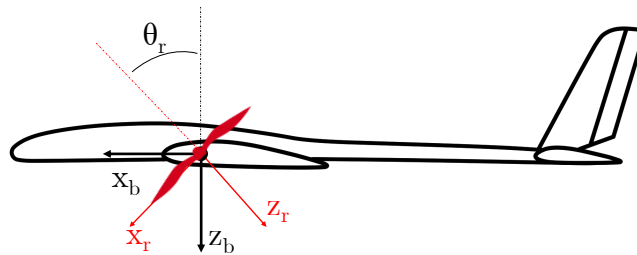


Figure 3.8: Rotor orientation or pitch (θ_r)

3.2.2. Number of rotors

Another main conceptual parameter is the amount of rotors. This mainly influences the way the aircraft manoeuvres and can be controlled. This is therefore an important input to the detailed design phase. For the preliminary sizing phase, the effect of the number of rotors is analyzed in the sensitivity analysis, outlined in Section 5.2.4.

3.2.3. Rotor configuration

The rotor configuration is defined by how the rotors are positioned with respect to each other and with respect to the wing. Possible rotor configurations are given in 3.9. This configuration will mainly influence how the rotors are integrated and fixed to the body. The integration onto the aircraft has a large impact on the aerodynamic interference between the VTOL system and AWE aircraft. It also influences the required structure to mount the VTOL systems. Furthermore, it will also effect the control strategy of the system.

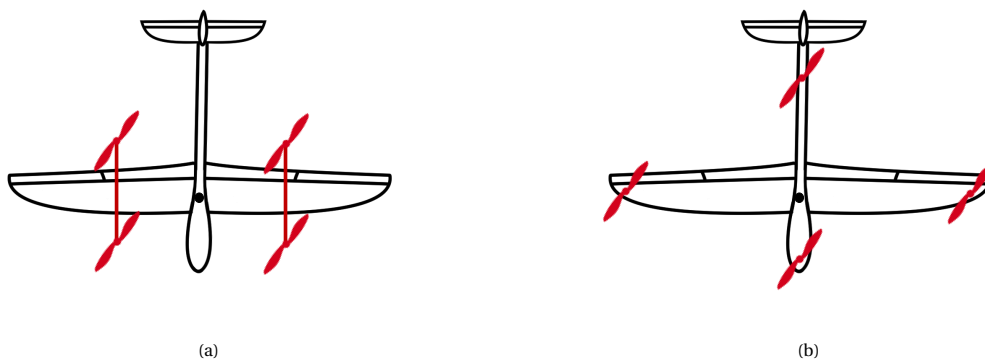


Figure 3.9: Possible rotor configurations

3.3. System sizing model

The developed preliminary sizing model is depicted in Figure 3.10. The main output parameter of interest is the VTOL system mass. The VTOL system mass is calculated based on component masses using Equation 3.4. Based on the state-of-the-art review, the rotors, motors and battery have been identified to be the main components of the VTOL system. To have a more accurate prediction of this mass, a mass fraction MF_{other} is introduced to include the masses other than the main components, such as electronics and additional structure. Next, also flight mechanics and required flight path play a major roll in the sizing of the VTOL system.

$$m_{\text{VTOL}} = \frac{m_{\text{rot}} + m_{\text{mot}} + m_{\text{bat}}}{1 - MF_{\text{other}}} \quad (3.4)$$

AWE aircraft characteristics include parameters such as mass $m_{\text{A/C}}$ and S as described in the requirements section. VTOL system parameters are θ_r , amount of rotors and subsystem parameters such as D_{rot} . Flight characteristics include the velocity, and flight path of the aircraft. Note that both aircraft and flight characteristics are input to all component models. A complete overview of all the system design parameters is given in section 3.6. Furthermore, an optimization approach is developed to optimize the remaining design variables and solve for the VTOL system mass. Further information about the optimization framework can be found in Chapter 3.7.

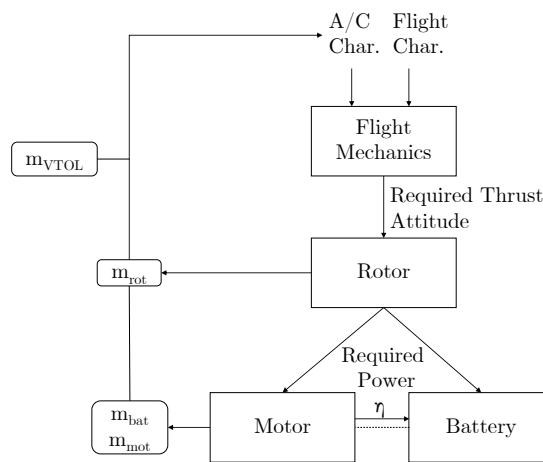


Figure 3.10: System model for preliminary sizing

3.4. Flight mechanics model

One of the main assumption taken in the VTOL sizing of Bauer [4], Rapp [37] and Fagiano [14] is neglecting aerodynamic forces of the aircraft in the thrust requirement. In the following section a model is developed from which the required thrust can be calculated taking into account the aerodynamic forces acting on the aircraft.

3.4.1. Assumptions

Before deriving the flight mechanics model, some assumptions are made. First, the earth is assumed flat as the effect of earth curvature and rotation are negligible for the problem at hand. This is an assumption frequently made for simulating aircraft dynamics. Second, the vehicle is a rigid body of constant mass. However, as the aircraft is taking off, the tether length increases and hence the weight. In this work the tether mass is assumed negligible. Furthermore, it is assumed that all forces act through the center of gravity, hence no acting moments are considered. Lastly, the focus is on the forces in the x-z plane of wind frame, therefore, a 2D scenario is considered.

3.4.2. Reference frames

In order to mathematically describe forces and velocity vectors it is common to introduce reference frames. In Table 3.3, the definitions of the frames used in this work are given. Note that in this work, the propulsion vector is able to rotate in the body x-z plane, therefore the y-axis of the propulsion-fixed frame equals the y-axis body-fixed frame. The application of the frames in this work is depicted in Figure 3.11.

Table 3.3: Reference frames

Reference frame	Origin	X-direction	Y-direction	Z-direction
Local wind frame (W)	Ground station	Downwind	Complete RHS ¹	Up
North-east-down frame (O)	Aircraft cg.	North	East	Down
Body-fixed frame (B)	Aircraft cg.	Aircraft nose	Complete RHS	In A/C sym. plane ²
Aerodynamic frame (A)	Aircraft cg.	Direction \mathbf{v}_a	Complete RHS	In A/C sym. plane
Propulsion-fixed frame (P)	Aircraft cg.	Complete RHS	y^B	Rotor axis (down)

3.4.3. Transformation matrices

In order to imply force equilibrium, all forces must be given in the same reference frame. To express a certain vector from one to another frame, transformation matrices are used. These are built upon the required angles which one should rotate one reference frame to obtain the other.

Local wind to NED frame

The transformation between the local wind frame and the NED frame is defined by angle ζ , which defines the direction of the wind. This angle represents the wind direction relative to the x-axis of the NED frame. Furthermore, while z is pointed upward in the local wind frame, it is pointed down in the NED frame. This leads to following transformation [37];

$$X^O = \mathbb{T}_{OW} X^W \quad (3.5)$$

$$\mathbb{T}_{OW} = \begin{bmatrix} \cos \zeta & \sin \zeta & 0 \\ \sin \zeta & -\cos \zeta & 0 \\ 0 & 0 & -1 \end{bmatrix} \quad (3.6)$$

NED to body-fixed reference frame

The transformation from earth-fixed to body-fixed reference system is defined by a sequence of three right handed rotations in the following order: yaw angle ψ (around z-axis), pitch angle θ (around y-axis) and roll angle ϕ (around x-axis) [19]. The transformation matrix is given by [25]:

¹RHS: right hand system

²Symmetry plane: plane in the middle of aircraft that defines aircrafts symmetry

$$X^B = \mathbb{T}_{BO} X^O \quad (3.7)$$

$$\mathbb{T}_{BO} = \begin{bmatrix} 1 & 0 & 0 \\ 0 & \cos \phi & \sin \phi \\ 0 & -\sin \phi & \cos \phi \end{bmatrix} \begin{bmatrix} \cos \theta & 0 & -\sin \theta \\ 0 & 1 & 0 \\ \sin \theta & 0 & \cos \theta \end{bmatrix} \begin{bmatrix} \cos \psi & \sin \psi & 0 \\ -\sin \psi & \cos \psi & 0 \\ 0 & 0 & 1 \end{bmatrix} \quad (3.8)$$

Body-fixed to aerodynamic reference frame

The transformation from body-fixed to aerodynamic reference frame is defined by two rotations with the aerodynamic angle of attack α and sideslip angle β respectively. The transformation matrix is given by;

$$X^A = \mathbb{T}_{AB} X^B \quad (3.9)$$

$$\mathbb{T}_{AB} = \begin{bmatrix} \cos \beta & \sin \beta & 0 \\ -\sin \beta & \cos \beta & 0 \\ 0 & 0 & 1 \end{bmatrix} \begin{bmatrix} \cos \alpha & 0 & \sin \alpha \\ 0 & 1 & 0 \\ -\sin \alpha & 0 & \cos \alpha \end{bmatrix} \quad (3.10)$$

The angle of attack (α) and sideslip angle (β) are calculated by expressing the apparent velocity \mathbf{v}_a in the body-fixed reference frame (Equation 3.14), according to Equations 3.16 and 3.17 using following procedure [25]:

Wind velocity given in the wind frame:

$$(\mathbf{v}_w)_W = [V_w \quad 0 \quad 0] \quad (3.11)$$

Wind velocity given in the body-fixed frame:

$$(\mathbf{v}_w)_B = (\mathbf{v}_w)_W \mathbb{T}_{BO}^T \mathbb{T}_{OW}^T \quad (3.12)$$

Apparent velocity given in the body-fixed frame:

$$(\mathbf{v}_a)_B = (\mathbf{v}_k)_B - (\mathbf{v}_w)_B \quad (3.13)$$

$$(\mathbf{v}_a)_B = [u_a^B \quad v_a^B \quad w_a^B] \quad (3.14)$$

$$V_a = \sqrt{u_a^{B2} + v_a^{B2} + w_a^{B2}} \quad (3.15)$$

Angle of attack and sideslip angle:

$$\alpha = \arctan \frac{w_a^B}{u_a^B} \quad (3.16)$$

$$\beta = \arcsin \frac{v_a^B}{V_a} \quad (3.17)$$

Body-fixed to propulsion-fixed reference frame

The transformation from body-fixed to propulsion-fixed is defined by a rotation with the rotor pitch angle θ_r , positive defined pitch up. The transformation is defined by;

$$X^P = \mathbb{T}_{PB} X^b \quad (3.18)$$

$$\mathbb{T}_{PB} = \begin{bmatrix} \cos \theta_r & 0 & -\sin \theta_r \\ 0 & 1 & 0 \\ \sin \theta_r & 0 & \cos \theta_r \end{bmatrix} \quad (3.19)$$

3.4.4. Forces and moments

Four forces act on the aircraft being gravity, aerodynamic force, propulsion force and the tether force.

Gravity

The gravity force is defined by Equation 3.20, where m_{tot} is the total aircraft mass (AWE aircraft + VTOL system mass).

$$(\mathbf{F}_g)_O = [0 \quad 0 \quad m_{\text{tot}}g] \quad (3.20)$$

Transforming to the wind frame:

$$(\mathbf{F}_g)_W = (\mathbf{F}_g)_O \mathbb{T}_{OW} \quad (3.21)$$

Aerodynamics

The aerodynamic force is given by Equation 3.25 and is defined by a lift force L, drag force D and side fore Y. For the aerodynamic coefficients, C_D , C_L and C_Y are a function of angle of attack α and sideslip angle β . A more detailed description of the aerodynamic model for the 2D scenario is given later in this section.

$$D = \frac{1}{2} \rho V_a^2 C_D(\alpha, \beta) S \quad (3.22)$$

$$L = \frac{1}{2} \rho V_a^2 C_L(\alpha, \beta) S \quad (3.23)$$

$$Y = \frac{1}{2} \rho V_a^2 C_Y(\alpha, \beta) S \quad (3.24)$$

$$(\mathbf{F}_a)_A = [-D \quad Y \quad -L] \quad (3.25)$$

Transforming to the wind frame:

$$(\mathbf{F}_a)_W = (\mathbf{F}_a)_A \mathbb{T}_{AB} \mathbb{T}_{BO} \mathbb{T}_{OW} \quad (3.26)$$

Propulsion

The propulsion force is defined by Equation 3.28, where T is the total rotor thrust.

$$(\mathbf{F}_p)_P = [0 \quad 0 \quad -T] \quad (3.27)$$

Transforming to the wind frame:

$$(\mathbf{F}_p)_W = (\mathbf{F}_p)_P \mathbb{T}_{PB} \mathbb{T}_{BO} \mathbb{T}_{OW} \quad (3.28)$$

Tether force

The take-off phase takes place without assistance of the tether. Furthermore, the tether weight is assumed negligible compared to the combined aircraft and VTOL system. Therefore, a model for the tether force is not required.

Moments

It is assumed that above mentioned forces all act through the center of gravity (c.g.). For the propulsion system, this can be achieved by carefully distributing the rotors onto the aircraft. Furthermore, aerodynamic moments are neglected as they can be balanced by actively using the control surfaces (or alternatively multi-copter control).

3.4.5. Steady flight model

For a steady flight, force and moment equilibrium are required. By the assumption taken in the discussion on moments, moment equilibrium is automatically met. Force equilibrium implies that the total net force is zero, applied in the local wind frame gives Equation 3.29.

$$(\mathbf{F}_{\text{tot}})_W = (\mathbf{F}_g)_W + (\mathbf{F}_a)_W + (\mathbf{F}_p)_W = 0 \quad (3.29)$$

For the purpose of the preliminary sizing model, a 2D situation is assumed. Furthermore, the wind comes from the north ($\zeta = 180^\circ$). The heading is either to the north ($\psi = 0^\circ$) or to the south ($\psi = 180^\circ$). Remaining assumptions are stated in Table 3.4.

Table 3.4: Steady flight model assumptions

Attitude	Flight path	Wind condition
$\theta_r = \theta_r$	$v_{k,x}^W = v_x$	$v_{w,x}^W = V_w$
$\theta = \theta$	$v_{k,y}^W = 0 \text{ m/s}$	$v_{w,y}^W = 0 \text{ m/s}$
$\phi = 0^\circ$	$v_{k,z}^W = v_c(+)$	$v_{w,z}^W = 0 \text{ m/s}$
$\psi = 0^\circ, 180^\circ$		

Under the following assumptions, the steady flight mechanics model is defined by Equations 3.30-3.35 for $\psi = 0^\circ$ and Equations 3.36-3.41 for $\psi = 180^\circ$. The model is visualised in Figure 3.11. All forces are expressed in the wind frame.

$\psi = 0^\circ$:

$$F_{\text{tot},x} = T \sin(\theta_r + \theta) + D \cos(\alpha - \theta) - L \sin(\alpha - \theta) = 0 \quad (3.30)$$

$$F_{\text{tot},z} = T \cos(\theta_r + \theta) - g m_{\text{tot}} + L \cos(\alpha - \theta) + D \sin(\alpha - \theta) = 0 \quad (3.31)$$

$$\alpha = \left(\frac{V_w \sin(\theta) - v_c \cos(\theta) - v_x \sin(\theta)}{V_w \cos(\theta) - v_x \cos(\theta) + v_c \sin(\theta)} \right) \quad (3.32)$$

$$V_a = \sqrt{(V_w \cos(\theta) - v_x \cos(\theta) + v_c \sin(\theta))^2 + (v_c \cos(\theta) - V_w \sin(\theta) + v_x \sin(\theta))^2} \quad (3.33)$$

$$L = \frac{1}{2} \rho V_a^2 C_L(\alpha) S; \quad (3.34)$$

$$D = \frac{1}{2} \rho V_a^2 C_D(\alpha) S; \quad (3.35)$$

$\psi = 180^\circ$:

$$F_{\text{tot},x} = L \sin(\alpha - \theta) - D \cos(\alpha - \theta) - T \sin(\theta_r + \theta) = 0 \quad (3.36)$$

$$F_{\text{tot},z} = T \cos(\theta_r + \theta) - g m_{\text{tot}} + L \cos(\alpha - \theta) + D \sin(\alpha - \theta) = 0 \quad (3.37)$$

$$\alpha = \left(\frac{v_x \sin(\theta) - V_w \sin(\theta) - v_c \cos(\theta)}{v_x \cos(\theta) - V_w \cos(\theta) + v_c \sin(\theta)} \right) \quad (3.38)$$

$$V_a = \sqrt{(v_x \cos(\theta) - V_w \cos(\theta) + v_c \sin(\theta))^2 + (v_c \cos(\theta) + V_w \sin(\theta) - v_x \sin(\theta))^2} \quad (3.39)$$

$$L = \frac{1}{2} \rho V_a^2 C_L(\alpha) S; \quad (3.40)$$

$$D = \frac{1}{2} \rho V_a^2 C_D(\alpha) S; \quad (3.41)$$

3.4.6. Aerodynamic model

In this section the 2D aerodynamic model is explained, completing the steady flight model. Considering aerodynamic forces, Y force equals zero and lift and drag forces are only depending on α ($\beta = 0^\circ$). Using CFD analysis and tests flight, an aerodynamic model for the AP2 is developed in [31]. Applying above mentioned assumptions, this model is given by equations 3.42-3.44 (α given in radians), which represents the aerodynamic coefficients in the body-fixed frame.

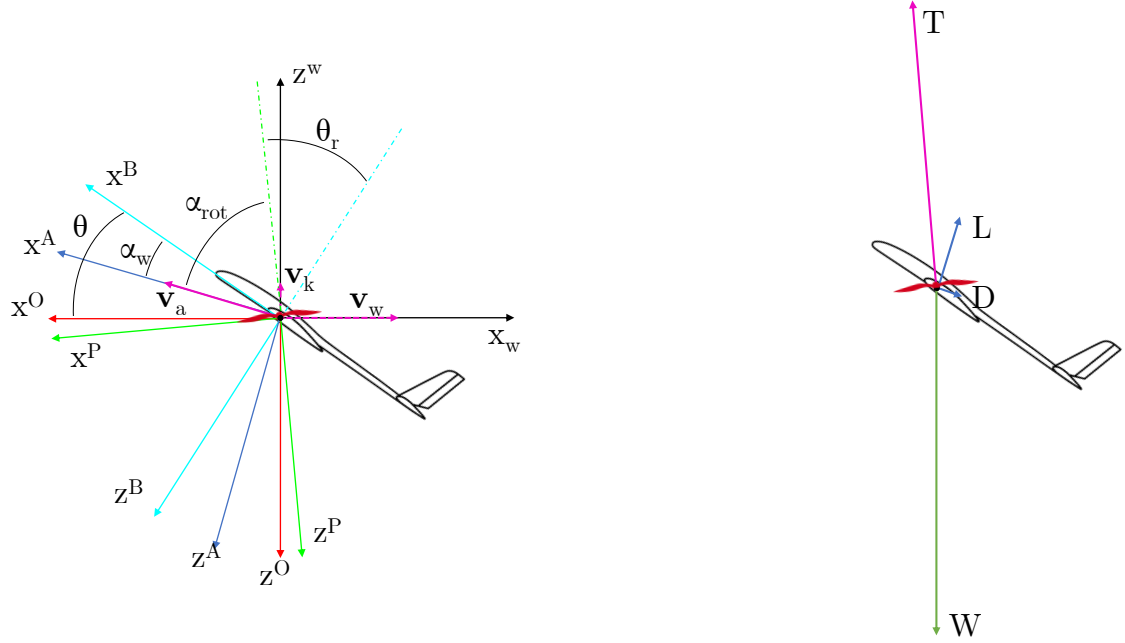
$$C_x = -0.0293 + 0.4784\alpha + 2.5549\alpha^2 \quad (3.42)$$

$$C_y = 0 \quad (3.43)$$

$$C_z = -0.5526 - 5.0676\alpha + 5.7736\alpha^2 \quad (3.44)$$

Converting to the aerodynamic frame:

$$(\mathbf{C}_a)_B = [C_x \quad C_y \quad C_z] \quad (3.45)$$

Figure 3.11: Steady flight mechanics model ($\psi = 0$)

$$(\mathbf{C}_a)_A = (\mathbf{C}_a)_B \mathbb{T}_{AB}^T = [-C_D \quad C_Y \quad -C_L] \quad (3.46)$$

Due to the nature of VTOL flight, high angles of attack and stall are likely to occur. Therefore an aerodynamic model for an angle of attack range of 360 degrees is required. In [5] such a model is proposed for the lift coefficient. In this work, a linear model for low angles of attack is blended with a flat plate model for higher of angles of attack. Since a more accurate model for the AP2 is known at small angle of attack, this model is used instead of the linear model proposed by [5]. The reasoning behind this approach is that after stall occurred, the behaviour of a wing is similar to a flat plate [5]. Flat plate lift coefficient is given by Equation 3.47 [5].

$$C_{L,flatplate} = 2\text{sign}(\alpha) \sin^2 \alpha \cos \alpha \quad (3.47)$$

Defining a blending function $\sigma(\alpha)$, the lift coefficient for all angles of attack can be calculated using;

$$C_L(\alpha) = (1 - \sigma(\alpha))C_{L,AP2}(\alpha) + \sigma(\alpha)C_{L,flatplate}(\alpha) \quad (3.48)$$

where,

$$\sigma(\alpha) = \frac{1 + e^{-M(\alpha - \alpha_0)} + e^{M(\alpha + \alpha_0)}}{(1 + e^{-M(\alpha - \alpha_0)})(1 + e^{M(\alpha + \alpha_0)})} \quad (3.49)$$

M and α_0 are transition rate and cut-off angle of attack (rad) respectively. A similar approach is taken for the drag coefficient in which the drag coefficient of a flat plate is given by Equation 3.50 [26]. For the lift coefficient, transition rate M and α_0 are determined to be 40° and 22° respectively based on stall prediction of Licitra [19]. For the drag coefficients 10° and 20° are used respectively.

$$C_{D,flatplate} = 2 \sin(\alpha)^2 \quad (3.50)$$

$$C_D(\alpha) = (1 - \sigma(\alpha))C_{D,AP2}(\alpha) + \sigma(\alpha)C_{D,flatplate}(\alpha) \quad (3.51)$$

3.5. Component models

The rotor, motor and battery are identified as the main VTOL system components as depicted in Figure 3.12, other components include the structure and electronic speed controller (ESC), flight controller and wiring. In this section the rotor, motor and battery models that are used for the preliminary sizing tool are explained.

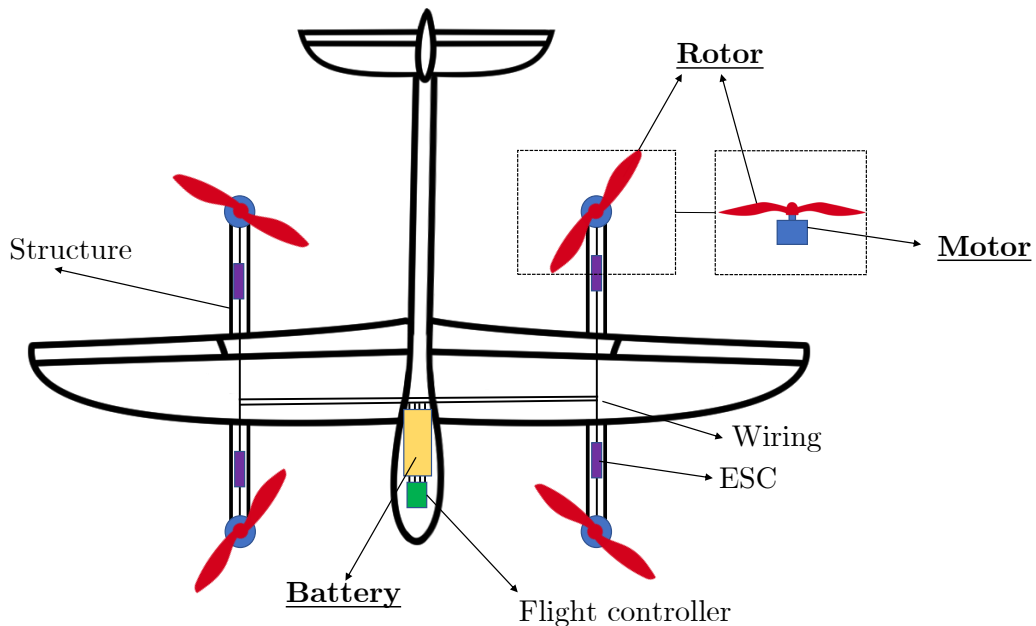


Figure 3.12: System decomposition

3.5.1. Rotor model

First component model that is described is the rotor model. From the system model (see Figure 3.10), it is clear that this model should accurately predict the required power in order to obtain the required thrust for a given flight condition. Nevertheless, this prediction is dependent on the design of the rotor. The design of the rotor goes through different design phases being general sizing, blade platform design and airfoil section design. In this work the general sizing of the rotor is considered with the main design parameter the rotor diameter. For this purpose, a rotor power and mass model are developed appropriate for the preliminary sizing of the VTOL system. Furthermore, also the rotor efficiency is discussed in this section.

Rotor power model

Based on the state-of-the-art review, an actuator disk model has found to be a simple but powerful model for first approximations of required motor power. When applied for an axial climb condition, required power can be calculated based on required thrust, rotor area and climb velocity (see Equation 2.32). However, it is found in this research that the assumption of an axial inflow of the rotor is invalid in most cases for the vertical take-off of an AWES. This is argued by the fact that when taking off in a high wind condition, the wind velocity adds a horizontal component to the velocity of the aircraft. Therefore, the rotor axial direction is not necessarily aligned with the apparent velocity vector. For this reason a rotor model is used which is valid for an oblique inflow.

In the state-of-the-art review two (2) such models were found taken into account oblique inflow. First model was proposed by Theys [46] and is purely based on momentum theory. Secondly, the model explained in [44] is a simplified BEM combined with Momentum Theory. This model requires the local relative velocity of the rotor to be expressed as:

$$\mathbf{v}_{\text{rel}}^P = [U^P V^P W^P] \quad (3.52)$$

With the velocity components expressed in a frame where the thrust is directed in the negative Z-axis (see Figure 3.13). The model can therefore consider a 3D inflow condition in the rotor. Also, the relative movement

of the rotor can be considered, when the speed at the rotor is different than the aircraft speed. For example, when there is angular motion and the rotor is displaced from the centre of gravity. For the purpose of the sizing model, the rotor velocity components are given by:

$$U^P = V_a \sin \alpha_{\text{rot}} \quad (3.53)$$

$$V^P = 0 \quad (3.54)$$

$$W^P = -V_a \cos \alpha_{\text{rot}} \quad (3.55)$$

Where (see Figure 3.11):

$$\alpha_{\text{rot}} = \alpha_w + \pi/2 + \theta_r; \quad (3.56)$$

Here it is assumed that the magnitude of the relative rotor velocity equals the aircraft apparent velocity, and the components are determined with the rotor inflow angle α_{rot} defined in Figure 3.13. Only the x-z plane is considered, so no velocity component in y ($V^P = 0 \text{ m/s}$)

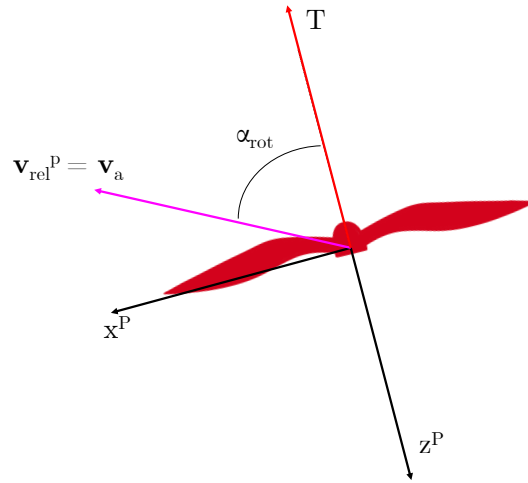


Figure 3.13: Rotor inflow

Applying the general momentum theory, following equation can be derived for the thrust [44]:

$$T_{MT} = 2\rho AV v_i \quad (3.57)$$

With V the total flow speed at the rotor (see Figure 3.14):

$$V = \sqrt{U^{P2} + V^{P2} + (W^P - v_i)^2} \quad (3.58)$$

Now using the blade element method (BEM), a relation can be found between the angle of attack of the blade elements and the total thrust of the rotor. Assuming that the rotor operates under ideal conditions with no stalled blade element and no reverse flow, the local angle of attack is given by [44]:

$$\alpha(\psi, r) = \left(\frac{W^P - v_i}{\Omega r + U^P \sin \psi + V^P \cos \psi} \right) + \theta_0 + \theta_1 \frac{r}{R} \quad (3.59)$$

For a blade with a linear twist distribution θ_0 and θ_1 represents the root blade angle and the linear twist respectively. Ω represents the angular rate (rad/s). Angle ψ defines the location of the blade in a single rotation, defined zero (0) when pointing in negative x-axis. r is the position of the blade element along the blade and R , the total blade length (radius of the rotor).

The total thrust can be obtained by integrating the lift of the blade elements over the blade length and over a full rotation and multiplying with the amount of blades (b). Assuming a constant lift curve slope a , constant

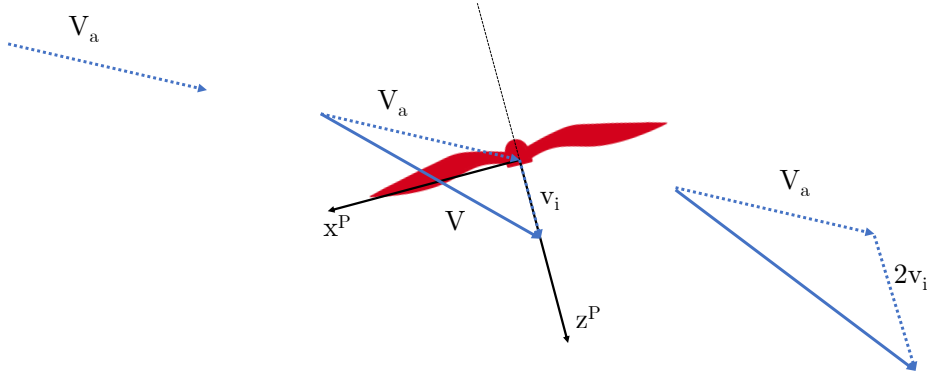


Figure 3.14: Rotor flow model

chord c and small angle approximation (to eliminate arctan), the following closed-form solution is obtained [44]:

$$T_{\text{BEM}} = \frac{\rho abcR}{4} \left((W^P - v_i)\Omega R + \frac{2}{3}(\Omega R)^2(\theta_0 + \frac{3}{4}\theta_1) + (U^{P^2} + V^{P^2})(\theta_0 + \frac{1}{2}\theta_1) \right) \quad (3.60)$$

Given the flight condition and motor RPM (fixed pitch), it is now possible to find thrust and induced velocity by solving Equations 3.96, 3.58 and 3.95 simultaneously. These are solved numerically in the optimization framework by means of constraints. This is explained in more detail in Chapter 3.7.

In the model from [44], induced power and profile power are considered. Applying the conservation laws, induced power is calculated using:

$$P_{\text{induced,ideal}} = T(v_i - W^P) \quad (3.61)$$

The profile power is necessary to overcome the skin friction drag acting on the blades while rotating. This drag component can be found similarly as the total thrust, now by integrating the drag of the blade element instead of the lift. Using the same assumptions as to derive the thrust equation, the profile power is given by:

$$P_{\text{profile}} = \frac{\rho C_{d_0} bc \Omega R^2}{8} \left((\Omega R)^2 + U^{P^2} + V^{P^2} \right) \quad (3.62)$$

Where C_{d_0} represents the zero lift drag coefficient of the blade airfoil. The total power is now given by:

$$P_{\text{tot}} = P_{\text{induced,ideal}} + P_{\text{profile}} \quad (3.63)$$

Application of the rotor models

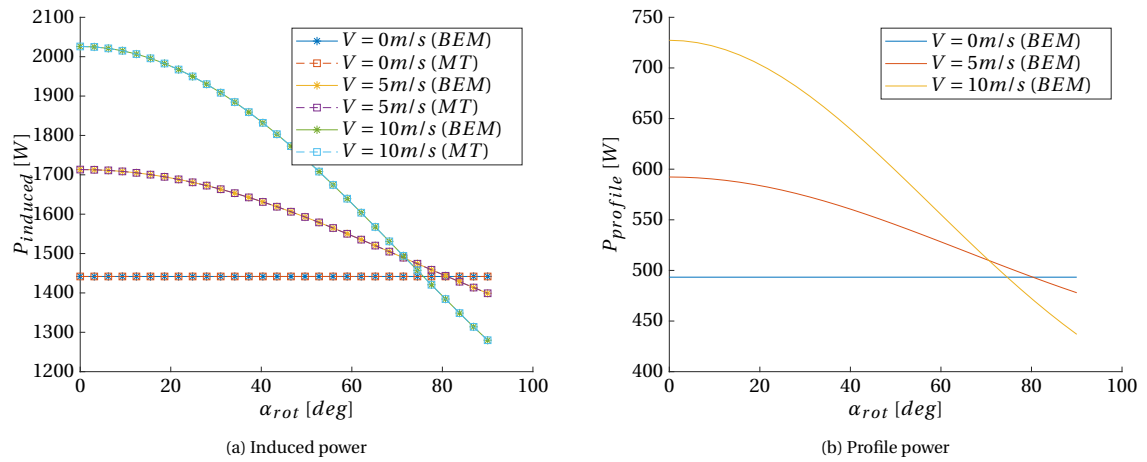
The results of both models are plotted in Figures 3.15 - 3.17 for a required thrust of 100N and a propeller diameter of 0.5m. Other rotor parameters, necessary for the BEM model, are given in Table 3.5.

In Figure 3.15a, the induced power is plotted against inflow angle for various flow speeds. It is verified that for 0 m/s inflow speed, the solution correspond to prediction given by the momentum theory for hover, and for axial inflow ($\alpha_{prop} = 0$ deg), the solution corresponds with the momentum theory for axial climb. Furthermore, it can be observed that induced power decreases with inflow angle. For an axial inflow, induced power increases with incoming flow. While for an incoming flow parallel to the rotor, induced power decreases. Both models predict the exact same value and trend. This is expected as they are both build on the fundamentals of general momentum theory. This also means that more detailed design parameters such as the number of blades, chord over radius and blade twist do not effect the induced power when taking the assumptions to derive the two models. Therefore, they are generally not considered in the preliminary sizing of the rotors.

Table 3.5: Rotor parameters

Parameter	Value	Reference
Number of blades [b]	2	Assumed
Lift slope [a]	$2\pi[1/rad]$	Assumed
Chord over radius [c_R]	0.16 [-]	[6]
Zero-lift drag [cd0]	0.03 [-]	Assumed
Root blade twist [θ_0]	30.8 [deg]	[6]
Linear blade twist [θ_1]	-21.9 [deg]	[6]

In Figure 3.15b, profile power is plotted against inflow angle for various flow speeds. This can however only be predicted with the simplified BEM model. A same trend can be observed as for the induced power, but with smaller magnitude. Note that the profile power is observed to highly depend on detailed parameters such as number of blades, chord over radius and blade twist.

Figure 3.15: Power estimation for T = 100N and $D_{prop} = 0.5m$

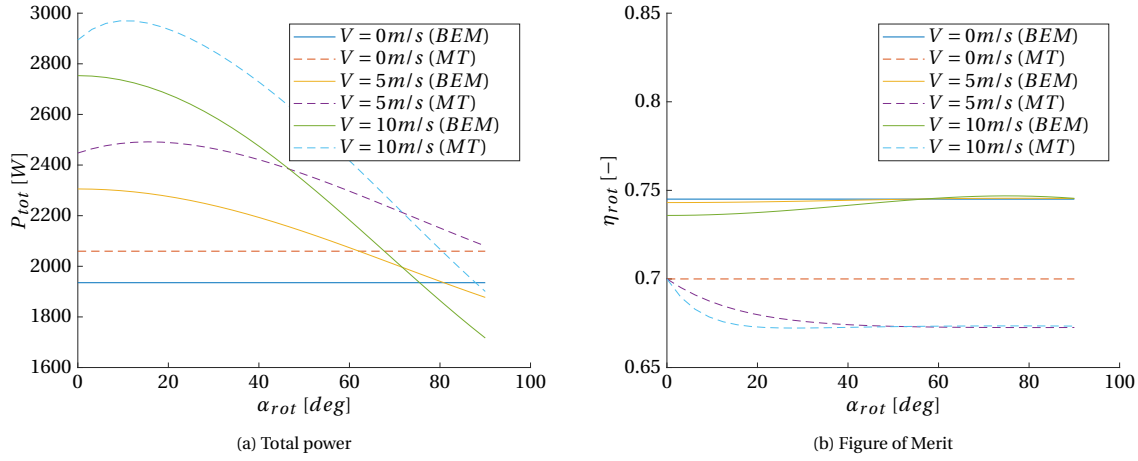
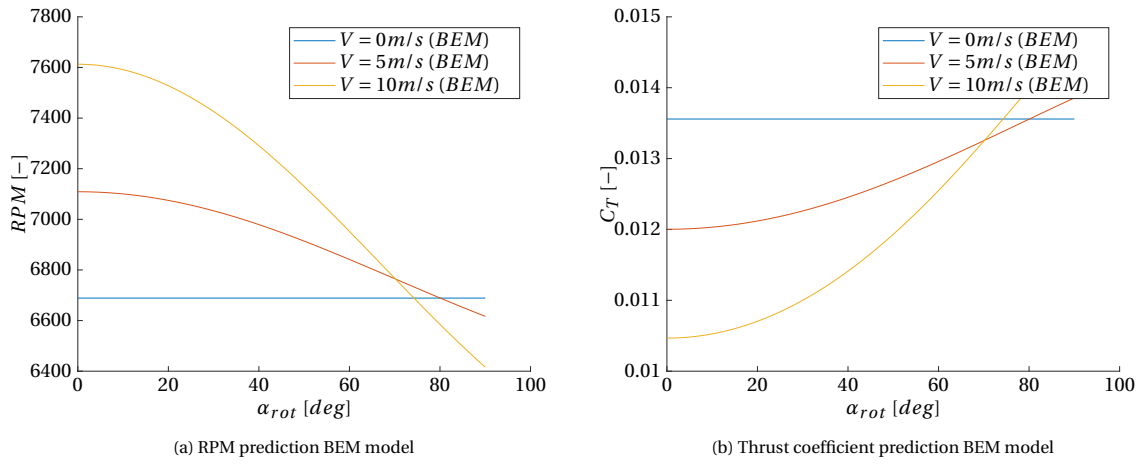
In Figure 3.16a, the total power is plotted against inflow angle for different flow speeds. For the simplified BEM model, the trend is the same as for induced and profile power. For the MT model proposed in [46], the total power first increases before decreasing with inflow angle. For a parallel inflow ($\alpha_{rot} = 90$ deg), the required power first increases with velocity and then decreases. This behaviour can be explained by the decrease in rotor efficiency, visualized in Figure 3.16b.

Finally, in Figure 3.17a and 3.17b, the required RPM and thrust coefficient are plotted against inflow angle, as predicted by the simplified BEM model.

Rotor efficiency

In the literature various definitions are used to indicate the rotor efficiency. In the literature on helicopter rotors, the term Figure of Merit is often used to indicate the ratio between ideal and measured power in a hover condition. Here, ideal power is calculated using momentum theory (induced power). The term rotor efficiency (η_{rot}), is used in more general flight conditions but also indicates the ratio between ideal and measured power. It should be noted that the efficiency depends on the flight condition and what condition a rotor is optimized for (e.g. hover or high speed).

Alternatively, total power can be calculated using equation 3.100, here κ represents an induced power correction factor, taking into account non-ideal flow. This factor is assumed independent on the flight condition, while $P_{induced,ideal}$ and $P_{profile}$ can be calculated depending on the flight condition using the BEM model (Equations 3.61 and 3.62). This allows a more accurate power estimation when multiple flight regimes are considered.

Figure 3.16: Power and efficiency estimation for $T = 100\text{N}$ and $D_{prop} = 0.5\text{m}$ Figure 3.17: Rotor characteristics for $T = 100\text{N}$ and $D_{prop} = 0.5\text{m}$

$$P_{tot} = \kappa P_{induced,ideal} + P_{profile} \quad (3.64)$$

A proper estimation of κ is then required to complete the power estimation model. It was already stated in the state-of-the-art review that for helicopter rotors $\kappa = 1.15$ is a typical value [28], while 1.5 is proposed by Winslow [50] for MAV scale rotors. When neglecting the profile power, this would correspond to rotor efficiencies of 87% and 67% (or FM = 0.87, 0.67) respectively. This decrease in efficiency for smaller rotors is also found in the statistical model of Tyan (Equation 2.34 [49]), plotted in Figure 3.18a.

In Figure 3.18b, FM is plotted against thrust coefficient in a hover condition (Equation 2.36 [28]). From this figure, it is clear that the profile power contribution is only significant at lower thrust coefficients ($C_T < 0.03$). In other words, if a rotor at high thrust coefficients, efficiency is merely determined by the inverse of κ . Recalling Figure 3.17b, it is clear that the assumed rotor design is operating at low thrust coefficients. By analysis it is observed that the thrust coefficient is highly dependent on more detailed rotor parameters such as the rotor pitch. Therefore, the profile power is assumed negligible in the preliminary sizing model. This assumption will have to be met in the detail design of the rotor.

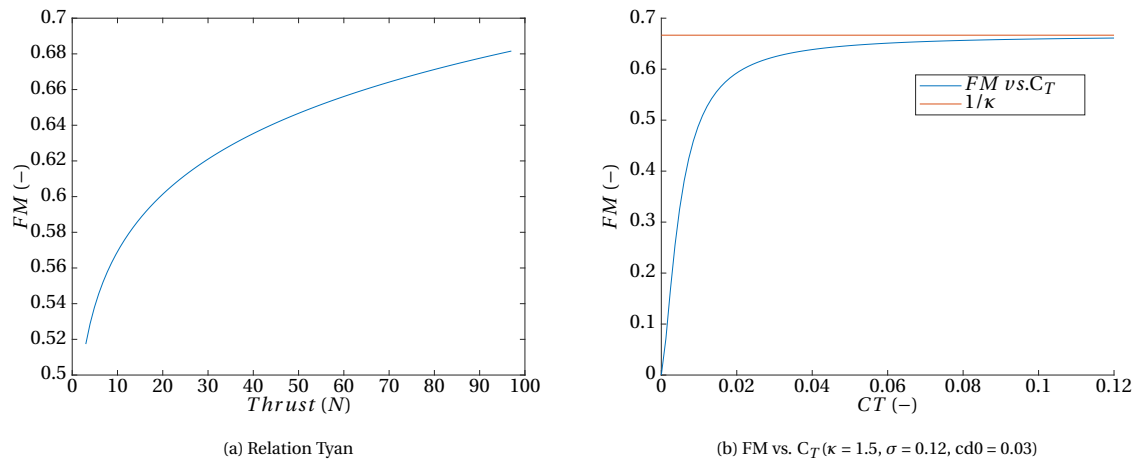


Figure 3.18

Conclusion on rotor power model

From the analysis of the rotor models, it can be concluded that the induced power is the most important power consideration. In the above presented model to calculate the induced power, the effect of oblique inflow is taken into account. This captures the most fundamental physics in the flight condition of a VTOL AWES. An induced power correction factor is applied to account for non-ideal effect, which is assumed independent of the flight condition. The profile drag is observed to be highly dependent on detailed rotor parameters such as the rotor pitch and twist distribution. Furthermore, the rotor can be designed such that the profile power contribution is small (high thrust coefficient). Therefore, for the purpose of the preliminary sizing tool the total power will be given according to:

$$P_{\text{tot}} = \kappa P_{\text{induced,ideal}} = \frac{1}{\eta_{\text{rot}}} P_{\text{induced,ideal}} \quad (3.65)$$

Where the rotor efficiency is now given by the inverse of the induced power factor κ . Based on the state-of-the-art analysis, a conservative value of 65%, optimum value of 70% and average value of 67.5% is used for the rotor efficiency in the preliminary sizing tool. Lastly, the efficiency correction suggested by [47] for skewed rotor inflow is not used in the preliminary sizing tool.

Rotor diameter

The rotor disk area is one of the main parameters influencing the required rotor power. From momentum theory in hover (see Equation 2.29), it is clear that the larger the rotor disk, the lower is the required induced power. On the other hand, the larger the rotor diameter, the heavier the rotor and the larger the drag in power generation flight if the rotors are exposed to the air. Later in this section an estimation of rotor mass is given. According to the state-of-the-art analysis no low fidelity model exist to date to asses the drag of in operating rotor. However, measures can be taken to minimize the drag of the inoperative rotor such as folding the rotors or putting them in a feathering position. Therefore, the drag of an inoperative rotor is excluded from the sizing model.

The rotor diameter also has an impact on aerodynamic interference between the rotor and the wing. The larger the rotor, the larger is the interference between the two, or the more difficult it is to mitigate the interference. Also the inertia of the aircraft is influenced by the rotor diameter, big rotors need to be placed further away from the center of gravity and result in a higher inertia. This will effect maneuverability and controllability of the aircraft. Also the larger the diameter, the larger the VTOL structure is which will increase weight and drag. Lastly, the rotor diameter also limited by geometry and aircraft lay-out. Because the rotor diameter has more impact than is taken into account in the preliminary sizing, the effect of rotor diameter is analysed in more detail in the sensitivity analysis (see Section 5.2.3).

Rotor mass

Several relations are found in the literature relating the rotor mass to the diameter. Among which the Roskam method [39], and parameterizations from Ampatis [2], Bershadsky [6] and [50]. In Figures 3.19a, 3.19b and

3.20a these parameterizations have been plotted. Reference values are obtained from commercial available plastic propellers (see Figure 3.20b). From these parameterizations, the one from Ampatis seems unrealistically large. Considering Roskam’s method, the mass of the rotor scales with power. For the scale of aircraft considered, it is assumed that the mass of the rotor only scales with diameter.

Winslow [50] and Bershadsky [6] agree on rotor mass. The difference between the two mass estimations is that Winslow takes into account more rotor parameters (rotor radius, solidity and number of blades), whereas Bershadsky considered multiple materials. However, Winslow parameterization is based on rotors up to 25g, while the parameterization of Bershadsky based on rotors up to 100g for carbon fibre rotors. Therefore, the parameterization of Bershadsky is more appropriate for the problem at hand. The total rotor mass is then given by:

$$m_{rot} = n_{rot} \left(0.001 \left(0.1207 (39.37 D_{rot} [m])^2 - 0.5122 (39.37 D_{rot} [m]) \right) \right) [kg] \tag{3.66}$$

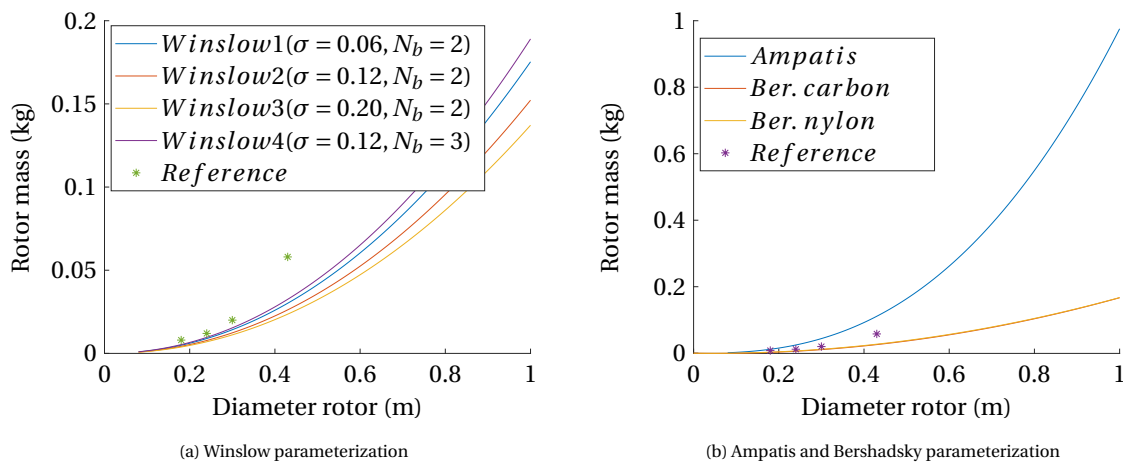


Figure 3.19

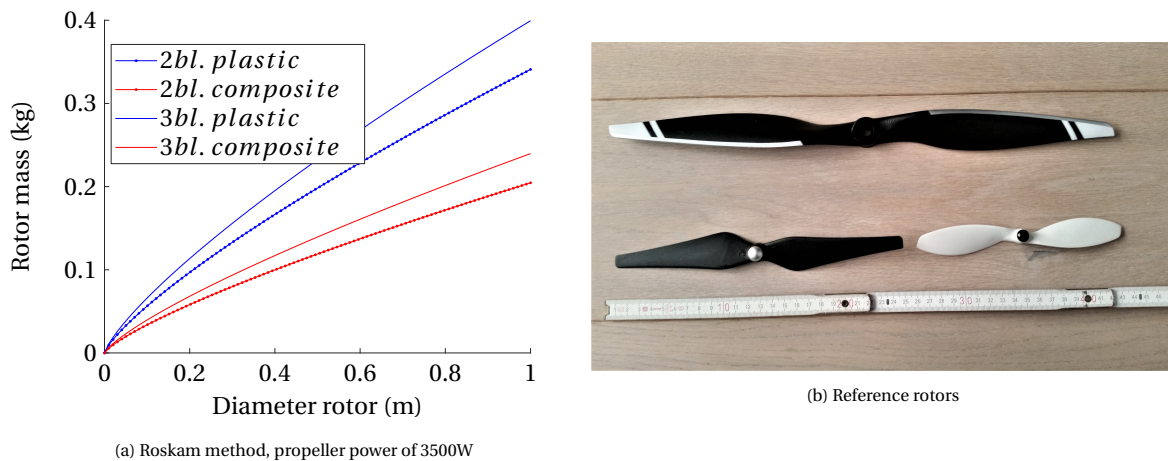


Figure 3.20

3.5.2. Motor model

In this subsection the motor model which is used in the design model is described.

Electrical model

In the state-of-the-art review, an electrical (classic three-constant) model has been described relating the inputs to the motor; current and voltage to output such as power, torque, efficiency and RPM. This model requires following motor parameters: I_0 , R_a , K_v , K_T . However looking at the system model (Figure 3.10), The only parameter of interest at the preliminary sizing phase is the mass and efficiency of the motor. Motor mass estimations have been found in the literature based on the required output power. Therefore this electrical model is not required for the sizing model. It can be used however in the detailed design phase to select an appropriate motor, or design one in more detail (see proposed design methodology in Figure 3.1).

Motor mass

Various motor mass relations are given in the state-of-the-art review. Most of them present a linear relation between motor mass and power defined by the motor specific power (μ_{mot}). Motors available on commercial websites, served for hobby rotor and RC-plane, show a specific power of around 4 kW/kg. This is similar to the values used by [17] and [35] and is used as conservative values for the specific power. The biggest motors available from MAD¹, which serve more professional drones, show a specific power closer to the prediction of [21], which predict a specific power to 9.5 kW/kg for the bigger motors (around 1kg). This prediction is used as an optimum value. Specific power prediction used in [4] of 5kW/kg is used as average value. The motor mass is calculated according to;

$$m_{mot} = \frac{f_{gust} \max(P_{i,req})}{\mu_{mot}} \quad (3.67)$$

where, i indicates a certain segment in the flight path and $P_{i,req}$ is the total power required for all rotors, calculated with the rotor model.

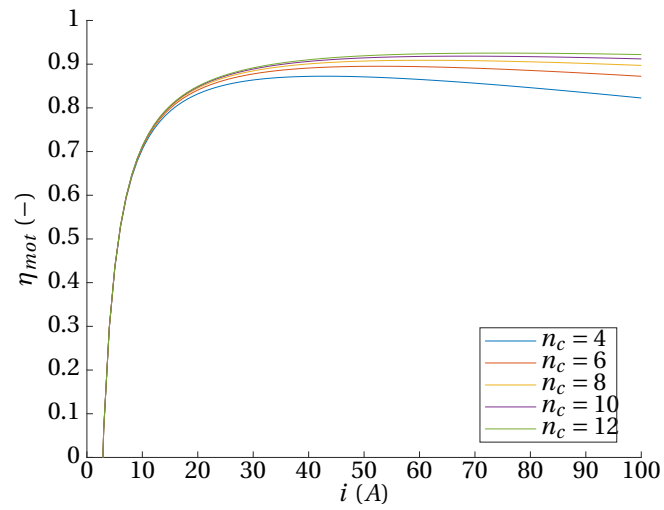
Motor efficiency

From electrical model following efficiency is derived (Equation 3.68). Here the driver efficiency η_D , is assumed 0.95 by Gur [22] and Gatti [17].

$$\eta_M = \eta_D \left(1 - \frac{i R_a}{V_k}\right) \left(1 - \frac{i_0}{i}\right) \quad (3.68)$$

As motor parameters R_a and i_0 are fixed for a certain motor, motor efficiency is dependent on both input current and voltage. Using motor parameterization proposed by Ampatis [2], a value of $R_a = 0.0227$ Ohm and $i_0 = 2.8355$ A are obtained for a motor of 1 kg. In Figure 3.21 the efficiency is plotted against current for batteries with different amount of cells. The voltage is determined by $V_k = 3.7 n_c$. It can be observed that a motor efficiency of 90% can be obtained when operating at design conditions. This value will be assumed as a fixed value for the motor efficiency in the preliminary sizing model.

¹<http://madcomponents.co/index.php/m30-100kv/>

Figure 3.21: Motor efficiency vs. current ($\eta_D = 1$)

3.5.3. Battery model

In this subsection the battery model which is used in the design model is described.

Electrical model

For the problem at hand, only a prediction of the battery mass is required, so similar to the motor, an electrical model is not required for the preliminary sizing model.

Battery mass

The mass of the battery is either determined by the required energy or power it has to deliver. In most cases in UAV design methods only the required energy is determined as the operating time is maximized. However, for the problem at hand, required energy can be low as only the take-off phase is considered. Power on the other hand can be quite high, as the entire aircraft is to be lifted solely on rotor power. Therefore, the battery specific power is an important consideration for the sizing of a VTOL system for AWESs. The battery mass is determined by Equations 3.69-3.71. Here E_{bat} and μ_{bat} are the battery specific energy and power respectively. η_{bat} , η_{mot} , η_D are the battery, motor and motor driver efficiency respectively. f_{DOD} is the depth of discharge, used to increase battery life.

$$m_{bat_E} = \frac{f_{control} \sum P_{i,req} t_i}{E_{bat} \eta_{bat} \eta_{mot} \eta_D f_{DOD}} \quad (3.69)$$

$$m_{bat_P} = \frac{f_{control} \cdot \max(P_{i,req})}{\mu_{bat} \eta_{bat} \eta_{mot} \eta_D} \quad (3.70)$$

$$m_{bat} = \max(m_{bat_E}, m_{bat_P}) \quad (3.71)$$

Little has been found in the literature on the specific power on LiPo batteries. In [4], a value of 5 kW/kg is assumed for the specific power. However, batteries available from commercial websites² show specific powers over 10 kW/kg. Therefore, a value of 5kW/kg and 10kW/kg is taken as conservative and average values respectively. For an optimum value it is assumed that the battery can be designed to meet the required specific power (hence ∞).

²https://hobbyking.com/nl_nl/turnigy-heavy-duty-2200mah-4s-60c-lipo-pack-w-xt60u.html

3.5.4. Other subsystems

The rotors, motors and battery have been identified as the main components to be considered for the preliminary sizing. However, other components are necessary as well such as an electronic speed controller and supporting structure. The design considerations are shortly described here.

ESC

The electronic speed controller (ESC) controls the speed of the motor. In [35], mass of ESC are assumed negligible for heavy lift drones. In the literature on small-scale UAV such as [50], [6], the weight of ESCs has been taken into account. ESC mass relations are developed in these papers depending on the maximum current flowing through the ESC. However as the current is not predicted in the preliminary sizing, the mass of the ESC is not considered. Instead, a mass fraction MF_{other} is defined, taken into account other components such as the ESC, to have an initial guess of the effect of other component masses on the system design. A value of 25% is assumed for this mass fraction.

Structure

A structure is required to attach the VTOL system to the aircraft. The structure is required to withstand all the loads during take-off and power generation. The mass of the structure will depend on these loads and the VTOL system configuration (see Figure 3.9). At this design phase it is not possible to accurately predict the mass of the structure, therefore it will also be included in the mass fraction for other components MF_{other} . Furthermore, the structure, in the form of pylons, can significantly contribute to the additional drag, next to the inoperative rotors. Again, an accurate estimation of this drag cannot be made at this stage. The effect of extra drag will however be taken into account by assuming a certain $C_{D,VTOL}$, which is added to the drag model of the AP2. $C_{D,VTOL}$ is assumed to equal the zero-lift drag of the AP2. In other words, it is assumed that the zero-lift drag of the AP2 doubles when a VTOL system is installed.

Flight controller and wiring

Finally, also the mass of the flight computer and wiring is assumed to be included in MF_{other} . The contribution of the flight computer mass is low as it can be integrated in the flight controller of the AWE aircraft.

3.6. Design parameters

In Table 3.6, all design parameters and their values are given. Note that the ones without reference are assumed values. Optimum design parameters values are the result of a detailed design phase, while conservative design parameter values are readily available on the market but representative for this research. Averages values fall in between. Note for design variables such as D_{prop} , no values have been assumed, but their values are optimized (see Chapter 3.7). In the sensitivity analysis the effect of taking conservative, optimum and average values will be analyzed. Note that the underlined parameters and the ones with an asterisk* are analyzed separately in the sensitivity analysis (see Chapter 5).

Table 3.6: Assumed design parameters

	Conservative	Optimum	Average	Unit
System				
n_{rot} (Amount of rotors)	4	4	4	[-]
Rotor				
κ	<u>1/0.65</u> [49]	<u>1/0.7</u> [28]	<u>1/0.675</u>	[-]
a (lift slope)	2π	2π	2π	[-]
b (Number of blades)	2	2	2	[-]
c/R (Chord to radius ratio)	0.16 [6]	0.16 [6]	0.16 [6]	[-]
c_{d0}	0.03	0.03	0.03	[-]
θ_0 (root blade twist)	30.8	30.8	30.8	[deg]
θ_1 (linear twist slope)	-21.9214	-21.9214	-21.9214	[deg]
Battery				
E_{bat} (Specific energy)	<u>130</u> [4]	<u>250</u> [6]	<u>190</u>	Wh/kg
μ_{bat} (Specific power)	5* [4]	∞ *	10*	kW/kg
f_{DOD}	0.8 [17]	0.8 [17]	0.8 [17]	[-]
η_{bat} (Battery efficiency)	0.95 [17]	0.95 [17]	0.95 [17]	[-]
Motor				
μ_{mot} (Specific power)	<u>4</u> [17] [35]	<u>9.5</u> [21]	<u>5</u> [4]	kW/kg
η_{mot} (Motor efficiency)	0.9 [2]	0.9 [2]	0.9	[-]
η_D (Driver efficiency)	0.95 [22] [17]	0.95 [22] [17]	0.95 [22] [17]	[-]
Other subsystems				
MF_{other}	0.25	0.25	0.25	[-]
$C_{D,VTOL}$	0.03	0.03	0.03	[-]
f_{gust}	1.8	1.8	1.8	[-]
$f_{control}$	1.5	1.5	1.5	[-]
Atmospheric parameters				
ρ	1.225	1.225	1.225	[kg/m ³]
g	9.81	9.81	9.81	[m/s ²]

3.7. Multi-disciplinary design optimization (MDO) framework

In the state-of-the-art review two (2) design approaches are given, being the classical approach and optimization approach. In this work an optimization framework is developed. The optimization framework in this work has two purposes. First, to solve for the constraints such that a feasible design is calculated. Secondly, the most optimum design is searched for. In this research the mass of the VTOL system is minimized.

3.7.1. Sizing model

The complete sizing model as described in previous sections is depicted in Figure 3.22. It consist of a flight mechanics model, rotor model, motor model, battery model and system model. The different models can also be viewed as different disciplines. Therefore, the problem can be identified as a multi-disciplinary problem. It is clear that this model cannot be solved by evaluating the models one after each other, as data needs to be exchanged between the disciplines and models. The disciplines are therefore coupled. Coupled models are found within the rotor model (momentum theory (MT) and blade element method (BEM)), within the flight mechanics model (x and z forces) and between the flight mechanics model and component/systems model. Coupled models require both feedback and feedforward exchange of information and require iterations to be solved. The motor and battery model are uncoupled. The rotor, motor/battery and system model are decoupled. Decoupled systems require feedforward data exchange and can be evaluated in sequence. Uncoupled systems require no data exchange and can be evaluated in parallel. In this work the MT and BEM rotor model links are "teared" and the models become uncoupled. This "tearing" is done by introducing the coupling variables as extra variables (consistency variables) to the optimization, to allow the models to be evaluated independently. This is also done for the x and z force components in the flight mechanics model. The coupling between the component/system model and flight mechanics model has been decoupled, feedforward exchange of the VTOL system mass is still allowed. The optimizer is responsible for the consistency of the disciplines as is explained in Section 3.7.2.

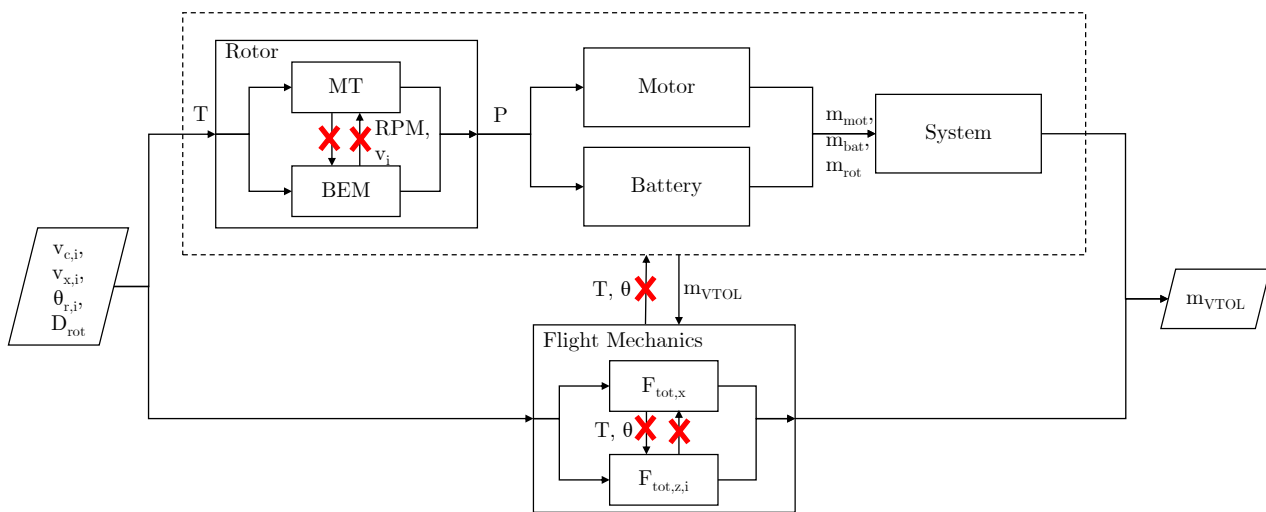


Figure 3.22: Coupled sizing model

3.7.2. Optimization architecture

In this section the framework used to solve to design problem is explained. In this work a variant of the individual discipline feasible (IDF) architecture is used. In this architecture all disciplines are uncoupled in the analysis. Consistency variables are introduced to exchange information between the disciplines. Here,

the consistency constraints ensure matching information at the optimal solution [27].

In this work a variant of IDF is used as feedforward data exchange between the disciplines is allowed (decoupled), while generally in an IDF architecture this is not allowed (uncoupled). How the systems are decoupled is explained in Section 3.7.1. By doing this, nested iterations of the coupled models within an optimization loop are avoided. By decoupling and ensuring consistency by means of consistency constraints, the optimization computational time is observed to decrease by a factor of 100 compared to an optimization with nested iterations (from 752.36 seconds to less than 10 seconds). One disadvantage of this approach however is that no feasible solution is guaranteed until convergence is reached by the optimizer.

In Figure 3.23, the used optimization architecture is visualized in an extended design structure matrix (XDSM) format [27]. The XDSM is derived from the design structure matrix (DSM), and allows to show data dependency and process flow in one diagram. In this diagram the rectangle represents a generic process or model. Green processes are characteristic to the sizing model, pink processes are characteristic to the optimization. The parallelogram indicate an input or output. A parallelogram in the same row of a process is output to that process (e.g. m_{bat} , is output to battery model). A parallelogram situated in the same column of a process are input to that process (e.g. $v_{c,i}$ and P_i , are input to the battery model). A grey shaded parallelogram is an input/output within the optimization procedure. A white parallelogram is input/output of the optimization. Note that the input to the optimizer is also indicated with a 0 (initial conditions) and output with * (optimal solution). Data dependency is indicated with the thick grey line. The thin black line (solid and dashed) indicates the flow of the process, together with the numbering in the processes. It is clear that the models are evaluated in sequence. The objective function f_0 (solid) and consistency constraints $c_{eq,c}$ (dashed) are evaluated in parallel by the optimizer. The rounded rectangle (here optimizer) indicates a driver of an iterative procedure. It is both the start (1) and end (7) of one iteration. After the iteration (7) the optimizer evaluates whether the solution is converged (stopping criteria is met). If not, a new design vector enters a new iteration (1).

0. Pass initial design vector to the optimizer.
- 1-5. Evaluate sizing models in sequence
6. Calculate objective and consistency constraints in parallel
7. Calculate new design vector based on f_0 and $c_{eq,c}$. If convergence criteria is met, return optimal solution \mathbf{x}^* ; else; return to 1.

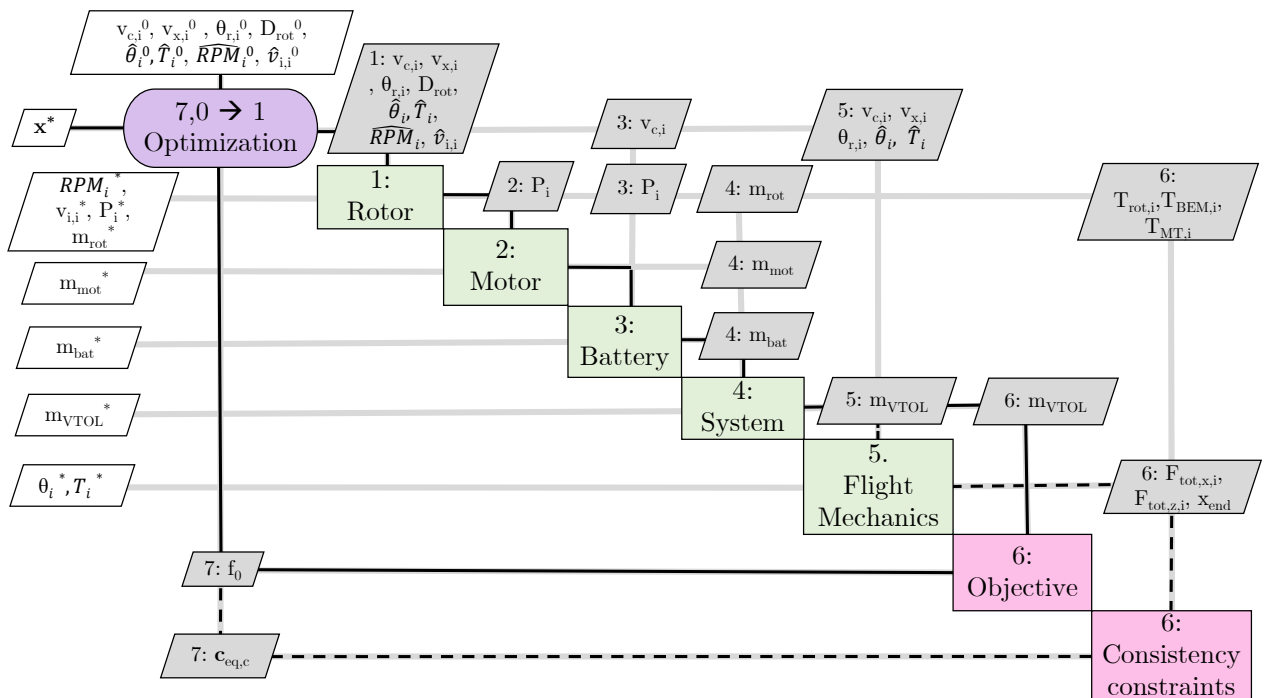


Figure 3.23: Optimization Architecture (XDSM format [27])

Finally, the equations used to compute the sizing models are depicted in Figure 3.24.

3.7.3. Variables, objective and constraints

Two different types of variables are identified in this problem, they are given in Table 3.7 with their initial conditions (IC), bounds and reference values. First, the design variables ($v_{c,i}$, $v_{x,i}$, $\theta_{r,i}$, D_{rot}) are always under the explicit control of the optimizer. It is found that these variables are most influential to the VTOL system design. Secondly, the consistency variables, which were introduced to uncouple the models. These are indicated with a $\hat{\cdot}$. Recall that the design parameters, which do not vary during optimization, are given in Table 3.6.

In the optimization multiple flight path segments, indicated with " i ", are considered for which the aircraft velocity can vary and rotor pitch in the case of a tilt-rotor concept. For fixed rotor the rotor pitch is kept constant through the different flight segments. In this research two (2) segments are considered. One for a vertical take-off until a clearance height is met and one to fly to the target position.

The initial conditions are varied for aircraft pitch and required equilibrium thrust to maximize the probability to find both a feasible and global optimum solution. The values given in the table are obtained by trial-and-error and are found to give proper solutions over wind speeds between 0 and 10 m/s. An initial value for RPM of 1000 is used and is varied with the values (1250,1500,1750) for the fixed rotor concepts. Other initial conditions are not varied. For the initial conditions the induced velocity is estimated with the hover equation (see Equation 2.27). For a fixed rotor concept the rotor pitch has been bounded by the given rotor pitch (e.g. -90° for tail-sitter).

Table 3.7: Optimization variables with their IC, bounds and ref. values

Variable	Initial condition	Lower bound	Upper bound	Ref. value
Design variables				
Climb speed ($v_{c,i}$) [m/s]	1.5	0.1	3.5	3
Horizontal speed ($v_{x,i}$) [m/s]	0	0, -15+ V_w ($i = 1, 2$)	0, 15+ V_w ($i = 1, 2$)	3
Rotor pitch ($\theta_{r,i}$) [deg]	0	-180	90	45
Rotor diameter (D_{rot}) [m]	0.5	0.1	2	1
Consistency variables				
Aircraft pitch ($\hat{\theta}_i$) [deg]	linspace(-45,180,12)	-45	180	45
Equilibrium thrust (\hat{T}_i) [N]	linspace(50, $m_{A/C}g$, 4)	1	2 $m_{A/C}g$	$m_{A/C}g$
Rotor RPM_i [-]	1000 (1250,1500,1750)	100	5000	1000
Rotor ind. velocity ($\hat{v}_{i,i}$) [m/s]	13.69 (hover, $D_{rot} = 0.5$)	0	20	6.85 (hover, $D_{rot} = 1$)

The objective of the optimization (VTOL system mass) given by Equation 3.72.

$$f_0(\mathbf{x}) = m_{VTOL}(\mathbf{x}) = \frac{m_{rot}(\mathbf{x}) + m_{mot}(\mathbf{x}) + m_{bat}(\mathbf{x})}{1 - MF_{other}} \quad (3.72)$$

The constraints in the optimization are the following;

- Force equilibrium (flight mechanics model)
- Meet the target position
- Physical consistency in the rotor model

Mathematically formulated as:

$$\mathbf{c}_{eq,c}(\mathbf{x}) = \begin{pmatrix} F_{tot,x,i} \\ F_{tot,z,i} \\ x_{end} - x_{target} \\ T_{BEM,i} - T_{MT,i} \\ T_{rot,i} - T_{MT,i} \end{pmatrix} = 0 \quad (3.73)$$

3.7.4. Optimizer and settings

The MATLAB function "fmincon" has been used to setup the optimization problem. The algorithm "sqp" is used. Design and consistency variables are normalized according with their reference values in Table 3.7, reference values for the objective values and constraints are given in Table 3.8. "MaxIterations" and "MaxFunctionEvaluations" are set on 1000 and 10000 respectively to maximize the changes of convergence before the iteration limit is reached. To maximize the probability of converging to a feasible solution, the problem is first solved for constraints only. Then, the new initial condition that satisfies the constraints is used to solve the final optimization. The optimization problem is run for multiple initial conditions, the minimum VTOL system mass is taken of all optimizations with positive exitflag (feasible and converged solution).

Table 3.8: Reference values objective and constraints

Objective/constraint	Reference value
$m_{VTOL}[kg]$	1/6 $m_{A/C}$
$F_{tot,x,i}[N]$	$m_{A/C}g$
$F_{tot,z,i}[N]$	$m_{A/C}g$
$x_{end} - x_{target}[m]$	100
$T_{BEM,i} - T_{MT,i}[N]$	$m_{A/C}g$
$T_{rot,i} - T_{MT,i}[N]$	$m_{A/C}g$

3.7.5. Feasibility and optimality check

The goal of the optimization is to find a feasible design which leads to the minimum amount of VTOL system mass within the imposed constraints. Whether the design is feasible within the constraints is checked by a proper sanity check of the result. To check if force equilibrium is satisfied the force vectors acting on the aircraft in the optimized condition are plotted. It is observed that the forces make sense in direction and magnitude and that they cancel out in the steady flight. The trajectory is plotted and verified to meet the target position and maximum tether length.

In contrast to the feasibility, the optimality of a design solution is much less trivial to prove. The optimizer algorithm used is gradient based and will converge to a local optimum. A global optimum can however not be guaranteed with the used optimization algorithm. However, to maximize the probability of getting a global optimum, initial conditions have been varied according to Table 3.7, and the minimum feasible value from all initial conditions results is taken. The required thrust plays a major role in the sizing of the VTOL system. It is observed that optimal solutions are the ones making most use of the aerodynamic lift, to minimize the required force. Solutions on different reference wind speeds (0m/s ,5 m/s ,10 m/s) are analyzed in more detail and there is confidence that these points are converged to a global optimum. Furthermore, the results

are plotted for multiple wind speeds. If smooth results (no sudden peaks) are obtained with respect to these reference results, it can be argued that all of the results are converged to a similar optimum, which is likely to be a global one. If a solution has been observed to fall below or above the general trend, it can be argued that it is converged to a different local minimum, which is either higher or lower. Initial conditions have been added until a smooth general trend was reached and confidence was gained that the trend consists of global optima.

Other optimization algorithms have been tried in order to check the optimality. The genetic algorithm is a non-gradient based algorithm, which tends to have a higher probability of finding a global optimum. This algorithm was not able to find a more optimal solution than the gradient based approach for the tested cases. Furthermore, the algorithm is much slower as it is not using gradient information. It can therefore be argued that the problem at hand can best be solved using a gradient based approach provided that the initial conditions are properly varied.

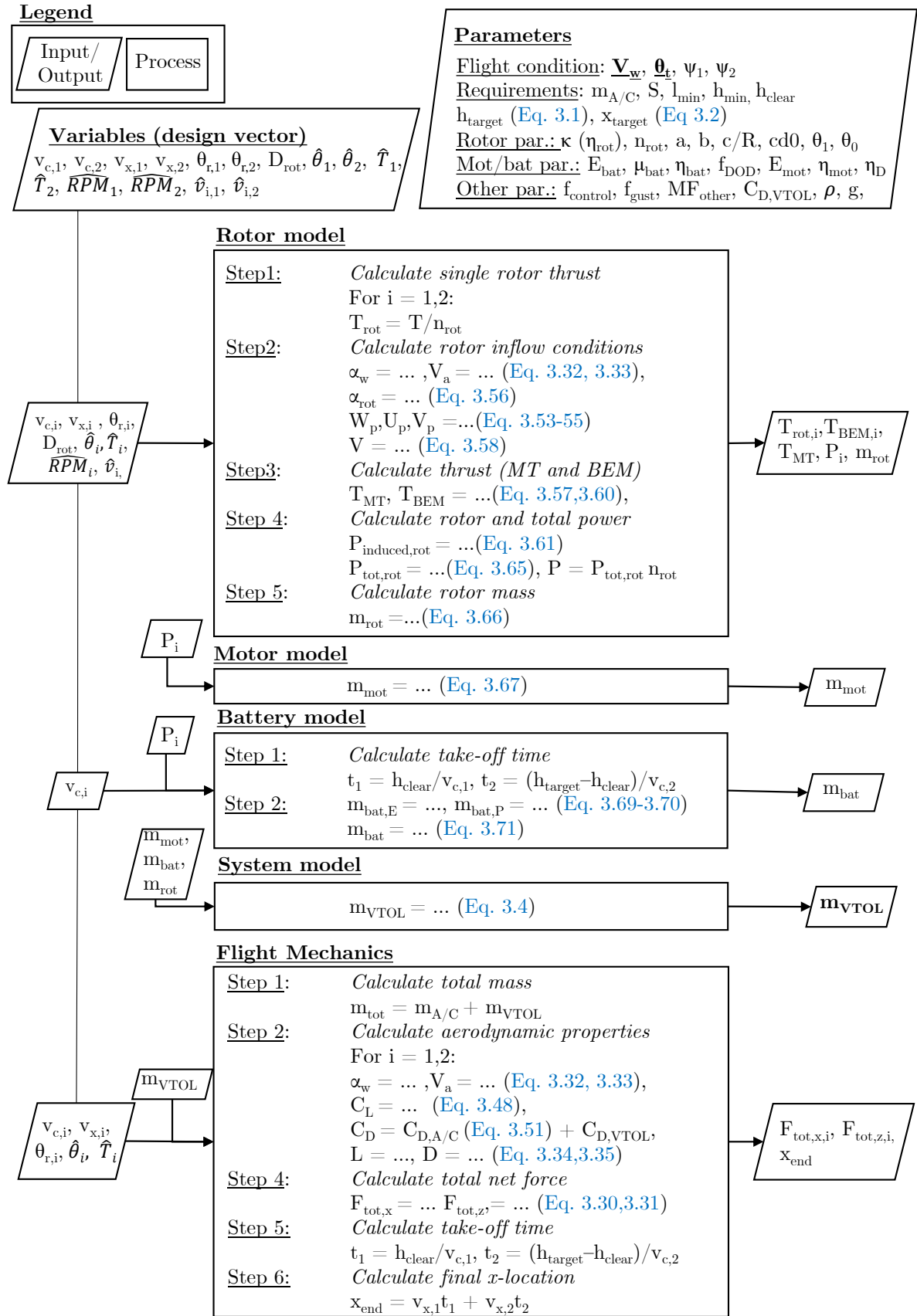


Figure 3.24: Sizing algorithm

3.8. Dynamic feasibility

In the sizing model, a steady flight condition is used to size the VTOL system. In this section a simulation model is described and applied with the purpose to assess the dynamic feasibility of the VTOL system that is sized assuming steady flight. To do so an aircraft model is built which captures the main dynamic effects. A controller (or autopilot) is built that guides the aircraft to the steady flight condition as optimized in the sizing algorithm. The control structure consists of a path planner, path controller, velocity controller and electronic speed controller. The aircraft model consists of the rotor model and aircraft dynamics. The simulation structure is depicted in Figure 3.25. The building blocks of this simulation structure are described in the following sections. For convenience, all vectors in this section are given in the wind frame.

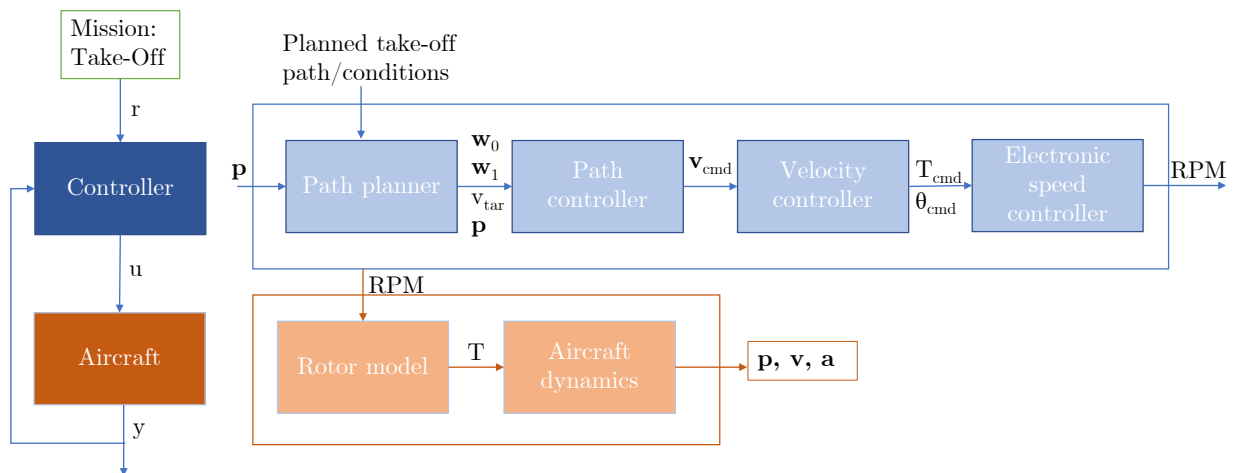


Figure 3.25: Simulation Structure

3.8.1. Controller

In this section the controller that is used for the simulation of the take-off is explained. In this research the VTOL system is controlled similar to multicopter. For these type aircraft control is maintained by controlling the forces of each rotor individually by changing the RPM of the motors accordingly. By controlling the individual RPM of each rotor the total thrust and moments on the aircraft can be controlled. This work is focused on the total thrust of the combined rotors and the thrust is divided equally among the rotors. The attitude control itself is not considered, but the dynamics are included in the form of a second order system (see section 3.8.2).

Following elements are identified in multicopter control (see Figure 3.26): a flight controller, electronic speed controller (ESC), motor and rotor. The battery provides the required power to all subsystems. In the control structure presented in Figure 3.25, the path planner, path controller and velocity controller are to be implemented in the flight controller (or computer), which will send a signal to the electronic speed controller based on the control algorithms and sensed data. This signal is then converted to a certain motor RPM by the electronic speed controller and a certain thrust delivered by the rotor. The control loop is closed by sensing the aircraft's motion, and changing the RPM accordingly.

Path planner

The take-off trajectory that is simulated is the one where both minimum height and tether length are limiting, corresponding to a target elevation angle of 41.8 degrees. This trajectory is visualized in Figure 3.27 and is

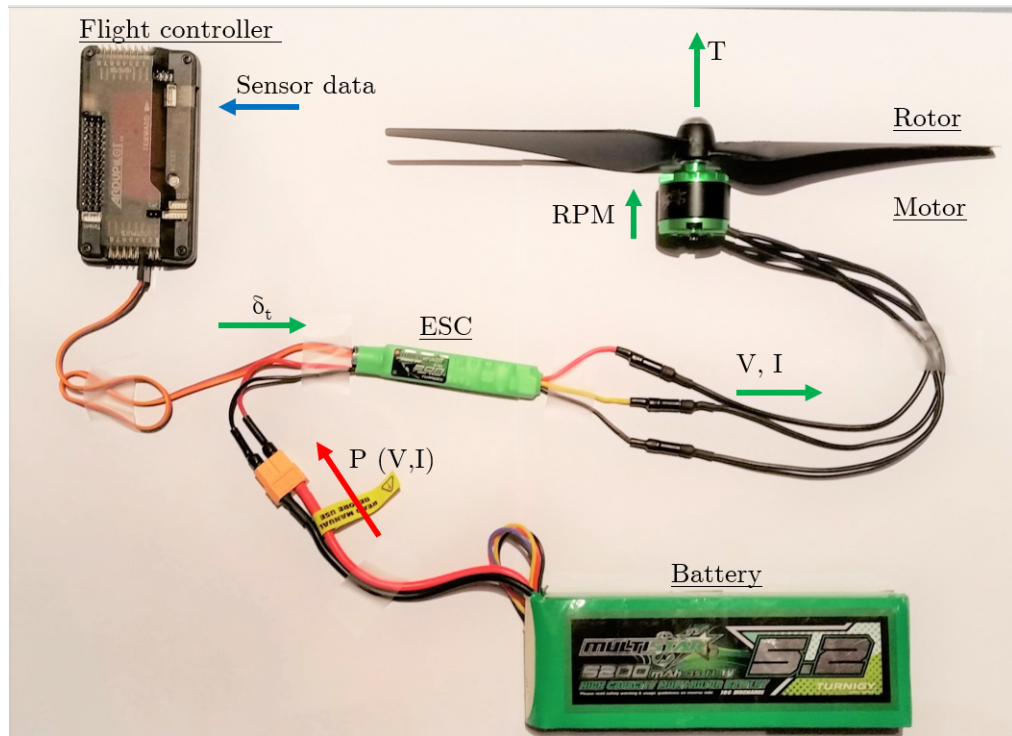


Figure 3.26: Multicopter controller

defined by (three) 3 waypoints (Equations 3.74-3.76). The target speed on the trajectory is optimized per segment by the sizing model and is calculated by Equation 3.78. The second segment is activated once the clearance height is met.

$$\mathbf{w}_0 = (0 \quad 0) \quad (3.74)$$

$$\mathbf{w}_1 = (0 \quad h_{clear}) \quad (3.75)$$

$$\mathbf{w}_2 = (x_{target} \quad h_{target}) \quad (3.76)$$

$$\mathbf{v}_i = (v_{c,i} \quad v_{x,i}) \quad (3.77)$$

$$v_{tar,i} = \sqrt{v_{c,i}^2 + v_{x,i}^2} \quad (3.78)$$

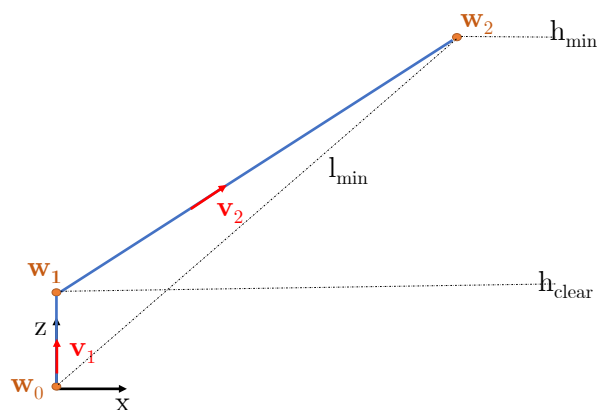


Figure 3.27: Path planner

Path controller

Now the flight path is defined, a controller is developed that guides the aircraft towards this path. The path controller described in [37], is used for this work. Here, the output of the path controller is a velocity vector aimed at the flight path. This is done by calculating a virtual target, \mathbf{p}_{vt} onto the flight path and aiming the velocity towards that target. A visualization of all the vectors is given in Figure 3.28.

The path to be flown is straight, so it can be defined using a vector, denoted \mathbf{s} .

$$\mathbf{s} = \mathbf{w}_1 - \mathbf{w}_0 \quad (3.79)$$

The position of the aircraft with respect to the first waypoint is given by;

$$\mathbf{p}_w = \mathbf{p} - \mathbf{w}_0 \quad (3.80)$$

The target point is based on the closest point of the path to the aircraft. As the path is straight, this point is given by an orthogonal projection of the aircraft position onto the path;

$$\mathbf{p}_{w,\perp} = \frac{\mathbf{p}_w^T \cdot \mathbf{s}}{\mathbf{s}^T \cdot \mathbf{s}} \mathbf{s} \quad (3.81)$$

The virtual target is now defined as a point on the path which is placed a distance Δ_{vt} away from the projected position in the flight direction. Mathematically;

$$\mathbf{p}_{vt} = \mathbf{w}_0 + (\|\mathbf{p}_{w,\perp}\|_2 + \Delta_{vt}) \frac{\mathbf{s}}{\|\mathbf{s}\|_2} \quad (3.82)$$

Now the virtual target is calculated, aiming the velocity vector towards that point is defined mathematically as;

$$\mathbf{v}_{cmd} = v_{tar} \frac{\mathbf{p}_{vt} - \mathbf{p}}{\|\mathbf{p}_{vt} - \mathbf{p}\|_2} \quad (3.83)$$

The inputs of this procedure are the aircrafts position \mathbf{p} , the waypoint ahead \mathbf{w}_1 , previous waypoint \mathbf{w}_0 and current target velocity v_{tar} . The aggressivity of the path controller is defined with Δ_{vt} . When defined as zero, the aircraft is guided perpendicular towards the flight path, which will result in an oscillation around the flight path due to the inertia of the system [37]. For large Δ_{vt} , the distance from the path will only decrease slowly. In this work Δ_{vt} of 1.5m is found to result in acceptable path-following performance.

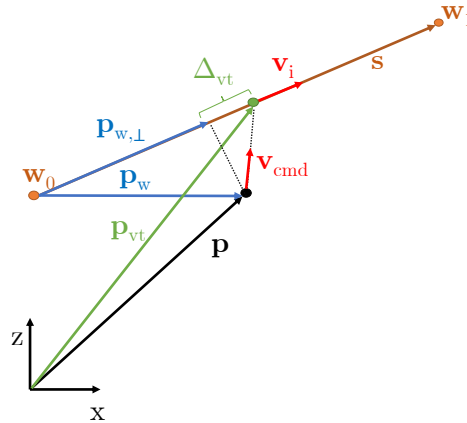


Figure 3.28: Path controller visualization

Velocity controller

In the path controller a kinematic velocity \mathbf{v}_{cmd} is calculated which guides the aircraft towards the flight path. In this section a controller is described to control the aircraft in order to reach this velocity. The purpose of the velocity controller is to calculate the total thrust and attitude command which will accelerate the aircraft towards the desired velocity. The velocity controller described in [37], is used for this work.

The control structure in Figure 3.29 is used to calculate a commanded acceleration based on the commanded velocity. To do so a reference acceleration \mathbf{a}_r and velocity \mathbf{v}_r are introduced, defined by a first order filter over the input signal. The time constant τ of the first order filter is constraint by the inner-loop dynamics, and determined such that the outer-loop dynamic are slower then the inner-loop to prevent instability. In this work a time constant of 1.4 s is found to result in acceptable path-following performance. A PI-controller is implemented to track the reference velocity. K_P and K_I gains of 2 and 1.5 respectively are found to result in acceptable path-following performance.

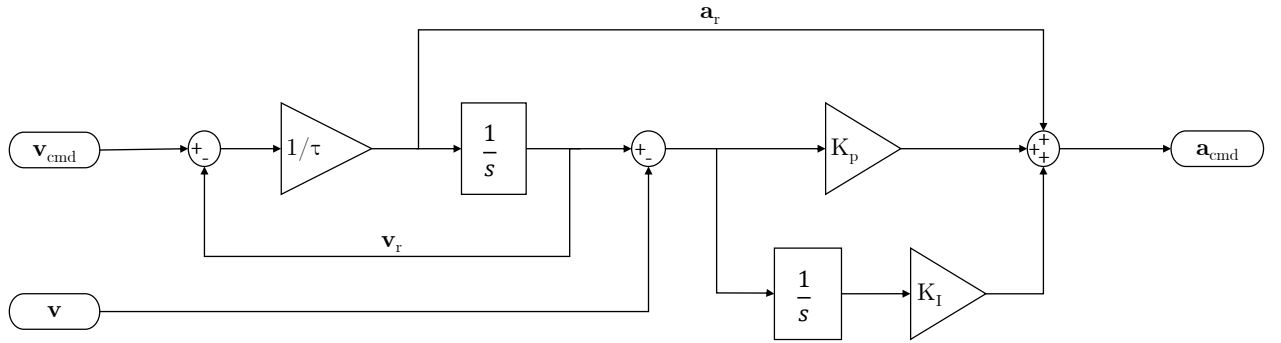


Figure 3.29: Velocity control structure [37]

Now the propulsion system is commanded to provide a force vector \mathbf{F}_{cmd} given by;

$$\mathbf{F}_{cmd} = m\mathbf{a}_{cmd} - \mathbf{F}_g - \mathbf{F}_a \quad (3.84)$$

based on Newtons second law. With \mathbf{F}_g , \mathbf{F}_a gravity force and aerodynamic force respectively. Note that for multicopter controllers, information on aerodynamic forces are mostly not available. However due to the hybrid nature of this aircraft, it is assumed that aerodynamic forces can be estimated using low fidelity models based on speed and angle of attack measurements from the aircraft.

Now the final step for the velocity controller is to convert the commanded force vector into a command thrust T_{cmd} and attitude θ_{cmd} . Note that as the focus of the simulation is on the dynamics in the x-z plane, dynamics in the x-y plane are neglected and the problem reduces to a 2D problem. With this assumption, T_{cmd} and θ_{cmd} are calculated according to;

$$T_{cmd} = \sqrt{F_{cmd,x}^2 + F_{cmd,z}^2} \quad (3.85)$$

$$\theta_{cmd} = \arctan \frac{F_{cmd,x}}{F_{cmd,z}} - \theta_r \quad (3.86)$$

with θ_r , the rotor pitch.

Electronic speed controller

A certain thrust and attitude is calculated that guides the aircraft to the destined flight path. For multicopter control, the attitude and total thrust are controlled by the thrust obtained by each rotor individually. In this work 4 rotors are used to control the aircraft total thrust and attitude. The attitude control is not considered

in this work, but is replaced by assuming a second order behaviour for the pitch dynamics. This is explained in more detail in next section. According to this assumption, the thrust required by one rotor simply equals the total commanded thrust divided by the amount of rotor, 4 in this case.

With the rotor pitch fixed, it is a change in RPM that controls the thrust. The RPM, delivered by the motor, is controlled by the electric speed controller based on an electrical signal δ_t (voltage). This signal is handled by the ESC as the square of the commanded angular speed. This is done in practice as the commanded thrust tends to be proportional with angular speed squared according to;

$$T_{rot} \approx K_T \Omega^2 \quad (3.87)$$

Using this model the electrical signal or square of the commanded angular speed is then given by;

$$\delta_t = \frac{T_{rot}}{K_T} = \frac{T_{cmd}}{n_{rot} K_T} \quad (3.88)$$

In this work the ESC-motor combination is modeled as a first order system for the RPM controller (see Figure 3.30), as described in [44]. Here the maximum motor power, resulting from the sizing model, is taken into account. This first order angular speed tracking requires following motor torque;

$$Q_E = \min\left(J_p(\sqrt{\delta_t} - \Omega) \frac{1}{\tau_{ESC}} + Q_P, \frac{P_{E,max}}{\Omega}\right); \quad (3.89)$$

With τ_{ESC} , the time constant for the electronic speed controller, a value of 0.05s is taken based on [44]. Q_P is the propeller/rotor torque, which is calculated with rotor model presented in next section. According to Newton's second law, the angular acceleration of the motor-rotor is then given by

$$\dot{\Omega} = \frac{1}{J_p} (Q_E - Q_P) \quad (3.90)$$

Which is integrated to obtain the angular speed. If not power limited, this results in a first order lag for the angular speed;

$$\dot{\Omega} = (\sqrt{\delta_t} - \Omega) \frac{1}{\tau_{ESC}} \quad (3.91)$$

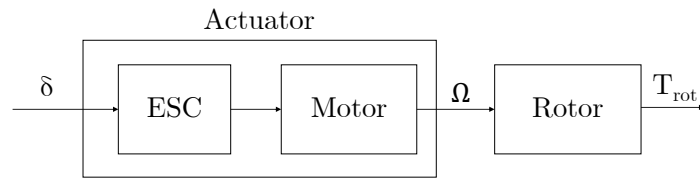


Figure 3.30: Actuator model

Some new parameters are introduced here. First the maximum electrical power $P_{E,max}$ is determined as a result of the preliminary sizing model. In this model a safety factor $f_{gust} = 1.8$ and $f_{control} 1.5$ are introduced to be applied on the steady state power to account for extra power to control and trim and to cope with gusts. Nevertheless, the motor is sized using f_{gust} , $P_{E,max}$ is determined using $f_{control}$ as the simulation is focused on steady winds and does not include gusts.

$$P_{E,max} = \frac{f_{control} \max(P_{i,req})}{n_{rot}} \quad (3.92)$$

The inertia of the rotor about its spin axis, J_P , is calculated by treating it as a circular rod, which inertia is given by;

$$J_P = \frac{1}{12} ML^2 = \frac{1}{12} \frac{m_{rot}}{n_{rot}} D_{rot}^2 \quad (3.93)$$

Lastly, the rotor constant K_T , is determined using the rotor model explained in next section, based on the design condition (second segment steady state) and according to;

$$K_T = \frac{T_{des}}{\Omega_{des}^2} \quad (3.94)$$

3.8.2. Dynamics

In this section the aircraft model that will be used for the simulator is explained. A rotor model is implemented which calculates the rotor thrust based on RPM and rotor inflow conditions. Furthermore, a model for the aircraft's dynamics in the x-z wind frame is given.

Rotor model

From the actuator controller, certain RPM values of the motor-rotor combination are obtained. In the actuator controller the required thrust was mapped to a commanded angular speed by means of the rotor constant. Therefore, according to this model the thrust would equal the inverse of this mapping for the obtained angular speed. In reality the obtained thrust is not only a function of angular speed but also of inflow conditions. The rotor model that is used in the simulator takes this into account. In this work the rotor model introduced in [44] is used. A similar model has been used for the sizing tool, although some different assumptions are taken in the simulation model.

Recall that the thrust predicted by the BEM method and momentum theory are given by;

$$T_{BEM} = \frac{\rho abcR}{4} \left((W^P - v_i)\Omega R + \frac{2}{3}(\Omega R)^2(\theta_0 + \frac{3}{4}\theta_1) + (U^{P^2} + V^{P^2})(\theta_0 + \frac{1}{2}\theta_1) \right) \quad (3.95)$$

$$T_{MT} = 2\rho AV v_i \quad (3.96)$$

In the sizing tool, consistency is obtained by constraints in the optimization architecture and adding induced velocity and RPM as consistency variables. Thrust was dictated by the flight mechanics model. Now, for the simulation model, thrust is to be solved for a certain RPM or angular speed under the given flow conditions. In the simulation, the inflow vector (U^P, V^P, W^P) (based on the dynamic model) and RPM are provided as input to the rotor model. The thrust is calculated by solving Equation 3.97 for induced velocity (v_i), and plugging v_i back in Equation 3.96.

$$f(v_i) = T_{BEM} - T_{MT} = \frac{\rho abcR}{4} \left((W^P - v_i)\Omega R + \frac{2}{3}(\Omega R)^2(\theta_0 + \frac{3}{4}\theta_1) + (U^{P^2} + V^{P^2})(\theta_0 + \frac{1}{2}\theta_1) \right) - 2\rho AV v_i = 0 \quad (3.97)$$

Solving Equation 3.97 requires finding the root of a fourth-order polynomial. In this work, it is solved numerically for the unknown induced velocity v_i , by means of the bisection method. The interval for the induced velocity in this method is chosen to be [-1,25] m/s. When solved for the induced velocity, thrust can be calculated using either Equations 3.95 or 3.96. Rotor design parameters are given in Table 3.9. The induced power, profile power and total power are calculated using;

$$P_{induced} = T(v_i - W^P) \quad (3.98)$$

$$P_{profile} = \frac{\rho C_{d_0} bc \Omega R^2}{8} \left((\Omega R)^2 + U^{P^2} + V^{P^2} \right) \quad (3.99)$$

$$P_{tot} = \kappa P_{induced} + P_{profile} \quad (3.100)$$

See section 2.6 for the derivation of these equations. Finally, the rotor torque is calculated by;

$$Q = \frac{P_{tot}}{\Omega} \quad (3.101)$$

Note again that contrary to the model in [44], an induced power factor κ is applied on the induced power in Equation 3.100, to provide a conservative power estimation. Furthermore also the profile power is taken into account in the simulation. This is not done in the sizing tool as it is too much dependent on detailed rotor parameters and is assumed to be optimized for the steady state flight condition. In the simulation it is added to see the effect of profile power in non-design conditions (transient condition).

Referring back to the design process, depicted in Figure 3.1, a detailed design of the rotor should be performed before entering the simulation. For this purpose the root blade twist θ_0 , has been optimized for minimum profile drag. A maximum blade angle of attack of 15 degrees is put as a constraint in this optimization. Note that this step is performed after the preliminary sizing. The rotor constant K_T used in the actuator model is obtained with the optimized root blade twist θ_0 and design conditions (thrust and inflow conditions segment 2).

Table 3.9: Rotor parameters

Parameter	Value	Reference
Number of blades [b]	2	Assumed
Lift slope [a]	$2\pi[1/rad]$	Assumed
Chord over radius [c_R]	0.16 [-]	[6]
Zero-lift drag [cd0]	0.03 [-]	Assumed
Root blade twist [θ_0]	(Optimized) [deg]	
Linear blade twist [θ_1]	-21.9 [deg]	[6]

Aircraft dynamics

The last block in the simulation is the aircraft dynamics. Both rotational as translational dynamics are considered in a two (2) dimensional plane (x-z windframe plane).

A. Rotational dynamics

Rotational dynamics of the aircraft in the x-z plane are given by the dynamics of the pitch. For a multicopter this is controlled by a difference in thrust for the front and back rotors creating a pitching moment. As explained in previous section, an attitude controller is not considered. The attitude dynamics are estimated in this work to behave like a second order system, characterised by the natural frequency ω_{sp} and damping ratio ζ_{sp} of the AP2 short-period eigenmotion. These are determined in the work of [19] to be 5.548 rad/s and 0.843 respectively. The transfer function of the pitch dynamics is than given by;

$$H_\theta(s) = \frac{\omega_{sp}^2}{s^2 + 2\zeta_{sp}\omega_{sp}s + \omega_{sp}^2} \quad (3.102)$$

B. Translational dynamics

The model used for the translational dynamics is similar to the flight mechanics model described in 3.4, the same assumptions will apply here with the exception that the flight is no longer steady. Acceleration is given by Newton's second law:

$$m\mathbf{a} = \mathbf{F}_p + \mathbf{F}_g + \mathbf{F}_a + \mathbf{F}_n \quad (3.103)$$

with m the total mass of the system (aircraft + VTOL system), \mathbf{F}_p , \mathbf{F}_g , \mathbf{F}_a , \mathbf{F}_n , propulsion, gravity, aerodynamic and normal force respectively. Velocity and position are than obtained by integrating the acceleration;

$$\mathbf{v} = \int \mathbf{a} dt \quad (3.104)$$

$$\mathbf{p} = \int \mathbf{v} dt \quad (3.105)$$

The normal force keeps the aircraft fixed at the ground when it is accelerating its rotor and not yet in air, it is given by;

$$F_{n,z} = \max(0, -F_{g,z} - F_{a,z} - F_{p,z}) \quad (3.106)$$

$$F_{n,x} = -F_{g,x} - F_{a,x} - F_{p,x} \quad (3.107)$$

for zero height $\leq 0.01\text{m}$ and zero otherwise. Gravity, propulsion and aerodynamic forces are calculated as given in Equations 3.30 and 3.31.

4

Concept design and analysis

This section describes the results obtained by applying the concept design & analysis process steps. First, in Section 4.1, preliminary reference results using sizing models as part of the state-of-the-art and literature are given for reference to contrast the results of this research, applying the proposed design methodology as described on previous chapter. In Section 4.2, results of the proposed sizing model are presented for the direct take-off approach and the different VTOL concepts. The different concepts being the tilt-rotor concept, tail-sitter concept, quad-plane concept and knee-sitter concept. The results of the detailed analysis are given as a function of wind speed and target elevation angle.

4.1. Preliminary results

In this section the results using models from other papers are given as a reference to contrast the results produced in this research. By contrasting these results with the ones from the proposed model, the effect of certain assumptions can be analyzed. The results of the state-of-the-art sizing models (described in Section 2.1) for VTOL AWES applied to the AP2 ($m_{A/C} = 36.8$ kg) are given in Table 4.1. It can be observed that the estimations for the VTOL system mass varies between the different implementations. A first explanation of these differences is the different assumptions on requirements and parameters taken in the literature. These assumptions are given in Figure 4.2.

In Table 4.1, results are given when the same requirements (from [14]) are applied (take-off velocity, altitude and time) as well as when a same rotor area is assumed ($A_{prop} = 1 m^2$) from [4]). The requirements and rotor area taken are the ones found most representative and applicable for the problem at hand.. From this initial analysis, it becomes already clear how much the design requirements and rotor area determine the VTOL system's mass. Still the results deviate, especially when looking at the distribution between the battery and motor component. Remaining differences are explained by different assumptions in thrust to weight ratio, energy density and specific motor mass.

Table 4.1: AP2 reference VTOL system mass estimation

	Initial estimations			Same TO requirements			Same TO requirements and A_{prop}		
	Fagiano [14]	Bauer [4]	Rapp [37]	Fagiano	Bauer	Rapp	Fagiano	Bauer	Rapp
$m_{VTOL}[kg]$	7.2	23.3	23.1	7.2	7.1	12.0	4.1	7.1	5.0
$m_{bat}[kg]$	1.9	17.8	7.9	1.9	3.7	6.2	1.1	3.7	2.6
$m_{mot}[kg]$	5.3	5.5	15	5.3	3.4	5.8	3.0	3.4	2.4

Now the same requirements are applied using the proposed design methodology, the next step is to conduct the concept analysis per selected VTOL concept.

Table 4.2: Parameter assumptions VTOL AWE literature

	Fagiano	Bauer	Rapp
Take-off velocity [m/s]	1	/	1
Target altitude [m]	100	/	180
Take-off time [min]	1.67	5	3
Thrust to weight ratio [-]	1	1	1.5
Safety factor on steering actuations [-]	/	1.5	/
Rotor efficiency [-]	0.7	0.5	0.8
Rotor area [m ²]	0.4	1	0.28
Specific energy battery [Wh/kg]	200	130	130
Specific power motor [kW/kg]	2.5	5	5

4.2. Direct take-off approach

Hereafter, the results are given for the different VTOL concepts using the direct take-off approach. The different VTOL concepts being the tilt-rotor concept, tail-sitter concept, quad-plane concept and knee-sitter concept. A comparison of the concepts is given at the end of this section. Concerning the design parameters, the average values from the design parameter Table 3.6 are used. The design variables are optimized for different wind speeds and elevation angle scenario's and are presented as such.

The analysis is done for the flight paths as depicted in Figure 4.1, defined by the target elevation angle θ_t . Two (2) segments can be identified in these flight paths. The first one will refer to the vertical path towards clearance height and second segment from clearance height to target position. The second segment is different for the different target elevation angles. In Figure 4.1a the minimum elevation angle is used, constraint by minimum tether length and minimum height. In Figure 4.1c, also the second segment is vertical with a target elevation of 90 degrees. In Figure 4.1b, the target elevation angle is taken to be the average. Furthermore, for this approach the heading is positive into the wind ($\psi = 0^\circ$) throughout the complete flight path for all cases.

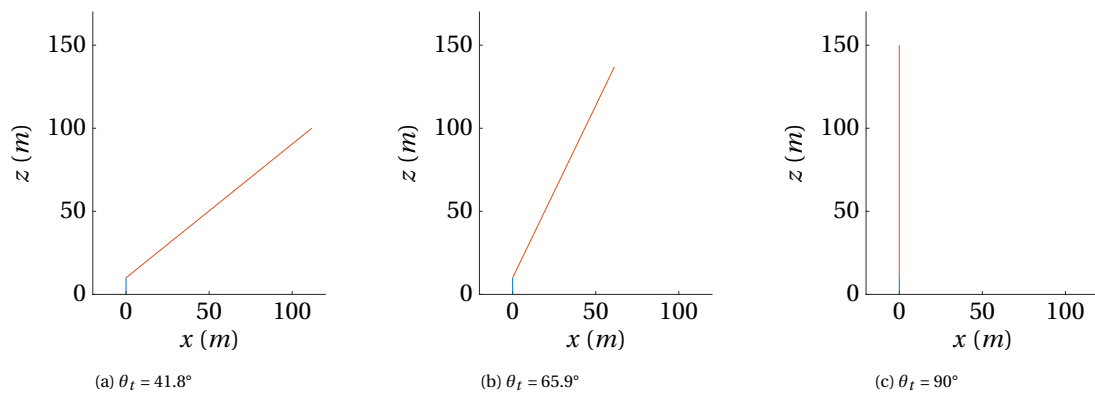


Figure 4.1: Flight paths for different target elevation angles

The optimal design variables are analyzed and plotted for different wind speeds and the three (3) different elevation angles using different variable sets. These variable sets include: the VTOL system and component masses (variable set 1); the required thrust and power of the VTOL system (variable set 2); angle of attack of the wing and the rotor (variable set 3); vertical and horizontal speed (variable set 4); aircraft pitch and rotor pitch (variable set 5); rotor diameter (variable set 6) and required specific power and specific energy of the battery (variable set 7).

4.2.1. Tilt-rotor concept

Hereafter, the results for a tilt-rotor concept are given.

Concept description

With a rotor that can be tilted during flight, this concept is able to optimize the angle of the rotor with respect to the body and change it during flight. The focus in this research for this concept is to investigate the potential of tilting the rotor depending on wind and flight conditions. No extra weight is taken into account for such a tilting mechanism, therefore results presented here represent a hypothetical optimum (flight under most optimal conditions).

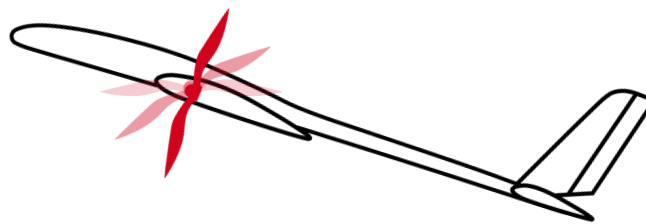


Figure 4.2: Tilt-rotor concept

Design variable analysis and findings

Variable set 1: System and component masses

The VTOL system mass for the tilt-rotor concept is plotted as a function of wind speed for different elevation angles in Figure 4.3a. For the elevation angles lower than 90° , VTOL system mass first increases slightly and then decreases with wind speed. For an elevation angle of 90° , mass decreases instantly with wind speed. It can be observed that the VTOL system mass does not change significantly with the elevation angle, furthermore the optimal elevation angle is depending on the wind speed. For 0 wind speed, the VTOL system mass agrees with the reference values given in Table 4.1. The mass decrease is up to 2.5 kg for wind speeds of 10 m/s, which is more than 50%.

The component masses are plotted in Figures 4.3b - 4.4b. The global trend of all components is decreasing mass with wind speed, with the highest contribution from the motor mass. Note that also the rotor mass brings a large contribution to total VTOL system mass for lower wind speed, whereas in most literature this mass is neglected. This large rotor mass is related to the large rotor diameters to which the optimizer converges, which decreases the required power and hence motor and battery mass. For the battery mass, a certain "dent" in the curve appears. This dent corresponds to the wind condition where battery specific power is no longer limiting the battery mass. This "dent" is also visible, yet to a lesser extent, in motor and rotor mass. In the sensitivity analysis on required battery specific power, this phenomenon is analyzed in more detail.

Variable set 2: Required thrust and power

The required thrust and power are analyzed and plotted as a function of wind speed for the different elevation angles in Figure 4.5. Due to the ability of the tilt-rotor to exploit the aerodynamic forces, there is a large decrease in required thrust with wind speed. For wind speed higher than 2 m/s, the required thrust is lowest for vertical take-off and increases with lower elevation angles. This can be explained by the fact that horizontal velocity in the direction of the wind lowers the apparent speed and hence the aerodynamic lift that can be obtained. This is however not the case for the required power as can be observed from Figure 4.5b. It can

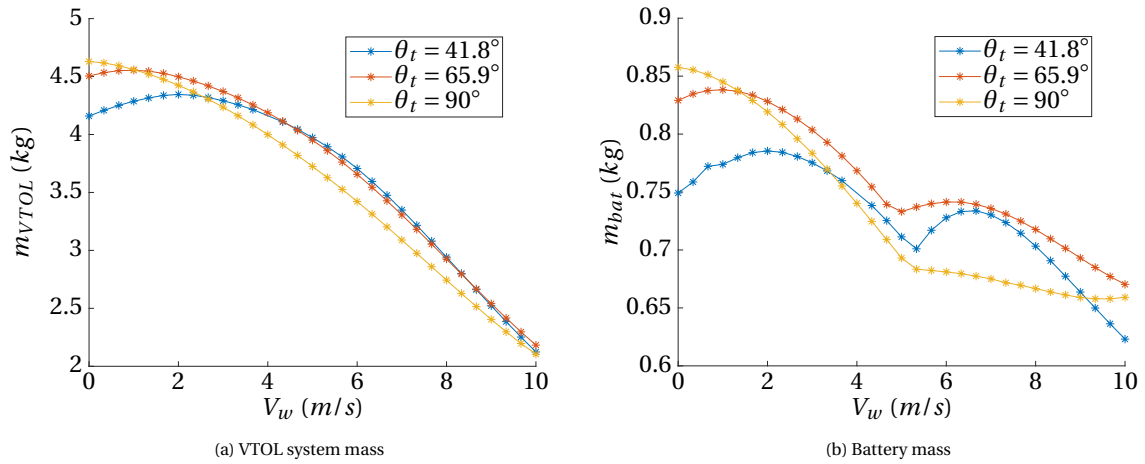


Figure 4.3: VTOL system and battery mass vs. wind speed for different elevation angle

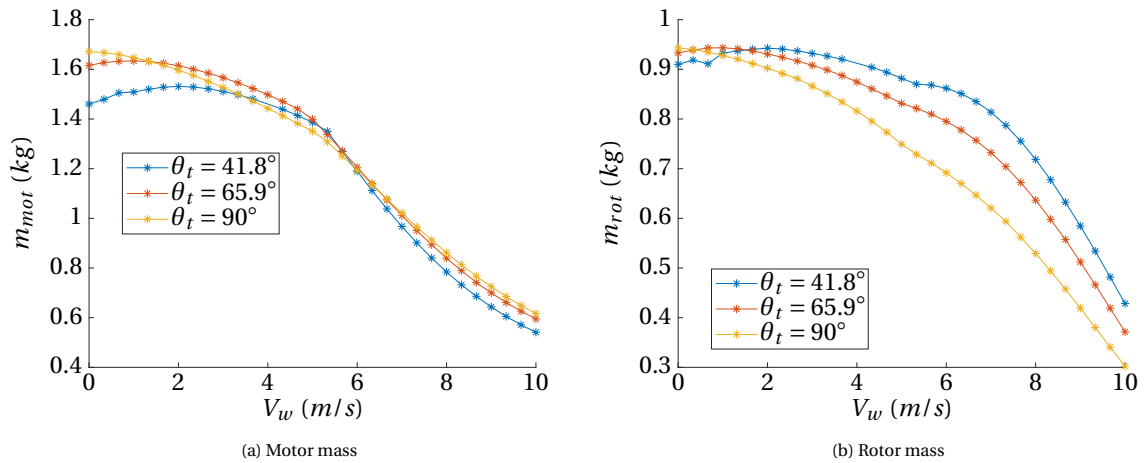


Figure 4.4: Motor and rotor mass vs. wind speed for different elevation angle

also be observed that the optimizer converges to a solution where the power requirements are the same for segment 1 (vertical) and segment 2. In other words, in both segments the full motor power capacity is used, as this leads to the minimum energy and hence battery requirement. Lastly, it is clear that the motor mass is dictated by the required power.

Variable set 3: Angle of attack of wing and rotor

The angle of attack of the wing and rotor are analyzed and plotted as a function of wind speed for the different elevation angles in Figure 4.6. It can be observed that the optimizer converges to the maximum wing angle of attack of 16.5 degrees to maximize the aerodynamic lift and for that to decrease required thrust. Also, the tracking of maximum angle of attack is delayed with wind speeds for lower elevation angles. The angle of attack of the rotor or inflow angle are found between 55° and 75° for wind speeds above 6 m/s (0 degree defined parallel to rotor axis). The inflow angle increases with lower elevation angle as the rotor is less tilted into the wing. A larger inflow angle decreases required power, which explains the trend in Figure 4.5b.

Variable set 4: Vertical and horizontal speed

The vertical and horizontal speed are analyzed and plotted as a function of wind speed for the different elevation angles in Figure 4.7. For the second and main segment in the flight path, optimal climb velocities are rising with elevation angle. For lower wind speeds the climb velocity does not change much with wind speed. However, after a certain wind speed is reached, climb velocity decreases with wind speed. In the first seg-

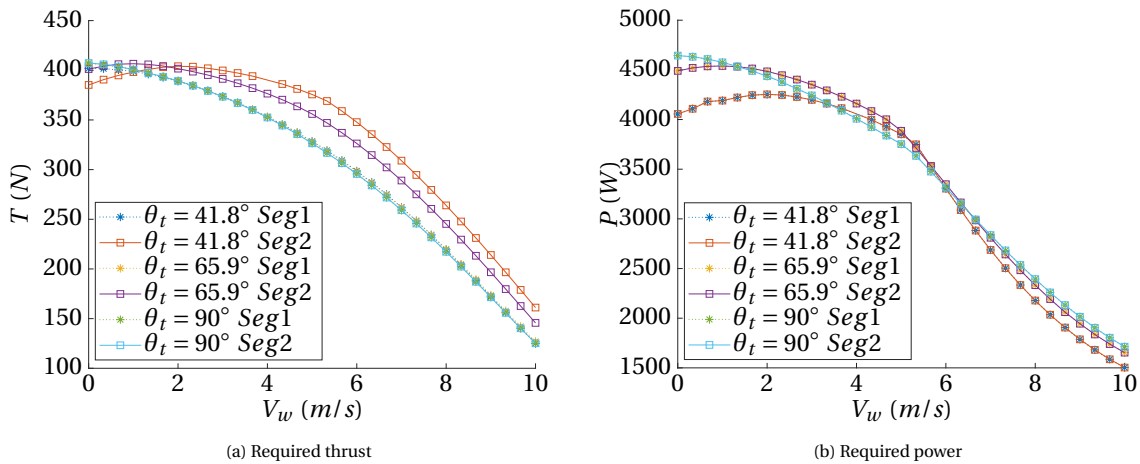


Figure 4.5: Required thrust and power for force equilibrium

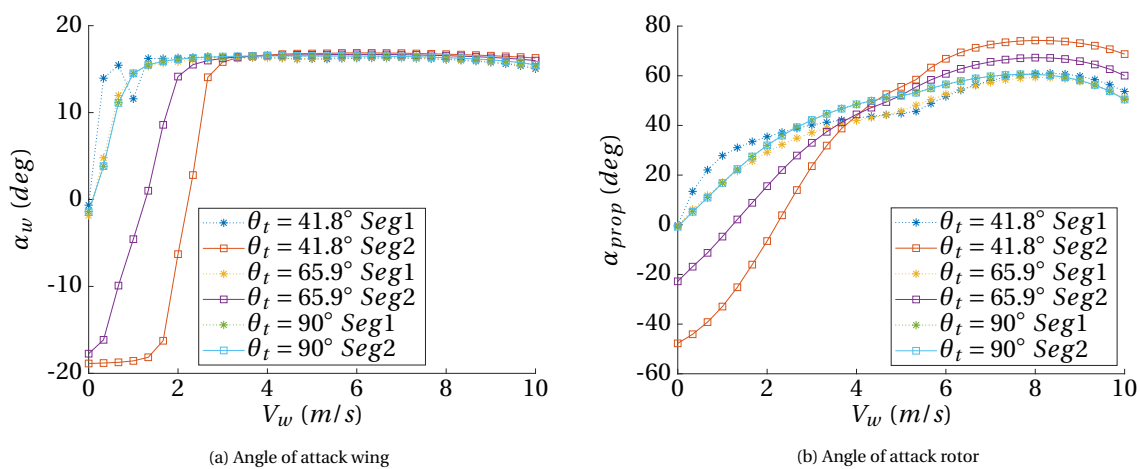


Figure 4.6: Angle of attack wing and rotor

ment the optimal climb velocity first increases and then decreases with wind speed. Presumably, the second segment, which is the largest one, dictates the power requirement. As explained, the optimizer converged to an equal power consumption in both segment. To do so, the climb speed in the first segment is adapting to consume this power. For the target elevation of 90 degrees, the climb speed in both segments is the same.

Variable set 5: Aircraft pitch and rotor pitch angle

The aircraft pitch and rotor pitch angle are analyzed and plotted as a function of wind speed for the different elevation angles in Figure 4.8. It can be observed that the body pitch angle decreases with wind speed as it is rotating with the apparent velocity to track the maximum angle of attack. Furthermore, there seems to be an inverse relation between optimal body pitch and rotor pitch in order to keep thrust aimed upwards. Note however for low wind speeds, when body pitch > 90 degrees, a better solution would be to have a heading of $\psi = 180$ degrees. For this heading the aircraft is not required to fly upside down, and a higher lift coefficient can be reached. Lastly, the optimal rotor pitch is in the range of -30° to -50° for wind speeds higher than 5 m/s. This value is also rather constant for wind speeds between 6-10 m/s. The optimal rotor pitch seems to increase in negative direction with increasing elevation angle.

Variable set 6: Rotor diameter

The rotor diameter is analyzed and plotted as a function of wind speed for the different elevation angles in Figure 4.11. The optimization converges to quite large rotor diameters ranging from 1.2m for low speeds to

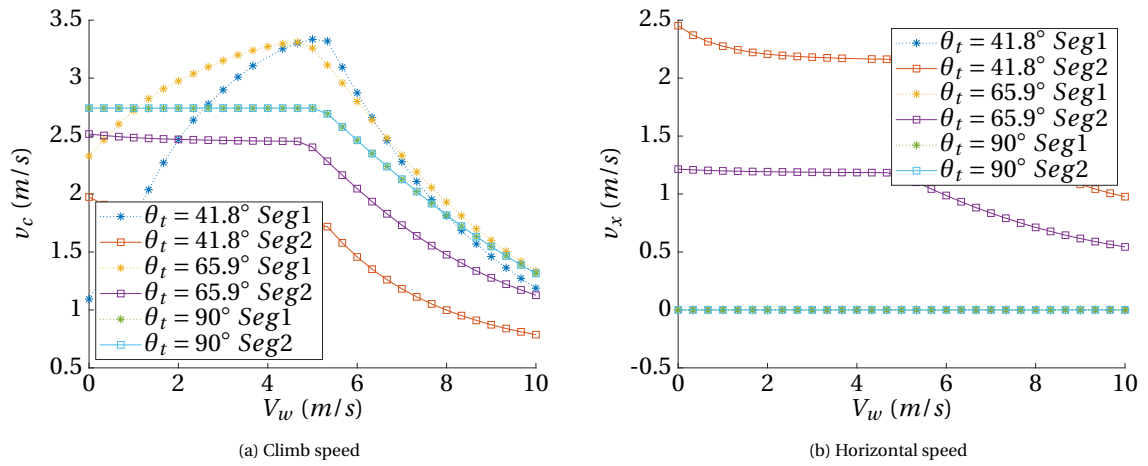


Figure 4.7: Climb and horizontal speed vs. wind speed for different elevation angle

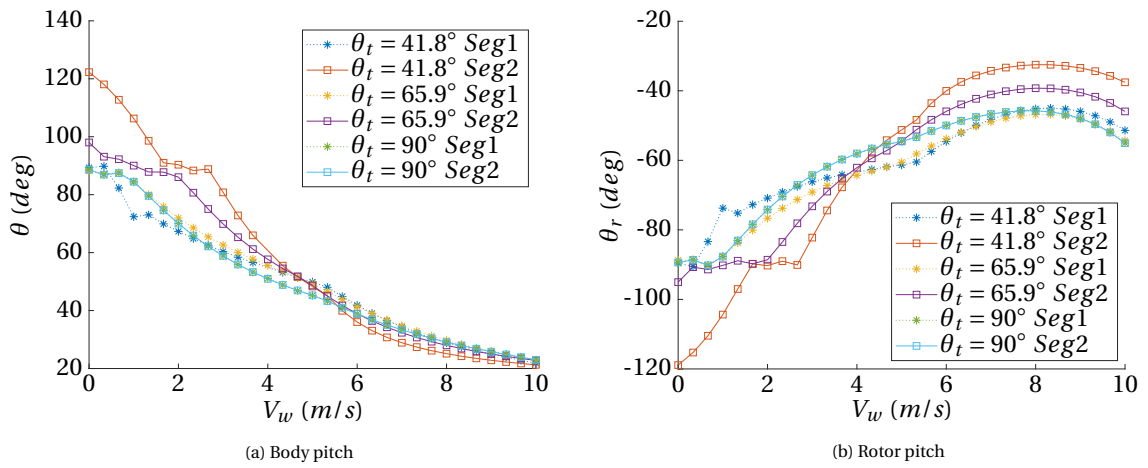


Figure 4.8: Aircraft pitch and rotor pitch vs. wind speed for different elevation angle

0.7m for a wind speed of 10 m/s and target elevation angle of 90°. To bring this in perspective it is visualized in Figure 4.10c. Note that as it is not optimized for drag, smaller rotors might be more optimal from a total performance perspective. A sensitivity analysis of the rotor diameter is given in the following chapter.

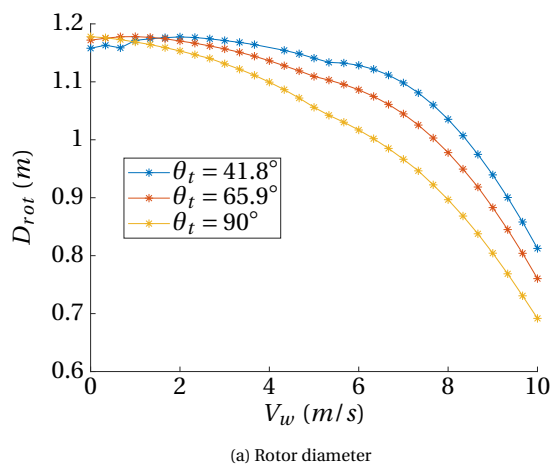


Figure 4.9

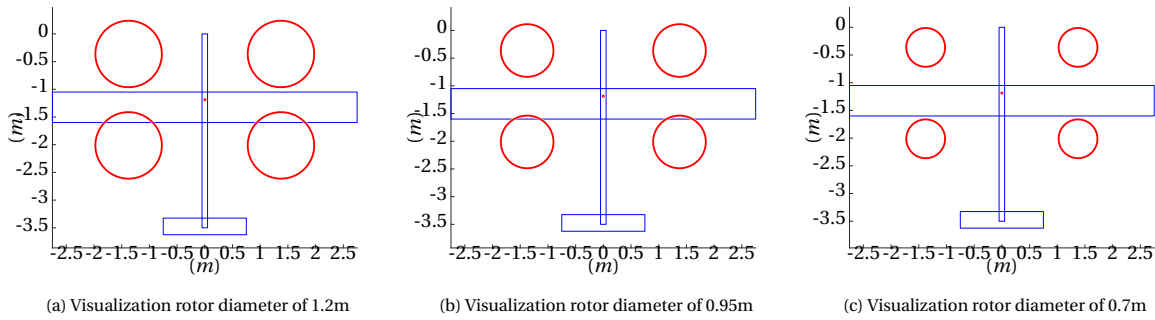
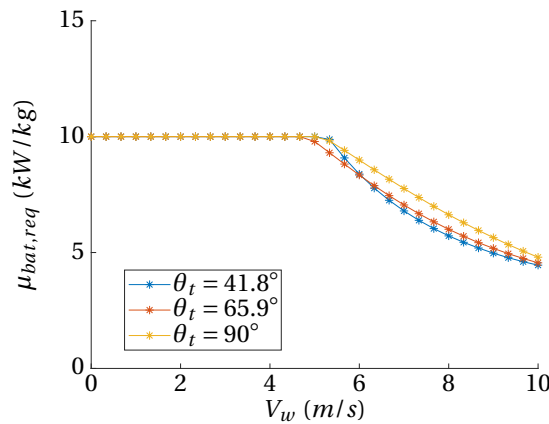


Figure 4.10

Variable set 7: Battery required specific power and specific energy

The battery required specific power are plotted as a function of wind speed and for the different elevation angles in Figure 4.11. For wind speeds below 5 m/s, the battery specific power of 10 kW/kg is limiting the design. For all wind speeds and conditions a specific energy of 684 kJ/kg is required (full battery).



(a) Required specific power battery

Figure 4.11

Visualization of aircraft attitude and forces

The attitude of and forces acting on the aircraft are visualized in Figures 4.12-4.16 for segment 1 and 2, elevation angle of 41.8° and wind speeds of 0-5-10 m/s.

For the first segment and zero wind speed, the aircraft nose is pointed upwards (blue arrow) to minimize drag. For a moderate wind speed (5 m/s), the nose is pointing at an angle of around 45 degrees, in this attitude the maximum obtainable lift is used to aid the rotors. Also for the higher winds speeds (10 m/s), the maximum lift is tracked. This requires a lower attitude pitch for the body, but the rotor needs to be tilted about 30 degrees with respect to vertical position.

For the second segment, the aircraft is oriented upside down for 0 wind speed. In this orientation some "negative" lift is acting upward. Note that in this situation it would be better to point nose in other direction (nose pointed down wind in low wind conditions, $\psi = 180^\circ$). For the moderate wind speeds (5 m/s), the nose is pointed forward again, similar to the first segment. The obtained aerodynamic lift is however less due to the decrease in apparent speed with the horizontal motion in wind direction. The same counts for high wind speeds (10m/s), with a more moderate tilt of the rotors.

Conclusion

For the tilt-rotor concept the required VTOL system mass decreases with wind speed for all target elevation angles. A VTOL system mass of 4.3kg is required for wind speeds below 4 m/s and decreases to 2.1kg for a wind-speed of 10 m/s. This decrease is possible by orienting the wing such that aerodynamic force aid the rotor during take-off, which reduces the power and energy demand. These results were expected to be achieved by the optimization framework. The difference in VTOL mass between the different target elevation angle strategies is low.

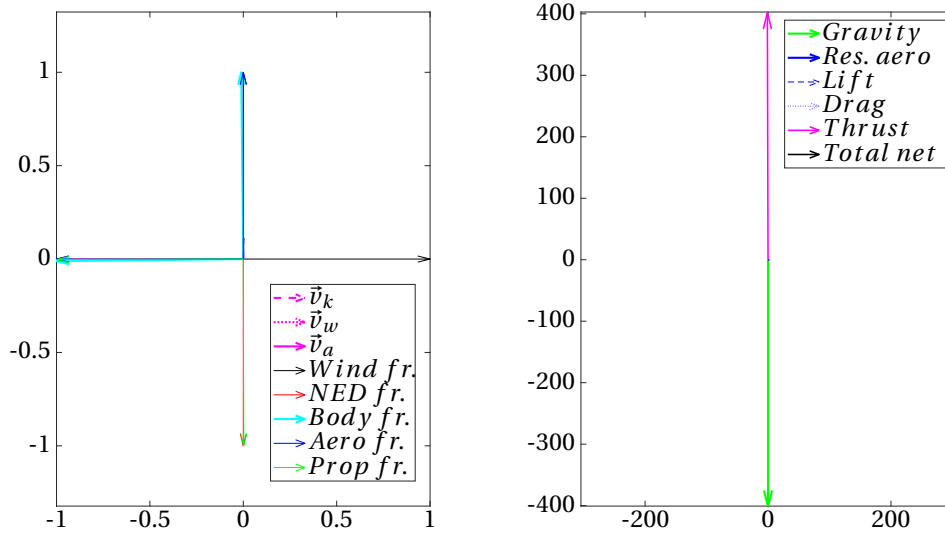


Figure 4.12: Attitude and force visualization segment 1 ($\theta_t = 41, 8^\circ, V_w = 0 \text{ m/s}$)

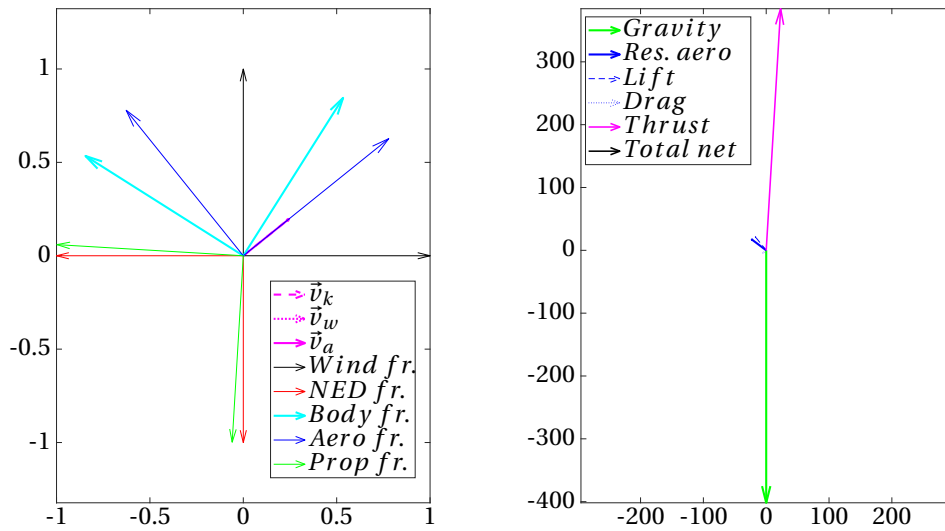


Figure 4.13: Attitude and force visualization segment 2 ($\theta_t = 41, 8^\circ, V_w = 0 \text{ m/s}$)

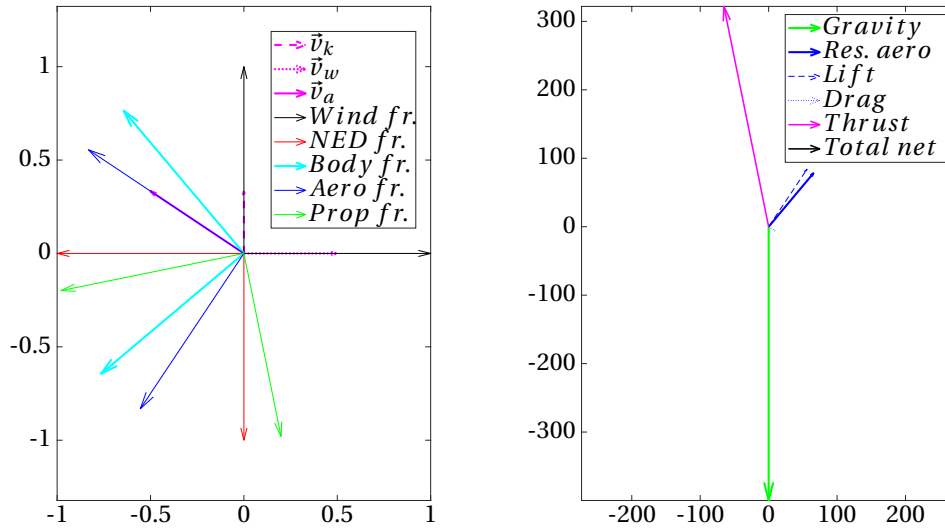


Figure 4.14: Attitude and force visualization segment 1 ($\theta_t = 41,8^\circ, V_w = 5m/s$)

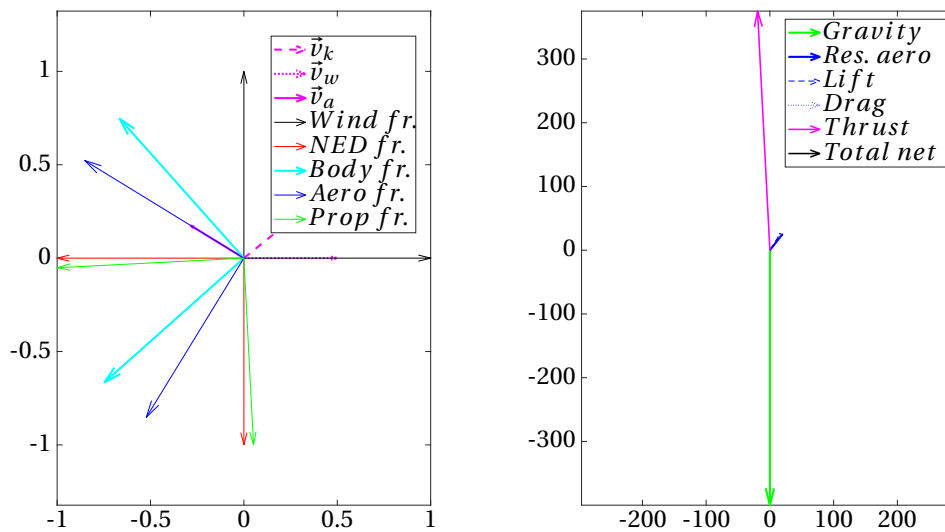


Figure 4.15: Attitude and force visualization segment 2 ($\theta_t = 41,8^\circ, V_w = 5m/s$)

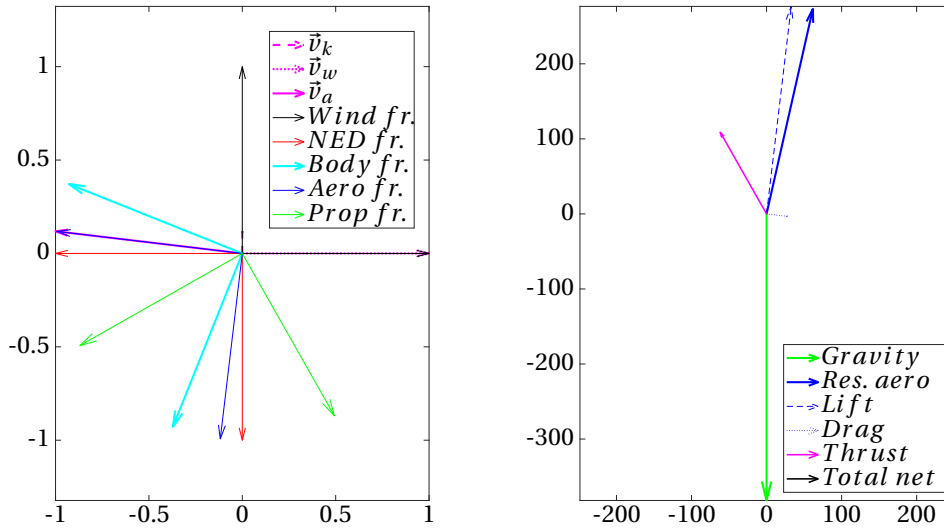


Figure 4.16: Attitude and force visualization segment 1 ($\theta_t = 41,8^\circ, V_w = 10m/s$)

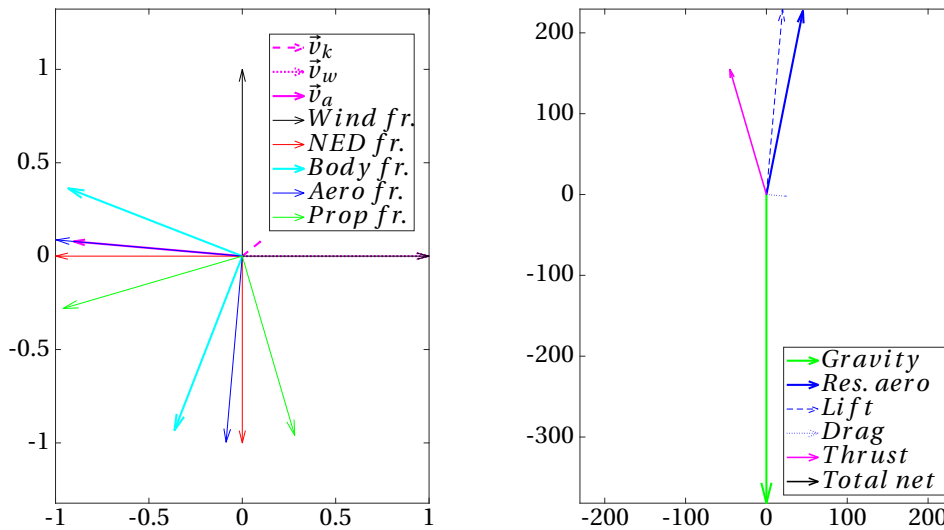


Figure 4.17: Attitude and force visualization segment 2 ($\theta_t = 41,8^\circ, V_w = 10m/s$)

4.2.2. Tail-sitter concept

Hereafter, the results for a tail-sitter concept are given.

Concept description

This concept is characterized by a rotor axis in the same direction as the aircraft body x-axis ($\theta_r = -90$) as depicted in Figure 4.18.

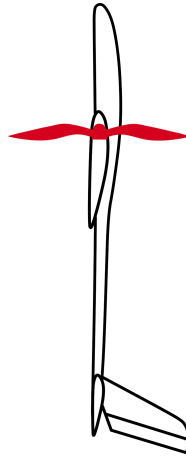


Figure 4.18: Tail-sitter concept

Design variable analysis and findings

Variable set 1: System and component masses

The VTOL system mass for the tail-sitter concept is plotted as a function of wind speed for different elevation angles in Figure 4.19a. It can be observed that, contrary to the tilt-rotor concept, the VTOL system mass is increasing with wind speed. This increase is more for higher elevation angles.

The component masses are plotted in Figures 4.19b - 4.20b. Battery and motor share the same trend as the VTOL system mass, whereas the rotor mass is decreasing with wind speed to a lesser extent. For the rotor mass there is no clear trend for wind speeds below 4 m/s. The deviation on rotor mass here is however small. Similar to the tilt-rotor, the motor mass makes the largest mass contribution.

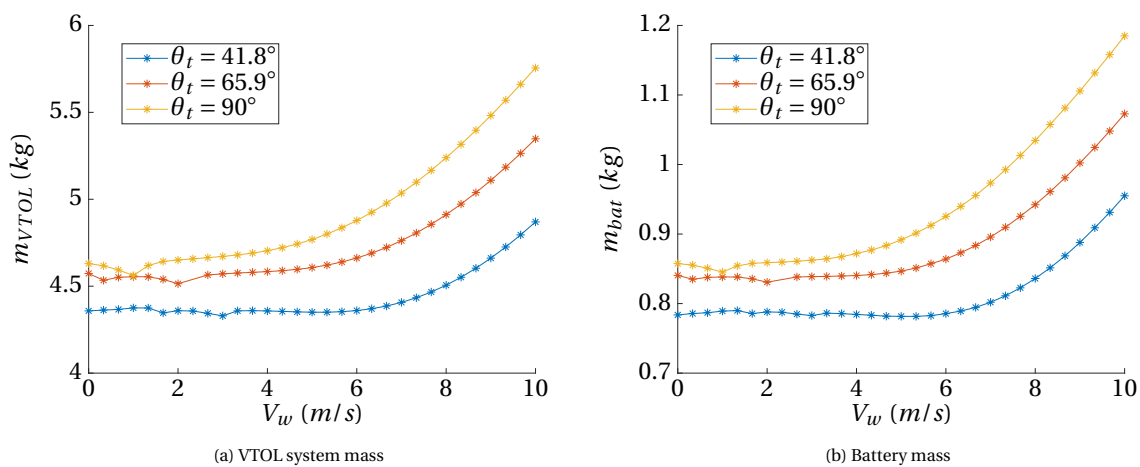


Figure 4.19: VTOL system and battery mass vs. wind speed for different elevation angle

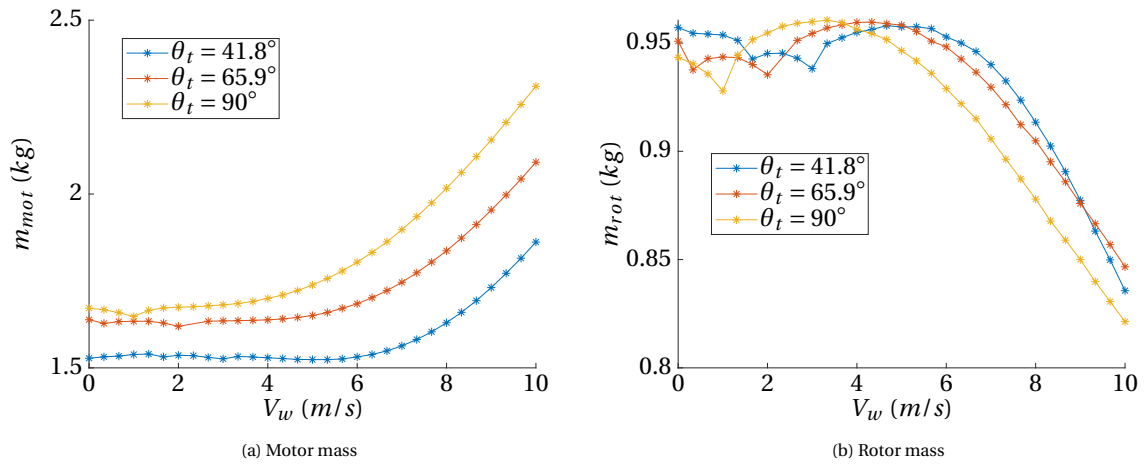


Figure 4.20: Motor and rotor mass vs. wind speed for different elevation angle

Variable set 2: Required thrust and power

The required thrust and power are analyzed and plotted as a function of wind speed for the different elevation angles in Figure 4.21. For the second and main segment, thrust is quite independent of wind speed. For the first segment it is decreasing slightly. In contrast to the thrust, there is an increase of required power with wind speed.

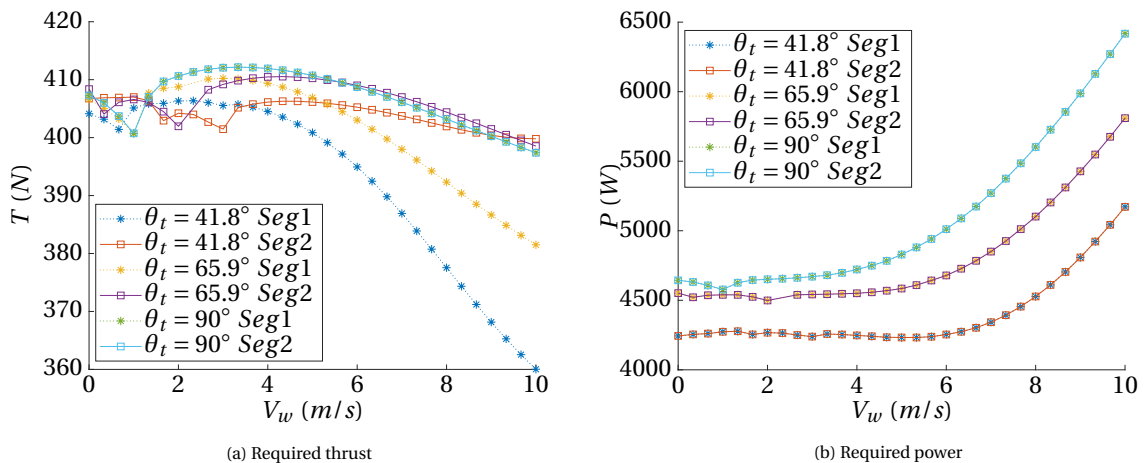


Figure 4.21: Required thrust and power for force equilibrium

Variable set 3: Angle of attack of wing and rotor

The angle of attack of the wing and rotor are analyzed and plotted as a function of wind speed for the different elevation angles in Figure 4.22. Observe that both are equal as the rotor and wing share the same x-axis. Because of the high angles of attack for most conditions, the aircraft is operating in a stall regime. On the other hand, for the rotor inflow angles these angles are quite low (40° - 60° , compared to 60° - 75° for tilt-rotor), resulting in an axial velocity component going into the rotor. This causes the high power requirement (see Figure 3.16a).

Variable set 4: Vertical and horizontal speed

The vertical and horizontal speed are analyzed and plotted as a function of wind speed for the different elevation angles in Figure 4.21. As compared to the tilt-rotor concept, there is no decrease in climb speed but a rather constant trend for the second segment. The optimized climb speeds are found between 1.8 and 2.7 m/s. The optimal climb speeds decreases with decreasing elevation and increases with wind speed for the

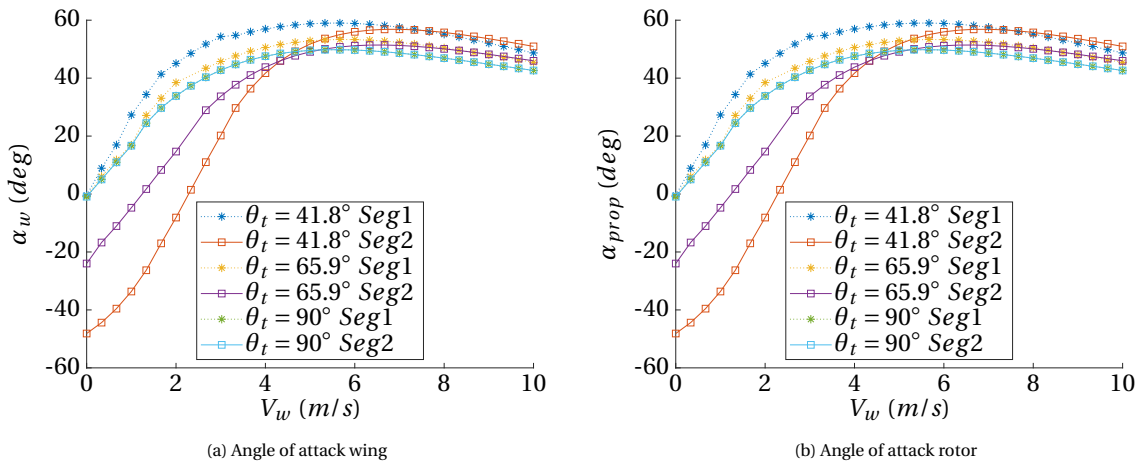


Figure 4.22: Angle of attack wing and rotor

target elevation angle of 41.8° . The trend for the first segment is different. While no clear trend exist for wind speeds below 4 m/s, the climb speed decreases for higher wind speeds. As the power is presumably dictated by the second (and largest) segment, the climb velocity in the first segment is adapted to consume the same power.

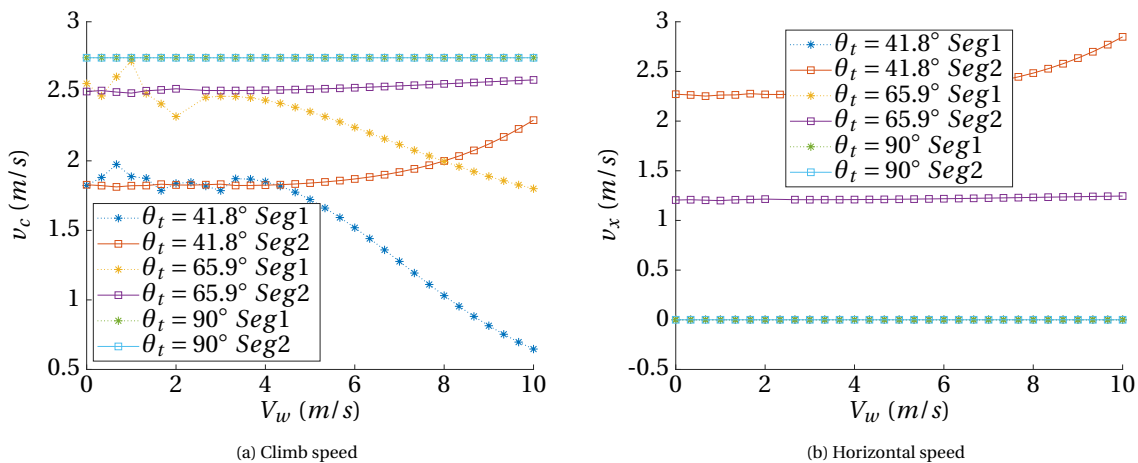


Figure 4.23: Climb and horizontal speed vs. wind speed for different elevation angle

Variable set 5: Aircraft pitch and rotor pitch angle

The aircraft pitch and rotor pitch angle are analyzed and plotted as a function of wind speed for the different elevation angles in Figure 4.21. The rotor pitch is now fixed. The aircraft pitches vertically up for low wind speeds to point the rotors up. The pitch decreases as the wind speed goes up such that the thrust forces is pointed more forward to counteract the aerodynamic force.

Variable set 6: Rotor diameter

The rotor diameter is analyzed and plotted as a function of wind speed for the different elevation angles in Figure 4.25a. Optimal rotor diameters for the tail-sitter concept are found between 1.18 and 1.1m. Contrary to the quad-plane concept presented in Section 4.2.3, there is a decreasing rotor diameter with wind speed above 6 m/s. With the rotor angle of attack of 50 degrees, a large portion of the incoming flow is parallel to the rotor axis. Recalling the required power for axial inflow (Equation 2.32), for large inflow velocities a large part of the required power is independent of the rotor area and behaves as $P = TV$. Therefore, large portion of the power cannot be decreased by increasing rotor area. This is a fundamental difference with respect to the

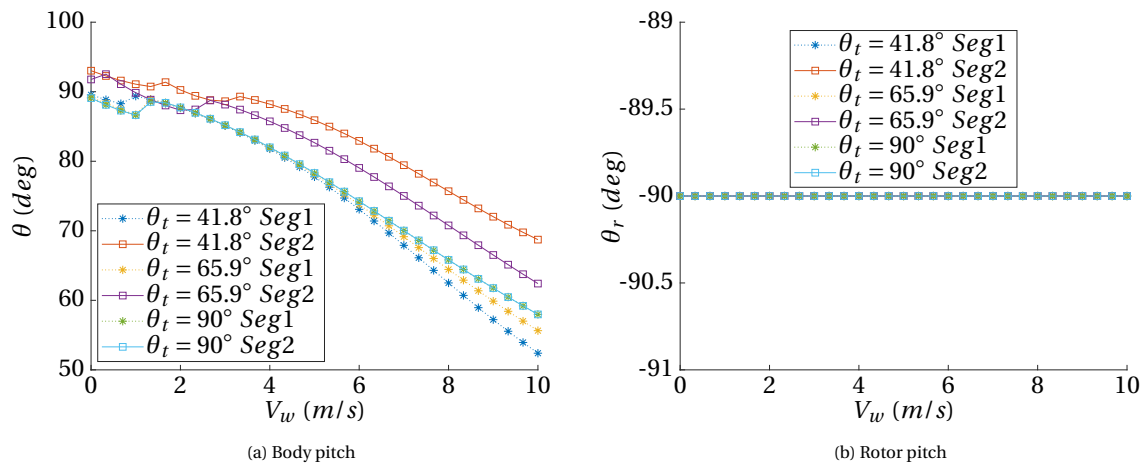


Figure 4.24: Aircraft pitch and rotor pitch vs. wind speed for different elevation angle

other concepts.

Variable set 7: Battery required specific power and specific energy

Both the maximum battery specific power (10 kW/kg) and energy (684 kJ/kg) are used for all conditions.

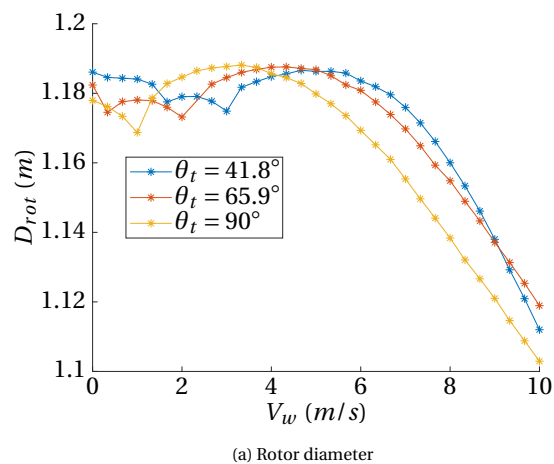


Figure 4.25

Visualization of aircraft attitude and forces

In Figure 4.26-4.30, the attitude of and forces on the tail-sitter concept are visualized for segment 1 and 2, elevation angle of 41.8° and wind speeds of 0-5-10 m/s. For the first segment, the tail-sitter experience little climb drag for 0 wind speed as the body is aligned with the flow. For a moderate wind speed of 5 m/s, the tail-sitter needs to tilt into the wind to compensate for the drag of the largely exposed and stalled wing. As also small lift is experienced in this condition, there is no significant change in total thrust required. The same holds for a higher wind speed of 10 m/s, but with a larger total aerodynamic force. Also for the second segment, the flow condition is the same. However due to the horizontal speed with the wind, the apparent velocity and hence aerodynamic forces are of lower magnitude.

Conclusion

Contrary to the tilt-rotor concept, the required VTOL system mass for the tail-sitter concept increases with wind speed and with higher target elevation angles. A VTOL system mass of 4.4kg is required for zero wind speed and increases to 4.9kg for a wind-speed of 10 m/s. Contrary to initial expectations. The weight penalty

is however not driven by the extra thrust that is required, but it is the power that is increasing with the wind. Due to the fact that the aircraft needs to tilt into the wind, more axial flow enters the rotor which increases the power requirement. This increase cannot be compensated with an increase in rotor area, which is a fundamental difference with other concepts.

Another remarkable observation that can be made is that there is a clear difference in trend below 3 m/s wind speed and above. This is particularly clear in Figures 4.20b, 4.21a, 4.23a, 4.23a, 4.24a, 4.25a. The trend above 3 m/s arises due to the increasing aerodynamic effects. Here the aerodynamic factor is dictating the trend. For small wind speed, aerodynamic effects are low, and there is no clear trend to what is the optimal condition. It can be argued that the ambiguous trend at low speed is due to the fact that there exist multiple local minimum which do not deviate significantly. Therefore, the exact value of the variables do not matter much as compared when aerodynamic effects are high. This also clear from the VTOL system mass (Figure 4.19a), which is rather constant with wind speed.

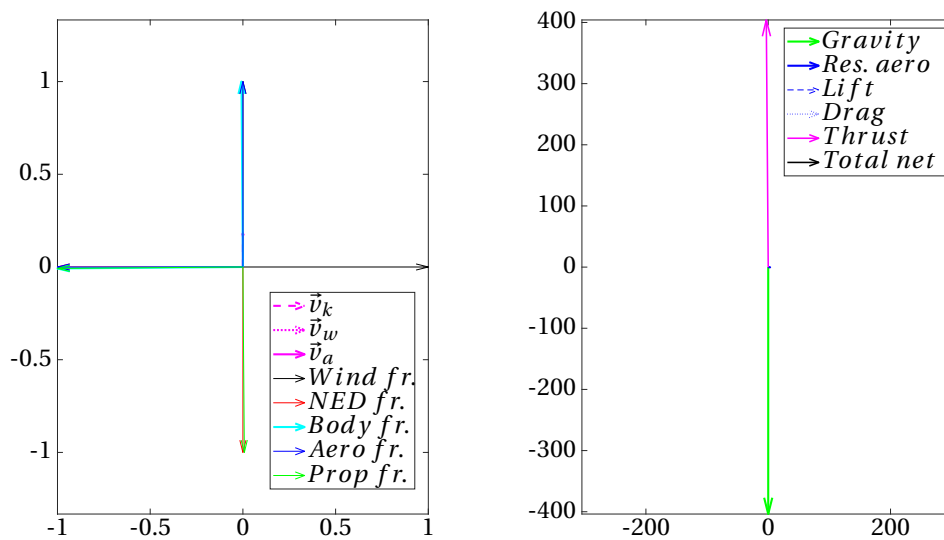


Figure 4.26: Attitude and force visualization segment 1 ($\theta_t = 41, 8^\circ, V_w = 0m/s$)

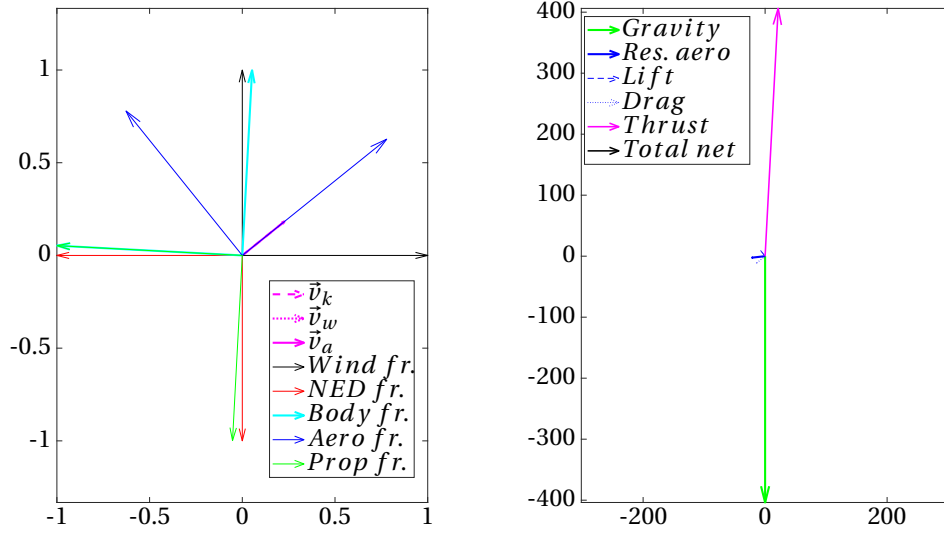


Figure 4.27: Attitude and force visualization segment 2 ($\theta_t = 41,8^\circ, V_w = 0 \text{ m/s}$)

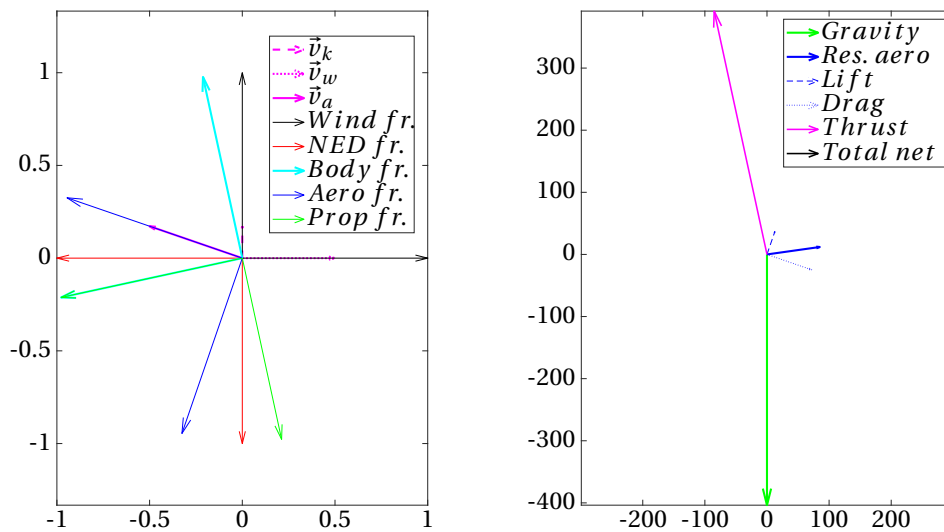


Figure 4.28: Attitude and force visualization segment 1 ($\theta_t = 41,8^\circ, V_w = 5 \text{ m/s}$)

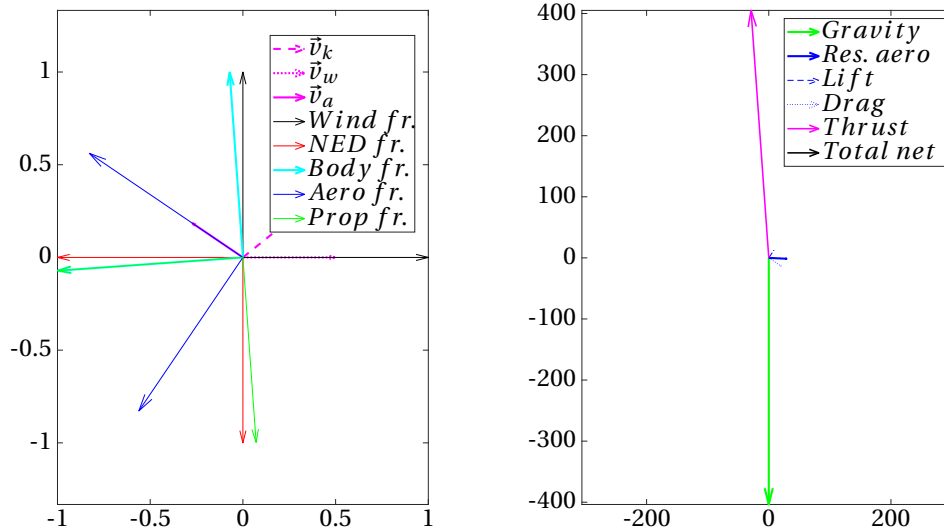


Figure 4.29: Attitude and force visualization segment 2 ($\theta_t = 41,8^\circ, V_w = 5m/s$)

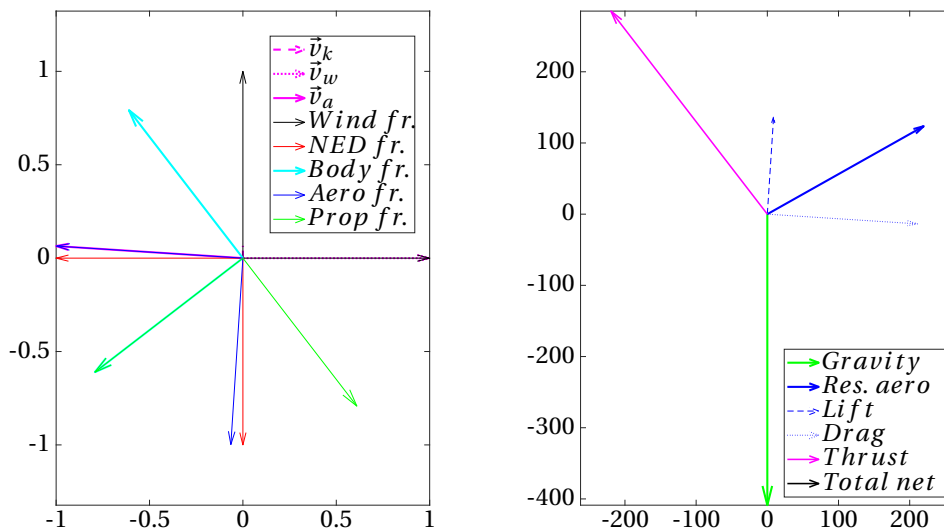


Figure 4.30: Attitude and force visualization segment 1 ($\theta_t = 41,8^\circ, V_w = 10m/s$)

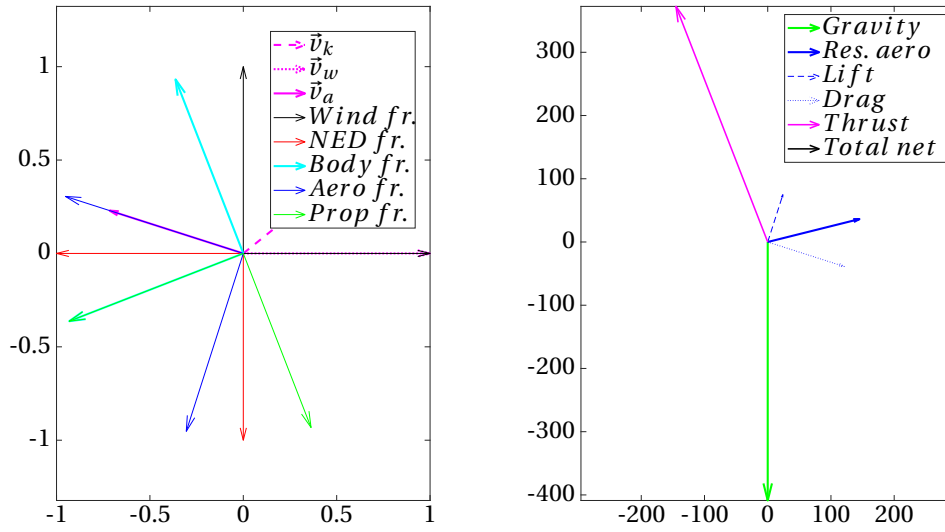


Figure 4.31: Attitude and force visualization segment 2 ($\theta_t = 41,8^\circ$, $V_w = 10\text{m/s}$)

4.2.3. Quad-plane concept

Hereafter, the results for a quad-plane concept are given.

Concept description

Concept is characterized by a rotor axis perpendicular to the aircraft body x-axis ($\theta_r = 0^\circ$) as depicted in Figure 4.32.



Figure 4.32: Quad-plane concept

Design variable analysis and findings

Variable set 1: System and component masses

The VTOL system mass for the quad-plane concept is plotted as a function of wind speed for different elevation angles in Figure 4.33a. There is no significant change in VTOL system mass until a wind speed of around 6 m/s where it increases slightly and then decreases slightly. From 4.5kg at zero wind speed to 4.7kg at 7.5 m/s and 4.3 at 10 m/s for the target θ_t of 41.8 degrees. The minimum mass is found for the lower θ_t .

The component masses are plotted in Figures 4.33b - 4.34b. At the tipping point of the VTOL system mass, battery mass and rotor suddenly increases while motor mass suddenly drops. After this abrupt change, motor and rotor mass are decreasing, explaining the decrease in VTOL system mass

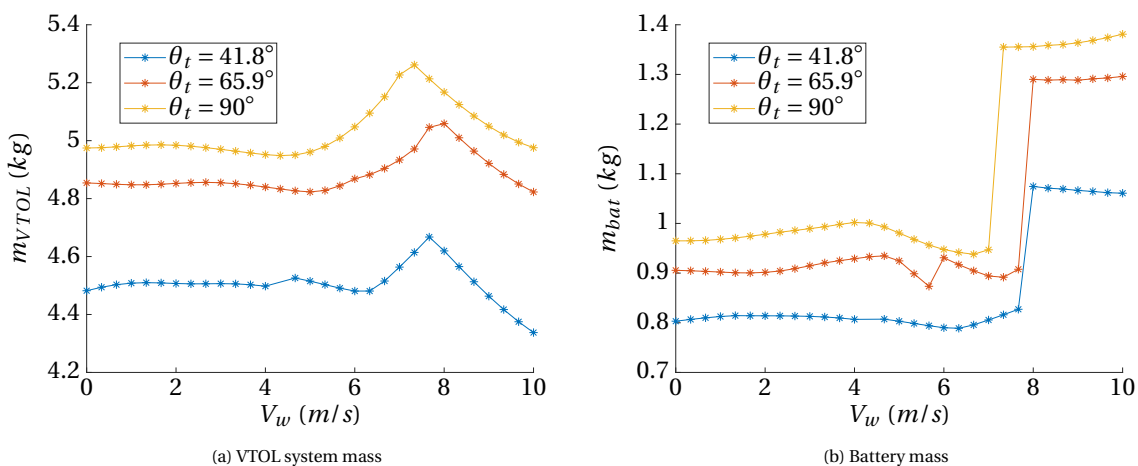


Figure 4.33: VTOL system and battery mass vs. wind speed for different elevation angle

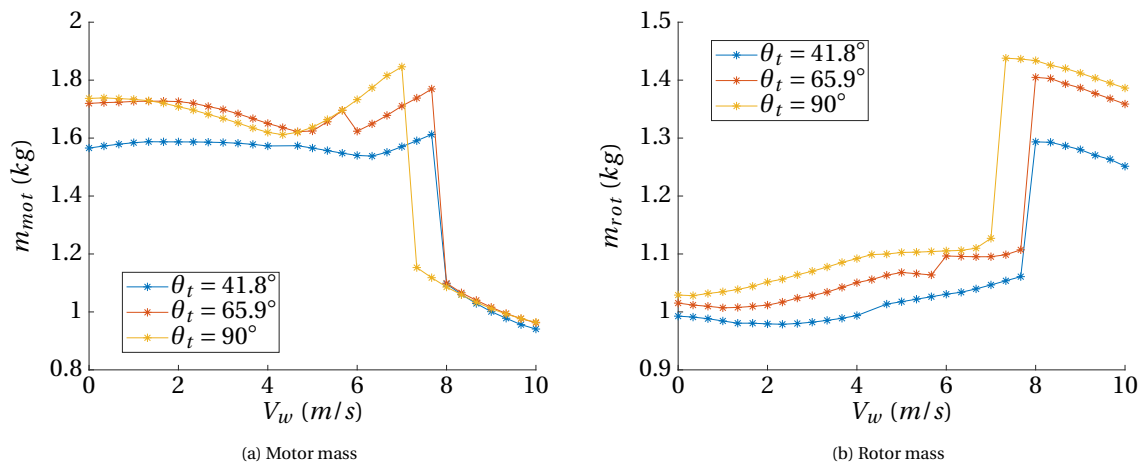


Figure 4.34: Motor and rotor mass vs. wind speed for different elevation angle

Variable set 2: Required thrust and power

The required thrust and power are analyzed and plotted as a function of wind speed for the different elevation angles in Figure 4.35. For the second segment, thrust increases slightly up to wind speeds of 7-8 m/s and then decreases with wind speed. For the first segment the required thrust is significantly higher than in the second segment between wind speeds of 4-7 m/s. Regarding the required power there is a sudden drop at 7-8 m/s, which also explains the sudden drop for the motor mass. After the drop, the power continues to decrease. The required power is found the same for both segments or lower in the first segment. The higher thrust in the first segment for the wind speeds between 4-7 m/s is possible due to a favorable rotor inflow condition in the first segment.

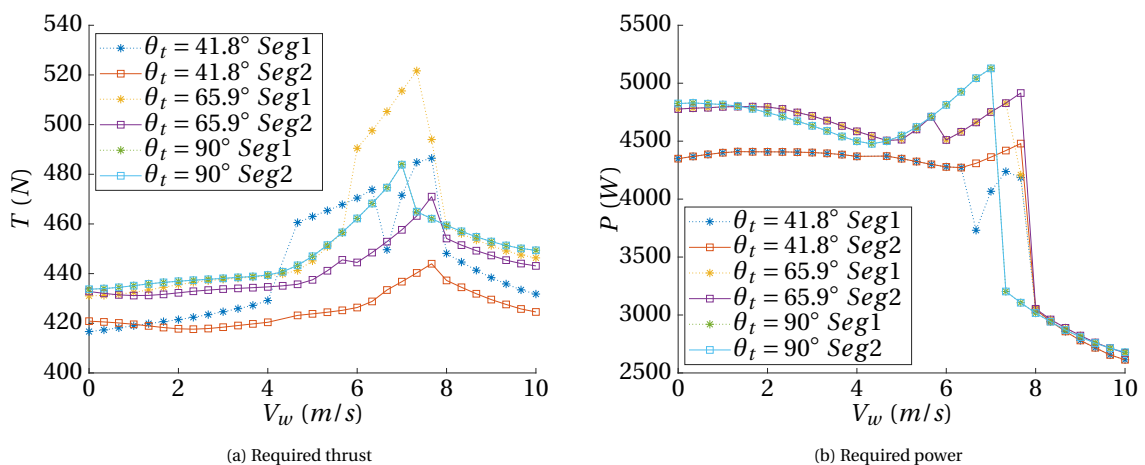


Figure 4.35: Required thrust and power for force equilibrium

Variable set 3: Angle of attack of wing and rotor

The angle of attack of the wing and rotor are analyzed and plotted as a function of wind speed for the different elevation angles in Figure 4.37. Also for both wing and rotor angle of attack, a sudden change is observed, linked to the drop for thrust and power. The angle of attack jumps from a value -25° to around -10° . Both lift conditions are negative at these conditions, but the jump avoids angle of attack of around -20° , at which the highest negative lift is obtained (see Figure 4.36). With increasing angle of attack after the jump, the aerodynamic force becomes less negative, hence the decrease in required thrust. The jump in the rotor inflow angle to around 80° brings the flow more parallel to the rotor for higher wind speed, which means a decrease in required power (see rotor model in Figure 3.15a).

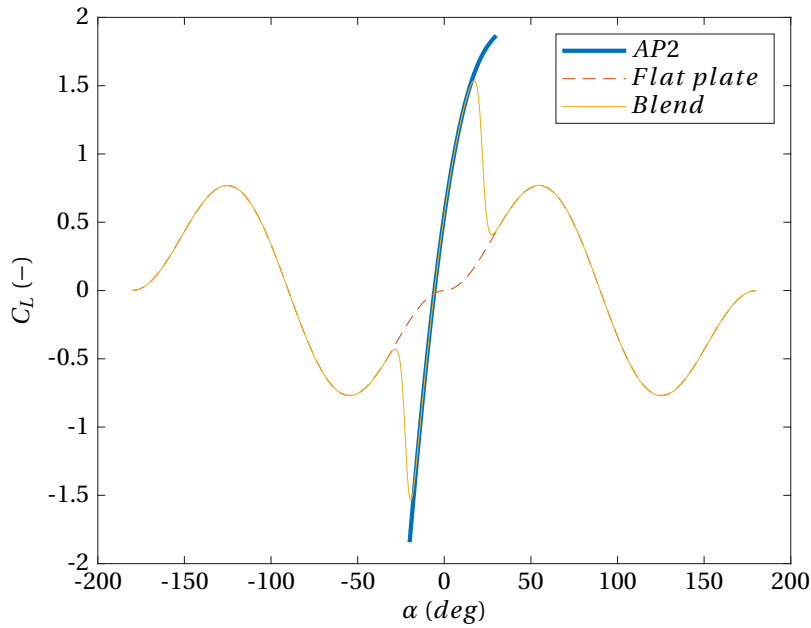


Figure 4.36: Lift coefficient over 360 degree of AoA

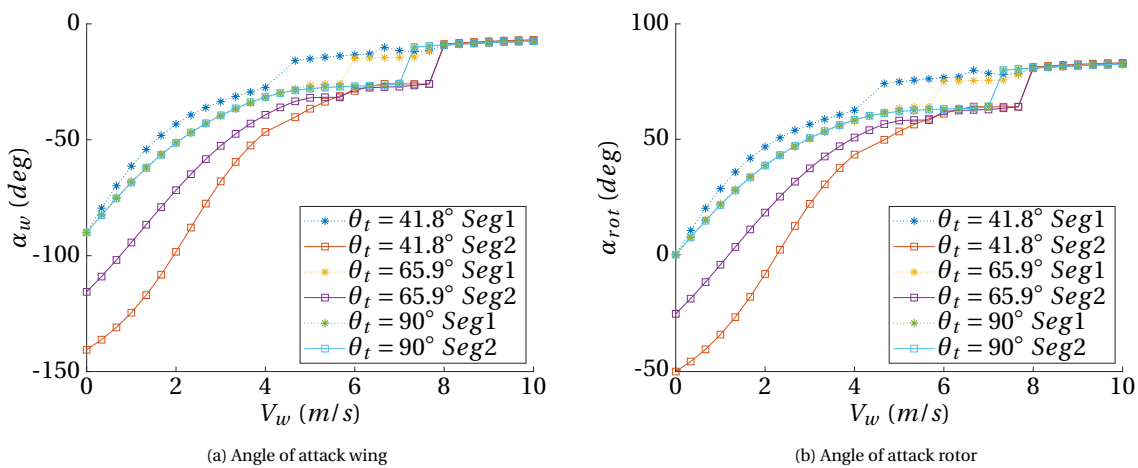


Figure 4.37

Variable set 4: Vertical and horizontal speed

The vertical and horizontal speed are analyzed and plotted as a function of wind speed for the different elevation angles in Figure 4.53. Again a sudden drop is observed. It is this drop in climb speed however, that causes the drop in angle of attack of both rotor and wing which causes on its turn a drop in required thrust and power. Despite the power decrease, this drop in velocity causes an increase in battery mass due to the longer duration of the climb and hence larger energy demand, which scales with the power multiplied with mission take-off time.

Variable set 5: Aircraft pitch and rotor pitch

The aircraft pitch and rotor pitch angle are analyzed and plotted as a function of wind speed for the different elevation angles in Figure 4.39. In this concept rotor pitch is fixed at 0 degrees, which requires the aircraft to pitch at an angle where there is force equilibrium. For the quad-plane concept the range in body pitch is rather small as compared to other concepts. Starting from zero wind speed the attitude is rather neutral with

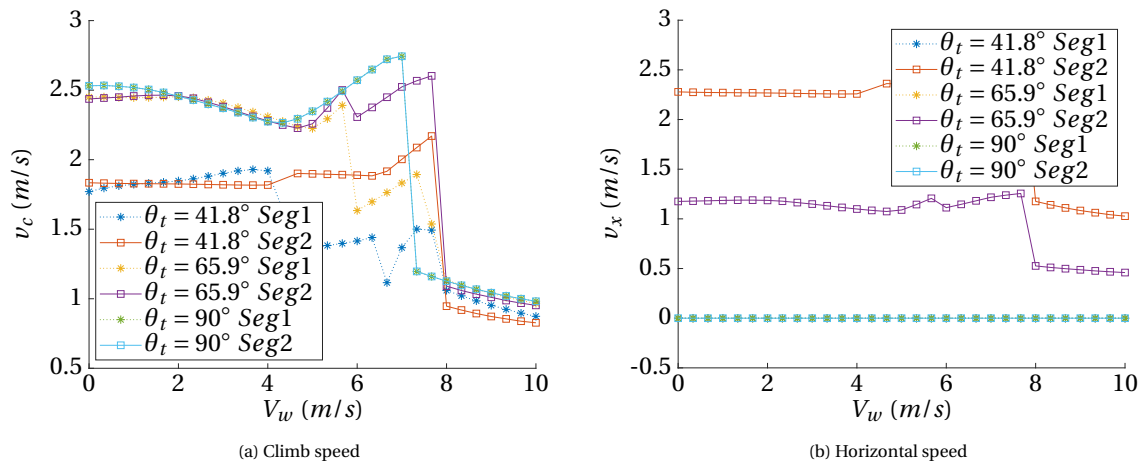


Figure 4.38: Climb and horizontal speed vs. wind speed for different elevation angle

increasing forward pitch with speed until the characterizing change comes which increases the pitch angle and then it decreases again.

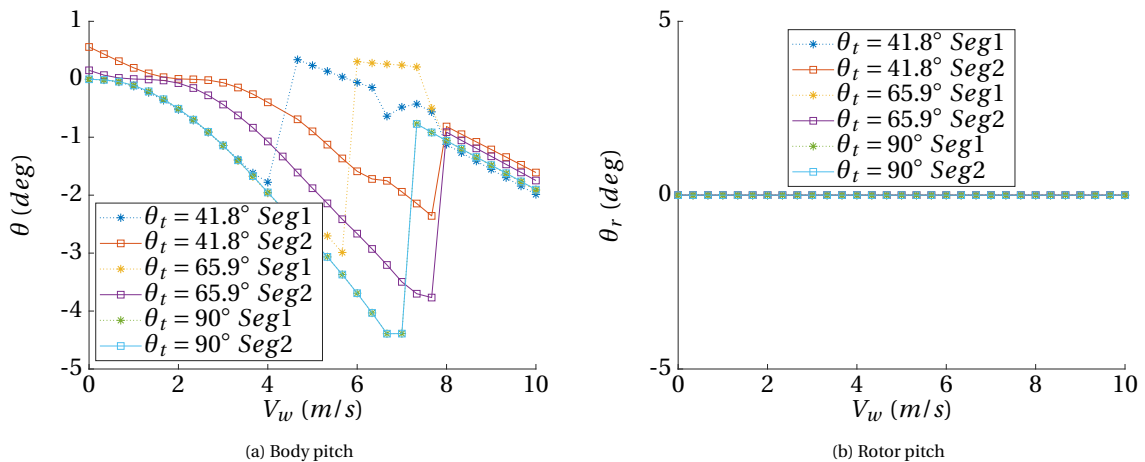


Figure 4.39: Aircraft pitch and rotor pitch vs. wind speed for different elevation angle

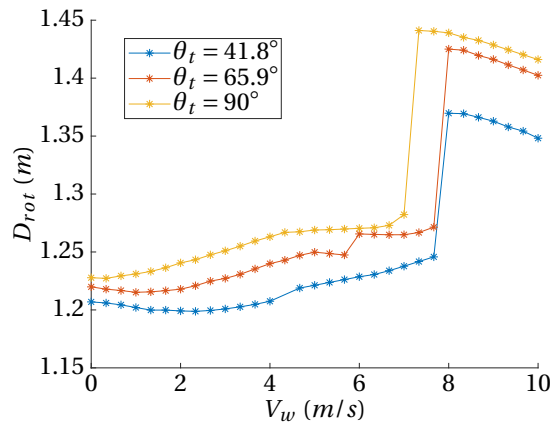
Variable set 6: Rotor diameter

The rotor diameter is analyzed and plotted as a function of wind speed for the different elevation angles in Figure 4.40a. The optimization converged to a large rotor diameter for this concept (1.2m-1.4m). Especially for high wind speeds, the optimal rotor diameter is very large (1.45m). This is however a penalty in terms of additional drag of the VTOL concept. It is questionable, if such a large rotor diameter will not be detrimental at power generation phase due to the drag of the big rotors. It is therefore recommended for the continuation of this work to investigate the effect of the rotor diameter further when pursuing this concept.

Variable set 7: Battery required specific power and specific energy

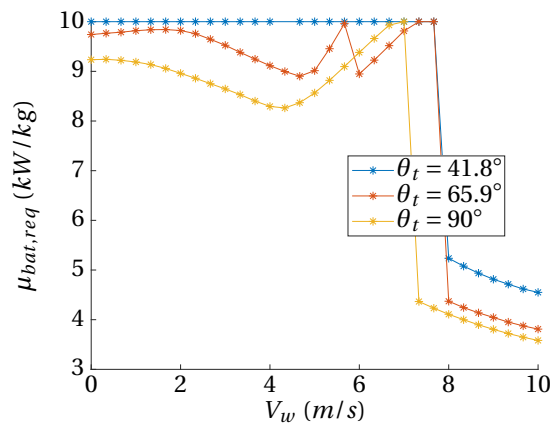
The battery required specific power are plotted as a function of wind speed and for the different elevation angles in Figure 4.41a. Regarding required specific power of the battery, the maximum of 10 kW/kg is used for the lower elevation angle up to 8 m/s wind speed. Here the required specific power drops to a value of around 5 kW/kg. Same drop occurs for the other elevation angles. However for lower wind speed the required specific power is slightly less than 10 kW/kg. The required specific energy of the battery is 684 kJ/kg for all conditions.

Visualization of aircraft attitude and forces



(a) Rotor diameter

Figure 4.40



(a) Required specific power battery

Figure 4.41

In Figure 4.42-4.46, the attitude and forces of the quad-plane concept are visualized for segment 1 and 2, elevation angle of 41.8° and wind speeds of 0-7.5-10 m/s.

For the first segment, only a drag component is counteracting the thrust for a wind speed of 0 m/s. The drag for zero wind speed is observed to be highest for the quad-plane concepts. Still the aerodynamic force is significantly low compared to the aerodynamic lift forces at higher wind speeds due to the mild climb speeds. For a wind speed of 7.5 m/s, negative lift is observed in the first segment due to the negative angle of attack with a magnitude of around 75N which adds to the thrust requirement. For higher winds speed of 10 m/s, the negative lift is reduced however due to the smaller negative angle of attack.

For the second segment, both lift and drag are counteracting the required thrust at 0 wind speed. However, due to the low apparent speed aerodynamic forces are rather low. For higher wind speeds of 7.5 m/s, the wing is in a stalled condition with both the drag and lift counteracting the thrust. Due to the reduced apparent speed with horizontal velocity, aerodynamic forces are lower in magnitude as compared to the first segment. For a wind speed of 10 m/s, the wing is no longer stalled, but producing a small lift (down force here) and drag force component counteracting the thrust force.

Conclusion

Similar to the tail-sitter concept, the required VTOL mass for the quad-plane concept increases with target elevation angle. However, regarding wind speed, there is a peak in required VTOL mass of 4.6 kg for a wind speed of 7.6 m/s, after that it decreases to a VTOL mass of 4.3 kg at 10 m/s. For zero (0) wind speed the

required VTOL system mass is 4.5 kg. Contrary to the tail-sitter this increase in VTOL mass is due to increase in thrust. This concept needs to counteract the negative lift forces.

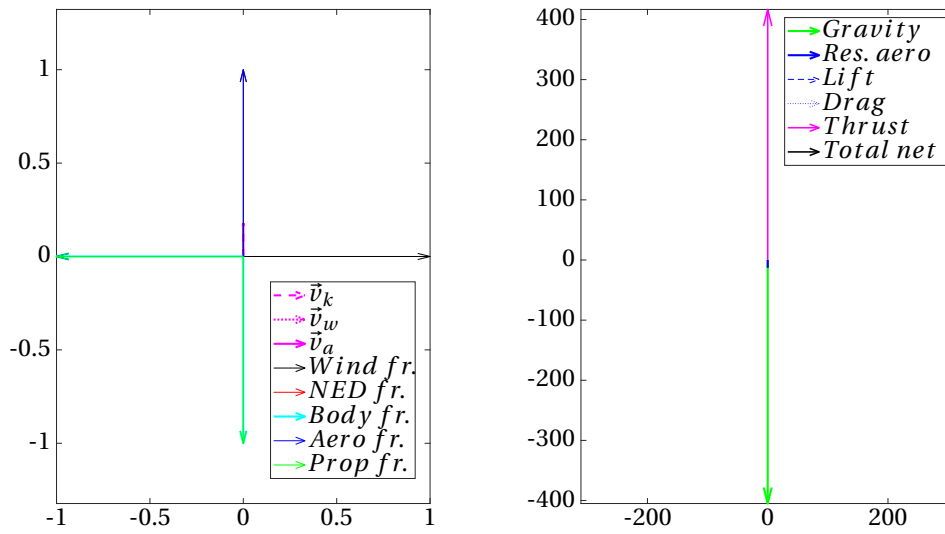


Figure 4.42: Attitude and force visualization segment 1 ($\theta_t = 41, 8^\circ, V_w = 0m/s$)

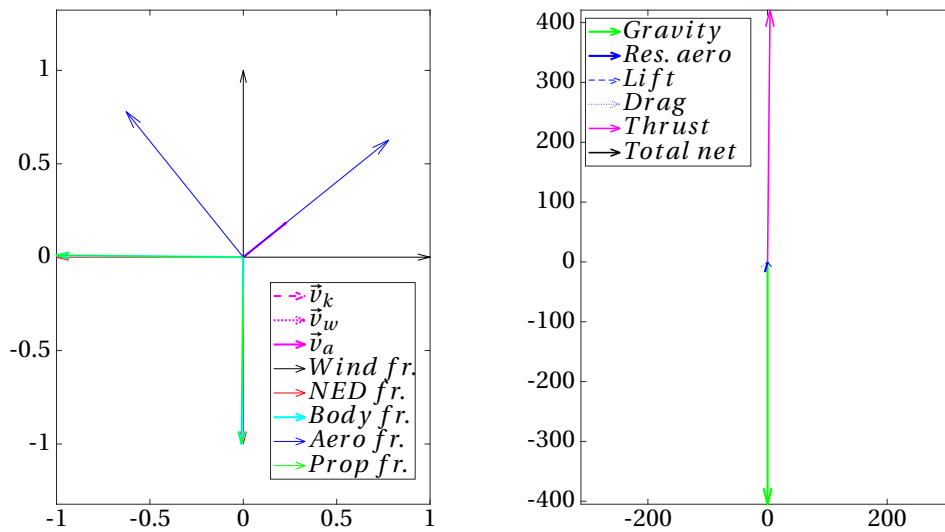


Figure 4.43: Attitude and force visualization segment 2 ($\theta_t = 41, 8^\circ, V_w = 0m/s$)

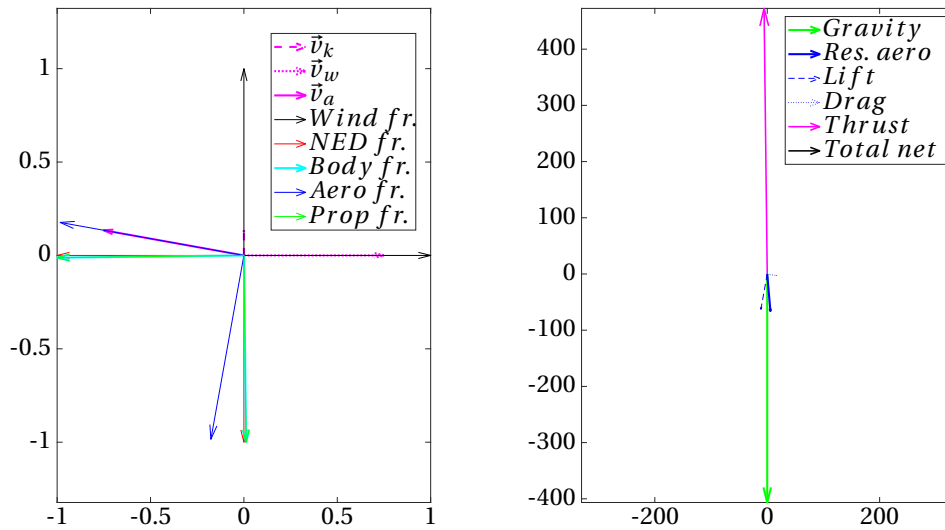


Figure 4.44: Attitude and force visualization segment 1 ($\theta_t = 41,8^\circ, V_w = 7,5m/s$)

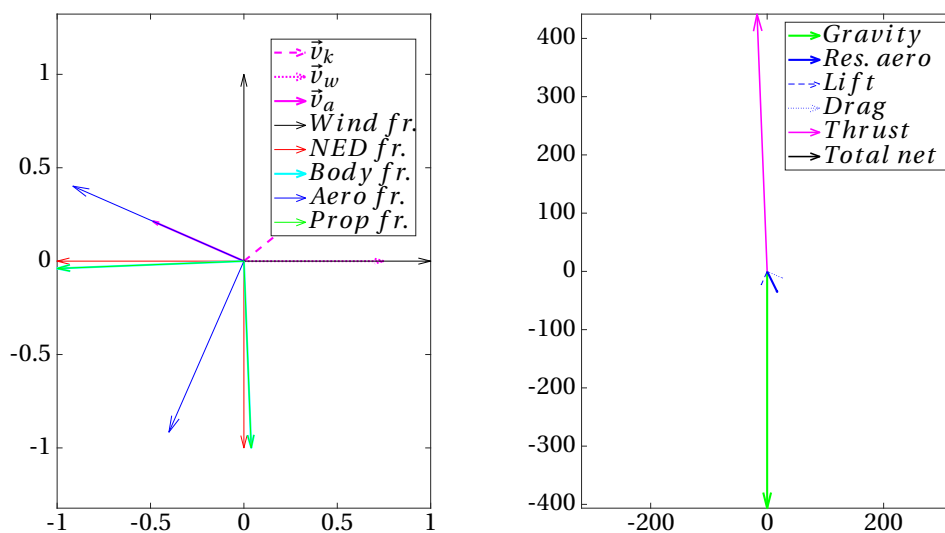
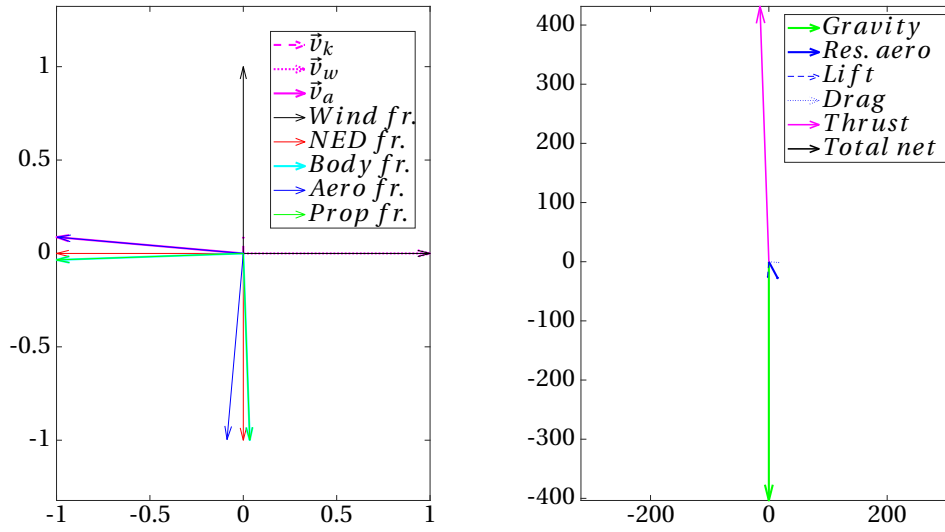
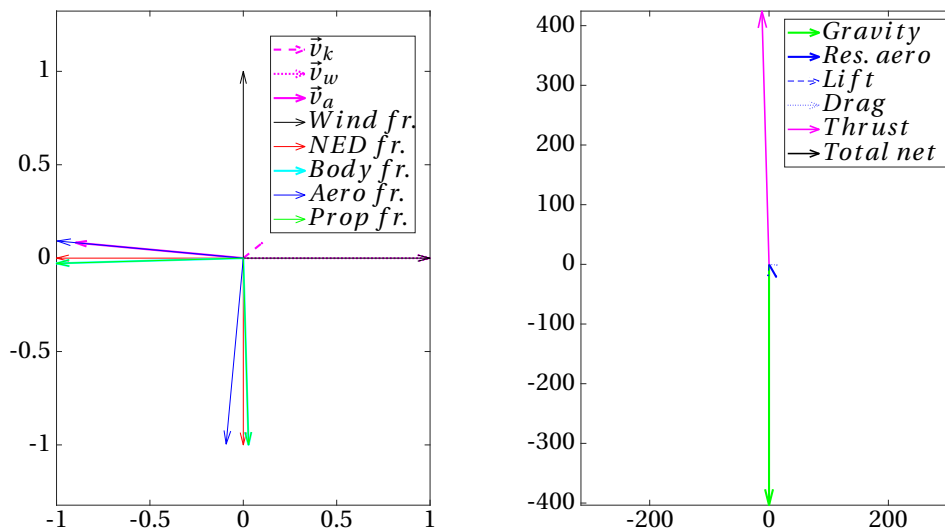


Figure 4.45: Attitude and force visualization segment 2 ($\theta_t = 41,8^\circ, V_w = 7,5m/s$)

Figure 4.46: Attitude and force visualization segment 1 ($\theta_t = 41,8^\circ, V_w = 10\text{m/s}$)Figure 4.47: Attitude and force visualization segment 2 ($\theta_t = 41,8^\circ, V_w = 10\text{m/s}$)

4.2.4. Knee-sitter (-30°) concept

Hereafter, the results for a knee-sitter concept are given. In the category of fixed rotor, it can be concluded that nor the tail-sitter nor quad-plane concept can benefit from aerodynamic forces, instead they have to fight against it. Therefore, based on the results of the tilt-rotor a new innovative concept has been introduced, named the knee-sitter concept. It is observed that the tilt-rotor has a rotor pitch between -30 and -40 degrees for the target elevation angle of 41.8 degrees and wind speeds between 6-10 m/s. So this new concept is introduced with a rotor fixed at -30 degrees, the "knee-sitter".

Concept description

This concept is characterized by a rotor axis tilted -30 degrees forward with respect to the quad-plane concept as depicted in Figure 4.48.

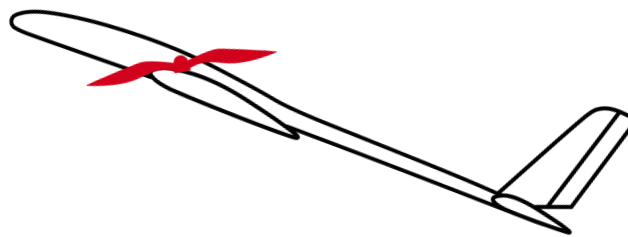


Figure 4.48: Knee-sitter concept

Design variable analysis and findings

Variable set 1: System mass and component masses

The VTOL system mass for the knee-sitter concept is plotted as a function of wind speed for different elevation angles in Figure 4.49a. It is clear from the plot that for all elevation angles the trend is a decreasing VTOL system mass as a function of wind speed, with a decrease of around 2.5kg by a wind speed of 10m/s for all elevation angles. The effect of elevation angle is low and the optimal elevation angle is depending on the wind speed as is observed as well for the tilt-rotor concept.

The component masses are plotted in Figures 4.49b - 4.50b. The global trend of all components is a decreasing mass with wind speed. For the battery mass there is a exception for lower wind speeds between 2-4 m/s, depending on the elevation angle, where a sudden increase is observed. This increase is compensated by a decrease in motor mass, which leads to an overall decrease in VTOL system mass. The decrease in motor mass is the biggest contributor to the overall VTOL mass decrease.

Variable set 2: Required thrust and power

The required thrust and power are analyzed and plotted as a function of wind speed for the different elevation angles in Figure 4.51. A decrease in thrust with wind speed can be observed for this concept as similar to the tilt-rotor concept. For wind speeds above 4 m/s the highest required thrust is for the lower elevation angle, but the difference in thrust is not more than 40N. The increase in required thrust is explained by the lower apparent speed for the lower elevation angle, lowering supporting the aerodynamic lift force. Also the required power is decreasing with wind speed. The differences between the different elevation angles is low.

Variable set 3: Angle of attack of wing and rotor

The angle of attack of the wing and rotor are analyzed and plotted as a function of wind speed for the different

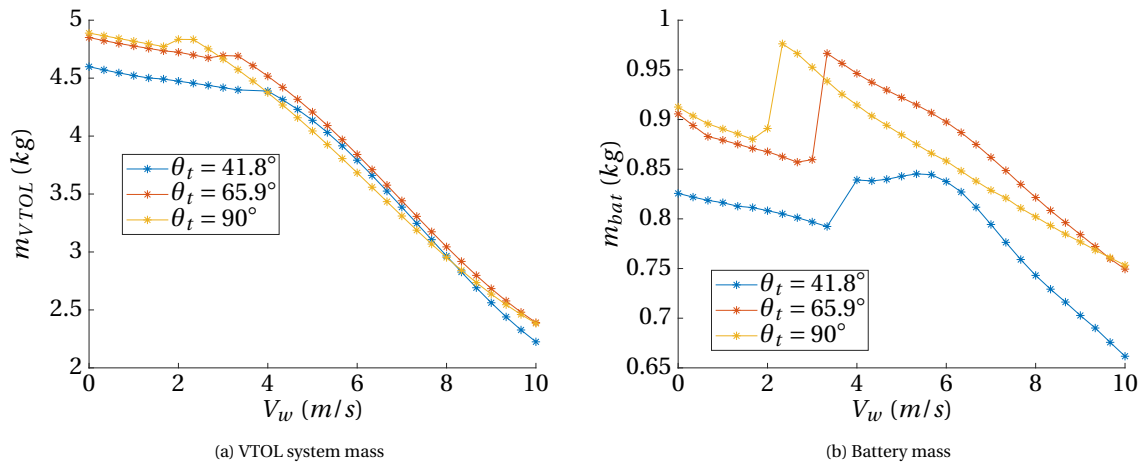


Figure 4.49: VTOL system and battery mass vs. wind speed for different elevation angle

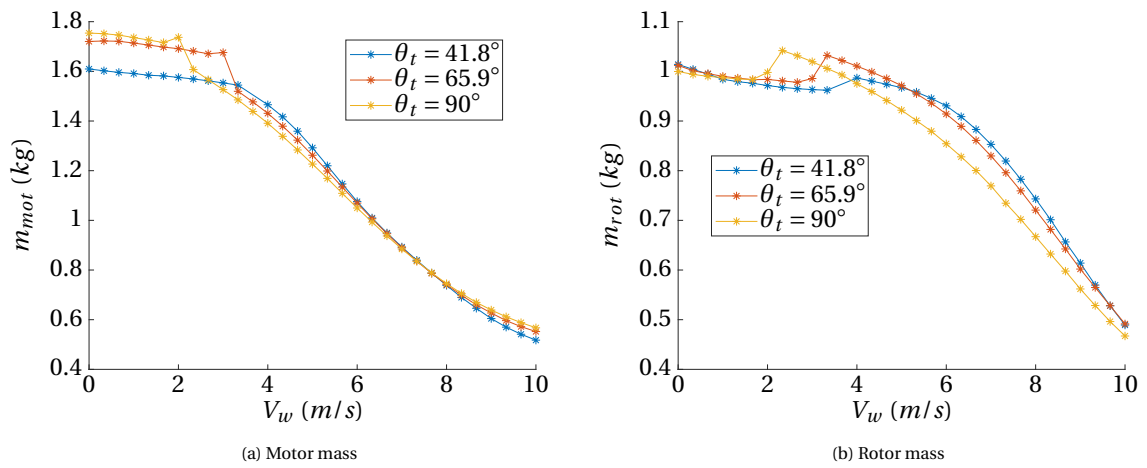


Figure 4.50: Motor and rotor mass vs. wind speed for different elevation angle

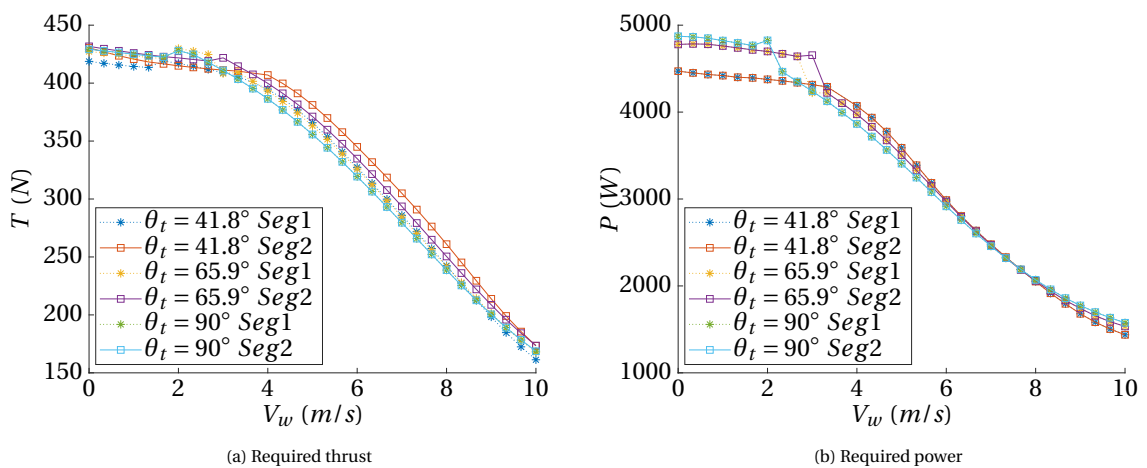


Figure 4.51: Required thrust and power for force equilibrium

elevation angles in Figure 4.52. In contrary to the tilt-rotor concept, maximum angle of attack cannot be tracked accurately, however the angle of attack which are found between 5-10m/s wind speed are all positive and in an attached flow region. Therefore, the lift can be exploited and the required thrust is decreasing.

Rotor inflow angles are found between 60°-80° for these wind speeds.

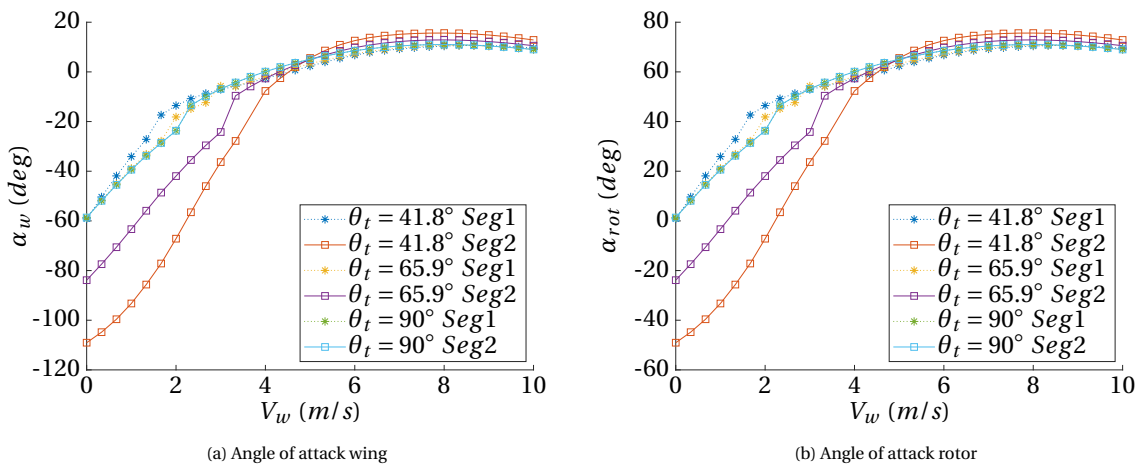


Figure 4.52

Variable set 4: Vertical and horizontal speed

The vertical and horizontal speed are analyzed and plotted as a function of wind speed for the different elevation angles in Figure 4.53b. For the second segment, climb velocity is decreasing with wind speed after being constant to wind speeds of 2-4m/s depending on the elevation angle. The trend for the first segment is similar for speeds above 4m/s. For lower winds speeds there is no clear trend.

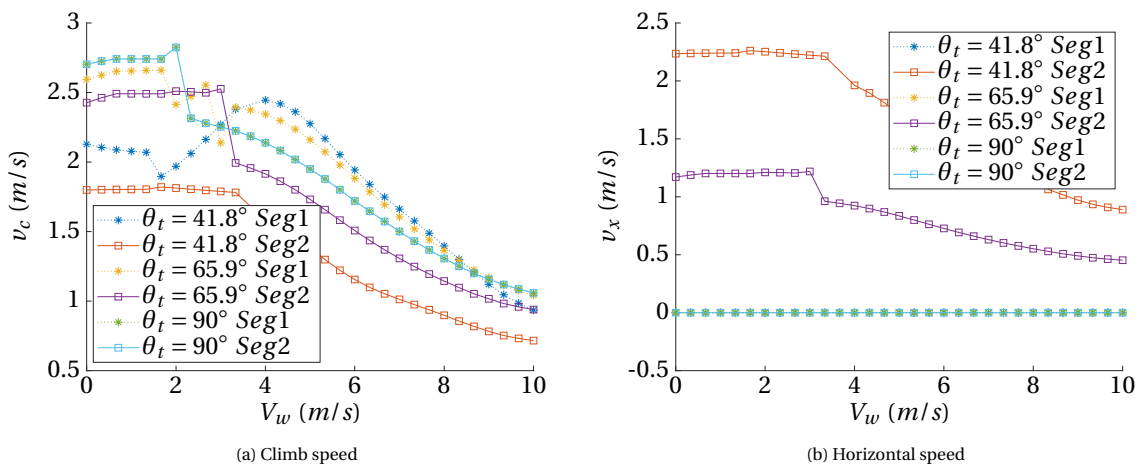


Figure 4.53: Climb and horizontal speed vs. wind speed for different elevation angle

Variable set 5: Aircraft pitch and rotor pitch

The aircraft pitch and rotor pitch angle are analyzed and plotted as a function of wind speed for the different elevation angles in Figure 4.54. The rotor pitch is constant to -30 degrees for this concept. There is a decrease in body pitch to account for the drag.

Variable set 6: Rotor diameter

The rotor diameter is analyzed and plotted as a function of wind speed for the different elevation angles in Figure 4.55a. Similar to the tilt-rotor concept there is a decrease in rotor diameter. This is also beneficial regarding the additional drag of the VTOL system.

Variable set 7: Battery required specific power and specific energy

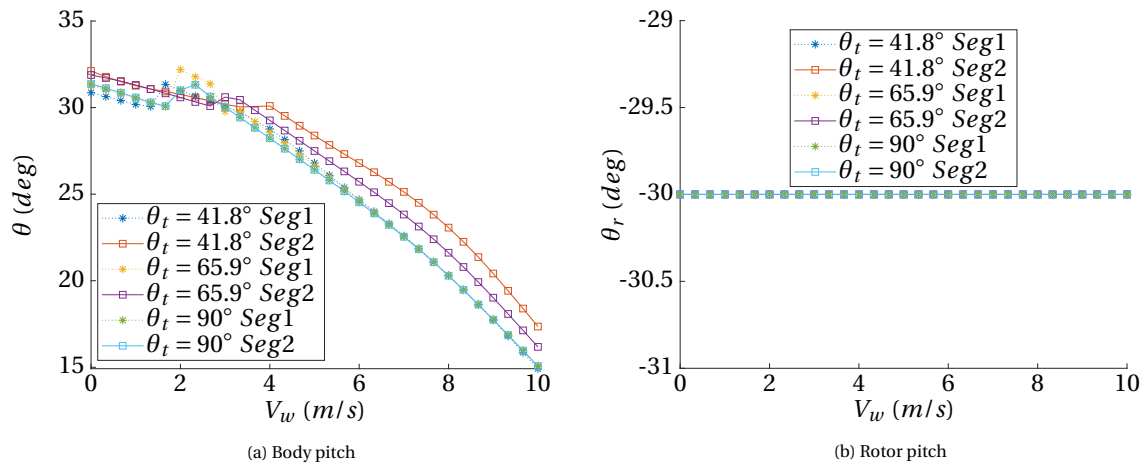


Figure 4.54: Aircraft pitch and rotor pitch vs. wind speed for different elevation angle

The battery required specific power are plotted as a function of wind speed and for the different elevation angles in Figure 4.56a. It can be observed that it the battery specific power of 10 kW/kg is only limiting at low wind speeds. The required specific energy of the battery is 684 kJ/kg for all conditions.

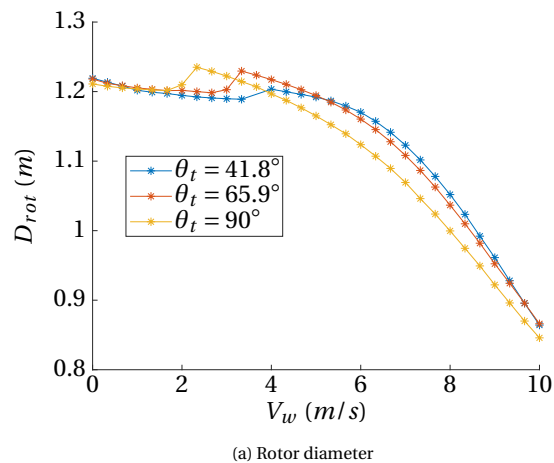


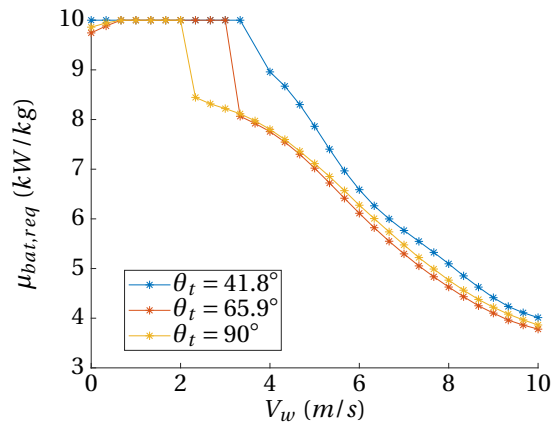
Figure 4.55

Visualization of aircraft attitude and forces

In Figure 4.57-4.61, the attitude and forces on the aircraft are visualized for segment 1 and 2, elevation angle of 41.8° and wind speeds of 0-5-10 m/s.

For the first segment, the aerodynamic force resulting from the vertical climb is counteracting the thrust vector for 0 wind speed as compared to the quad-plane the exposed area is quite large. For a moderate wind-speed of 5 m/s, the apparent speed aligns with the body frame and the resulting aerodynamic force is pointing upward as can be seen from Figure 4.59. The same holds for a higher wind speed of 10 m/s, but as both angle of attack as the apparent speed are larger, so is the aerodynamic force.

For the second segment, the aerodynamic force is counteracting the aircraft's movement for 0 wind speed. The resulting aerodynamic force is larger than the first segment, as the exposed area is now higher. For a moderate and high wind speed of 5 m/s and 10 m/s, the condition is similar to the first segment. The obtained aerodynamic lift is however less due to the decrease in apparent speed with the horizontal motion in wind direction.



(a) Required specific power battery

Figure 4.56

Conclusion

For the knee-sitter, similar to the tilt-rotor concept, the VTOL system mass is now found to decrease again for all elevation angles. A VTOL system mass of 4.6kg is required for zero winds speed and decreases to 2.2kg for a wind-speed of 10 m/s.

Similar to the tail-sitter concept, a remarkable observation that can be made is that there is a clear difference in trend below 3-4 m/s wind speed and above. This distinction is clear in all variable plots. The trend above 3 m/s arises due to the increasing aerodynamic effects. Furthermore, this concept operates in an attached flow regime for wind speeds above 3-4 m/s, which increases the aerodynamic effects.

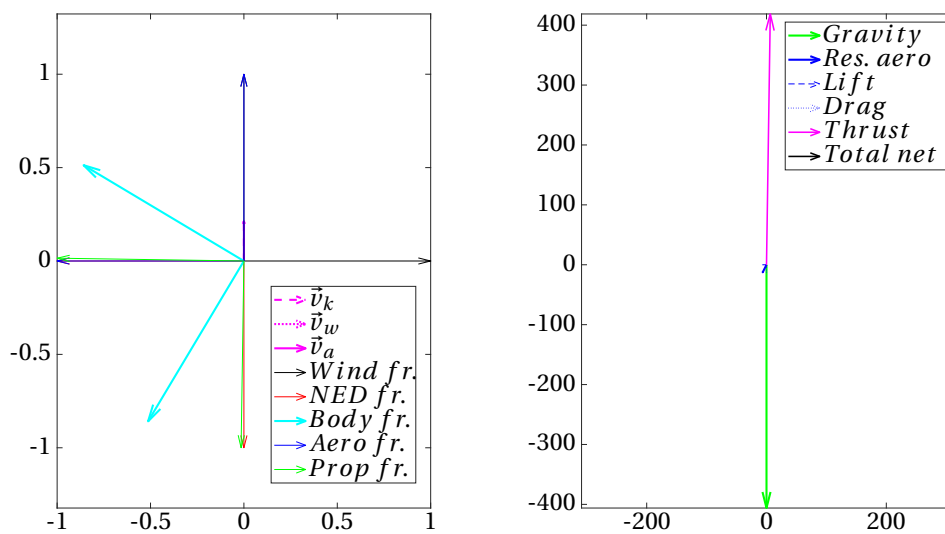


Figure 4.57: Attitude and force visualization segment 1 ($\theta_t = 41,8^\circ, V_w = 0m/s$)

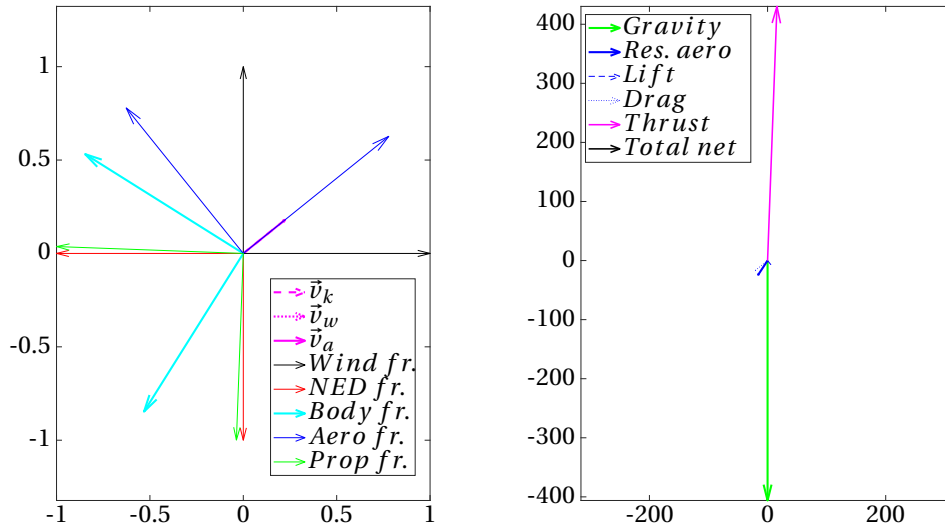


Figure 4.58: Attitude and force visualization segment 2 ($\theta_t = 41, 8^\circ, V_w = 0 m/s$)

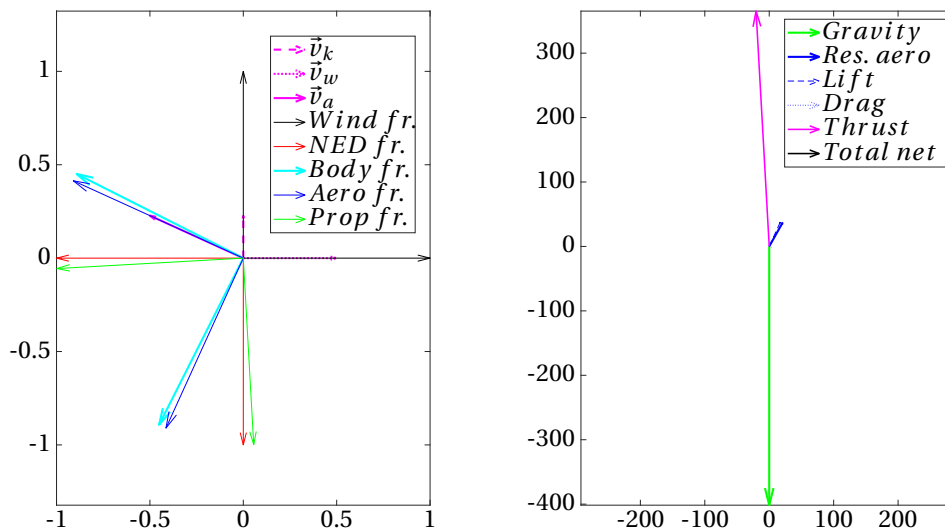


Figure 4.59: Attitude and force visualization segment 1 ($\theta_t = 41, 8^\circ, V_w = 5 m/s$)

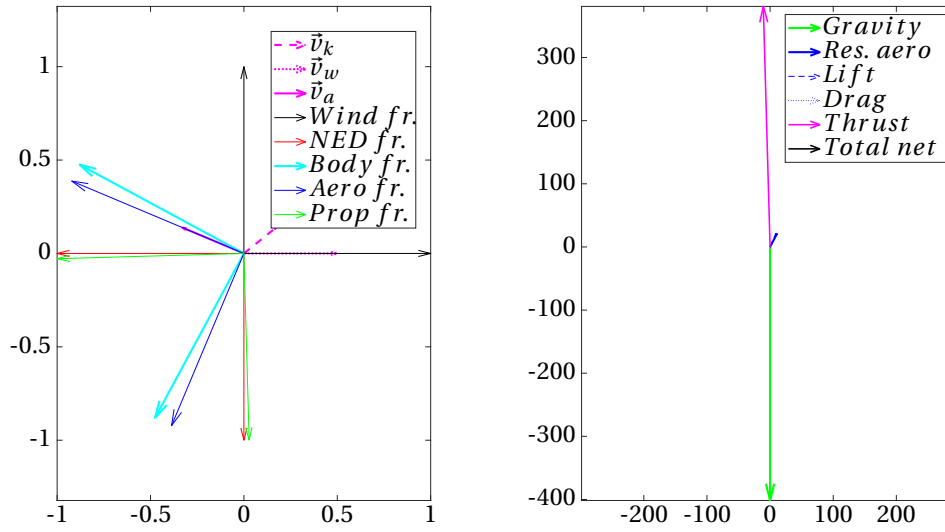


Figure 4.60: Attitude and force visualization segment 2 ($\theta_t = 41,8^\circ, V_w = 5m/s$)

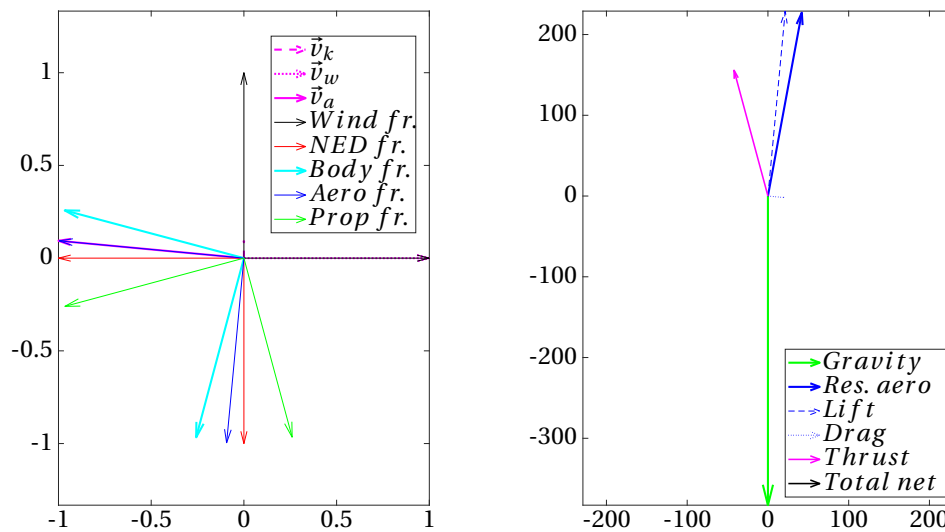


Figure 4.61: Attitude and force visualization segment 1 ($\theta_t = 41,8^\circ, V_w = 10m/s$)

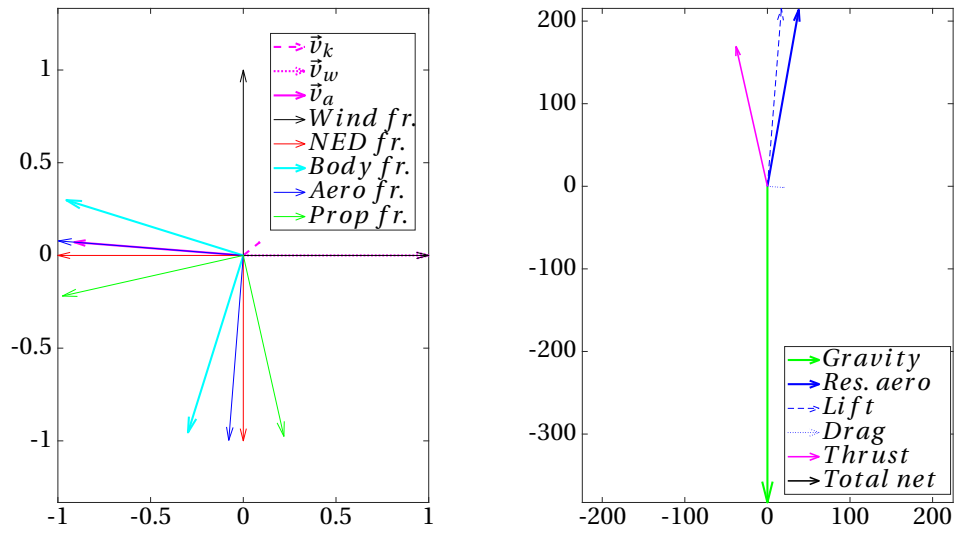


Figure 4.62: Attitude and force visualization segment 2 ($\theta_t = 41,8^\circ$, $V_w = 10\text{m/s}$)

4.2.5. Knee-sitter variants

In previous section a concept is analyzed with a fixed rotor tilt at -30° , named the knee-sitter concept. Naturally, a rotor can also be fixed at other angles. In this section results are given for rotors fixed at -15° and -45° .

The VTOL system mass of the -15° concept is plotted as a function of wind speed for different elevation angles in Figure 4.63a. The mass is decreasing with wind speed for all elevation angles. The target elevation angle of 41.8° result in the lowest mass for all wind speeds.

The VTOL system mass of the -45° concept is plotted as a function of wind speed for different elevation angles in Figure 4.63b. The mass is decreasing with wind speed for all elevation angles. The optimal target elevation angle for this concept is 90° for wind speeds above 3 m/s and 41.8° for winds speeds below 3 m/s.

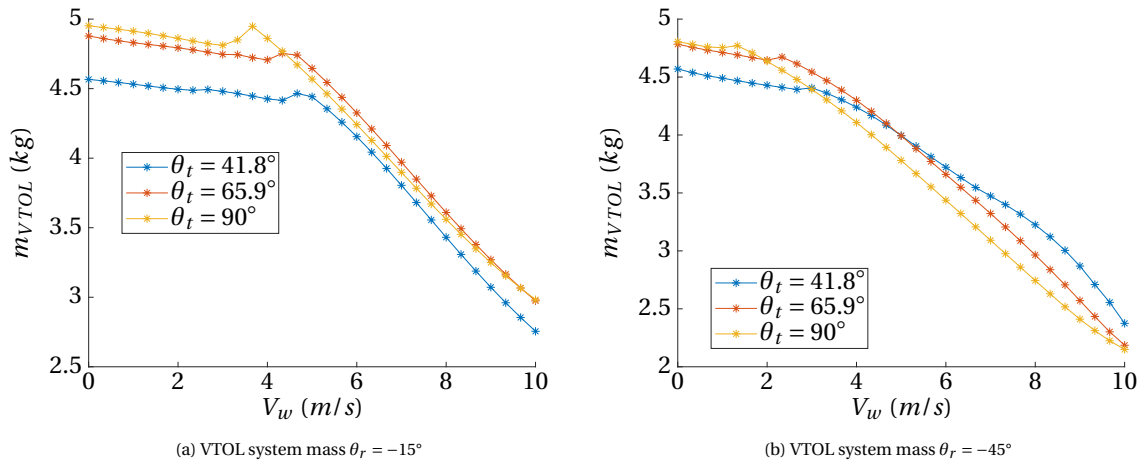


Figure 4.63: VTOL system vs. wind speed for different elevation angle

4.2.6. Concept comparison

Four (4) concepts are explained in previous sections, augmented with 2 variants of the knee-sitter concept: knee-sitter -15° and -45° . In this sections the concepts are compared. In Figure 4.64a the VTOL mass of the different concepts is plotted as a function of wind speed for an elevation angle of 90° (straight up). According to expectations, the tilt-rotor concepts sets the lowest possible value, as it is optimal at every wind condition. From the presented concepts, tail-sitter and knee-sitter -45° concept are reaching this limit for certain wind conditions. For the tail-sitter this is however limited to very low wind speeds (<1 m/s). For the knee-sitter -45° concept, this happens at higher wind speeds above 6 m/s. Therefore, taking note that the knee-sitter -45° concept does not require any tilting mechanism it can be considered an optimal choice, considering VTOL system mass and when taking a perfectly vertical take-off approach. For wind speeds above 5m/s, the knee-sitter -30° concept is next in line, followed by knee-sitter -15° concept and quad-plane concept. The concept performing worst at climb speeds above 8 m/s is the tail-sitter.

In Figure 4.64b the VTOL mass of the different concepts is plotted as a function of wind speed for an elevation angle of 41.8° . According to the expectations, the tilt-rotor concepts sets the lowest possible value, as it can optimize θ_r for every wind condition. For the higher wind speeds (7-10 m/s) knee-sitter -30° has now a lower VTOL system mass than the knee-sitter -45° concept and getting close to the tilt-rotor optimal limit. Therefore, the knee-sitter -30° concept can be considered an optimal choice for wind speeds above 7m/s, considering VTOL system mass and when taking a take-off approach to an elevation angle of 41.8° . For wind speeds above 7 m/s, the knee-sitter -45° concept is next in line, followed by knee-sitter -15° concept and quad-plane concept. The concept performing worst at climb speeds above 8 m/s is again the tail-sitter.

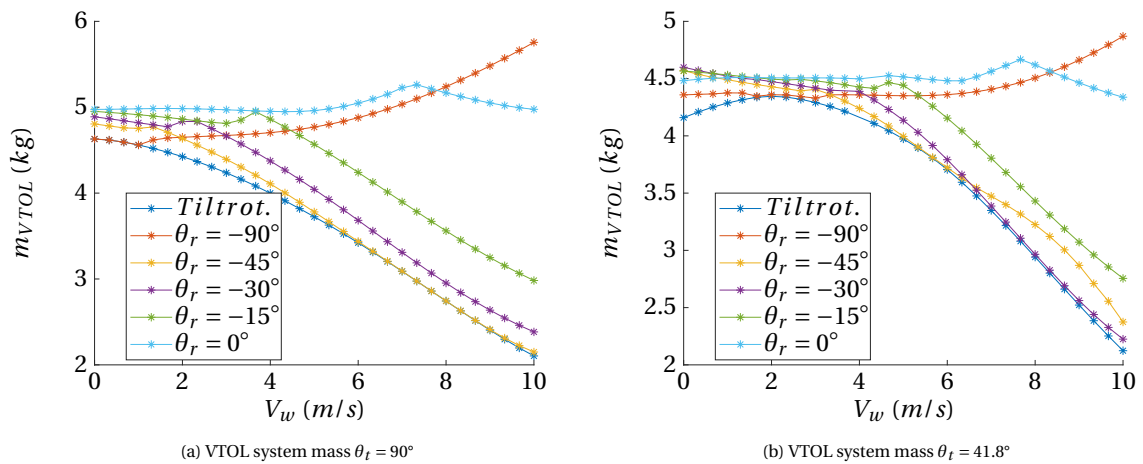


Figure 4.64: VTOL system vs. wind speed for different concepts

4.3. Synthesis of concept analysis

In this research the VTOL system mass, component masses and other variables have been plotted and analyzed for different concepts, different wind speeds and different target elevation angles. When going further to the detailed design of the VTOL system of a selected concept, required wind speed range and take-off approach (target elevation angle) needs to be determined based on this research.

4.3.1. Concept choice

Based on the mass analysis, the optimal concept is depending on the required wind speed range and target elevation angle. Furthermore, also the additional drag of the VTOL system is an important factor when considering the concept choice.

A. Wind speed range and target elevation angle dependency

In Section 4.2.6, the concepts have been compared by plotting VTOL system masses against wind speed. When the VTOL system is required to operate in the complete wind speed range 0-10m/s, the maximum VTOL system mass in this range is critical and dictates the VTOL system mass and design. This value is given in Table 4.3. It is clear that the heaviest concept for this wind speed range is the tail-sitter concept with 5.8kg, which is about 1kg heavier than the other concepts. The lightest concept is the tilt-rotor with 4.3kg, other concepts are however close with a value of around 4.6kg and 4.7kg for knee-sitter (-15°, -30°, -45°) and quad-plane respectively, for a target elevation angle of 41.8°.

Referring back to the operation of an AWE aircraft, the AWES cannot produce any power below the cut-in speed. It is therefore reasonable, that the AWE aircraft is not required to take-off below this speed. In Table 4.3, the required VTOL system masses are given for a wind speed range of 4-10m/s. Concept such as the tilt-rotor and knee-sitter -45° concept can take advantage of the aerodynamic lift of the wind and therefore have a lower required VTOL mass. Same holds for a wind-speed range of 8-10 m/s, where the aerodynamic advantage is most pronounced for the tilt-rotor (2.7kg), knee-sitter -30° (3.0kg) and knee-sitter -45° (2.7kg) concepts. Here the benefit is up to 3.1 kg (53%), compared to the heaviest concept (5.8kg).

While 8-10 m/s seems a narrow range, it should be noted that when looking at Figure 4.64a and 4.64b, the lowest wind speed sets the critical VTOL system mass. Therefore, extrapolating these results, concepts benefiting from the aerodynamic effect have a wind speed range of 8+ m/s. There is one exception to this, the tail-sitter, which VTOL mass increases with wind speed.

Lastly, when the AWE aircraft is only required to take-off at low wind speeds, the difference between the concepts is small. Here the lowest target elevation angle results in the lowest VTOL system mass.

A side-note to the above results is that it should be taken into account that a tilting-mechanism for the tilt-rotor requires extra mass, which is not taken into account in the above results.

Table 4.3: VTOL system mass for different concepts, wind speed range and target elevation angle θ_t

Concept	Tilt-rotor		Quad-plane		Knee-sitter -15°		Knee-sitter -30°		Knee-sitter -45°		Tail-sitter	
	41.8°	90°	41.8°	90°	41.8°	90°	41.8°	90°	41.8°	90°	41.8°	90°
0-10m/s	4.3kg	4.6kg	4.7kg	5.3kg	4.6kg	5.0kg	4.6kg	4.9kg	4.6kg	4.8kg	4.9kg	5.8kg
4-10m/s	4.2kg	4kg	4.7kg	5.3kg	4.5kg	4.9kg	4.4kg	4.4kg	4.2kg	4.1kg	4.9kg	5.8kg
8-10m/s	2.9kg	2.7kg	4.6kg	5.2kg	3.4kg	3.6kg	3.0kg	3.0kg	3.2kg	2.7kg	4.9kg	5.8kg
0-4m/s	4.3kg	4.6kg	4.5kg	5.0kg	4.6kg	5.0kg	4.6kg	4.9kg	4.6kg	4.8kg	4.4kg	4.7kg

B. Drag dependency

Next to the additional mass, the concept choice also influences the extra drag in power generation flight phase with an exposed VTOL system. It is expected that the orientation of the rotor on the AWE aircraft has a significant effect on this additional drag and other aerodynamic interference effects. Here the tilt-rotor can have the benefit of positioning the rotor in a beneficial orientation for power generation flight phase, which might mitigate the penalty of the extra weight of the tilting mechanism.

To make a trade-off between a drag and weight penalty, the effect of extra weight and drag in the power

generation phase should also be analyzed in future work.

4.3.2. Target elevation angle choice

For the direct take-off approach, different target elevation angles have been analyzed as depicted in Figure 4.1. The choice of the target elevation angle will depend on the transition manoeuvre and the analysis presented in this research. For the quad-plane (0°) concept and tail-sitter (-90°) concept the lowest target elevation angle of 41.8° is most optimal in terms of mass due to the lower take-off target height. For the knee-sitter (-30° concept) there is no significant difference between the different target elevation angles. For the knee-sitter -45° concept and tilt-rotor, the elevation angle of 90° is most optimal in terms of mass. This is due to higher apparent velocity and hence larger aerodynamic effect by avoiding to take-off from the wind direction.

Regarding transition manoeuvre, it can be argued that the transition manoeuvre is easier and safer for low elevation angles. In this condition the winch can be used to assist the transition. Furthermore, the power generation phase takes place at elevation angles between 20° - 70° [19]. Therefore, for the take-off target elevation angles within this range, the AWE aircraft is already close to a power generation flight path. A detailed study on the transition manoeuvre is left for future work.

4.3.3. Wind speed range choice

It has been shown in Section 4.3.1 that the required wind speed significantly effects the VTOL system mass of all concepts. It was also shown that for the tilt-rotor, knee-sitter -30° and -45° concepts, the VTOL system mass is significantly reduced when the minimum wind speed requirement is increased. This also means that the AWE aircraft cannot take-off for low wind speeds (e.g. below 8 m/s). The effect of this restriction on yearly energy production will have to be taken into account when trading the wind-speed requirement against VTOL system mass. This is left for future work.

4.3.4. Operational considerations

Once a VTOL system is designed and developed the motor, rotor and battery mass are fixed. However, in this research it has been observed that operational conditions such as climb and horizontal speed highly influence thrust and power during take-off. Furthermore they highly depend on the wind-speed. For safety reasons it is recommended to follow a take-off approach where required power and energy are minimized. This can be done by measuring the wind speed at the ground before take-off, assuming a uniform wind profile and taking off with the horizontal and climb speed obtained from the developed sizing tool as part of this research.

4.3.5. Landing considerations

In this research the take-off requirements of the AWE VTOL system are analysed in detail. One benefit of the VTOL system compared to other take-off and launch systems is that the same system can also be used for landing purposes. Compared to horizontal landing, vertical landing can be carried out with much more precision and hence requires a small landing spot. If the VTOL system is used for landing purposes, it should also be sized accordingly. The detailed effects of sizing for landing can easily be analyzed by extending the developed sizing tool for landing purposes.

Some arguments regarding landing requirements can be made based on this research. It can be argued that for a certain wind speed the motor sizing is critical for take-off and therefore supporting a landing manoeuvre would only require extra battery capacity. The battery can be charged during the power generation phase for both take-off and landing. If the battery can also be charged on the ground, the battery is only required to be sized for landing or take-off, whichever is more critical. The argument that the take-off is critical for motor sizing is of course only valid if both take-off and landing have the same wind speed range requirement. This is something that needs to be considered when setting the wind speed requirement. Furthermore, it can be argued that landing can take place into the wind, which relaxed requirements on the motor and battery. Also, large part of the landing can be performed by sailing down as a normal sailplane.

Regarding the concept choice it should be analyzed if a rotor fixed at e.g. knee-sitter -30° or -45° , can also benefit from aerodynamic effects during landing. For the tilt-rotor, this is conceivable, as it can optimize the rotor tilt angle to benefit from aerodynamic forces, also during landing.

5

Sensitivity analysis

In previous section the results have been presented assuming design parameters and requirements that are regarded most suitable for the problem statement. Being a technology in an infant phase, there is much uncertainty however in the exact assumed values. Therefore, the sensitivity of these assumptions on the results is analyzed here in more detail. In Section 5.1 the effect of the assumptions on the VTOL system mass is analyzed. In Section 5.2 the effect of specific design parameters is analyzed. For the sensitivity analyses in Section 5.1 and 5.2, the most optimal condition is analyzed, which is reached with the tilt-rotor concept. In Section 5.3, the dynamic feasibility is checked for the tail-sitter, quad-plane and knee-sitter concept. Furthermore, the lowest elevation angle is taken (41.8°), as this approach is closest to the current practice of Makani and TwingTec. Parameters which are not mentioned to be varied are taken from the design parameter table (Table 3.6).

5.1. Effect of requirements

For the VTOL system sizing analysis, requirements were imposed as an input to the design model. These requirements include the minimum target height, minimum tether length and clearance height. In this section the effect of different requirements is analyzed.

5.1.1. Clearance height and non-tilting

The effect of varying clearance height is analyzed. In this analysis the tilt is kept fixed for the different segments of the flight path, that to better capture the effect of the clearance height requirement. In Figure 5.1, the VTOL system mass is plotted for different clearance height. It can be observed that the clearance height barely effects the VTOL system mass.

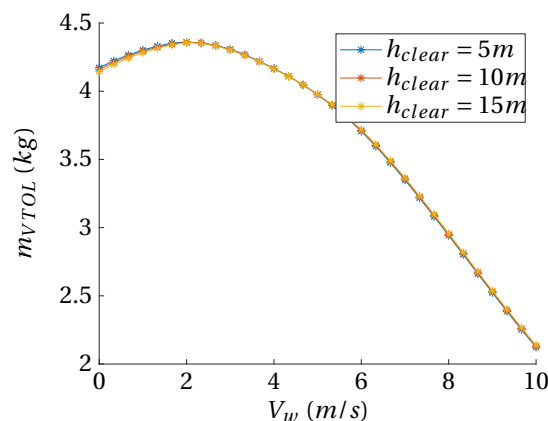


Figure 5.1: VTOL system mass vs. wind speed for different clearance height ($\theta_t = -41.8^\circ$)

5.1.2. Minimum height and tether length

In Chapter 4, the target height has been varied by varying the elevation angle between the minimum value given by the minimum height and perfect vertical take-off (90°). In this section the assumed minimum tether length is varied in 2 different ways. First variation will keep elevation constant as depicted in Figure 5.2a. The second variation will use the minimum height as is depicted in Figure 5.2b.

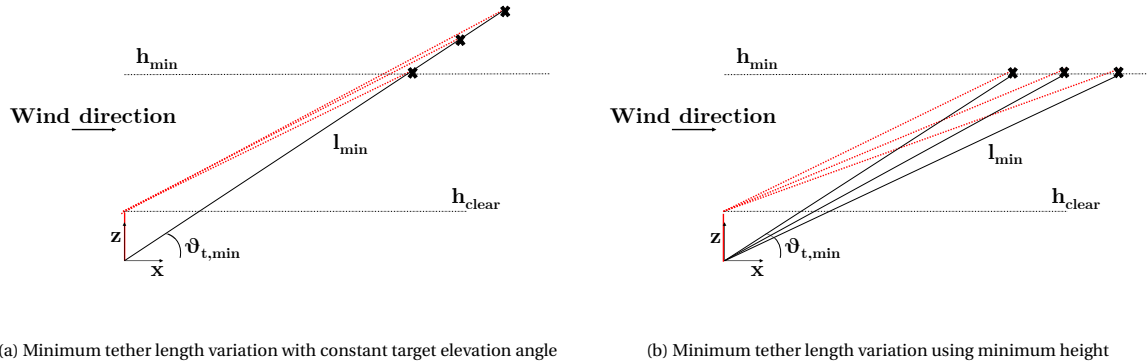


Figure 5.2

Variable set 1: System and component masses

The VTOL system mass for the 2 variations are plotted in Figure 5.3. For the first variation the plot is shifted up-ward. That means that the VTOL mass increases slightly with tether length at every winds speed. For the second variation the plot is shifted side-wards. This means that the VTOL mass actually decreases for low speeds. This is due to the fact that the tilt-rotor concept can exploit the aerodynamic force even at low wind by flying a negative angle of attack upside down (or similarly with nose heading down wind). For wind speeds higher than 3m/s, VTOL system mass increases with tether length, similar to the first variation. However, the increase in VTOL system mass seems to decrease with wind speed, which can not be observed in the first variation. Regarding component masses, both motor and battery mass increase with tether length for the first variation. For the second variation, there is no clear trend at speeds below 3 m/s. Furthermore, the battery mass increases while motor mass increases for wind speeds between 3-7 m/s, but slightly decrease at higher wind speeds.

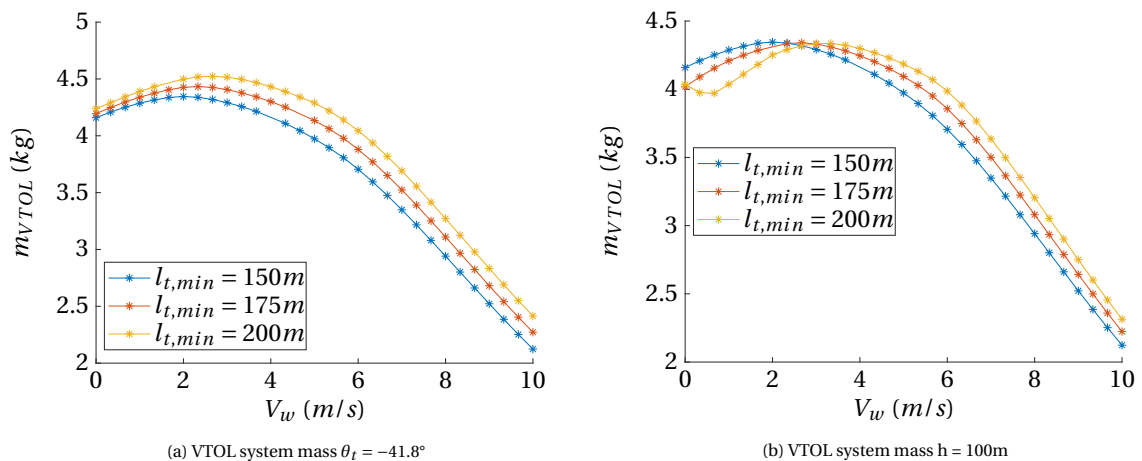


Figure 5.3: VTOL system vs. wind speed for minimum tether length

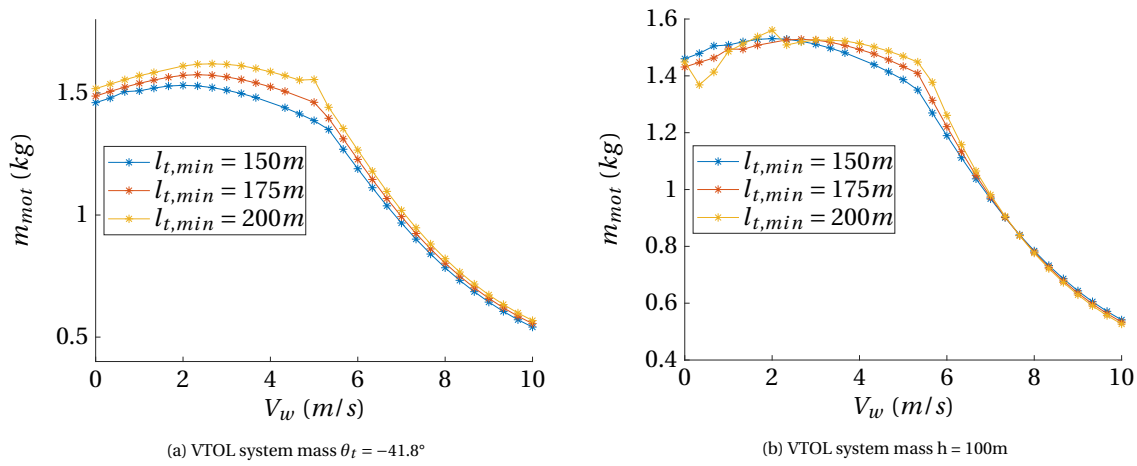


Figure 5.4: VTOL system vs. wind speed for minimum tether length

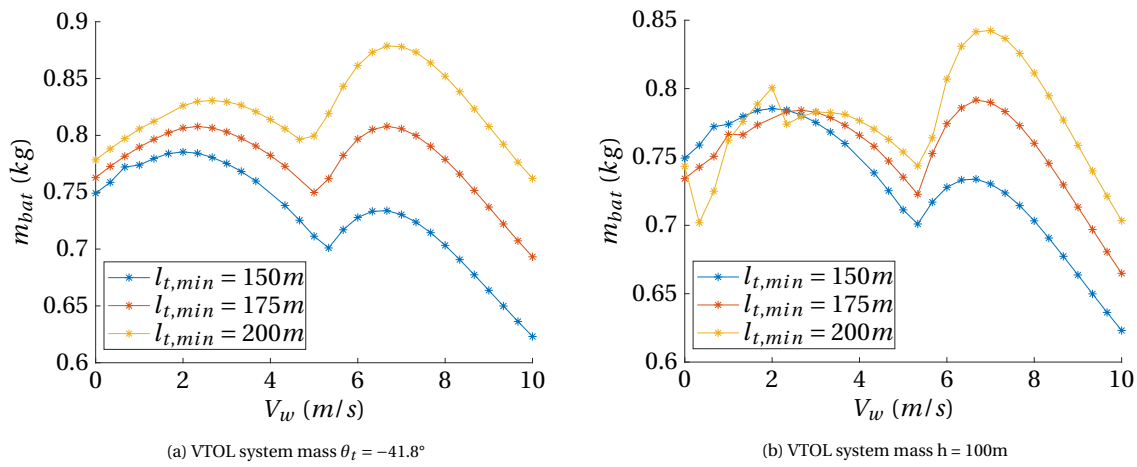


Figure 5.5: VTOL system vs. wind speed for minimum tether length

Variable set 2: Required thrust and power

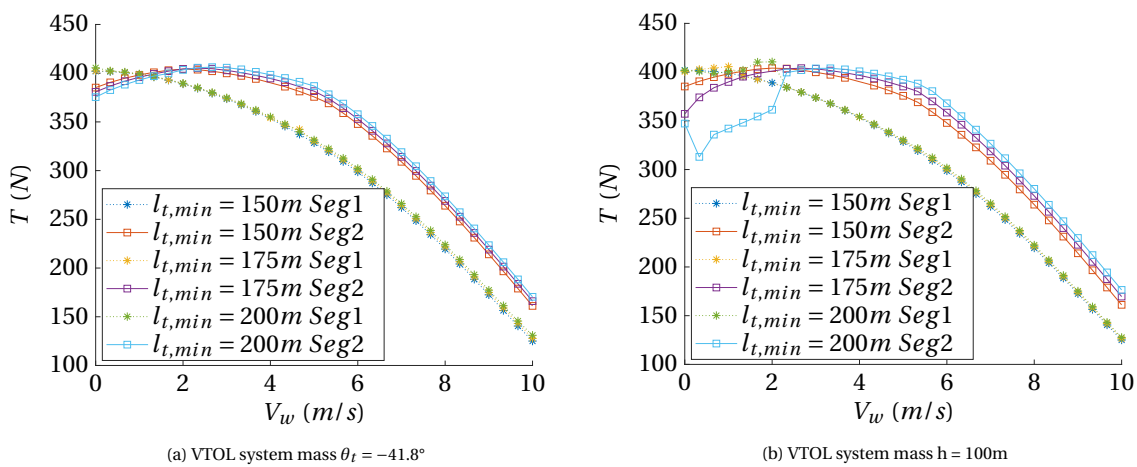


Figure 5.6: VTOL system vs. wind speed for minimum tether length

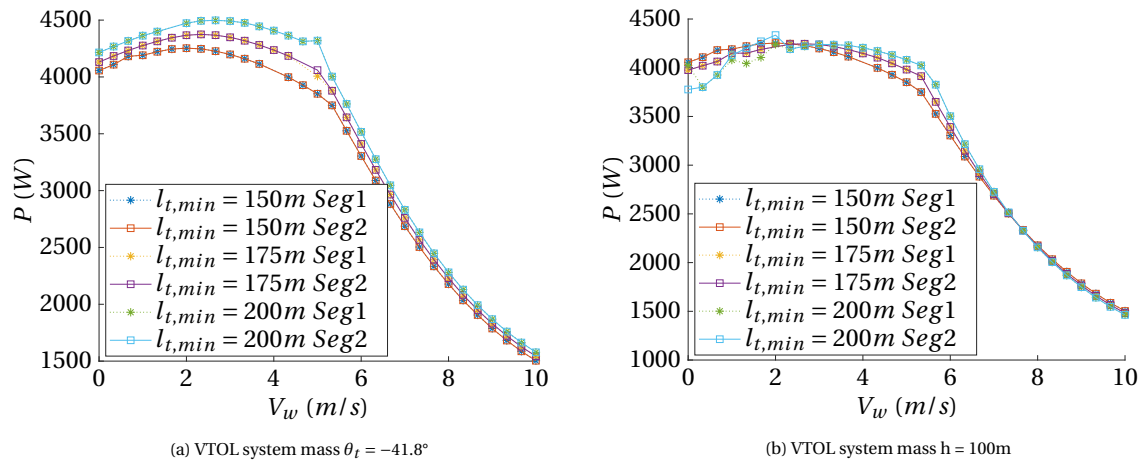


Figure 5.7: VTOL system vs. wind speed for minimum tether length

Variable set 3: Climb speed

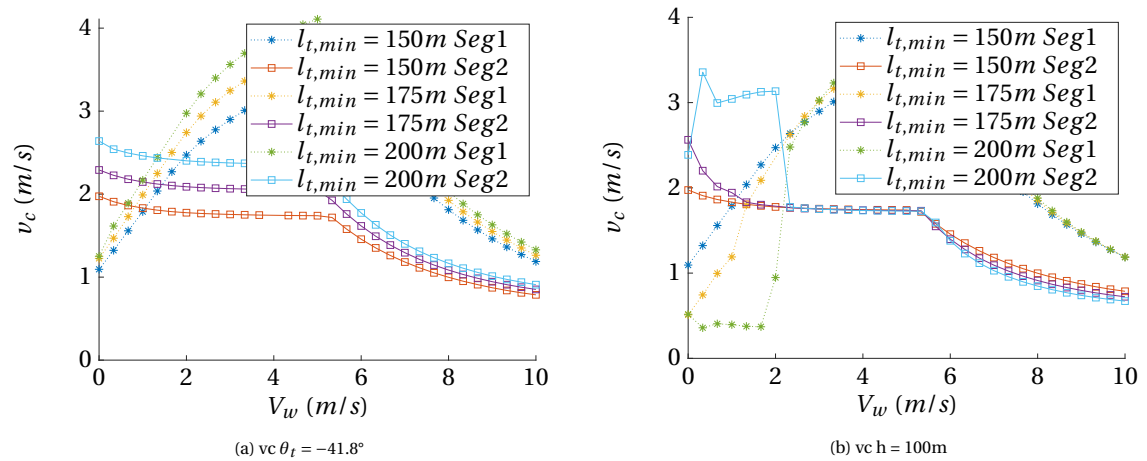


Figure 5.8: v_c vs. wind speed for minimum tether length

Variable set 4: Rotor pitch

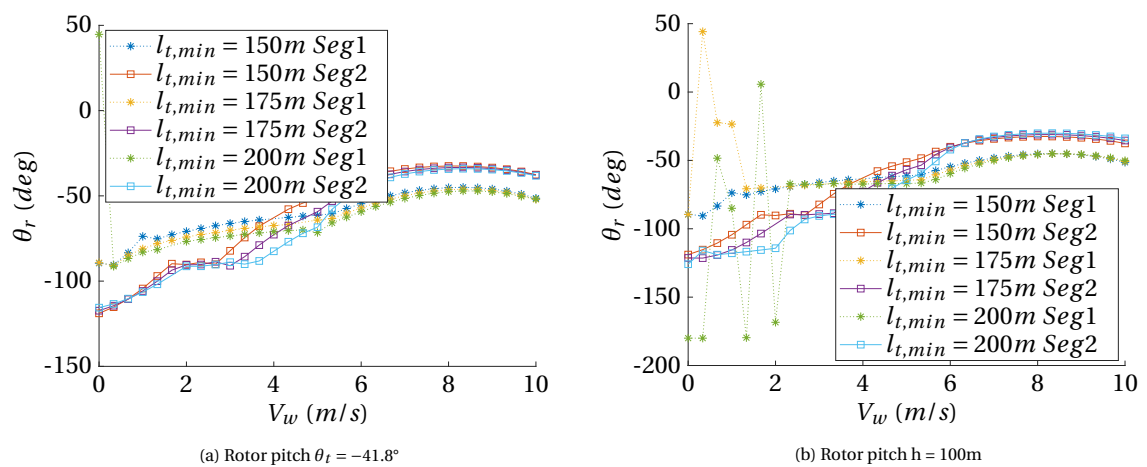


Figure 5.9: Rotor pitch vs. wind speed for minimum tether length

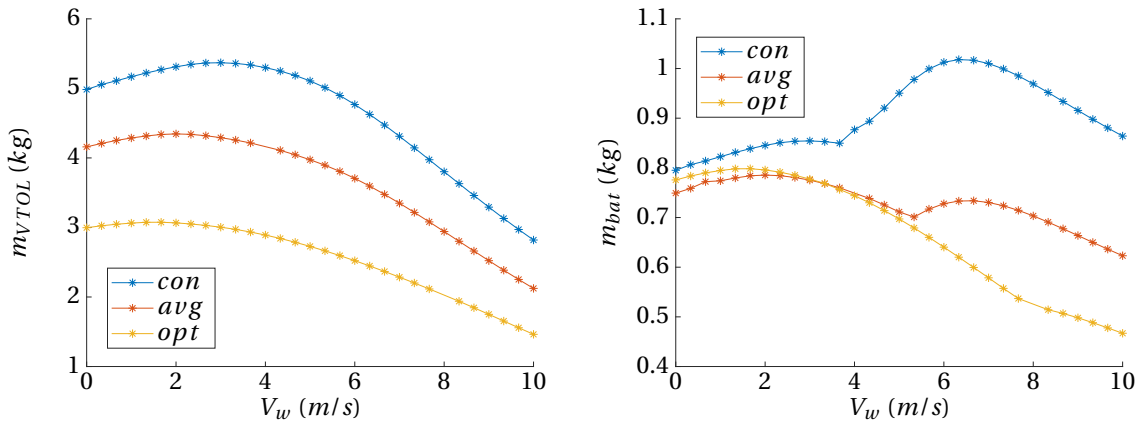
5.2. Effect of assumed design parameters

In this section the effect of varying selected key design parameters on the VTOL system mass is analyzed. The effect of using average, conservative or optimum values for rotor efficiency, specific energy of battery and specific motor power is first analyzed, followed by the specific power of the battery, rotor diameter and amount of rotors.

5.2.1. Average, optimal and conservative design parameters

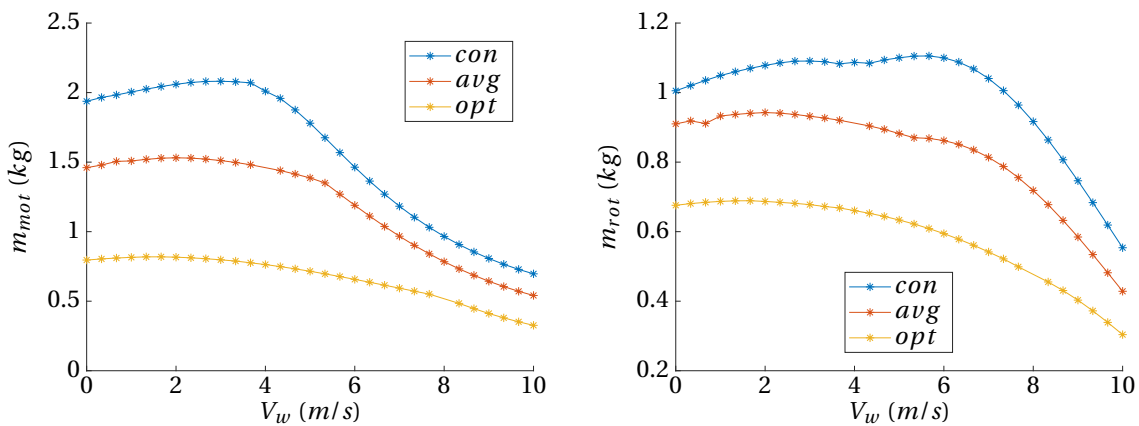
In this section, the effect of using average, conservative or optimum values for rotor efficiency, specific energy of battery and specific motor power is first analyzed. Their values are given in the design parameter table 3.6.

Variable set 1: System and component masses



(a) VTOL system mass vs. wind speed for different parameter assumptions (b) Battery mass vs. wind speed for different parameter assumptions

Figure 5.10



(a) Motor mass vs. wind speed for different parameter assumptions (b) Rotor mass vs. wind speed for different parameter assumptions

Figure 5.11

Variable set 2: Climb speed and rotor pitch

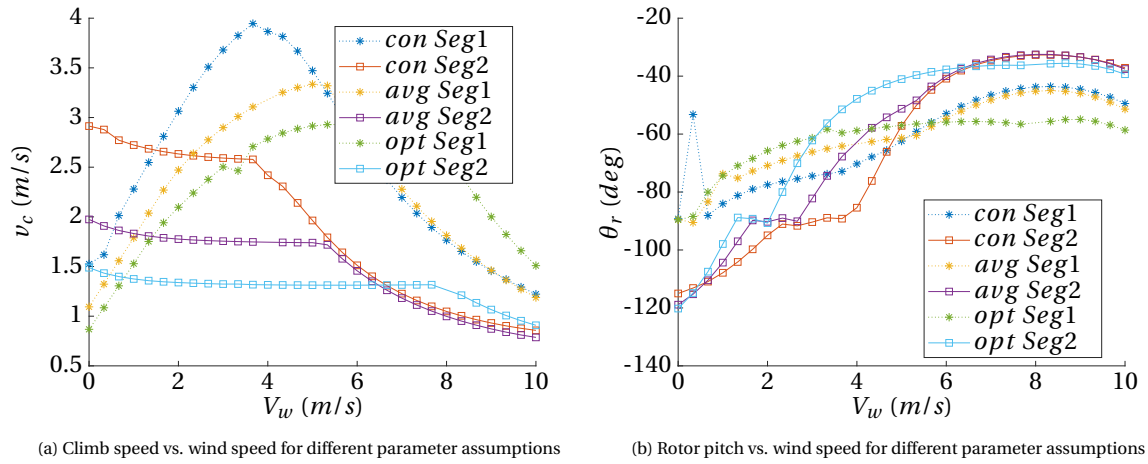


Figure 5.12

Variable set 3: Required power and rotor diameter

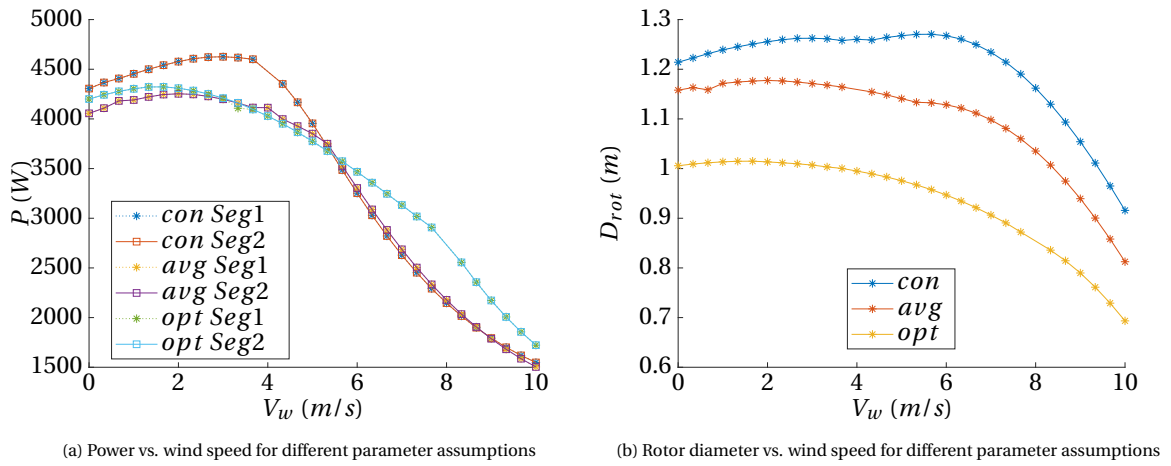


Figure 5.13

Variable set 3: Battery specific power and energy

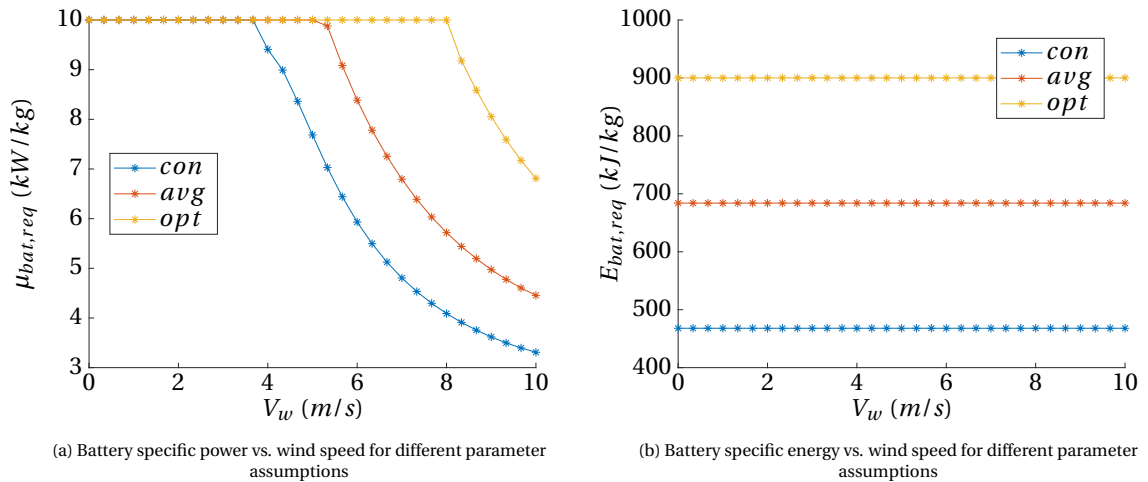


Figure 5.14

5.2.2. Battery specific power

The VTOL system mass is plotted for different battery specific power in Figure 5.15a. The effect of battery specific power is most pronounced at lower wind speeds, where the highest power is required. At speeds below 6 m/s the VTOL system mass increases with lower battery specific mass. The same counts for battery and rotor mass depicted in Figure 5.15b and 5.16b. It is now clear that the dent in battery mass is caused by the battery specific power. On the other hand, motor mass tends to decrease with battery specific power as the effect of power is more pronounced in battery mass.

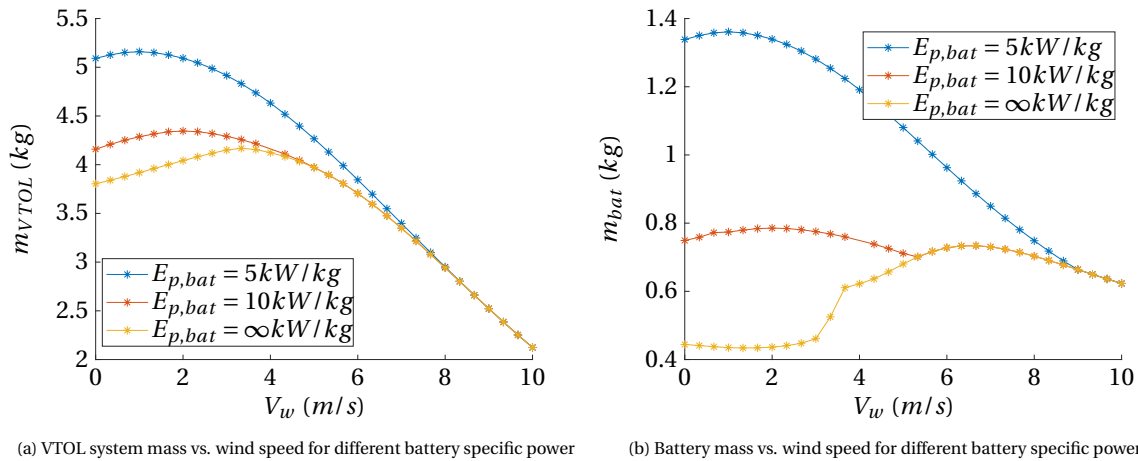


Figure 5.15

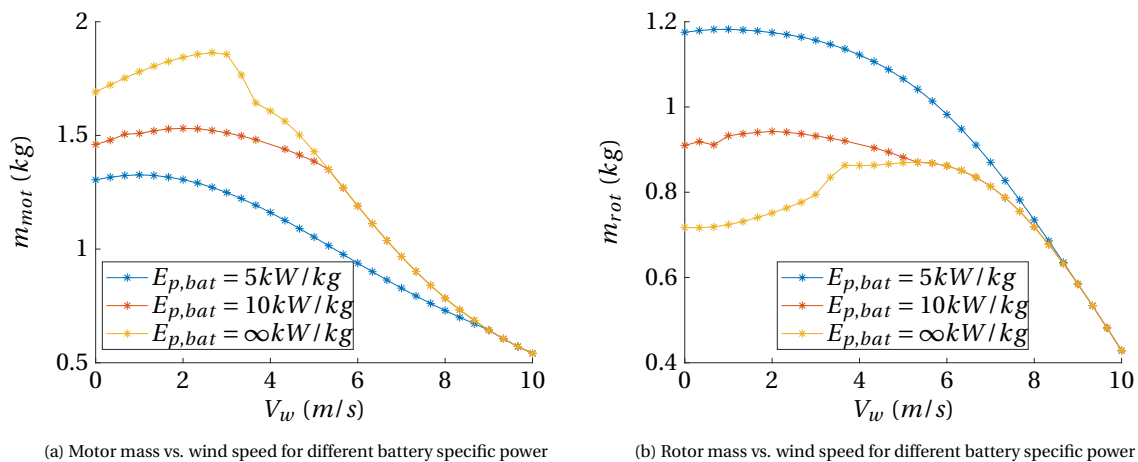


Figure 5.16

Climb speed is depicted in Figure 5.17a. One can observe an increasing climb speed with battery specific power. Regarding rotor pitch, depicted in Figure 5.17b (legend in 5.17a), there is an earlier tendency (lower wind speeds) for the rotor pitch to tilt to angles of -40 to -30 degrees for a limited battery specific power of 5 kW/kg. This result is in favor of the knee-sitter concept.

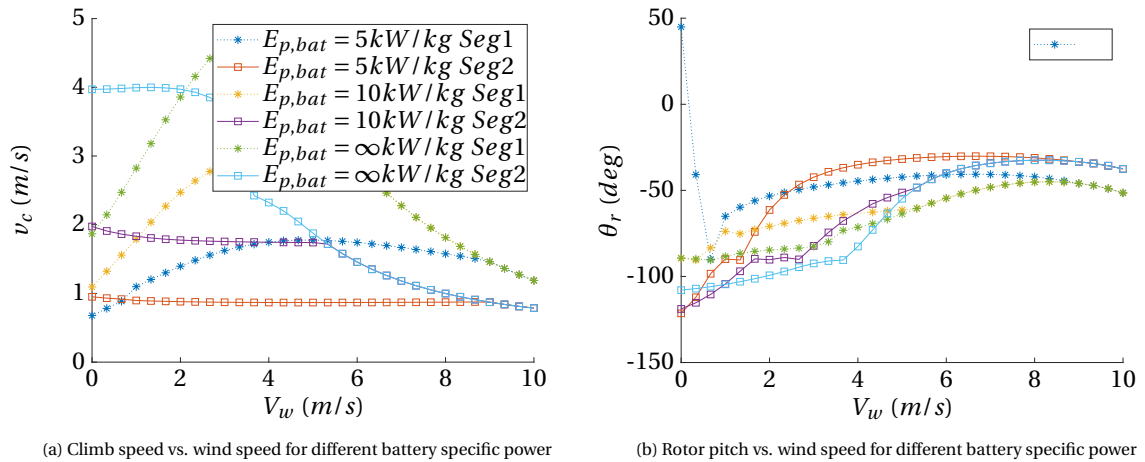


Figure 5.17

The required battery specific power is depicted in Figure 5.18a.

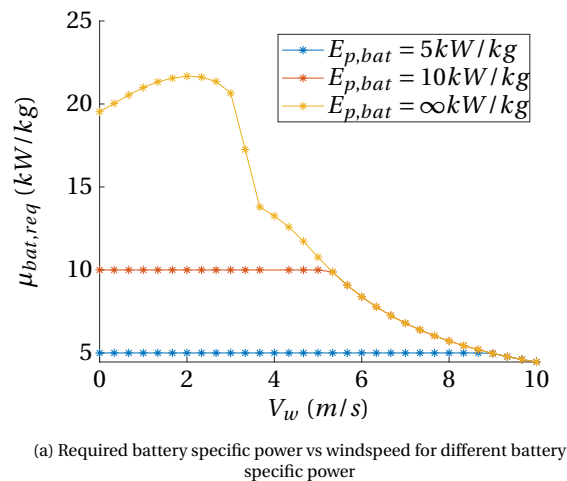
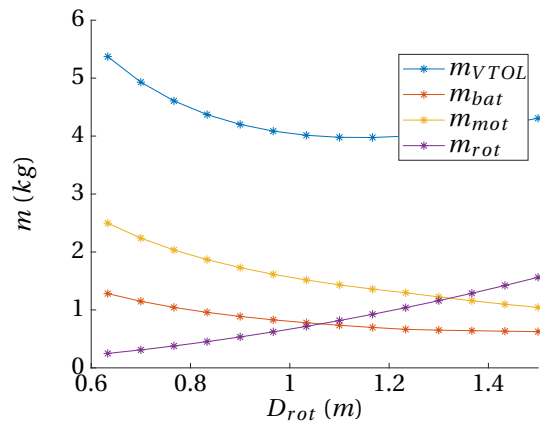


Figure 5.18

5.2.3. Rotor diameter

VTOL system mass and components are plotted against the rotor diameter in Figure 5.19a for a wind speed and target elevation angle of 5m/s and 41.8 degrees respectively. Because there is a decreasing trend in motor and battery mass with increasing rotor diameter and an increasing mass in rotor mass, there exists an optimum VTOL mass for a diameter. For the flight condition in this figure, the optimum is 1.15m. It should be noted however that smaller rotors are in general easier to integrate and require a smaller structure and hence more beneficial in terms of additional drag during power generation phase. From the figure it can be observed that lowering the rotor diameter to e.g 0.9m, results in a weight penalty of only 200 grams, but could mean a significant drag reduction. On the other hand, when lowering the diameter further the weight penalty starts to growing quicker.



(a) VTOL system and component mass vs rotor diameter ($V_w = 5\text{ m/s}, \theta_t = 41.8^\circ$)

Figure 5.19

5.2.4. Number of rotors

The VTOL system mass is plotted against wind speed for different amount of rotors in Figure 5.20. The VTOL system mass decreases with more rotors, but the effect is low. The system components share the same trend as with the VTOL system mass. The diameter of the rotor and total rotor area is plotted in Figure 5.21a and 5.21b respectively. Note that the total rotor diameter is constraint to 2m, which explains the deviating trend of the one (1) rotor case. The optimal rotor diameter decreases with increasing number of rotors. On the other hand the total rotor area increases with number of rotors.

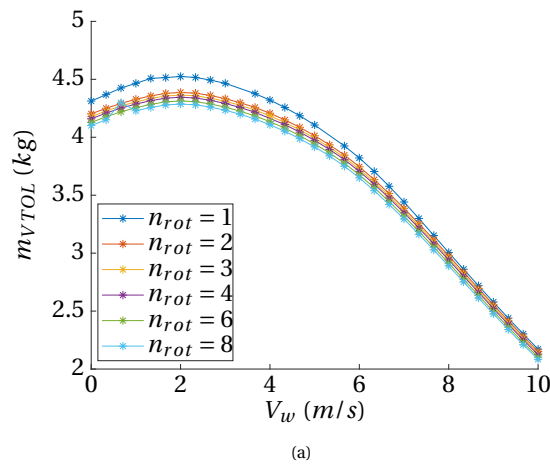


Figure 5.20: VTOL system mass vs. wind speed for different amount of rotors

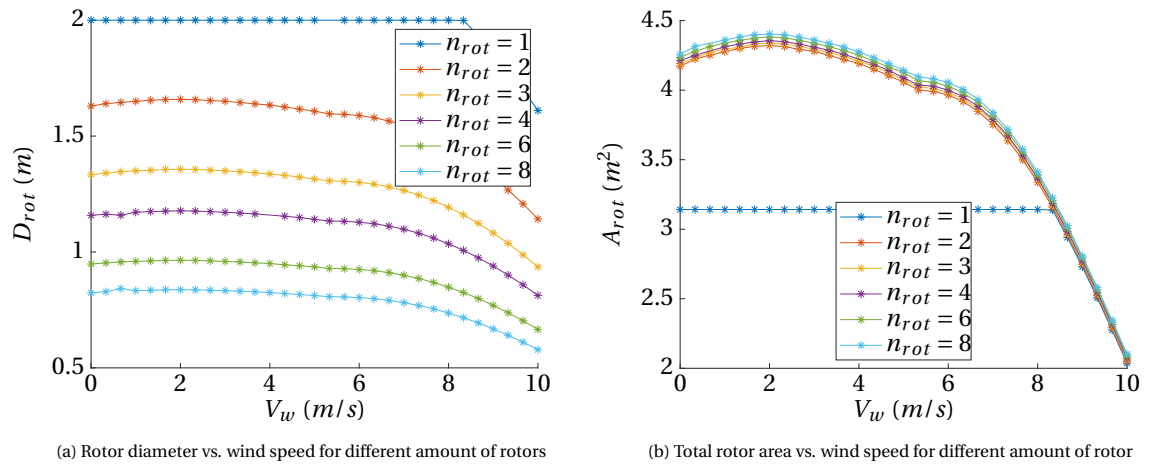


Figure 5.21

5.3. Dynamic feasibility results

In this section the results of the simulation model are given for 3 concepts; tail-sitter, quad-plane and knee-sitter. For each concept, a low wind condition (5m/s) and high wind condition (10 m/s) is simulated. For all conditions, the target elevation angle is set to 41.8°. The tuned controller parameters are given in Table 5.1. For all the concepts and wind conditions the results of the sizing and rotor design are given, simulation results and eventually a resizing of the battery is done based on the simulation. For the simulation results four (4) sets of variables sets are given; aircraft path and velocity (set 1), aircraft attitude and angle of attack of wing and rotor (set 2), rotor thrust and power (set 3) and the forces acting on the aircraft (set 4). For the thrust and power also the hover thrust and power are plotted in the graphs to serve as a reference, hover thrust is given by the total weight of the aircraft and hover power by the momentum equation for a hover condition:

$$P_{\text{hover}} = \kappa \sqrt{\frac{T_{\text{hover}}^3}{2\rho n_{\text{rot}}(D_{\text{rot}}/2)^2\pi}} \quad (5.1)$$

Furthermore, rotor induced power P_{ind} , total power P_{tot} and motor power P_E are plotted. Parameters that are not specifically mentioned are used from the design parameter Table 3.6 and simulator parameters are given in Section 3.8.

Table 5.1: Controller settings

D_{vt}	1.5 m
τ_r	1.4 s
K_P	2
K_I	1.5

After the simulation, a resizing calculation takes place. This takes into account the total energy consumed during the take-off simulation. The total energy is obtained by integrating the power signal over the take-off trajectory. The battery mass is calculated in the same way as the sizing tool (Equation 3.71). The resizing serves as a sensitivity analysis on the battery capacity resulting from the sizing model. Furthermore, the assumption of neglecting the profile power in the sizing tool is tested by running the simulation with (P_{tot}) and without including profile power (P_{ind}), and calculating the corresponding battery mass. Note that both total (P_{tot}) and induced (P_{ind}) power are given in the variable plots. Regarding the motor mass, it is found the maximum motor power (resulting from the sizing) is sufficient to successfully fulfill the take-off phase.

5.3.1. Tail-sitter concept

In this section simulation results for the tail-sitter concept are given for winds speeds of 5 m/s and 10 m/s.

A. $V_W = 5 \text{ m/s}$

Results sizing and rotor design

The sizing results and rotor design parameters for the tail-sitter concept which are used to validate the dynamic feasibility are given in Table 5.2.

Table 5.2: Results sizing and rotor design

Sizing		Rotor design and input sim.	
$m_{VTOL}[kg]$	4.3504	$P_{E,max}[W]$	$(4232.5377/n_{\text{rot}}) * f_{\text{control}}$
$m_{bat}[kg]$	0.78163	$T_{des}[N]$	$405.9227/n_{\text{rot}}$
$m_{mot}[kg]$	1.5237	$\alpha_{rot,des}[deg]$	51.7723
$m_{rot}[kg]$	0.95743	$J_p[kgm^2]$	0.0281
$v_{c,1}[m/s]$	1.7217	$\theta_0[deg]$	38.4848
$v_{x,1}[m/s]$	0	$K_T[]$	0.0105
$v_{c,2}[m/s]$	1.8401		
$v_{x,2}[m/s]$	2.2858		
$D_{rot}[m]$	1.1863		

Simulation results

Variable set 1: Flight path and velocity

Looking at the simulated flight path depicted in Figure 5.22a, it can be concluded that the flight path can be flown within the available power limit. The kinematic speed of the aircraft is depicted in Figure 5.22b. The controller is able to accurately track the reference speed. Due to the short time of the first segment, the target speed is met at the end of the segment. However, 80% of the target speed has been reached after 2 seconds. The speed components are depicted in Figure 5.23. For the transition from first to second segment some oscillation around the target speed can be observed. After about 15 seconds these are died out and the target speed is reached. The total take-off phase takes around 60 seconds.

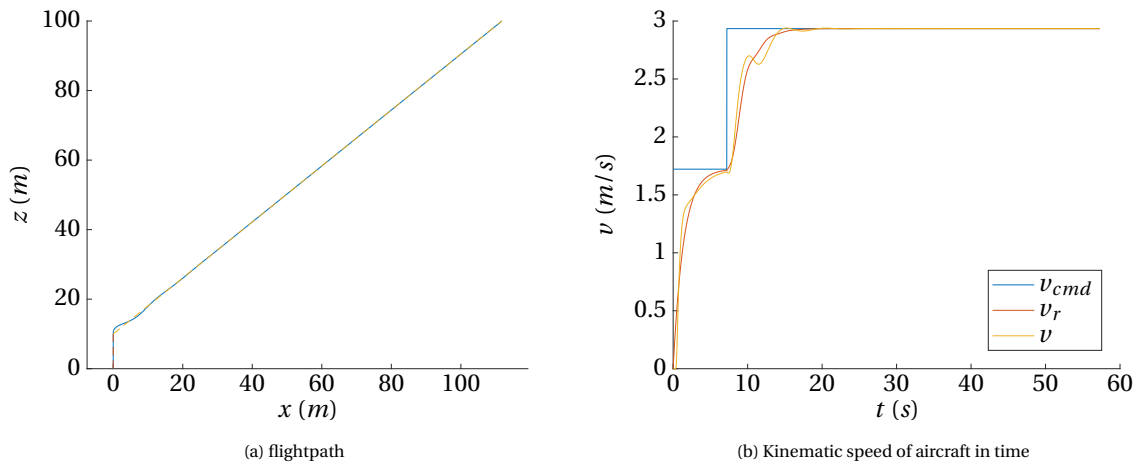


Figure 5.22

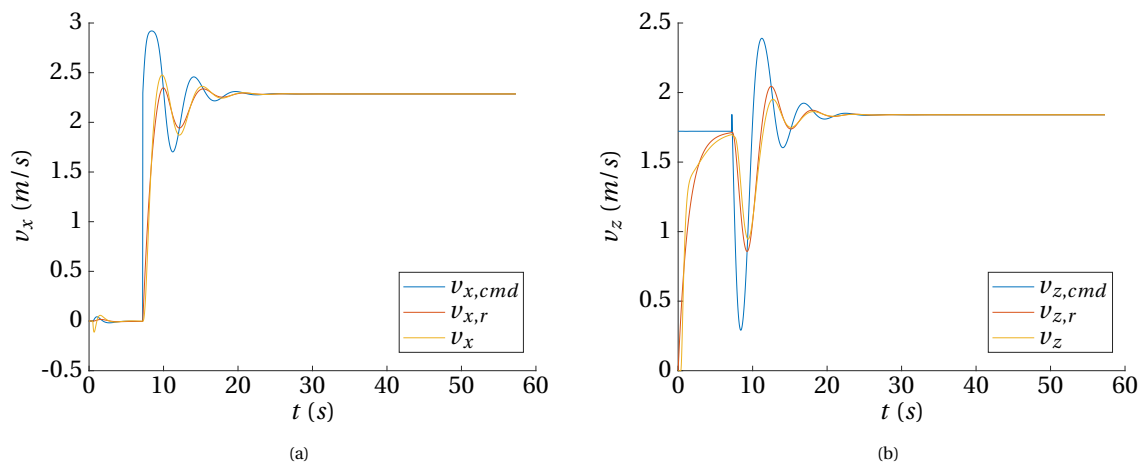


Figure 5.23: Kinematic speed components

Variable set 2: Aircraft attitude and angle of attack

The aircraft attitude and angle of attack of rotor and wing are depicted in Figure 5.24a and 5.24b, respectively. An initial θ of 90 degrees is commanded to tilt the aircraft upwards. Note that the initial θ is 0, so it first has to tilt, before it can take-off. In reality it is more likely, that the tail-sitter aircraft is already tilted upward. The aircraft quickly finds its "equilibrium" pitch angle of around 77 degrees with which it ascends for the first segment. Regarding angle of attack decreases from 72 degrees to 59 degrees while acceleration upwards. Note that for the tail-sitter the angle of both rotor and wing are the same. To transition from the first to second segment the aircraft increases pitch to come to an equilibrium pitch angle of 86 degrees. While doing so the angle of attack first increases to 70 degrees and then decreases to 52 degrees. As expected, the tail-sitter is operating in stalled condition all time.

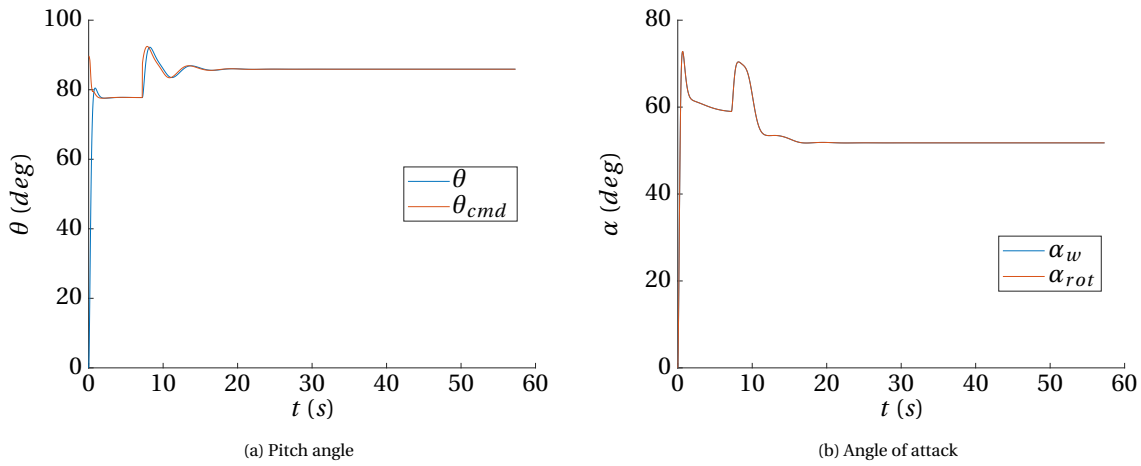


Figure 5.24

Variable set 3: Thrust and power

The aircraft thrust and power are depicted in Figure 5.25a and 5.25b, respectively. After the acceleration peak, where a maximum thrust of 488N is reached, the thrust drops to a value close to hover thrust, around 400N. When transitioning from first to second segment, there is a short oscillation in the thrust after which is reached again a value close to hover thrust. A similar behaviour exist for the power, but the power requirement is higher than hover power. With the simulation taken into account profile power, power increases by around 10% with respect to the induced power.

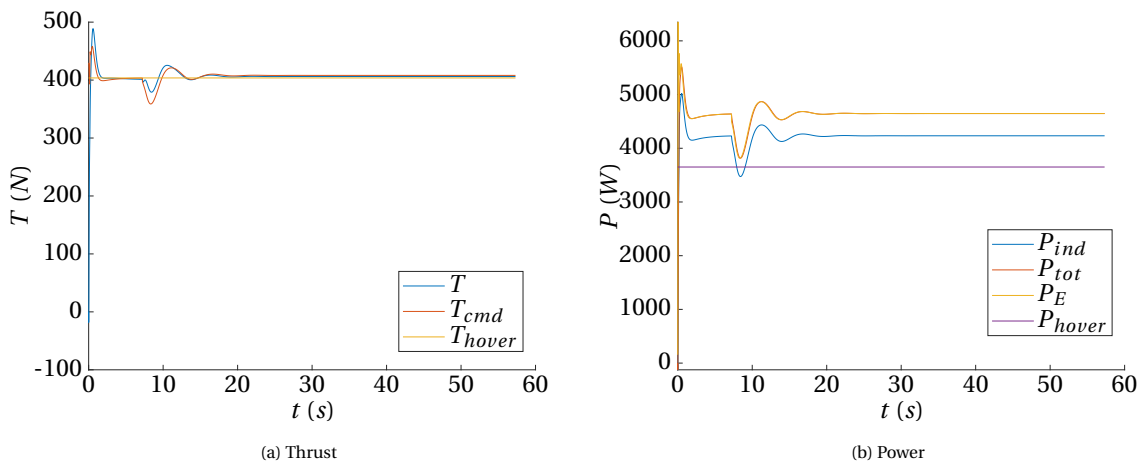


Figure 5.25

Variable set 4: Forces

The force components of aerodynamic force, gravity force, propulsion force and resulting force are depicted in Figure 5.26. The main forces acting are the gravity and propulsion forces. There is barely an aerodynamic lift force, but a significant amount of drag, especially for the first segment.

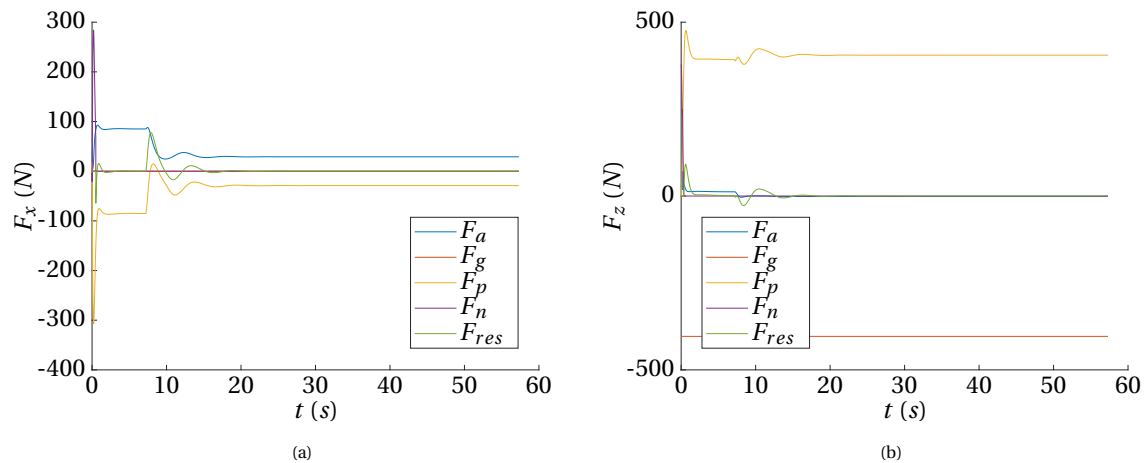


Figure 5.26: Component forces

Results resizing

A resized battery mass based on the simulation is given in Table 5.3. Here the mass of the battery is given for three (3) cases: as a result of the preliminary sizing, as a result of the simulation using the induced power and as a result of the simulation including the profile power. When the rotor profile power is neglected (P_{ind}), the battery mass increases with 4.5% compared to the sizing result. Extra power is required during the transient and acceleration phase. Furthermore, the take-off phase takes also longer due to the acceleration time and requires more energy. Nevertheless, 4.5% is low and can be justifiably neglected in the preliminary sizing when including a safety factor. When including profile power in the simulation the battery mass increases with 14.7% compared to the sizing result. Hence an additional 10.2% due to the profile power. Compared to the safety factor ($f_{control}$) of 50% that is taken into account in the preliminary sizing, this is acceptably low and can be neglected in the preliminary design phase.

Table 5.3: Resizing based on simulation

	Preliminary sizing	Simulation (P_{ind})	Simulation (P_{tot})
m_{bat}	0.78163kg	0.8165kg (+4.5%)	0.8962kg (+14.7%)

B. $V_W = 10$ m/s

Results sizing and rotor design

The sizing results and rotor design parameters for the tail-sitter concept which are used to validate the dynamic feasibility are given in Table 5.4.

Table 5.4: Results sizing and rotor design

Sizing		Rotor design and input sim.	
$m_{VTOL}[kg]$	4.87	$P_{E,max}[W]$	$(5171.5808/n_{rot}) * f_{control}$
$m_{bat}[kg]$	0.995	$T_{des}[N]$	$399.7988/n_{rot}$
$m_{mot}[kg]$	1.8618	$\alpha_{rot,des}[deg]$	50.95
$m_{rot}[kg]$	0.83565	$J_p[kgm^2]$	0.0215
$v_{c,1}[m/s]$	0.64664	$\theta_0[deg]$	39.0909
$v_{x,1}[m/s]$	0	$K_T[]$	0.0077
$v_{c,2}[m/s]$	2.2927		
$v_{x,2}[m/s]$	2.8481		
$D_{rot}[m]$	1.112		

Simulation results

Variable set 1: Flight path and velocity

Looking at the simulated flight path depicted in Figure 5.27a, it can be concluded that the flight path can be flown within the available power limit. The kinematic speed of the aircraft is depicted in Figure 5.27b. The controller is able to accurately track the reference speed. Due to the low climb speed in the first segment, the target speed can already be tracked after a few seconds. The speed components are depicted in Figure 5.28. For the transition from first to second segment some oscillation around the target speed can be observed. After about 15 seconds these are died out and the target speed is reached. Due to the lower climb speed in the first segment, there is also less overshoot during transition as compared to the 5 m/s wind speed condition. The total take-off phase takes around 60 seconds.

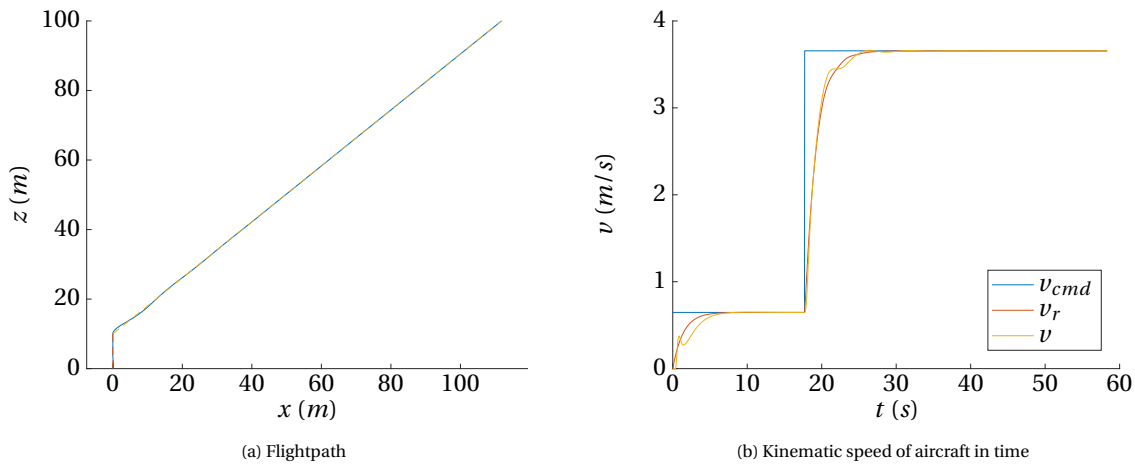


Figure 5.27

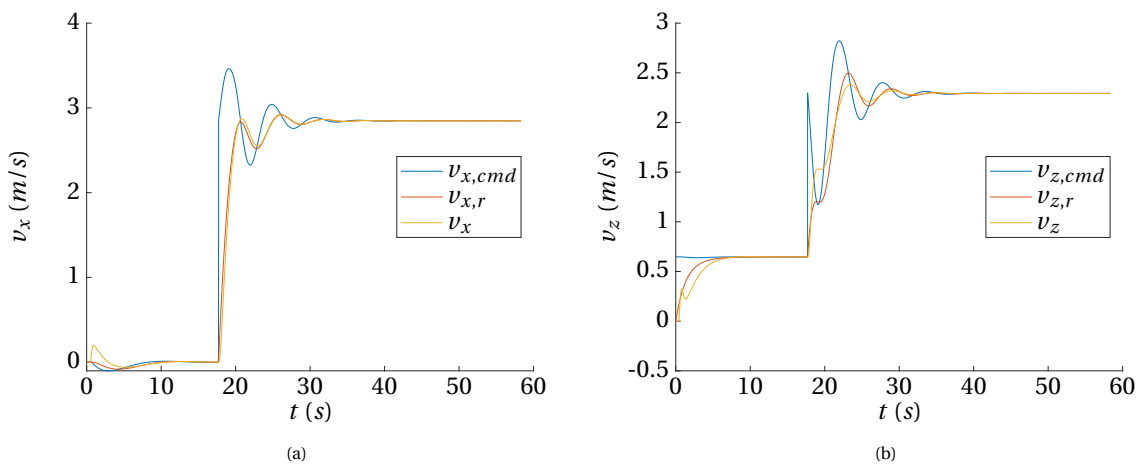


Figure 5.28: Kinematic speed components

Variable set 2: Aircraft attitude and angle of attack

The aircraft attitude and angle of attack of rotor and wing are depicted in Figure 5.29a and 5.29b, respectively. An initial θ of 90 degrees is commanded to tilt the aircraft upwards. The aircraft quickly finds a steady pitch angle of around 52 degrees with which it ascends for the first segment. Due to the high wind speed, this is much lower as compared to the low wind speed. Regarding angle of attack decreases from 56 degrees to 48.71 degrees while acceleration upwards. Note that for the tail-sitter the angle of both rotor and wing are the same. During the transition from the first to second segment the aircraft increases pitch to come to an equilibrium pitch angle of 67 degrees. While doing so the angle of attack first increases to 57 degrees and then decreases to 50 degrees. As expected, the tail-sitter is operating in stalled condition all time. Comparing this with the lower wind speed, the pitch dynamics are much milder, and the range of angle of attack at which the tail-sitter

is operating is much smaller.

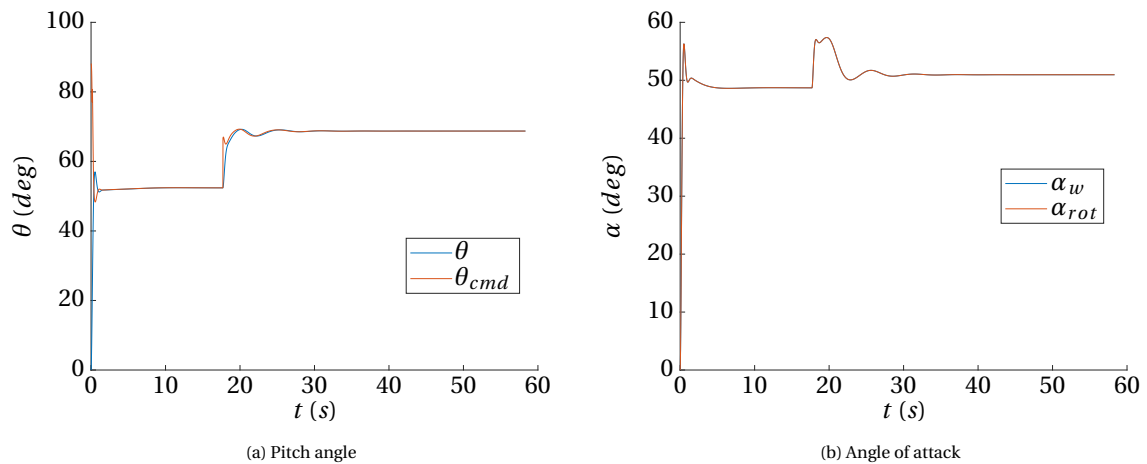


Figure 5.29

Variable set 3: Thrust and power

The aircraft thrust and power are depicted in Figure 5.30a and 5.30b, respectively. After the acceleration peak, where a maximum thrust of 380N is reached, the thrust drops slightly to a value close to hover thrust, around 360N. These are lower values as compared to the lower wind speed condition. The difference between commanded thrust T_{cmd} and obtained thrust T , arises due to the difference rotor model to map thrust to angular speed, and to calculate thrust from the angular speed. When transitioning from first to second segment, there is a short oscillation in the thrust after which it reaches again a value close to hover thrust. A similar behaviour exist for the power, but the power requirement is higher than hover power. And taken into account profile power, power increases by around 9% with respect to the induced power. During the transient and acceleration phase, power does not increase significantly as compared to the steady state.

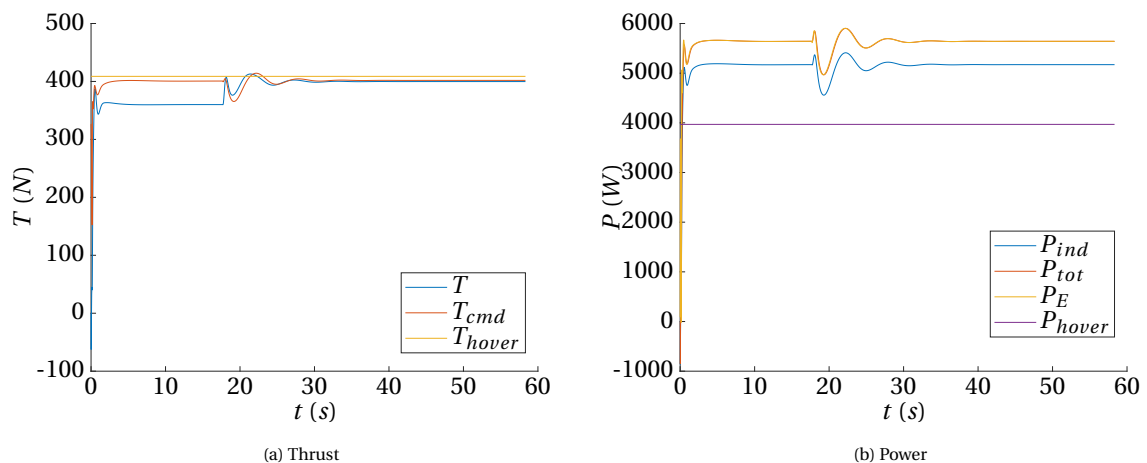


Figure 5.30

Variable set 4: Forces

The force components of aerodynamic force, gravity force, propulsion force and resulting force are depicted in Figure 5.31. The main forces acting are the gravity and propulsion forces, aerodynamic lift (first segment) and aerodynamic drag ($F_{a,x}$) (both segments).

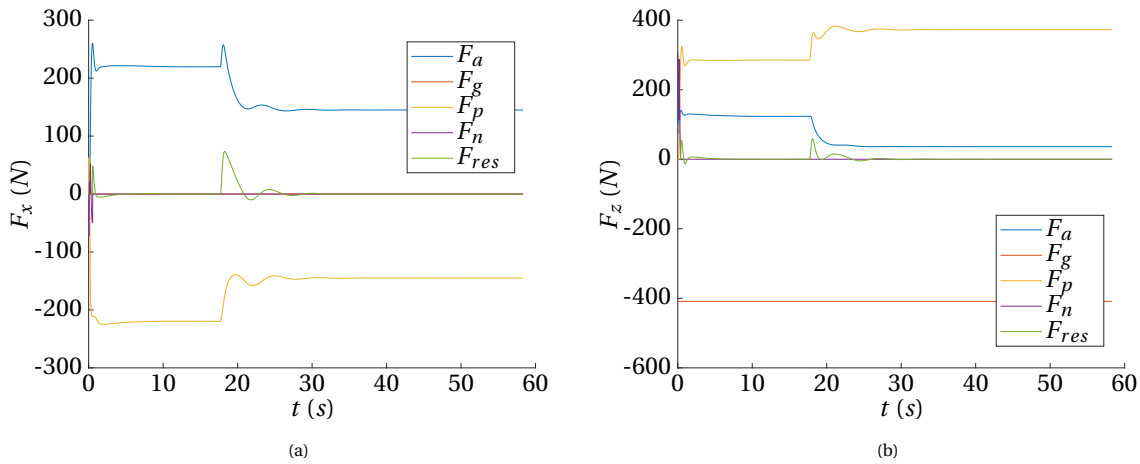


Figure 5.31: Component forces

Results resizing

A resized battery mass based on the simulation is given in Table 5.5. Here the mass of the battery is given for three (3) cases: as a result of the preliminary sizing, as a result of the simulation using the induced power and as a result of the simulation including the profile power. When the rotor profile power is neglected (P_{ind}), the battery mass increases with 1.7% compared to the sizing result. This is lower compared to the simulation with wind speed 5m/s. This is explained by the fact that the power does not increase much above the steady state value for the transient phase. 1.7% is low and can be justifiably neglected in the preliminary sizing when including a safety factor. When including profile power in the simulation the battery mass increases with 11% compared to the sizing result. Hence an additional 9.3% due to the profile power. Compared to the safety factor ($f_{control}$) of 50% that is taken into account in the preliminary sizing, this is acceptably low and can be neglected in the preliminary design phase.

Table 5.5: Resizing based on simulation

	Preliminary sizing	Simulation (P_{ind})	Simulation (P_{tot})
m_{bat}	0.995kg	1.0123kg (+1.7%)	1.1041kg (+11%)

5.3.2. Quad-plane concept

In this section simulation results for the quad-plane concept will be given for winds speeds of 5 m/s and 10m/s.

A. $V_W = 5$ m/s

Results sizing and rotor design

The sizing results and rotor design parameters for the quad-plane concept which are used to validate the dynamic feasibility are given in Table 5.6.

Table 5.6: Results sizing and rotor design

Sizing		Rotor design and input sim.	
$m_{VTOL}[kg]$	4.5151	$P_{E,max}[W]$	$(4348.7608/n_{rot}) * f_{control}$
$m_{bat}[kg]$	1.5656	$T_{des}[N]$	$423.7985/n_{rot}$
$m_{mot}[kg]$	0.8031	$\alpha_{rot,des}[deg]$	53.4042
$m_{rot}[kg]$	1.0176	$J_p[kgm^2]$	0.0316
$v_{c,1}[m/s]$	1.3686	$\theta_0[deg]$	38.4848
$v_{x,1}[m/s]$	0	$K_T[]$	0.0118
$v_{c,2}[m/s]$	1.8982		
$v_{x,2}[m/s]$	2.3581		
$D_{rot}[m]$	1.2213		

Simulation results

Variable set 1: Flight path and velocity

Looking at the simulated flight path depicted in Figure 5.32a, it can be concluded that the flight path can be flown within the available power limit. The kinematic speed of the aircraft is depicted in Figure 5.32b. The speed components are depicted in Figure 5.33. For the transition from first to second segment some oscillation around the target speed can be observed. After about 10 seconds these are died out and the target speed is reached.

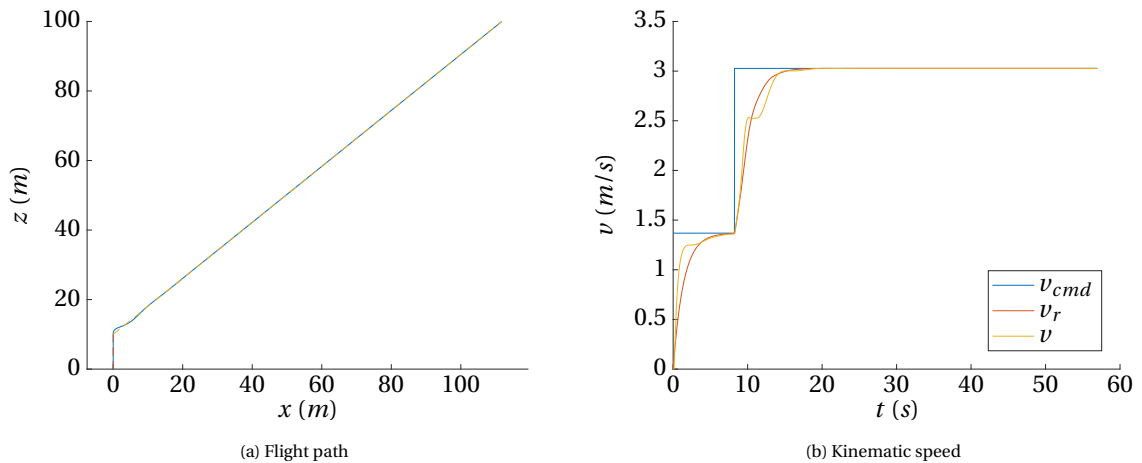


Figure 5.32

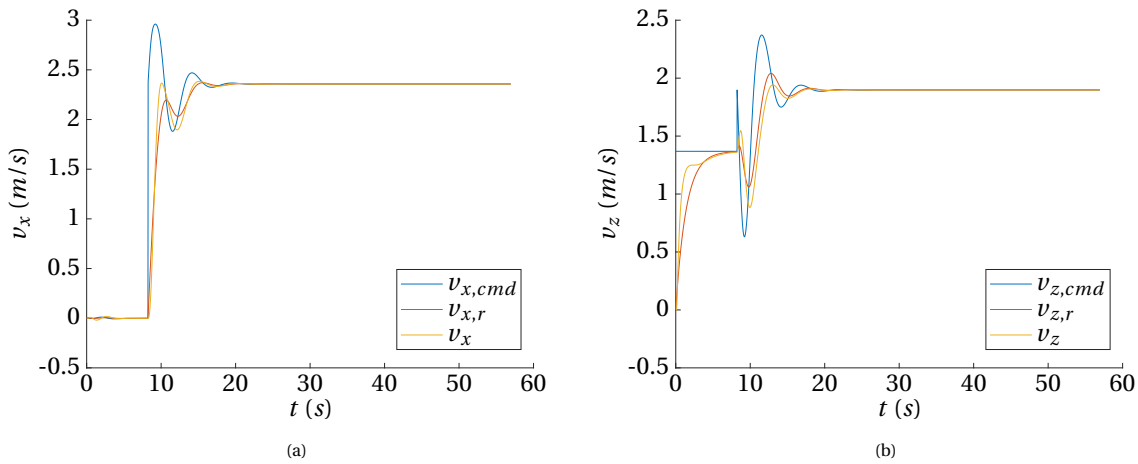


Figure 5.33: Kinematic speed components

Variable set 2: Aircraft attitude and angle of attack

The aircraft attitude and angle of attack of rotor and wing are depicted in Figure 5.34a and 5.34b, respectively. The aircraft takes off with 0 degree pitch attitude in the first segment. During the acceleration upward, the angle of attack decreases to -15°. Then, during the transition from first to second segment, aircraft pitches up to accelerate backwards. This is accompanied with a short increase in angle of attack after which it decreases to -37 degrees. The total duration of the take-off phase is around 60 seconds.

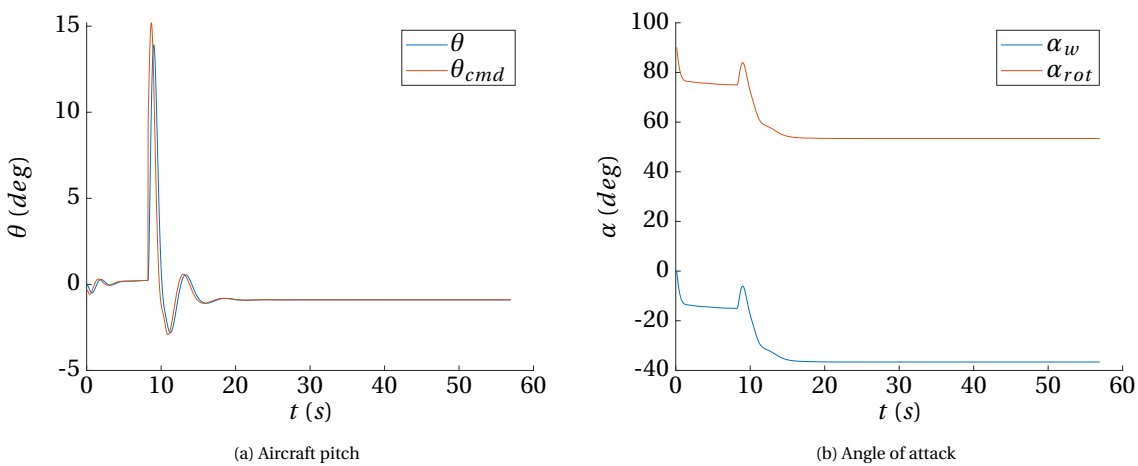


Figure 5.34

Variable set 3: Thrust and power

The aircraft thrust and power are depicted in Figure 5.35a and 5.35b, respectively. Thrust is quite constant during the first segment, than drops when the aircraft pitches up to transition and increases again in steady state flight. The first segment requires more thrust. The behaviour of the power is similar after a short peak to wind up the rotors. The power requirement when steady state is reached is the same for both segments.

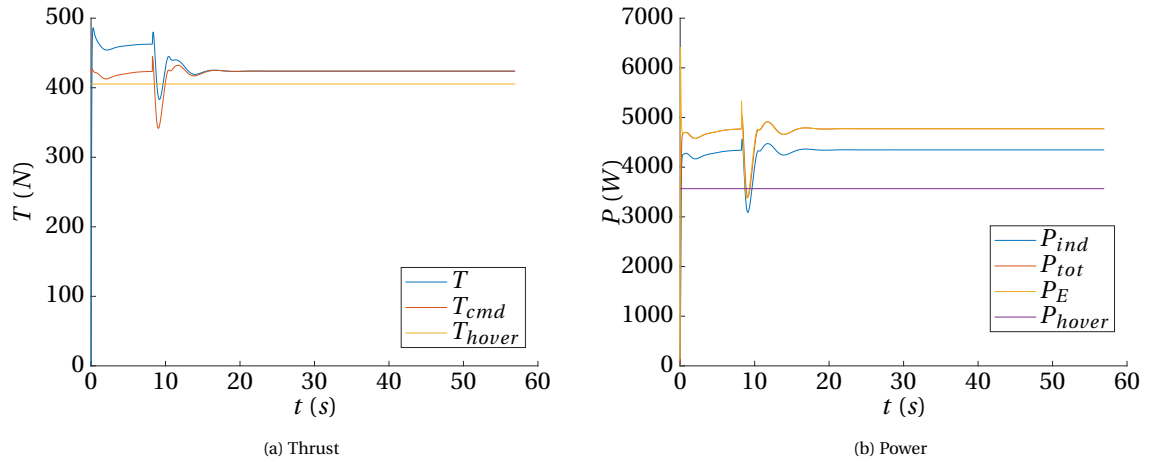


Figure 5.35

Variable set 4: Forces

The force components of aerodynamic force, gravity force, propulsion force and resulting force are depicted in Figure 5.36. The main forces acting are the gravity and propulsion forces. Aerodynamic forces are low.

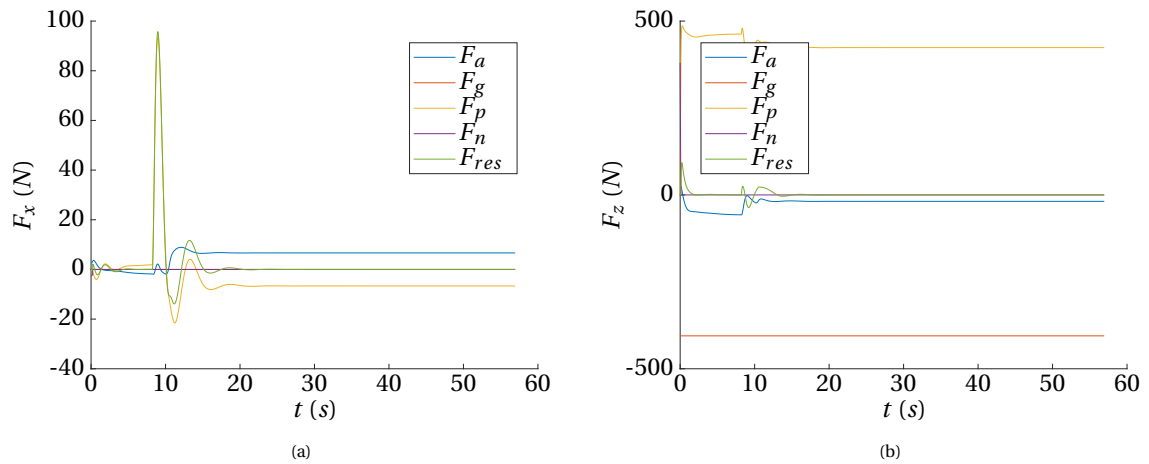


Figure 5.36: Component forces

Results resizing

A resized battery mass based on the simulation is given in Table 5.7. Here the mass of the battery is given for three (3) cases: as a result of the preliminary sizing, as a result of the simulation using the induced power and as a result of the simulation including the profile power. When the rotor profile power is neglected (P_{ind}), the battery mass increases with 3.3% compared to the sizing result. Extra power is required during the transient and acceleration phase. Furthermore, the take-off phase takes also longer due to the acceleration time and requires more energy. Nevertheless, 3.3% is low and can be justifiably neglected in the preliminary sizing when including a safety factor. When including profile power in the simulation the battery mass increases with 13.4% compared to the sizing result. Hence an additional 10.1% due to the profile power. Compared to the safety factor ($f_{control}$) of 50% that is taken into account in the preliminary sizing, this is acceptably low and can be neglected in the preliminary design phase.

Table 5.7: Resizing based on simulation

	Preliminary sizing	Simulation (P_{ind})	Simulation (P_{tot})
m_{bat}	0.8031kg	0.8294kg (+3.3%)	0.9106kg (+13.4%)

B. $V_W = 10 \text{ m/s}$ **Results sizing and rotor design**

The sizing results and rotor design parameters for the quad-plane concept which are used to validate the dynamic feasibility are given in Table 5.8.

Table 5.8: Results sizing and rotor design

Sizing		Rotor design and input sim.	
$m_{VTOL}[kg]$	4.3376	$P_{E,max}[W]$	$(2613.7259/n_{rot}) * f_{control}$
$m_{bat}[kg]$	1.0608	$T_{des}[N]$	$424.5613/n_{rot}$
$m_{mot}[kg]$	0.94094	$\alpha_{rot,des}[deg]$	83.1241
$m_{rot}[kg]$	1.2514	$J_p[kgm^2]$	0.0474
$v_{c,1}[m/s]$	0.87366	$\theta_0[deg]$	30.3
$v_{x,1}[m/s]$	0	$K_T[]$	0.0128
$v_{c,2}[m/s]$	0.82708		
$v_{x,2}[m/s]$	1.0274		
$D_{rot}[m]$	1.3482		

Simulation results**Variable set 1: Flight path and velocity**

Looking at the simulated flight path depicted in Figure 5.37a, it can be concluded that the flight path can be flown within the available power limit. The kinematic speed of the aircraft is depicted in Figure 5.37b. The speed components are depicted in Figure 5.38b. For the transition from first to second segment some oscillation around the target speed can be observed. After about 10 seconds these are died out and the target speed is reached. The total take-off phase takes around 120 seconds.

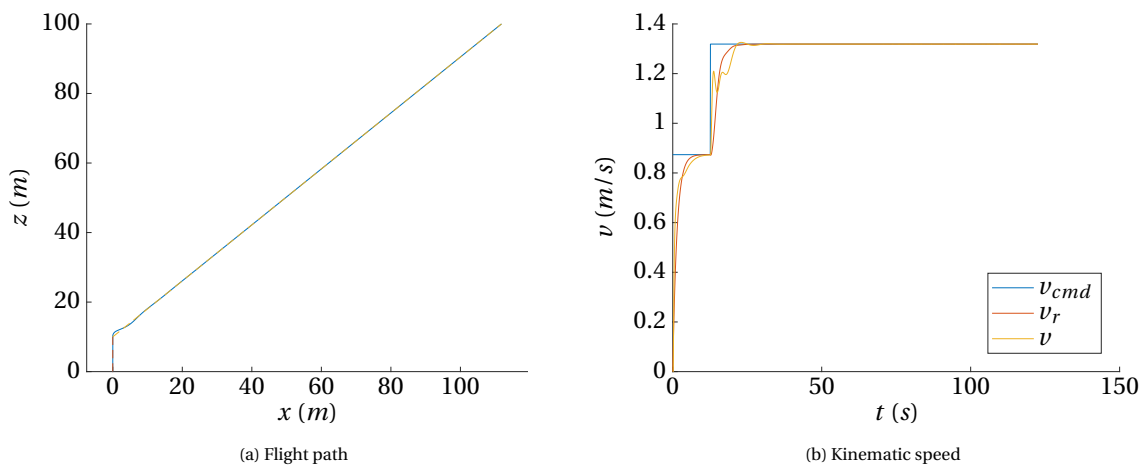


Figure 5.37

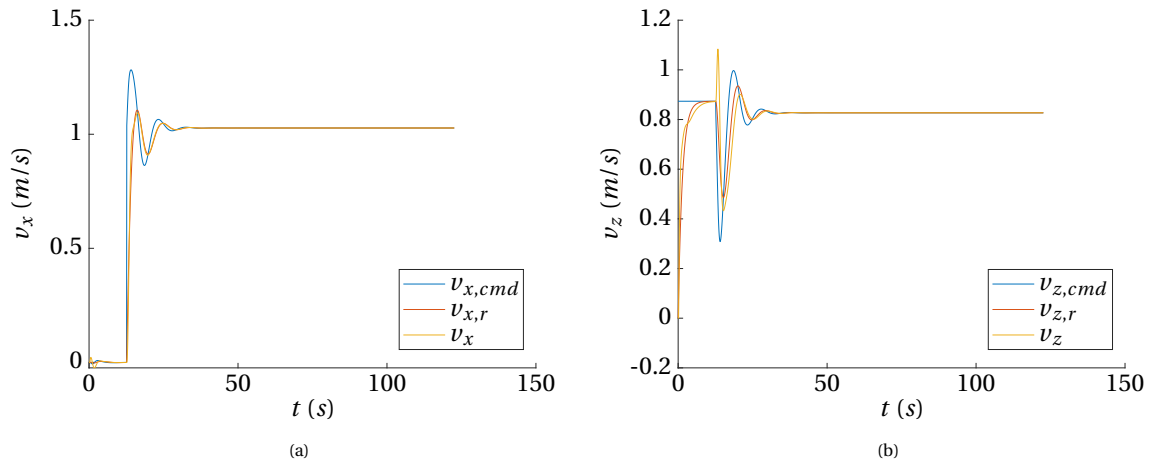


Figure 5.38: Kinematic speed components

Variable set 2: Aircraft attitude and angle of attack

The aircraft attitude and angle of attack of rotor and wing are depicted in Figure 5.39a and 5.39b, respectively. The behaviour of both pitch and angle of attack are similar to the low wind speed simulation, but now the magnitude by which they vary are much smaller. The angle of attack does not go below -8 degrees.

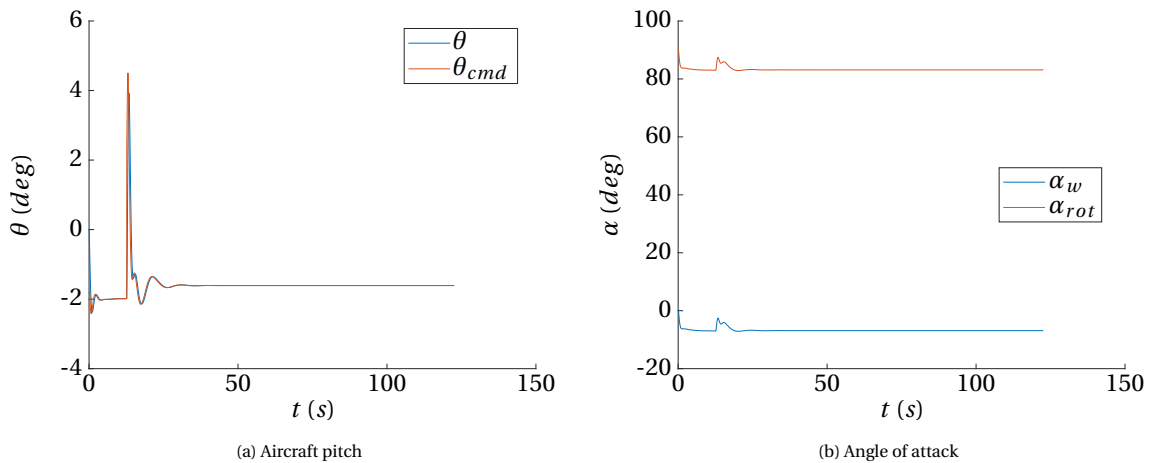


Figure 5.39

Variable set 3: Thrust and power

The aircraft thrust and power are depicted in Figure 5.40a and 5.40b, respectively. Thrust is found slightly higher than hover thrust throughout the simulation, with a drop occurring when pitching up for the transition. The behaviour of the power is similar after a short peak to wind up the rotors. The power requirement when steady state is reached is the same for both segments. The profile drag is remarkably higher by adding an additional 24 % to the power requirement.

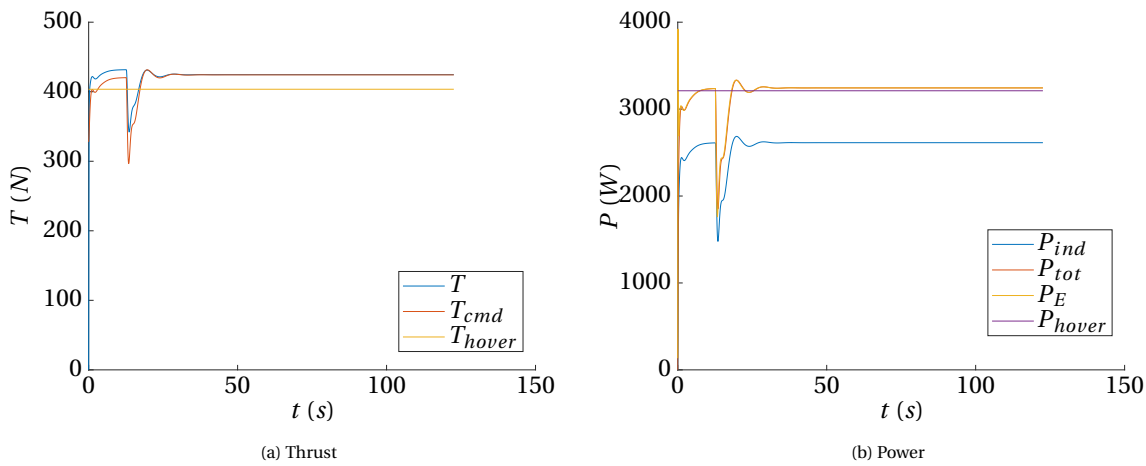


Figure 5.40

Variable set 4: Forces

The force components of aerodynamic force, gravity force, propulsion force and resulting force are depicted in Figure 5.36. The main forces acting are the gravity and propulsion forces. Aerodynamic forces are low.

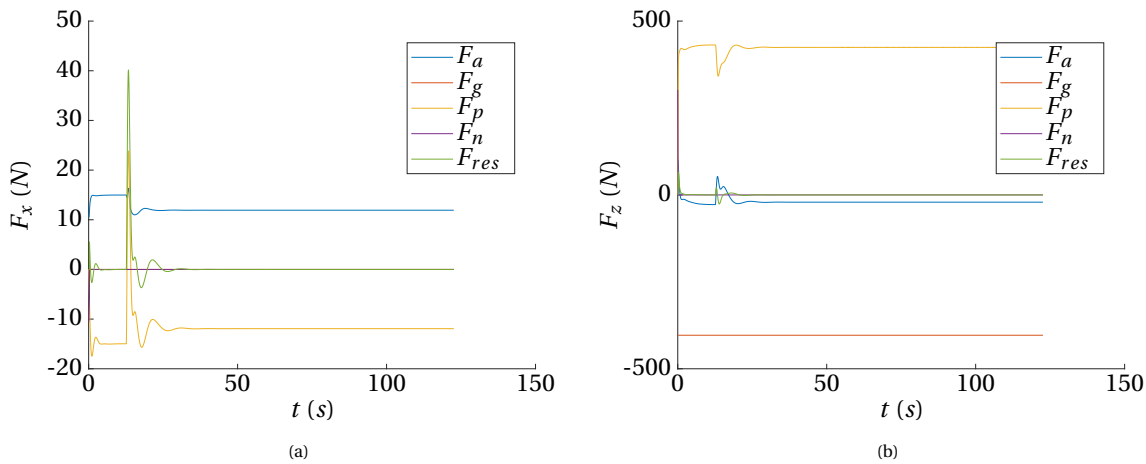


Figure 5.41: Component forces

Results resizing

A resized battery mass based on the simulation is given in Table 5.9. Here the mass of the battery is given for three (3) cases: as a result of the preliminary sizing, as a result of the simulation using the induced power and as a result of the simulation including the profile power. When the rotor profile power is neglected (P_{ind}), the battery mass increases with 0.5% compared to the sizing result. This is very little, mainly because the power requirement during transition drops. This slight increase is due to the slightly higher take-off time (extra time to accelerate) and hence required energy. When including profile power in the simulation the battery mass increases with 25% compared to the sizing result. Hence an additional 24.5% due to the profile power. This is much higher compared to previous simulations. It is not clear 100% clear what drives this high profile mass due to the multiple factors that play a role. Presumably, the high rotor diameter and low root blade twist result in this high profile power. It is recommended for future work to analyse this in more detail.

Table 5.9: Resizing based on simulation

	Preliminary sizing	Simulation (P_{ind})	Simulation (P_{tot})
m_{bat}	1.0608kg	1.0686kg (+0.5%)	1.3257kg (+25%)

5.3.3. Knee-sitter (-30°) concept

In this section simulation results for the knee-sitter concept will be given for winds speeds of 5 m/s and 10m/s.

A. $V_W = 5 \text{ m/s}$

Results sizing and rotor design

The sizing results and rotor design parameters for the knee-sitter concept which are used to validate the dynamic feasibility are given in Table 5.10.

Table 5.10: Results sizing and rotor design

Sizing		Rotor design and input sim.	
$m_{VTOL}[kg]$	4.1361	$P_{E,max}[W]$	$(3588.9362/n_{rot}) * f_{control}$
$m_{bat}[kg]$	0.84289	$T_{des}[N]$	$381.1459/n_{rot}$
$m_{mot}[kg]$	1.292	$\alpha_{rot,des}[deg]$	65.5938
$m_{rot}[kg]$	0.96718	$J_p[kgm^2]$	0.0286
$v_{c,1}[m/s]$	2.2751	$\theta_0[deg]$	37.2727
$v_{x,1}[m/s]$	0	$K_T[]$	0.0103
$v_{c,2}[m/s]$	1.3805		
$v_{x,2}[m/s]$	1.7149		
$D_{rot}[m]$	1.192		

Simulation results

Variable set 1: Flight path and velocity

Looking at the simulated flight path depicted in Figure 5.42a, it can be concluded that the flight path can be flown within the available power limit. The kinematic speed of the aircraft is depicted in Figure 5.42b. The speed components are depicted in Figure 5.43. For the transition from first to second segment some oscillation around the target speed can be observed. After about 10 seconds these are died out and the target speed is reached.

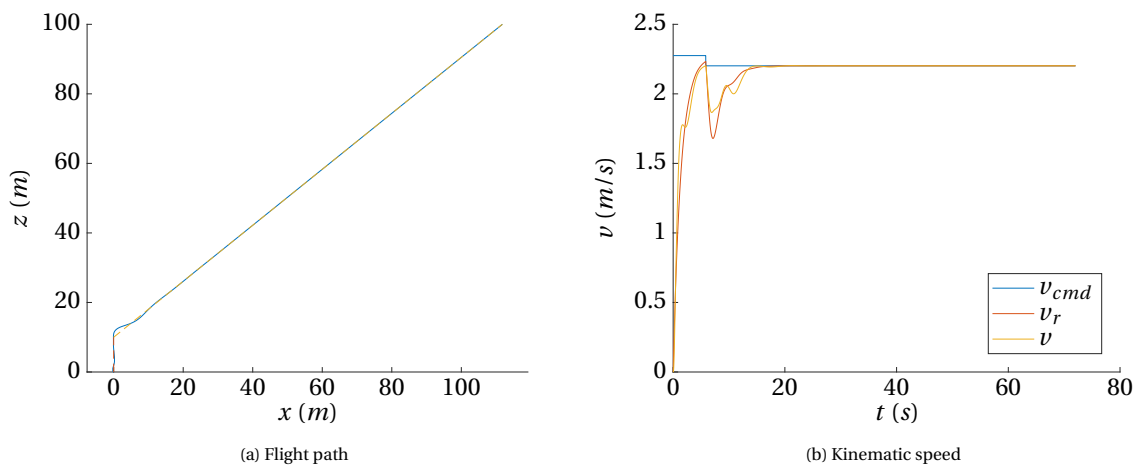


Figure 5.42

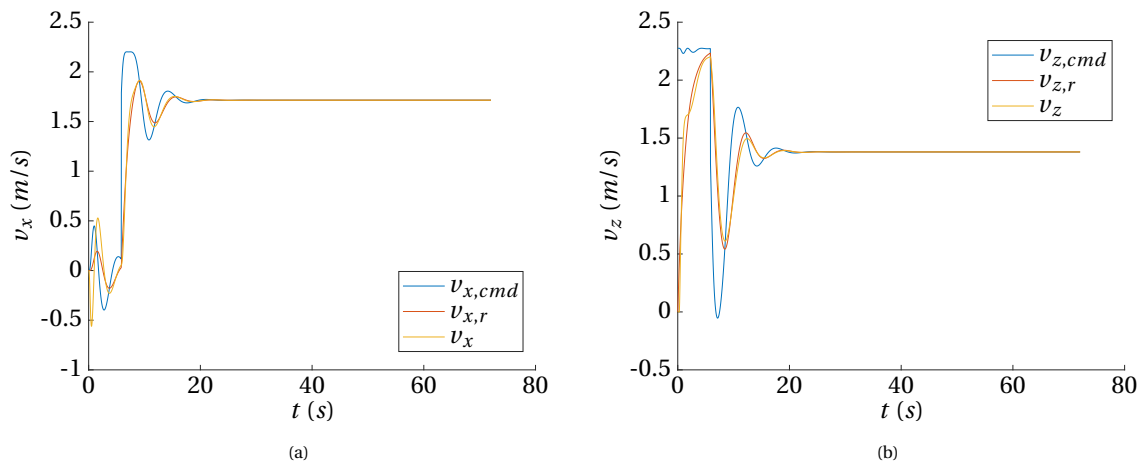


Figure 5.43: Kinematic speed components

Variable set 2: Aircraft attitude and angle of attack

The aircraft attitude and angle of attack of rotor and wing are depicted in Figure 5.44a and 5.44b, respectively. To transition from first to second segment, a similar manoeuvre than the quad-plane is made; pitching up the aircraft to 37 degrees. This corresponds to an increase in wing angle of attack of 18.5 degrees, which is slightly above stall. Pitch then decreased and also the angle of attack accordingly. The wing is operating in an angle of attack range between 3.5 and 18.5 degrees, this is a much more attractive operating range as compared to the quad-plane or tail-sitter.

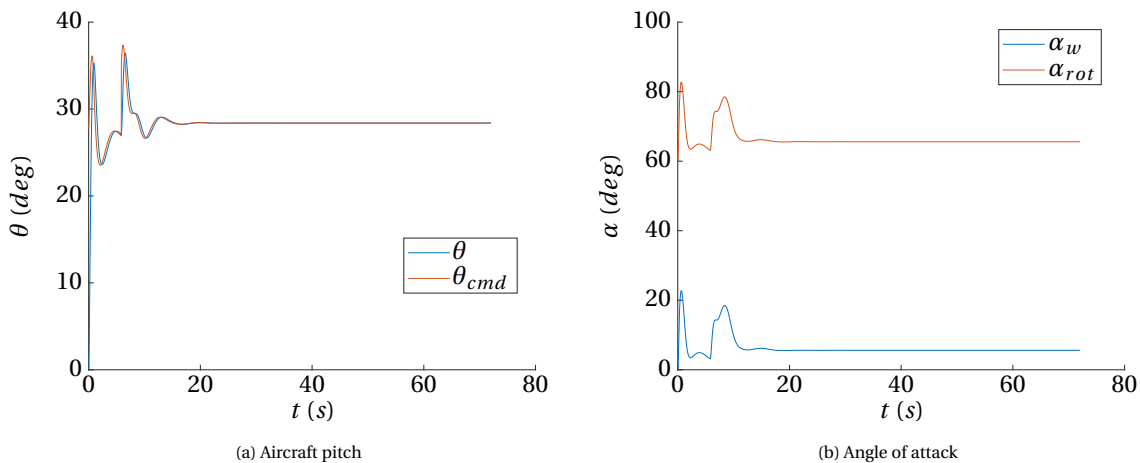


Figure 5.44

Variable set 3: Thrust and power

The aircraft thrust and power are depicted in Figure 5.45a and 5.45b, respectively. Contrary to the quad-plane, the thrust is now below the gravity force. The thrust also decreases to transition between the segments as was also found for the quad-plane. The behaviour of the power is similar after a short peak to wind up the rotors. The power requirement when steady state is reached is the same for both segments. The profile drag adds an additional 11 % to the power requirement.

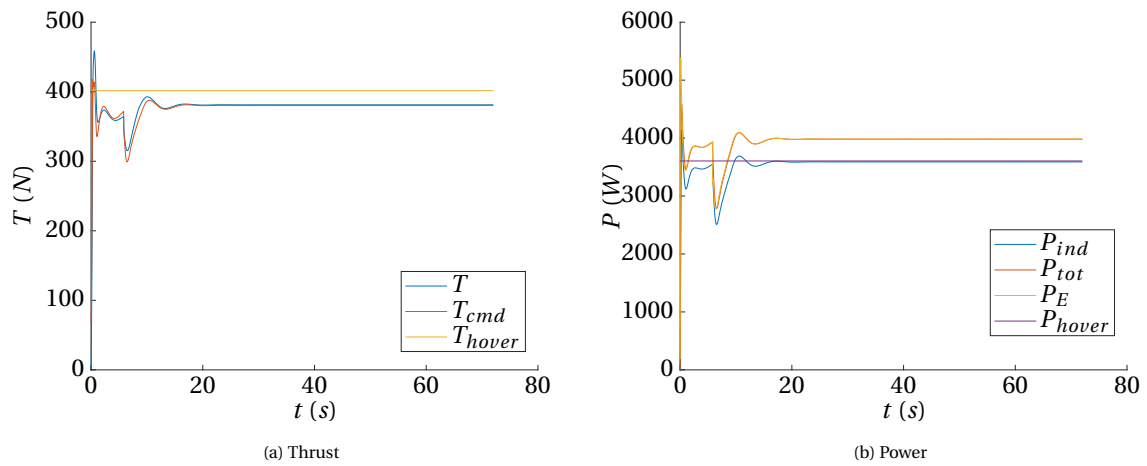


Figure 5.45

Variable set 4: Forces

The force components of aerodynamic force, gravity force, propulsion force and resulting force are depicted in Figure 5.46. The main forces acting are the gravity and propulsion forces. Aerodynamic forces are low, yet favourable.

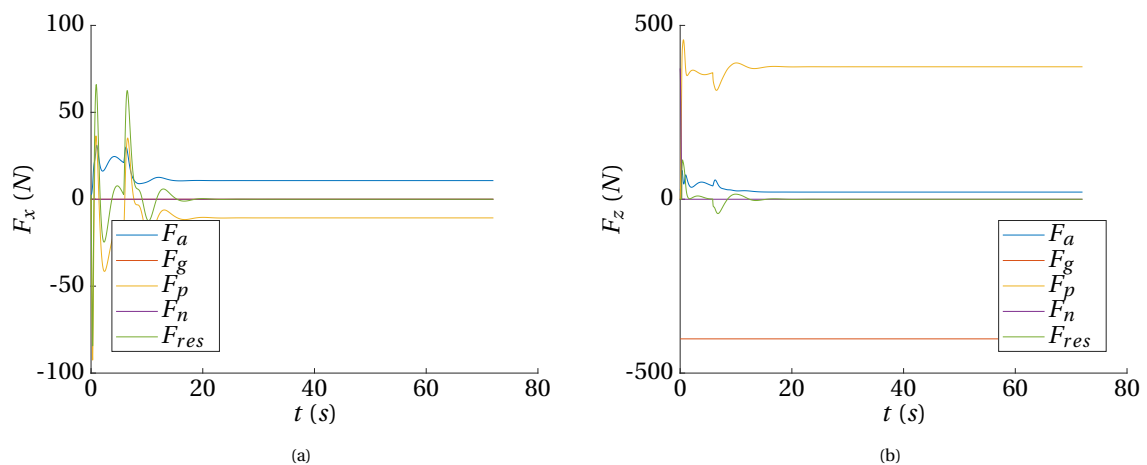


Figure 5.46: Component forces

Results resizing

A resized battery mass based on the simulation is given in Table 5.11. Here the mass of the battery is given for three (3) cases: as a result of the preliminary sizing, as a result of the simulation using the induced power and as a result of the simulation including the profile power. When the rotor profile power is neglected (P_{ind}), the battery mass increases with 2.4% compared to the sizing result. Extra power is required during the transient and acceleration phase. Furthermore, the take-off phase takes also longer due to the acceleration time and requires more energy. Nevertheless, 2.4% is low and can be justifiably neglected in the preliminary sizing when including a safety factor. When including profile power in the simulation the battery mass increases with 13.6% compared to the sizing result. Hence an additional 11.2% due to the profile power. Compared to the safety factor ($f_{control}$) of 50% that is taken into account in the preliminary sizing, this is acceptably low and can be neglected in the preliminary design phase.

Table 5.11: Resizing based on simulation

	Preliminary sizing	Simulation (P_{ind})	Simulation (P_{tot})
m_{bat}	0.84289kg	0.8631kg (+2.4%)	0.9574kg (+13.6%)

B. $V_W = 10 \text{ m/s}$ **Results sizing and rotor design**

The sizing results and rotor design parameters for the knee-sitter concept which are used to validate the dynamic feasibility are given in Table 5.12.

Table 5.12: Results sizing and rotor design

Sizing		Rotor design and input sim.	
$m_{VTOL}[kg]$	2.2247	$P_{E,max}[W]$	$(1437.69/n_{rot}) * f_{control}$
$m_{bat}[kg]$	0.66171	$T_{des}[N]$	$173.32/n_{rot}$
$m_{mot}[kg]$	0.51757	$\alpha_{rot,des}[deg]$	72.8593
$m_{rot}[kg]$	0.48922	$J_p[kgm^2]$	0.0076
$v_{c,1}[m/s]$	0.93572	$\theta_0[deg]$	33.9394
$v_{x,1}[m/s]$	0	$K_T[]$	0.0025
$v_{c,2}[m/s]$	0.71604		
$v_{x,2}[m/s]$	0.8895		
$D_{rot}[m]$	0.86423		

Simulation results**Variable set 1: Flight path and velocity**

Looking at the simulated flight path depicted in Figure 5.47a, it can be concluded that the flight path can be flown within the available power limit. The kinematic speed of the aircraft is depicted in Figure 5.47b. The speed components are depicted in Figure 5.48. For the transition from first to second segment some oscillation around the target speed can be observed. After about 10 seconds these are died out and the target speed is reached. In this simulation less oscillation occurs in the velocity than for other concepts.

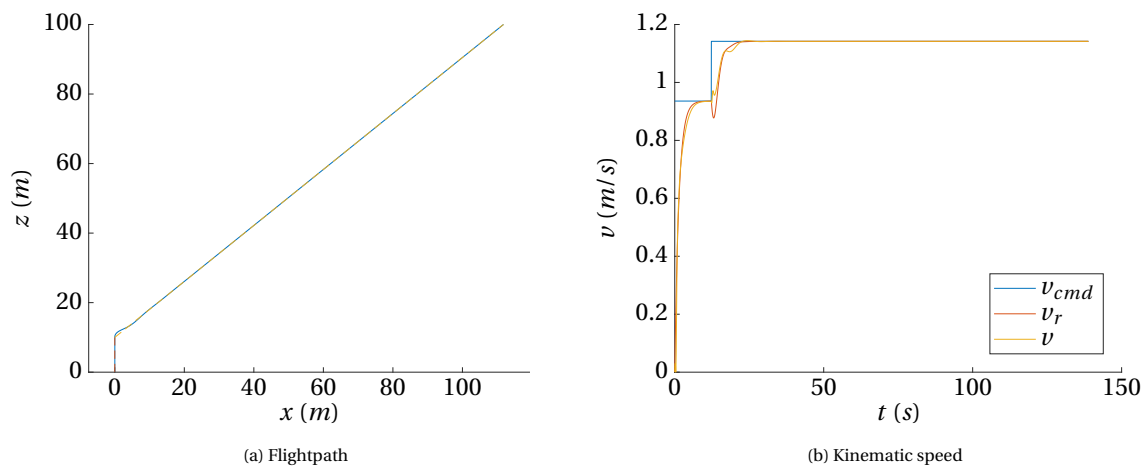


Figure 5.47

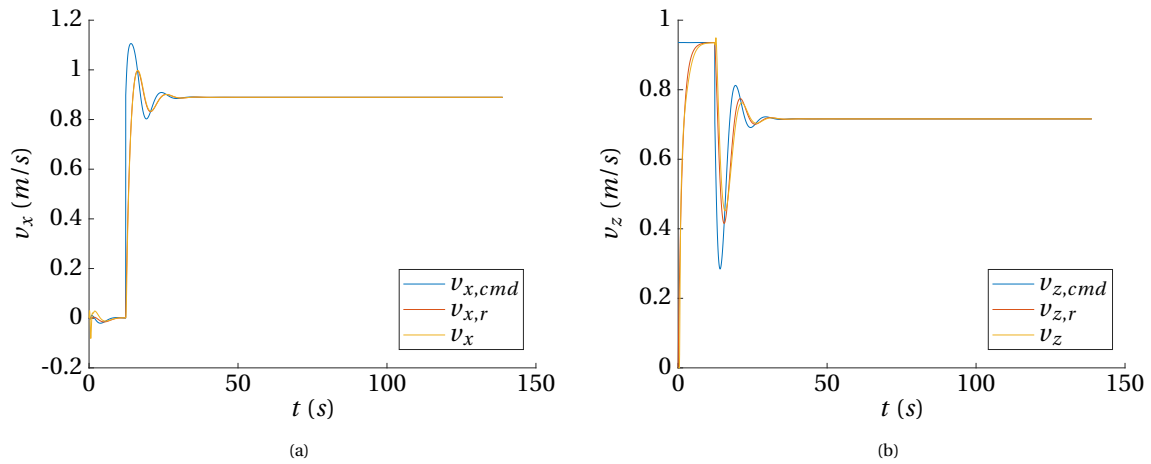


Figure 5.48: Kinematic speed components

Variable set 2: Aircraft attitude and angle of attack

The aircraft attitude and angle of attack of rotor and wing are depicted in Figure 5.49a and 5.49b, respectively. The behaviour for both angles is found similar to the low speed simulation. An important result here is the angle of attack operating regime. With the exception of the startup phase, the angle of attack ranges between 15.8 and 9.6 degrees. The take-off phase for this concept and wind condition can therefore be executed without stall and with positive angles of attack, meaning that the aerodynamic lift force can be used as an advantage throughout the whole take-off manoeuvre.

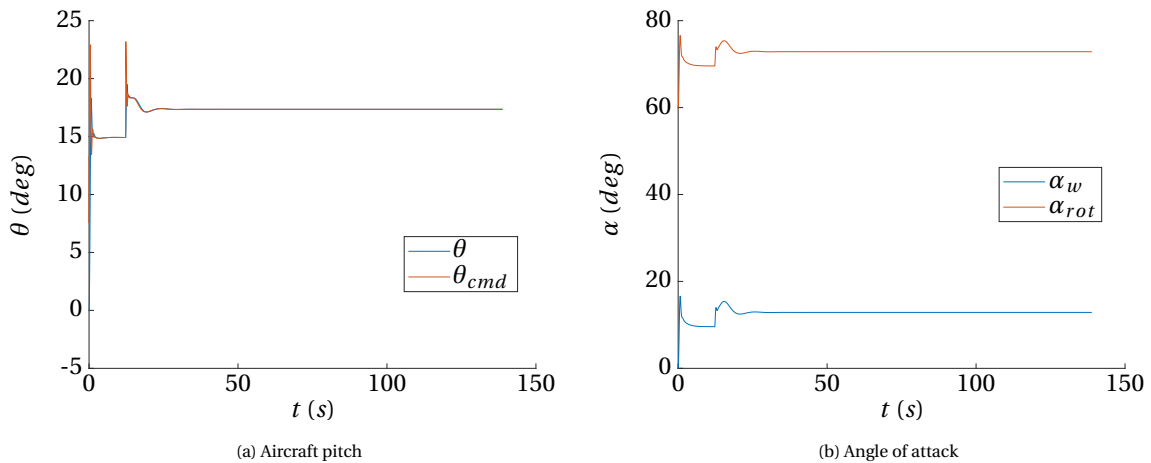


Figure 5.49

Variable set 3: Thrust and power

The aircraft thrust and power are depicted in Figure 5.50a and 5.50b, respectively. The effect that the angle of attack is positive and below stall becomes clearly visible in the thrust and power requirement. For both transient and steady state condition, they are found far below the zero wind hover requirement.

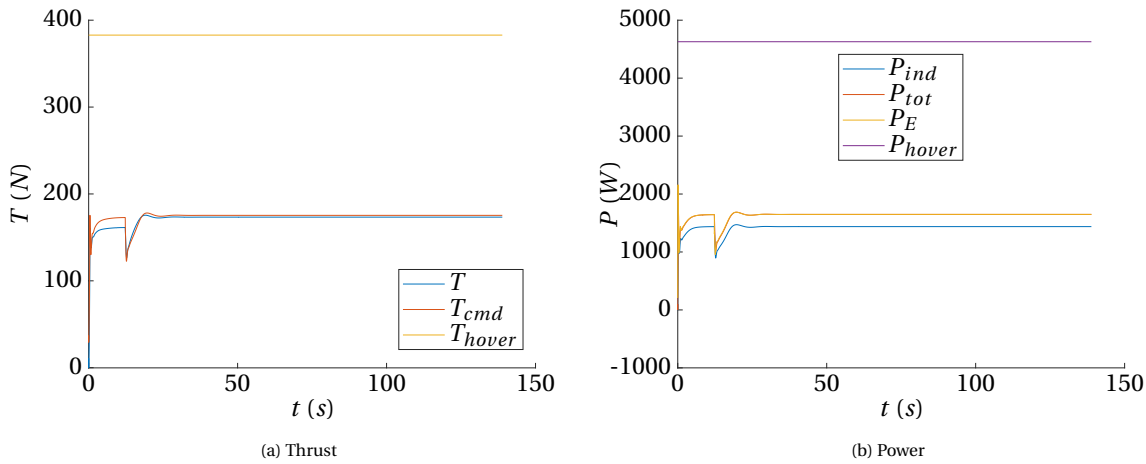


Figure 5.50

Variable set 4: Forces

The force components of aerodynamic force, gravity force, propulsion force and resulting force are depicted in Figure 5.51. The main forces acting are the gravity and propulsion and aerodynamic forces. Aerodynamic forces are high and favourable.

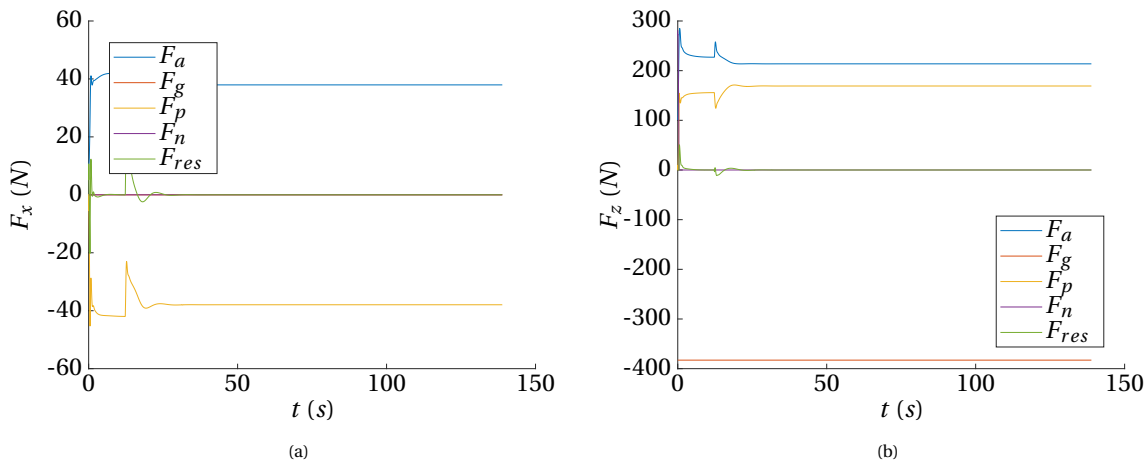


Figure 5.51: Force components

Results resizing

A resized battery mass based on the simulation is given in Table 5.5. Here the mass of the battery is given for three (3) cases: as a result of the preliminary sizing, as a result of the simulation using the induced power and as a result of the simulation including the profile power. When the rotor profile power is neglected (P_{ind}), the battery mass increases with 0.8% compared to the sizing result. This is lower compared to the simulation with wind speed 5m/s. This is explained by the fact that the power does not increase much above the steady state value for the transient phase. When including profile power in the simulation the battery mass increases with 15.5% compared to the sizing result. Hence an additional 14.7% due to the profile power. This is 3.5% higher than in the simulation with a wind speed of 5m/s. Presumably this is caused by the lower rotor root blade twist (pitch). A detailed analysis of the profile power is left for future work. Compared to the safety factor ($f_{control}$) of 50% that is taken into account in the preliminary sizing, this is still acceptably low and can be neglected in the preliminary design phase.

Table 5.13: Resizing based on simulation

	Preliminary sizing	Simulation (P_{ind})	Simulation (P_{tot})
m_{bat}	0.66171kg	0.6669kg (+ 0.8 %)	0.7642kg (+15.5%)

5.4. Synthesis dynamic feasibility

A simulation is performed for the tail-sitter, quad-plane and knee-sitter concepts, for a wind speed of 5m/s and 10m/s. These simulations have shown that, under the assumptions of the simulation, the maximum motor power (from sizing model) is sufficient to successfully fulfill the take-off phase. It is found that the maximum motor power is only used to accelerate the rotor initially. It is not required in the transient flight phases.

Based on the simulation, the required energy is calculated and the battery is resized for each simulation. For each simulation there is a resizing using the induced power (similar to the sizing tool) and one including the profile power.

It is found that under the same assumptions of the sizing model (neglecting profile power), extra required battery capacity falls in between 0.5% - 4.5%. The higher values are found for the low wind speed (5%). There is no significant difference here for the different concepts. The extra battery capacity is required due to additional energy required in the acceleration and transient phases. Because these values are low, ignoring dynamic effects and acceleration is justified in the sizing model.

Furthermore, a resizing is done including the profile power. The profile power as a percentage of the total power for the different simulations is given in Table 5.14. The value for the quad-plane concept for a wind speed of 10 m/s is remarkably high. When looking at Table 5.14, there is an inverse relation between the rotor root twist θ_0 and the additional power. The rotor root twist θ_0 is optimized (minimized profile power) for the design conditions (i.e. $\alpha_{rot,des}$), and constraint by a maximum angle of attack along the blade. It can be observed from Table 5.14 that the higher rotor inflow angle $\alpha_{rot,des}$, the lower θ_0 and the higher the additional profile power. There seem to be no direct relation between the rotor diameter and the additional profile power. A more detail analysis of the rotor design at high rotor inflow angle is left for future work.

Table 5.14: Profile power as a percentage of total power for the different simulations

	$P_{prof}[\%]$	$D_{rot}[m]$	$\theta_0[deg]$	$\alpha_{rot,des}[deg]$
Tail-sitter (5m/s)	10.2	1.18	38.5	51.8
Tail-sitter (10m/s)	9.3	1.11	39.1	51.0
Quad-plane (5m/s)	10.1	1.22	38.5	53.4
Quad-plane (10m/s)	24.5	1.35	30.3	83.1
Knee-sitter (5m/s)	11.2	1.19	37.3	65.9
Knee-sitter (10m/s)	14.7	0.86	33.9	72.9

Except for the 24.5%, the additional profile power is acceptable low compared to the the safety factor ($f_{control}$) of 50% that is taken into account in the preliminary sizing, and can be neglected in the preliminary design phase.

6

Conclusions, recommendations and future work

6.1. Conclusions

This research is focused on state-of-the-art analysis and review, sizing, design analysis and simulation of different vertical take-off and landing (VTOL) system concepts applicable for airborne wind energy systems (AWES) launch mechanisms. The most important research questions, derived from the state-of-the-art analysis are: 1. What VTOL concept is most suitable for AWE applications? and 2. How do the aerodynamic forces of the AWES effect the VTOL system design? These are addressed and thoroughly analyzed in this research.

The concepts that are considered are: tilt-rotor, tail-sitter, quad-plane and a newly introduced knee-sitter as depicted in Figure 6.1. This new concept introduced in this research is based on the analysis and the results of the tilt-rotor concept. The knee-sitter concept features a rotor tilted 30 degrees forward compared to the quad-plane rotor position (0°). All concepts have been sized for a wind-speed range of 0-10 m/s, and three (3) target elevation angle strategies: 41.8 degrees, 65.9 degrees and 90 degrees. This research provides a fundamental baseline when pursuing one of the presented VTOL system concepts.

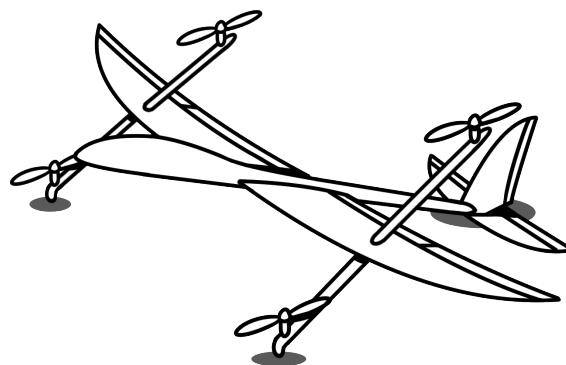


Figure 6.1: Concept drawing knee-sitter

For the tilt-rotor concept the required VTOL system mass decreases with wind speed for all target elevation angles. A VTOL system mass of 4.3kg is required for wind speeds below 4 m/s and decreases to 2.1kg for a wind-speed of 10 m/s. This decrease in mass is made possible by tilting the rotor such that the AWE aircraft wing operates under a positive and non-stalled angle of attack in the wind. This results in a large aerodynamic force that aids the rotors during take-off and reduces the power and energy demand of the VTOL system

significantly. This research concludes that the difference in VTOL mass between the target elevation angle strategies is low.

Contrary to the tilt-rotor concept, the required VTOL system mass for the tail-sitter concept increases with wind speed and with higher target elevation angles. A VTOL system mass of 4.4kg is required for zero wind speed and increases to 4.9kg for a wind speed of 10 m/s. Contrary to initial research expectations. This increase is not increase in thrust, which is actually slightly decreasing with the wind speed. The analysis shows that it is the required power that is increasing due to an increase of axial inflow velocity.

Similar to the tail-sitter concept, the required VTOL mass for the quad-plane concept increases with the target elevation angle. However, regarding wind speed, there is a peak in required VTOL mass of 4.6 kg for a wind speed of 7.6 m/s, and it decreases after 7.6m/s to a VTOL mass of 4.3 kg at a wind speed of 10 m/s. For zero (0) wind speed the required VTOL system mass is 4.5 kg. This contrary to the tail-sitter this increase in VTOL system mass is due to an increase in thrust. This concept needs to counteract the negative lift forces.

In the category of fixed rotor, it can be concluded that nor the tail-sitter nor the quad-plane concept can benefit from aerodynamic forces, instead, they have to counteract it. In order to combine the potential advantages and based on the results of the tilt-rotor, a new innovative concept has been introduced, named the knee-sitter concept. From the detailed analysis of the tilt-rotor, it is observed that the tilt-rotor has a rotor pitch between -30 and -40 degrees for the target elevation angle of 41.8 degrees and wind speeds between 6-10 m/s. So this new concept is introduced with a rotor fixed at -30 degrees, named as the "knee-sitter". For the knee-sitter, similar to the tilt-rotor concept, the VTOL system mass is now found to decrease again for all elevation angles. A VTOL system mass of 4.6kg is required for zero wind speed and decreases to 2.2kg for a wind-speed of 10 m/s. This approximates the result of the tilt-rotor concept.

The concepts are compared for a target elevation angle of 41.8° and 90°. The tilt-rotor concept sets the lower requirement on VTOL system mass as it can tilt its rotors in the most optimal configuration at any time. However, no extra mass of the tilting mechanism is accounted for to do so. While the knee-sitter concept can also benefit from the aerodynamic forces without requiring a tilting mechanism, this research on mass analysis concludes that the knee-sitter concept is the concept of choice for the vertical take-off and landing (VTOL) system concept applicable for airborne wind energy systems (AWE) launch mechanisms.

One drawback of the knee-sitter however is that, due to the fixed rotor orientation, the drag in the power generation phase can be penalizing. Whereas the tilt-rotor can also tilt the rotor in a way that this drag is reduced. Furthermore, the tilt-rotor might offer more control authority during gusts as the rotors can be moved separately from the AWE aircraft. Therefore control can be decoupled from aircraft attitude. On the other hand, drawbacks of the tilt-rotor include reduction of structural integrity and additional complexity. Also with the tail-sitter concept, the orientation of the rotors is less penalizing regarding drag in the power generation phase.

A dynamic simulation has proved the feasibility of the sizing results for the tail-sitter, quad-plane and the new knee-sitter concept for a wind speed of 5 m/s and 10 m/s and a target elevation angle of 41.8 degrees. These simulations have shown that, under the assumptions of the simulation, the maximum motor power (from sizing model) is sufficient to successfully fulfill the take-off phase. For the knee-sitter concept, the AWE aircraft wing was operating at positive and non-stall angles of attack during the complete take-off manoeuvre. Therefore the aerodynamic force can be used to aid the rotors throughout the complete take-off.

It is found that the maximum motor power is only used to accelerate the rotor initially. It is not required during the transient flight phases. Furthermore, it is found that the additional power and energy, required for acceleration and transient phases are sufficiently low (max +4.5%) compared to the safety factor of 1.5 which has been taken into account in the preliminary sizing model. Therefore, ignoring dynamic effects and acceleration is justified in the sizing model. The profile power is found to cause an additional 11%, on average and can also be neglected in the sizing model. For the simulation of the quad-plane concept at 10 m/s, the additional profile power was found to be remarkably higher with a value of 24.5%. This needs to be analysed in future work.

6.2. Recommendations and future work

Hereafter, recommendations are made concerning the developed sizing model, optimization framework, simulation, results and operational considerations for the VTOL system.

Sizing model

The specific power of the battery is found to be an important parameter of the sizing of the VTOL system battery. Due to the nature of the relatively short take-off phase, power consumption is high, but consumed energy is relatively low. Little has been found on figures of the specific power of a LiPo battery. It is recommended for future work to analyse this parameter more in depth and to use a more accurate value in the sizing model.

In the sizing model the mass of the rotor is estimated using the parameterization given in [6]. This parameterization is based on rotors with a mass up to 100g. From the optimized results, the heaviest rotors were 350g. The parameterization is therefore extrapolated which can lead to an erroneous estimate of the rotor mass. It is recommended for future work to develop a rotor mass parameterization based on heavier rotors. This parameterization can be done similar to [50], here more rotor parameters are taken into account such as amounts of blades and rotor solidity.

The aerodynamic model is based on experimental results for the AP2 at low angles of attack, blended with a flat plate model for high angles of attack (beyond stall). This model can be improved by providing a 360-degree angle of attack range aerodynamic model for the AP2 using CFD or wind tunnel experiment. Furthermore, during take-off apparent speed, dictated by the wind speed, is low. Therefore, also the Reynolds number is low. The aerodynamic model can be further improved by providing figures at these low Reynolds numbers. Especially an accurate model near stall is useful, as the optimal results operate at these angles of attack to maximize the aerodynamic lift during take-off. It can, therefore, have a significant impact on the sizing of the VTOL system.

For the rotor model a combination of BEM and MT given in [44] is used to predict the rotor power. For the preliminary sizing, the induced power prediction with an appropriate induced power factor κ is used. For this purpose, also the generalized momentum theory (without BEM) can be used as it gives the same power prediction. It is important to emphasize that for this problem a generalized momentum theory should be used instead of one applied for hover or axial climb, as the oblique inflow has a major effect on the power prediction. On the other hand, for more detailed design models this BEM model is a good starting point.

For this work, the tether weight has been assumed and agreed negligible. In a next iteration the weight can be considered by adding the weight of the tether at maximum length during vertical take-off to the AWE aircraft weight. In the preliminary sizing model, a mass fraction of 25% is used to take into account masses of other subsystems such as the VTOL structure and ECS. This fraction can be updated in the sizing model after the detailed design phase or when more knowledge about these subsystems is obtained.

Regarding the wind speed, uniform wind speed is assumed throughout the take-off phase. Generally, the wind is increasing with altitude. For the concept taking advantage of the wind to take-off (tilt-rotor and knee-sitter concept), the minimum wind speed at the ground is critical for the sizing of the motors. For the concept that must counteract the wind (tail-sitter), the maximum wind is critical for the sizing of the motor. For the battery sizing, and average wind speed can be taken if the specific power is not limiting. If the battery specific power is limiting, maximum power drives the battery mass.

Optimization framework

For the problem at hand, the optimizer converges to large rotors diameters, in most cases found above 1m (total 4 rotors). This can result in a high drag penalty for the VTOL system. It is recommended to examine this drag penalty and apply bounds to the rotor diameter in the optimization accordingly.

In this research, the clearance height and target elevation angle were kept fixed during the optimization. In the next iteration, they can be variables in the optimization. This might be beneficial for fixed-rotor concepts, to avoid a stall flow region over the AWE aircraft wing or to attain a certain angle of attack.

The multi-disciplinary optimization framework is constructed in a way that it can be easily extended with more detailed models. For example, a more detailed blade element model can be used to design and optimize

the rotor. The battery model can be extended to include electrical parameters such as voltage, energy capacity and cell count. Furthermore, more segments can be added to the flight path, which allows analysing an indirect take-off approach. Also, landing can be added, when the sizing model is extended with a suitable rotor model for landing.

The variation of initial conditions was found critical to converge to a global optimum. In the future, other optimization algorithms can be tested which can rid the need for this variation. The optimization framework is constructed in a way that the optimization algorithm can be easily exchanged.

Simulation (dynamic feasibility)

In the simulation wind is modelled as a uniform profile. Generally, the wind speed has a profile where the wind-speed is increasing with altitude. Especially if the system is sized for a certain wind speed range, it is important to simulate the behaviour also outside this range. Also, close to the ground, the ground effect can be added to the simulation. The ground effect might aid the rotors close to the ground where there is less wind to lift the AWE aircraft.

In the simulation, the aerodynamic force is looped back to the controller, this might not be possible in a real application or only with a low fidelity aerodynamic model. Due to the complex nature of aerodynamics, errors will arise between real aerodynamic forces and estimated once. The controller is required to cope with this when implementing the controller in a prototyping phase.

A limitation to the rotor model in the simulation is the small angle of attack assumption for the BEM model. This can lead to erroneous results outside the conditions where the rotor is designed for. Using an extended version of the BEM model, where lift and drag coefficients are taken from look-up tables with an appropriate angle of attack range, this problem can be avoided.

The dynamic feasibility of tail-sitter, quad-plane and knee-sitter are validated for a wind speed of 5m/s and 10m/s. In future work, the dynamic feasibility of the tilt-rotor concept needs to be validated. This requires an additional controller for the rotor tilt actuator to be added to the existing simulation.

Results

For the variable analysis, variables are plotted for a wind-speed range of 10m/s. It is recommended, especially when perusing the tail-sitter concept, to extend this range.

In this research the focus was on the sizing of the VTOL system in a direct take-off approach scenario. The sizing tool also lends itself to analyze the indirect take-off scenario by e.g. adding an extra segment in the flight path.

Due to aerodynamic drag, the aircraft must pitch in the wind to counteract this force. Here a tether force might aid, avoiding the need for the aircraft to tilt. In this way, power might be reduced due to the decrease in the axial inflow of the rotors. This also can provide the aircraft more positive aerodynamic lift, in the case of a quad-plane concept.

For the dynamic feasibility of the tail-sitter, quad-plane and knee-sitter it is recommended to perform this simulation for more wind speeds, also for very high wind speeds, to validate the design.

Operational considerations

During the power generation phase, one (1) or more rotors from the VTOL system can generate power to load the batteries of the VTOL system and AWE aircraft. This is however not possible for the quad-plane concept, due to the orientation of the rotors parallel to the flow. Here, a deployment mechanism can be developed to reduce drag in the power generation phase. For other fixed positions, power generation might be possible due to the axial flow component in the rotor.

Regarding operation, also a semi-tilt rotor can be introduced and analysed in future work. This concept can tilt its rotor before take-off (based on measured wind speed) and after, but without active control during take-off. This might lower the requirements and complexity of a tilt-system. This concept also has the advantage that the rotors can be tilted in a position for minimum drag or to generate auxiliary power during the power generation phase. Furthermore, for landing the rotors can be tilted in a position optimum for landing. The results from the tilt-rotor analysis can be used as a look-up table to set the rotor tilt.

Another variant of the tilt-rotor concept is one where not all rotors can tilt, but only the most critical ones, e.g. the ones installed on the wing, to reduce aerodynamic interference with the wing. Furthermore, when using a tri-copter configuration (3 rotors), with one rotor installed at the tail, the AWE aircraft nose is free from disturbances. This avoids disturbing laminar flow at the nose of the AWE aircraft.

Outlook

Additional drag caused by the VTOL system on the AWE aircraft performance is still an unknown area, but yet an important design decisions. Therefore, as part of future work, this needs to be further analysed, including trade-off drag versus the weight of the VTOL system and their relative importance.

The amount of time the AWES is on the ground (e.g. maintenance, extreme weather conditions, after emergency landing) should be estimated, together with the energy loss per year if the VTOL system cannot operate above or below a certain wind speed. Therefore, this must be further analysed.

According to the developed design methodology, the next design phase is the detailed design of the VTOL system. These phases include the detailed rotor design, autopilot (controller) design, electrical system design (determining motor, battery and ESC electric properties) and finally, aerodynamic consideration (lay-out design). These design activities should be performed by discipline specialists.

Regarding the detailed design of the rotor, the rotor should be carefully designed for oblique inflow condition. Higher fidelity models are required in future work to analyse this effect. For the aerodynamic considerations, such as interference effects between the VTOL system and AWE aircraft, a detailed CFD study should be performed.

In the sizing model, a safety factor is included in the power to consider the power required for general control and control during gusts. To have a better understanding of this requirement and to validate it a six (6) degree of freedom (DOF) simulation should be developed in which wind and gusts can be simulated. To start, the 2D simulation model presented in this work can be used as a base-line extended with a pitch controller.

Furthermore, also the transition to power generation phase should be simulated with a six (6) DOF model. A winch model is required if the transition is assisted with the winch. The transition can be simulated with the 2D model, by adding the winch model. The aircraft should then be controlled to accelerate to an apparent speed above stall, where the aerodynamic lift takes over the function of the rotors. This is easiest by acceleration into the wind. If a transition simulation is performed, it should be validated whether the transition manoeuvres put any significant constraints on the VTOL system regarding the required power and energy.

In future work landing should be considered, one of the challenges here will be the rotor model as general momentum theory is not valid if the inflow velocity enters in the direction of thrust. This might be the case due to a downward velocity component.

Bibliography

- [1] Mirac Aksugur and Gokhan Inalhan. Design methodology of a hybrid propulsion driven electric powered miniature tailsitter unmanned aerial vehicle. *Journal of Intelligent and Robotic Systems: Theory and Applications*, 57(1-4):505–529, 2010. ISSN 09210296. doi: 10.1007/s10846-009-9368-0.
- [2] C. Ampatis and E. Papadopoulos. Parametric Design and Optimization of Multi-Rotor Aerial Vehicles. *Springer Optimization and Its Applications*, 91(3):1–25, 2014. ISSN 19316836. doi: 10.1007/978-3-319-04720-1_1.
- [3] Ozlem Armutcuoglu, Mehmet Serif Kavsoglu, and Ozan Tekinalp. Tilt Duct Vertical Takeoff and Landing Uninhabited Aerial Vehicle Concept Design Study. *Journal of Aircraft*, 41(2):215–223, 2008. ISSN 0021-8669. doi: 10.2514/1.271.
- [4] Florian Bauer, Christoph M. Hackl, Keyue Smedley, and Ralph M. Kennel. Multicopter-Based Launching and Landing of Lift Power Kites. 2016.
- [5] RANDAL W. BEARD and TIMOTHY W. McLAIN. *Small Unmanned Aircraft: Theory and Practice*.
- [6] Dmitry Bershinsky, Steve Haviland, and Eric N. Johnson. Electric Multirotor UAV Propulsion System Sizing for Performance Prediction and Design Optimization. pages 1–22, 2016. doi: 10.2514/6.2016-0581.
- [7] E. Bontekoe. Up! How to Launch and Retrieve a Tethered Aircraft. *Master of Science Thesis, TU Delft, Faculty of Aerospace Engineering*, 2010.
- [8] Rieck Burkhard, Ranneberg Maximilian, Candade Ashwin, Bormann Alexander, and Skutnik Stefan. Comparison of Launching Landing Approaches.
- [9] R. W. Jr. Boswinkle C.C. Critzos, H.H. Heyson. Aerodynamic characteristics of NACA 0012 airfoil section at angles of attack from 0 degrees to 180 degrees. 1955.
- [10] D. Cheng, A.C. Charles, S. Srigrarom, and H. Hesse. Morphing Concept for Multirotor UAVs Enabling Stability Augmentation and Multiple-Parcel Delivery. *AIAA Science and Technology Forum and Exposition*, 2019.
- [11] Antonello Cherubini, Andrea Papini, Rocco Vertechy, and Marco Fontana. Airborne Wind Energy Systems: A review of the technologies. *Renewable and Sustainable Energy Reviews*, 51:1461–1476, 2015. ISSN 18790690. doi: 10.1016/j.rser.2015.07.053.
- [12] Puspita Triana Dewi, Ghazali Suhariyanto Hadi, Muhammad Ramadhan Kusnaedi, Aris Budiarto, and Agus Budiyo. Design of Separate Lift and Thrust Hybrid UAV. *The Journal of Instrumentation, Automation and Systems*, 2(2):45–51, 2018. doi: 10.21535/jias.v2i2.697.
- [13] Moritz Diehl. Airborne Wind Energy : Basic Concepts and Physical Foundations. pages 3–22. doi: 10.1007/978-3-642-39965-7.
- [14] L. Fagiano and S. Schnez. On the take-off of airborne wind energy systems based on rigid wings. *Renewable Energy*, 107:473–488, 2017. ISSN 18790682. doi: 10.1016/j.renene.2017.02.023.
- [15] L. Fagiano, E. Nguyen-Van, F. Rager, S. Schnez, and C. Ohler. Automatic Take-Off of a Tethered Aircraft for Airborne Wind Energy: Control Design and Experimental Results. *IFAC-PapersOnLine*, 50(1):11932–11937, 2017. ISSN 24058963. doi: 10.1016/j.ifacol.2017.08.1456.
- [16] W. Froude. On the Elementary Relation Between Pitch, Slip, and Propulsive Efficiency. 1920.
- [17] Mauro Gatti and Fabrizio Giulietti. Preliminary design analysis methodology for electric multirotor. *IFAC Proceedings Volumes (IFAC-PapersOnline)*, 2(PART 1):58–63, 2013. ISSN 14746670. doi: 10.3182/20131120-3-FR-4045.00038.

- [18] K. Geebelen, H. Ahmad, M. Vukov, S. Gros, J. Swevers, and M. Diehl. An experimental test set-up for launch/recovery of an Airborne Wind Energy (AWE) system. pages 4405–4410, 2014. doi: 10.1109/acc.2012.6315033.
- [19] Licitra Giovanni. Identification and Optimization of an Airborne Wind Energy System. 2018.
- [20] Herman Glauert. *Airplane Propellers. In: Aerodynamic Theory*. Springer, Berlin, Heidelberg. ISBN 978-3-642-89630-9.
- [21] Jay Gundlach. Designing Unmanned Aircraft Systems: A Comprehensive Approach. 2014.
- [22] Ohad Gur and Aviv Rosen. Optimizing Electric Propulsion Systems for UAVs. (September 2008), 2012. doi: 10.2514/6.2008-5916.
- [23] M. Hepperle. Electric Flight – Potential and Limitations. *presented at the AVT-209 Workshop on Energy Efficient Aircraft Configurations, Technologies and Concepts of Operation, Sao José dos Campos*, 2013.
- [24] John H Horlock. Actuator Disk Theory: Discontinuities in Thermo Fluid Dynamics. 1978.
- [25] J.C. van der Vaart E. de Weerd C.C. de Visser A.A. in 't veld E. Mooij J.A. Mulder, W.H.J.J. van Staveren. *flight Dynamics, Lecture notes*. Delft University of Technology, 2013.
- [26] Haibo Jiang, Yanru Li, and Zhongqing Cheng. Relations of Lift and Drag Coefficients of Flow around Flat Plate. *Trans Tech Publications, Switzerland*, 2014. doi: 10.4028/www.scientific.net/AMM.518.161.
- [27] Andrew B. Lambe and Joaquim R. R. A. Martins. Extensions to the design structure matrix for the description of multidisciplinary design, analysis, and optimization processes. *Structural and Multidisciplinary Optimization*, 46:273–284, 2012. doi: 10.1007/s00158-012-0763-y.
- [28] J. Gordon Leishman. *Principles of Helicopter Aerodynamics*. Cambridge Aerospace Series, 2002.
- [29] Miles L Loyd. Crosswind Kite Power. *Journal of Energy*, 4(3):106–111, 1980.
- [30] C.A. Luongo. Next Generation More-Electric Aircraft: A Potential Application for HTS Superconductors. *IEEE Transactions on Applied Superconductivity*, vol. 19, no. 3, pp. 1055–1068, 2009.
- [31] Elena Malz, Jonas Koenemann, and Sebastian Gros. A reference model for airborne wind energy systems for optimization and control. 2018.
- [32] B.W. McCormick. *Aerodynamics of VISTOL flight*. New York, Academic Press.
- [33] Matthew McCrink and James W. Gregory. Blade Element Momentum Modeling of Low- Re Small UAS Electric Propulsion Systems. *33rd AIAA Applied Aerodynamics Conference*, (June):1–23, 2015. doi: 10.2514/6.2015-3296. URL <http://arc.aiaa.org/doi/10.2514/6.2015-3296>.
- [34] Koji Muraoka, Noriaki Okada, and Daisuke Kubo. Quad Tilt Wing VTOL UAV: Aerodynamic Characteristics and Prototype Flight. (April):6–13, 2012. ISSN 2009-1834. doi: 10.2514/6.2009-1834.
- [35] Wayne Ong, Spot Srigrarom, and Henrik Hesse. Design Methodology for Heavy-Lift Unmanned Aerial Vehicles with Coaxial Rotors. 9781624105(January):7–11, 2019. doi: 10.2514/6.2019-2095.
- [36] Ugur Ozdemir, Yucel Orkut, Aktas Aslihan, and Vuruskan Yasin. Design of a commercial hybrid VTOL UAV system Design of a Commercial Hybrid VTOL UAV System. (May 2013), 2016. doi: 10.1007/s10846-013-9900-0.
- [37] Sebastian Rapp and Roland Schmehl. Vertical Takeoff and Landing of Flexible Wing Kite Power Systems. *Journal of Guidance, Control, and Dynamics*, 41(11):2386–2400, 2018. ISSN 0731-5090. doi: 10.2514/1.g003535.
- [38] Daniel P. Raymer. Aircraft Design: A Conceptual Approach (Edition). (AIAA education series), 2006.
- [39] J. Roskam. Airplane design, part v: component weight estimation. *Roskam Aviation Corporation, Ottawa, Kansas*, page 85, 1985.

- [40] M. K. Rwigema. Propeller Blade Element Momentum Theory with Vortex Wake Deflection. *International Congress of the Aeronautical Sciences*, pages 1–9, 2010. URL <http://www.ewp.rpi.edu/hartford/~ernesto/S2013/MMEES/Papers/ENERGY/6AlternativeEnergy/McCosker/Rwigema2010.pdf>.
- [41] Adnan S. Saeed, Ahmad Bani Younes, Chenxiao Cai, and Guowei Cai. A survey of hybrid Unmanned Aerial Vehicles. *Progress in Aerospace Sciences*, 98:91–105, 2018. ISSN 03760421. doi: 10.1016/j.paerosci.2018.03.007.
- [42] Watcharapol Saengphet and Chalothorn Thumthae. Conceptual Design of Fixed Wing-VTOL UAV for AED Transport. (December), 2016.
- [43] R. Schmehl. Airborne Wind Energy an introduction to an emerging technology, 2019. URL <http://awesco.eu/awe-explained/#presently-pursued-concepts>.
- [44] Brian L. Stevens, Frank L. Lewis, and Eric N. Johnson. Modeling and Simulation of Miniature Aerial Vehicles. 2015.
- [45] Roland Hugh Stone and K C Wong. Preliminary Design of a Tandem-Wing Tail-Sitter UAV Using Multi-Disciplinary Design Optimisation. *International Aerospace Congress*, (May):707–720, 1997.
- [46] B Theys and J De Schutter. Parameter selection method and performance assessment for the preliminary design of electrically powered transitioning VTOL UAVs. 2016.
- [47] B. Theys, G. Dimitriadis, P. Hendrick, and J. De Schutter. Experimental and numerical study of micro-aerial-vehicle propeller performance in oblique flow. *Journal of Aircraft*, 54(3):1076–1084, 2017. ISSN 00218669. doi: 10.2514/1.C033618.
- [48] Maxim Tyan, Nhu Van Nguyen, and Jae-woo Lee. A Hybrid VTOL-Fixed Wing Electric UAV Sizing Methodology Development. (October), 2016.
- [49] Maxim Tyan, Nhu Van Nguyen, Sangho Kim, and Jae Woo Lee. Comprehensive preliminary sizing/re-sizing method for a fixed wing – VTOL electric UAV. *Aerospace Science and Technology*, 71, 2017. ISSN 12709638. doi: 10.1016/j.ast.2017.09.008.
- [50] Justin Winslow, Vikram Hrishikeshavan, and Inderjit Chopra. Design Methodology for Small-Scale Unmanned Quadrotors. *Journal of Aircraft*, (January):1–9, 2017. ISSN 0021-8669. doi: 10.2514/1.c034483.
- [51] M. Zanon, S. Gros, and M. Diehl. Rotational start-up of tethered airplanes based on nonlinear mpc and mhe.